Springer Proceedings in Materials

Partha Ghosal
C. Barry Carter
Kutti Ragunath Vinothkumar
Rajdeep Sarkar *Editors*

# Applications of Microscopy in Materials and Life Sciences

## Proceedings of 12th Asia-Pacific Microscopy Conference

Springer

# Springer Proceedings in Materials

Volume 11

**Springer Proceedings in Materials** publishes the latest research in Materials Science and Engineering presented at high standard academic conferences and scientific meetings. It provides a platform for researchers, professionals and students to present their scientific findings and stay up-to-date with the development in Materials Science and Engineering. The scope is multidisciplinary and ranges from fundamental to applied research, including, but not limited to:

- Structural Materials
- Metallic Materials
- Magnetic, Optical and Electronic Materials
- Ceramics, Glass, Composites, Natural Materials
- Biomaterials
- Nanotechnology
- Characterization and Evaluation of Materials
- Energy Materials
- Materials Processing

To submit a proposal or request further information, please contact one of our Springer Publishing Editors according to your affiliation:

European countries: **Mayra Castro** (mayra.castro@springer.com)
India, South Asia and Middle East: **Priya Vyas** (priya.vyas@springer.com)
South Korea: **Smith Chae** (smith.chae@springer.com)
Southeast Asia, Australia and New Zealand: **Ramesh Nath Premnath** (ramesh.premnath@springernature.com)
The Americas: **Michael Luby** (michael.luby@springer.com)
China and all the other countries or regions: **Mengchu Huang** (mengchu.huang@springer.com)

More information about this series at http://www.springer.com/series/16157

Partha Ghosal · C. Barry Carter ·
Kutti Ragunath Vinothkumar · Rajdeep Sarkar
Editors

# Applications of Microscopy in Materials and Life Sciences

## Proceedings of 12th Asia-Pacific Microscopy Conference

Springer

*Editors*
Partha Ghosal
Defence Metallurgical Research Laboratory
Hyderabad, Telangana, India

Kutti Ragunath Vinothkumar
National Centre for Biological Sciences
Bengaluru, India

C. Barry Carter
Department of Materials Science & Engineering
University of Connecticut
Storrs Mansfield, CT, USA

Rajdeep Sarkar
Defence Metallurgical Research Laboratory
Hyderabad, Telangana, India

ISSN 2662-3161 ISSN 2662-317X (electronic)
Springer Proceedings in Materials
ISBN 978-981-16-2981-5 ISBN 978-981-16-2982-2 (eBook)
https://doi.org/10.1007/978-981-16-2982-2



This Springer imprint is published by the registered company Springer Nature Singapore Pte Ltd.
The registered company address is: 152 Beach Road, #21-01/04 Gateway East, Singapore 189721, Singapore

# Preface

The Asia-Pacific Microscopy Conference (APMC), a very popular and successful conference series, is held every four years since 1956 under the aegis of the Committee of Asia-Pacific Societies of Microscopy (CAPSM), which is a member of the International Federation of Societies for Microscopy (IFSM). These conferences are held in different cities of Asia-Pacific region in collaboration with different local bodies of microscopy to promote electron microscopy and various allied techniques and their application in carrying out scientific research towards the development of science and technology. The conferences provide a platform for the young researchers and microscopists to interact with world-renowned scientists in the field and also with the industrial partners. Across the globe, several electron microscopy bodies or unions such as International Microscopy Congresses (IMC), European Microscopy Congresses (EMC), Multinational Congresses on Microscopy (MCM), Microscopy Society of America (MSA) and IFSM regularly organize electron microscopy conferences or workshops in different parts of the worlds.

The Electron Microscope Society of India (EMSI), which is one of the affiliated organizations of CAPSM and IFSM, organized the 12th APMC at Hyderabad, India, during 3–7 February 2020. The conference included a wide range of topics under three main streams—material sciences, life sciences and microscopy techniques. Dedicated sessions on microscopy of metals and alloys, glass, ceramics, composites, high energy materials, functional materials, thin films and coatings, low-dimensional materials, electronic and photonic materials and other materials were included under material science. Sessions on microscopy techniques included aberration-corrected TEM and STEM, SEM–FIB, ion beam microscopy, electron diffraction and crystallography, EBSD, orientation microscopy in TEM/PED, microscopy-based microanalysis, SPM, spectroscopy analysis, cryo-electron microscopy, 3D-APT, in situ techniques, etc. Sessions under life sciences dealt with microscopy and imaging associated with bio-nanotechnology, medical applications, host–pathogen interaction, brain structure, animal physiology and development, application in paleontology, flow cytometry, diseases and immunocytochemistry, multimodal molecular imaging in health and disease, imaging methods in medicine, virology and taxonomy and other related topics.

There were lectures by world-renowned speakers presenting the advancement in microscopy along with the new findings in materials and life sciences using different microscopic techniques. Young researchers, students and scholars below the age of 40 were encouraged to submit new and highlighting results in their respective fields, which were evaluated under the category student/young researchers. Around 600 abstracts were submitted for the conference including the invited and contributory presentations.

Upon completion of the conference, we planned to publish a few papers as proceedings of the conference along with Springer Nature and requested the speakers to send their papers for the publication. We are extremely grateful to those who have submitted full paper for the proceedings. These papers include submission on materials sciences, life sciences and instrumentation techniques. All of the submitted papers went through a rigorous peer-review process, and a total of 26 papers were accepted for publication. We hope this proceedings will definitely help the young researchers in the field of microscopy to carry forward their research, as most of the papers are in new areas and new findings, in the respective area.

Hyderabad, India — Partha Ghosal
Storrs Mansfield, USA — C. Barry Carter
Bengaluru, India — Kutti Ragunath Vinothkumar
Hyderabad, India — Rajdeep Sarkar

# Contents

## Life Science

# About the Editors

**Dr. Partha Ghosal** is a senior Scientist G in DMRL, Hyderabad and is heading the Electron Microscopy Group. He received his Ph.D. from Indian Institute of Technology (IIT-BHU), Varanasi in the field of Metallurgical Engineering in 1996 and worked on the effect of crystal defects in the diffraction theory for ordered HCP alloys. He spent one year as DAAD visiting scientist in TU Clausthal, Germany to work on EBSD techniques. Currently, he is working in the area of advanced characterization techniques, along with SEM, EBSD, FIB, TEM, HRTEM and Raman-AFM systems. His current interests include in-situ mechanical testing and heating experiments of nano and advanced materials inside electron microscopes and advanced Raman analysis for these materials. Extensive electron microscopic works on Ti-based alloys, W-based alloys and nano-composites are also in the scope of his interest. He is involved in establishing an advanced materials characterization centre for the country at DRDO. He has around 146 international papers, over 100 invited presentations and 3 patents to his credit. He is a fellow of EMSI with 25 years of research experience. He is member of Electron Crystallography (IUCr) from India. He is reviewer of 11 reputed international journals and life member of professional national bodies such as IIM, MRSI, EMSI and MSI.

**Dr. C. Barry Carter** is a Research Professor and Emeritus Professor at the University of Connecticut, USA. He holds a B.A., M.A. and Sc.D. from Cambridge University, an M.Sc. from Imperial College, London, and a D.Phil. from Oxford University. After 6 years in Oxford, he moved to Cornell where he spent 14 years leaving as a full Professor. He spent 16 years as Professor and the 3M Endowed Multidisciplinary Chair in the Department of Chemical Engineering and Materials Science at the University of Minnesota and 5 years as Head of UConn's Department of Chemical, Materials and Biomolecular Engineering. He is a CINT Distinguished Affiliate Scientist at Sandia National Lab. He had earlier held visiting positions at LANL, Chalmers, NIMS in Tsukuba, Bristol University, Max Planck Institute in Stuttgart, the Institute for Physical Chemistry in Hanover and the Ernst Ruska Center in Jülich. He has been awarded a Guggenheim Fellowship and the

Alexander von Humboldt Senior Award. He is the Editor-in-Chief of the Journal of Materials Science, a journal cited more than 55,099 times in 2019 and 2 million downloads in 2020. His research interests focus on the application of different microscopies to understand how the structure and chemistry of materials determine their properties and behavior. He works on several projects including a study of the deformation of Ta and its growth in thin-film form, electrospinning of $TiO_2$, lithiation of nanomaterials, especially Sn whiskers and $MoS_2$, for battery applications, and how the crystallization dynamics control the properties of phase-change materials.

**Dr. Kutti Ragunath Vinothkumar** is a Structural Biologist and Biochemist based at National Centre for Biological Sciences, Bengaluru, India. He pursued his Ph.D. in Membrane protein structural biology from Max-Planck Institute of Biophysics, Frankfurt. Dr. Vinothkumar subsequently joined the Laboratory of Molecular Biology, Cambridge, where he was associated with Dr. Richard Henderson, a pioneer in the field of electron cryomicroscopy. In 2017, he joined National Centre for Biological Sciences, Bengaluru, where his lab research interests spans from macromolecular complexes in signalling to enzymes involved in bioremediation. In addition, Dr. Vinothkumar also directs the National CryoEM facility housed in the Institute of Stem Cell Science and Regenerative Medicine, which along with NCBS is part of the Bangalore Life Science campus.

**Dr. Rajdeep Sarkar** is a scientist at the Defence Metallurgical Research Laboratory (DMRL), Hyderabad, India. He received his Bachelor of Engineering (Metallurgy) degree from the National Institute of Technology (NIT), Durgapur in 2003. He completed his M.Tech. and Ph.D. degree in Metallurgical and Materials Engineering from Indian Institute of Technology (IIT), Kharagpur in 2005 and 2015, respectively. His area of specialization includes structural and sub-structural characterization (using TEM and related techniques) of materials, like titanium alloys, super alloys, tungsten alloys and nano-materials, along with structure-property correlation. He is life member of the Indian Institute of Metals (IIM), Electron Microscope Society of India (EMSI) and Materials Research Society of India (MRSI). He has currently a credential of 64 publications in peer-reviewed international journals.

# Materials Science

# Electron Microscopy: An Important Tool for Preparation and Characterization of Asymmetric Ceramic-Polymer Composite Nanofiltration Membrane


**Sanjukta Roy, Swachchha Majumdar, Ganesh C. Sahoo, and Priyanka Mondal**

**Abstract** Membrane technology has emerged as an important tool in sustainable management of water and energy owing to its high efficiency and low footprint. Ceramic polymer composite membranes are an emerging category which tends to combine the merits of both pure ceramic and polymeric membranes. The present work elucidates the role of electron microscopy in preparation and characterization of novel ceramic-supported-polymeric asymmetric composite membrane developed by successive pore size reduction of commercial macroporous ceramic support. In each step of preparation process, formation of a layer (ceramic intermediate layers and polymeric functional layer) with conforming properties was evaluated and its morphology was studied in details with the help of Field Emission Scanning Electron Microscopy (FESEM) analysis. An amine-functionalized composite membrane was developed using polyethyleneimine as functional layer material over modified alumina-based ceramic substrate. The membrane was found to exhibit a water permeability of 3.9-3.1 L m-2 h-1 bar-1 and a low molecular weight cut-off (< 2000) suggesting its nanofiltration nature toward contaminant rejection. The membrane demonstrated a maximum removal of 93.5% of Crystal Violet dye from 25 mg/l aqueous solution at 4 bar pressure. The excellent stability of the membrane in high-pressure application suggests its potential use in other nanofiltration application.

S. Roy · S. Majumdar · G. C. Sahoo · P. Mondal
Water Technology Division, CSIR-Central Glass and Ceramic Research Institute, 196, Raja S.C. Mullick Road, Kolkata 700 032, India

S. Roy · P. Mondal (✉)
Academy of Scientific and Innovative Research (AcSIR), CSIR-HRDC Campus, Sector 19, Kamla Nehru Nagar, Ghaziabad, Uttar Pradesh 201002, India



P. Ghosal et al. (eds.), *Applications of Microscopy in Materials and Life Sciences*, Springer Proceedings in Materials 11,
https://doi.org/10.1007/978-981-16-2982-2_1

## 1 Introduction

Membrane technology occupies an integral position among the various existent separation technologies due to its lower footprint when compared to conventional methods of separation [1, 2]. The prevalent membranes that have found wide industrial application are mainly either polymeric or ceramic in nature. Concurrently substantial research is being carried out to bridge the gap between the properties of 'all-ceramic' and 'all-polymeric' membranes, and thus, the concept of ceramic-polymeric composite membranes has emerged that aim at blending the merits of both the types of membranes. Ceramic-supported-polymeric membranes combine the mechanical robustness of the ceramic support along with the pore size tunability of polymeric functional layer.

The fabrication of a stable and conformal ceramic-supported-polymeric composite membrane essentially depends on the proper amalgamation of the two materials in terms of adhesion with each other, which in turn depends on the properties of the ceramic substrate and the polymer used as functional layer material. Moreover, microstructure and functionality of the substrate have a significant impact on the formation of defect-free thin-film active layer irrespective of the membrane material, ceramic, or polymeric. Thus, in case of ceramic-supported-polymeric composite membranes, proper surface modification of ceramic substrate and congruent functionalities of the polymeric counterpart plays a crucial role in preparation of a high-quality membrane [3].

The present work elucidates the role of electron microscopy in preparation and characterization of novel ceramic-supported-polymeric composite nanofiltration membrane for application in contaminated wastewater treatment. The asymmetric composite membrane was developed by successive pore size reduction of commercial macroporous ceramic support via incorporation of consecutive layers over it. In each step of the preparation process, formation of a layer (ceramic intermediate layers and polymeric functional layer) with conforming properties was evaluated, and its morphology was studied in details with the help of field emission scanning electron microscopy (FESEM) analysis. An amine-functionalized composite membrane was developed using polyethylenimine as functional layer material over modified alumina-based ceramic substrate and its efficacy in removal of crystal violet (CV) dye from aqueous solution was studied.

## 2 Materials and Methods

Indigenously developed tubular clay-alumina based low cost ceramic microfiltration membrane of pore size 1.6 μm and OD/ID 10 mm/7 mm was used as primary support. The base macroporous support was modified using super ground alumina and boehmite sol in order to develop a ceramic substrate with requisite pore size and functionality for thin polymeric top layer formation. Modification of the

support was carried out by incorporation of two successive ceramic intermediate layers. The first layer was developed by coating an aqueous slurry comprising of super ground alumina and boehmite (4:1) along with polyvinyl alcohol (PVA) as binder. The coating was followed by sintering at 1200 °C. The second intermediate layer was formed by coating aqueous slurry consisting of 10 wt% boehmite sol and PVA. The coating was sintered at 600 °C. The modified substrate was then successively dip coated with 5 wt% crosslinker (glutaraldehyde) solution and 1 wt% functional layer material (polyethyleneimine) solution. The resulting composite membranes were kept in room temperature for 6 h to allow for proper crosslinking and then thoroughly rinsed and stored in distilled water till further use. Membranes, each having length of 150 mm and effective filtration area of 0.0027 $m^2$, were used for clean water permeability, molecular weight cut-off, and dye rejection study [4].

The prepared membrane was characterized with the help of FESEM (Gemini Zeiss Supra™, 35VP, Germany), energy-dispersive X-ray (EDX) analysis (Carl Zeiss, ΣIGMA, Germany), Brunauer–Emmett–Teller (BET) pore size analysis (Quantachrome, USA), contact angle goniometer (DSA25S, Kruss, Germany), atomic force microscopy (AFM) (Nanonics, Israel), and thermogravimetric analysis (TGA) (NETZSCH STA 449 F3 Jupiter).

## 3 Results and Discussion

### *3.1 FESEM and EDX Analysis*

Figure 1a shows the cross-sectional view of the pristine ceramic support where high porosity can be observed throughout. The surface view (Fig. 1b) further confirms its macroporous nature. Figure 1c shows cross section of the ceramic-polymer composite membrane prepared over the support. The FESEM image clearly reveals the asymmetric nature of the composite membrane. Region I in the figure depicts the macroporous ceramic support structure followed by layers II and III denoting the two ceramic intermediates of decreasing pore size. Thickness of layer II is $\sim$10 μm and layer III is $\sim$5 μm. The final polymeric top layer (layer IV) is $\sim$1 μm in thickness. Formation of continuous and defect-free polymeric top layer can be confirmed from the surface FESEM image (Fig. 1d).

The cross-sectional EDX analysis of the composite membrane (Fig. 2) shows high intensity of aluminum in the support and intermediate layers. The fluctuations in the intensities of the elements in the intermediate layers are mainly due to sample roughness. A decline in aluminum and oxygen intensity and simultaneous sharp rise in carbon intensity at the top edge, resulting in a cross-over of the peaks, denotes the thin polymeric functional layer of about 1 μm thickness.

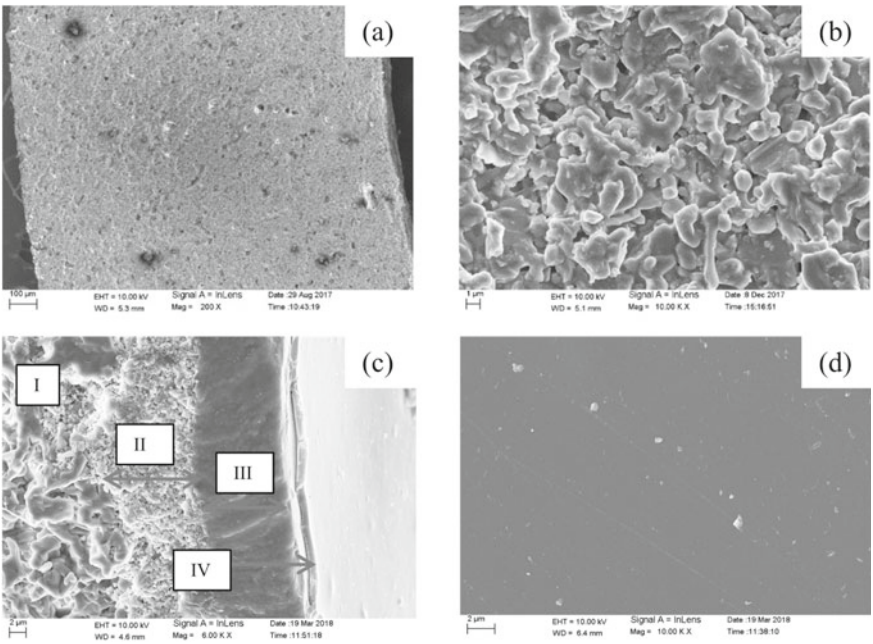


**Fig. 1** FESEM images of **a** cross section and **b** surface of pristine ceramic support, **c** cross section and **d** surface of prepared composite membrane

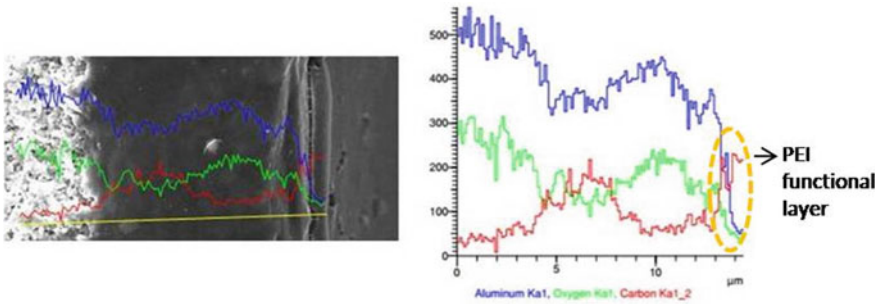


**Fig. 2** EDX analysis of cross section of prepared composite membrane

## *3.2 Pore Size and Contact Angle Analysis*

BET analysis has been performed to find out the final pore size of the composite membrane. Nitrogen has been used as the adsorbate gas. The analysis reveals average pore size of the functional layer of the composite membrane to be 1.9 nm. Thus, a microporous membrane could be formed on the modified ceramic support with a single polymeric layer. Also, contact angle of the functional top layer is measured to be 54.2°, which suggests its hydrophilic nature.

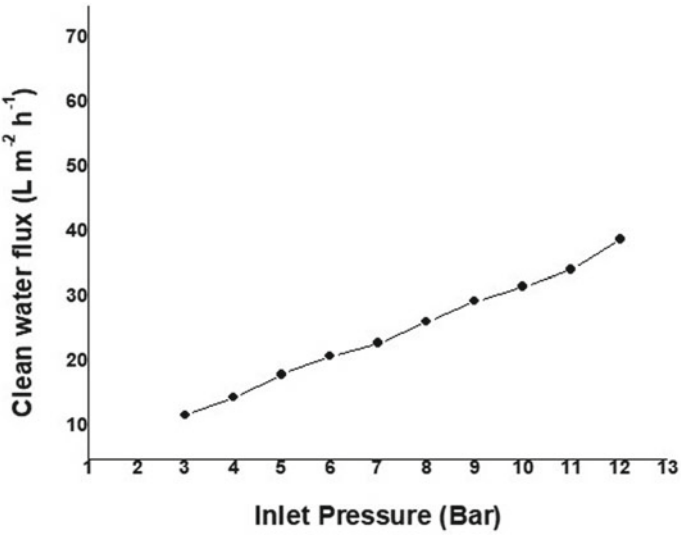


**Fig. 3** Clean water permeability study of prepared composite membrane

## 3.3 Clean Water Permeability Study

The flux and rejection study of the prepared membrane has been carried out in a cross-flow filtration setup. The composite membrane has been initially compacted at 12 bar for 1 h, and water fluxes were measured at inlet pressures ranging from 3 to 12 bar. The pure water permeability was determined by Darcy's Law as follows:

$$J_w = L_p \cdot \Delta P = \frac{\Delta}{\mu \cdot R_m} \tag{1}$$

Clean water flux through the composite membrane at different inlet pressures is shown in Fig. 3. The permeability coefficient is in the range of 3.1–3.9 L $m^{-2}.h^{-1}.bar^{-1}$.

## 3.4 Molecular Weight Cutoff (MWCO) and Dye Removal Efficiency Study

MWCO of the membrane when studied with different molecular weights of polyethylene glycol (PEG) revealed >90% removal was obtained with 2000 molecular weight (Fig. 4a). Thus, the rejection behavior of the prepared composite membrane suggests its potential application in nanofiltration process.

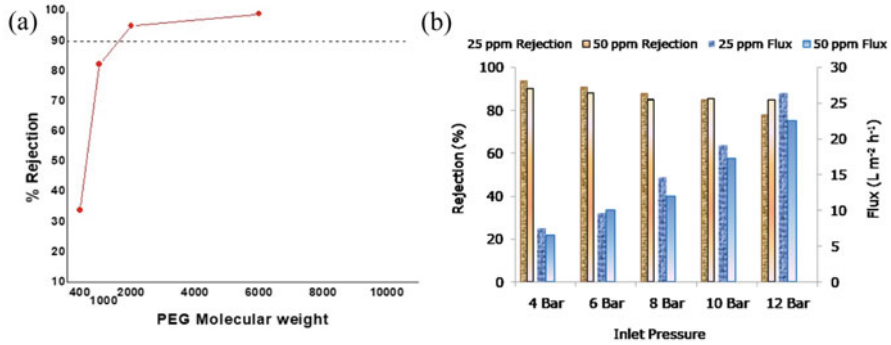


**Fig. 4** **a** MWCO study of composite membrane **b** Flux and rejection of aqueous CV dye solution through composite membrane

Consequently, dye removal capacity of the composite membrane was evaluated using two different concentrations of CV dye solutions, 25 mg $L^{-1}$ and 50 mg $L^{-1}$. Acceptable rejection of dye was obtained for both the concentrations with the highest rejection of 93.5% at 4 bar with 25 mg $L^{-1}$ concentration (Fig. 4b). Such high rejection of a low molecular weight dye (408 Da) CV with a membrane of MWCO 2000 as prepared in the present work has not been reported previously [5, 6]. Donnan exclusion phenomenon and steric hindrance between the cationic dye and the positively charged PEI functional layer played a significant role in high rejection of the low molecular weight (408 Da) dye.

Flux was higher for lower dye concentration at most of the inlet pressures and was found to increase with increase of inlet pressure, which was well in accordance with the principle of filtration. Rejection percentage of dye was also higher for lower feed concentration and was found to decrease with increase of inlet pressure. Such a behavior can be accounted for taking into consideration the role of concentration polarization phenomenon in the filtration process. The increase in dye concentration in the feed and increase in operating pressure results in enhanced concentration polarization effect which causes a drop in the rejection rate [7]. Thus, there remains a scope of further improvement of membrane structure for reduction/mitigation of concentration polarization aiding in enhancement of membrane performance.

## *3.5 Composite Membrane Fouling Behavior Study*

AFM analysis of the composite membrane surface before and after 24 h of filtration operation was performed to study the fouling behavior. Similar approach for qualitative assessment of membrane fouling propensity has been adopted by other

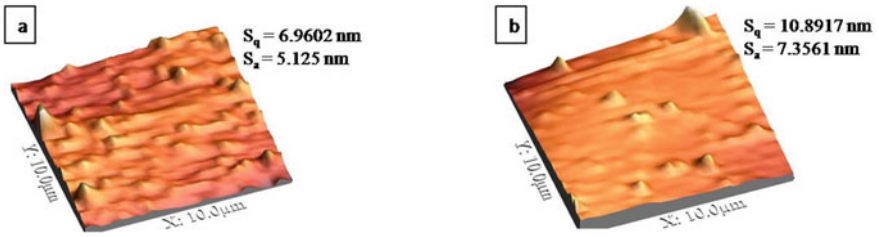


**Fig. 5** AFM analysis of composite membrane surface **a** before and **b** after dye filtration

researchers where AFM images of clean and fouled membranes were compared [8, 9]. In typical membrane fouling studies, duration of each cycle of filtration operation is 2–8 h depending on the rate of flux declination [10, 11]. Since no significant flux declination was observed after 24 h of filtration operation in this case, the antifouling nature of the membrane was confirmed by AFM analysis. Figure 5 reveals that the membrane surface appears to be smoother after filtration due to some accumulation of dye molecules in the valleys. However, significant changes in membrane RMS roughness ($S_q$) and average roughness ($S_a$) do not appear after dye filtration which suggests the absence of severe fouling. Repulsion between the similarly charged membrane surface and dye along with the hydrophilic nature of PEI results in less severe fouling of the membrane.

## *3.6 Chemical and Thermal Stability of Prepared Composite Membrane*

The acid and alkali stability of the composite membrane was analyzed by immersing the membrane in pH 2 hydrochloric acid solution and pH 10 sodium hydroxide solution of for 24 h. The PEG 2000 rejection of the membrane after immersion was noted. The thermal stability of the membrane was evaluated by TGA analysis of the unsupported GA-PEI bilayer in air atmosphere. The change in PEG 2000 rejection of the composite membrane after immersion in acidic and basic solutions of extreme pH was noted (Fig. 6a). It was observed that only 3% drop in rejection occurred after immersion in HCl solution of pH 2 and 7% drop occurred after immersion in pH 10 NaOH solution. This confirmed the excellent acid–base stability of the composite membrane suggesting its application in a wide range of pH. The TGA analysis of unsupported GA-PEI bilayer revealed no significant mass loss up to 100 °C indicating superior thermal stability of the membrane (Fig. 6b).

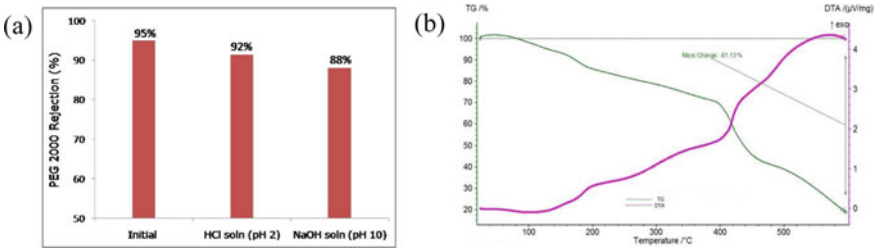


**Fig. 6** **a** Changes in PEG 2000 rejection of the composite membrane after immersion in extreme pHs **b** TGA analysis of unsupported GA-PEI bilayer

## 4 Conclusions

A novel ceramic-supported-polymeric composite membrane has been developed by incorporation of ceramic intermediate layers and a thin polymeric functional layer over macroporous ceramic support. FESEM study has been used as a principal tool to characterize the membrane structure in each step of preparation. The characteristics of the substrate and the individual layers which are crucial for membrane stability and performance, such as thickness, porous nature, roughness, and defects were analyzed using FESEM. EDX analysis further confirmed the chemical structure of the prepared membrane. The composite membrane was found to exhibit a water permeability of 3.1–3.9 L $m^{-2}$ $h^{-1}$ $bar^{-1}$ and a low molecular weight cutoff (2000) suggesting its nanofiltration nature toward contaminant rejection. It demonstrated a maximum removal of 93.5% of CV dye from 25 mg/l aqueous solution at 4 bar pressure. The excellent stability of the composite membrane in high pressure operation suggests its potential use in other nanofiltration application.

**Acknowledgements** The authors are grateful to Department of Science and Technology (DST/INSPIRE/04/2016/000597) and Council for Scientific and Industrial Research (31/15(0150)/2019-EMR-1), Government of India for providing financial support for accomplishment of the work.

## References

1. Marchetti P, Solomon MFJ, Szekely G, Livingston AG (2014) Molecular Separation with Organic Solvent Nanofiltration: A Critical Review. Chem Rev 114:10735–10806
2. Wang Z, Wei Y-M, Xu Z-L, Cao Y, Dong Z-Q, Shi X-L (2016) Preparation, characterization and solvent resistance of γ-Al2O3/α-Al2O3 inorganic hollow fiber nanofiltration membrane. J Membr Sci 503:69–80
3. Amelio A, Sangermano M, Kasher R, Bernstein R, Tiraferri A (2017) Fabrication of nanofiltration membranes via stepwise assembly of oligoamide on alumina supports: Effect of number of reaction cycles on membrane properties. J Membr Sci 543:269–276

4. Roy S, Majumdar S, Sahoo GC, Bhowmick S, Kundu AK, Mondal P (2020) Removal of As (V), Cr(VI) and Cu(II) using novel amine functionalized composite nanofiltration membranes fabricated on ceramic tubular substrate. J Hazard Mater 399: 122841
5. Chakraborty S, Bag BC, Dasgupta S, De S, Basu JK (2003) Separation and fractionation of dye solution by nanofiltration. Sep Sci Technol 38:219–235
6. Zheng Y, Yao G, Cheng Q, Yu S, Liu M, Gao C (2013) Positively charged thin-film composite hollow fiber nanofiltration membrane for the removal of cationic dyes through submerged filtration. Desalination 328:42–50
7. Déon S, Dutournie P, Fievet P, Limousy L, Bourseau P (2013) Concentration polarization phenomenon during the nanofiltration of multi-ionic solutions: Influence of the filtrated solution and operating conditions. Water Res 47:260–2272
8. Hepsen R, Kaya Y (2012) Optimization of membrane fouling using experimental design: an example from dairy wastewater treatment. Ind Eng Chem 51:16074–16084
9. Zhao X, Wu Y, Zhang X, Tong X, Yu T, Wang Y, Ikuno N, Ishii K, Hu H (2019) Ozonation as an efficient pretreatment method to alleviate reverse osmosis membrane fouling caused by complexes of humic acid and calcium ion. Front Environ Sci Eng 13(4):55
10. Meng S, Zhang M, Yao M, Qiu Z, Hong Y, Lan W, Xia H, Jin X (2019) Membrane fouling and performance of flat ceramic membranes in the application of drinking water purification. Water 11:2606
11. Song Y, Sun Y, Chen M, Huang P, Li T, Zhang X, Jiang K (2020) Efficient removal and fouling-resistant of anionic dyes by nanofiltration membrane with phosphorylated chitosan modified graphene oxide nanosheets incorporated selective layer. J Water Process Eng 34: 101086

# Development of Thin Aluminide Coatings on Alloy 800 Substrate


**R. S. Dutta, P. Mishra, Vishal Singh, and K. Singh**

**Abstract** Magnetron sputtering using aluminium as a target material was employed on Fe–Ni–Cr containing austenitic Alloy 800 substrates. Electron microscopic examination with elemental analysis on magnetron-sputtered substrates indicated formation of ~1.0 μm thick oxygen-rich Al–Fe–Ni–Cr containing layer just below the uppermost aluminium-rich deposited layer. Magnetron-sputtered + thermally–treated (1273 K for 18 h) substrates revealed formation of thin (~5 μm) aluminide layers at the upper surface comprising primarily Fe–Al rich layer with adjoining layers of Fe–Ni-Cr–Al type followed by Ni–Al rich layer. Thin multi-layered alloy substrate exhibited microhardness value of ~405 (±15) Vickers hardness number (VHN) while for alloy substrate, that was recorded as 310 (±10) VHN. The scratch test conducted on thin multilayered alloy substrate in the load range of 1–10 N indicated friction coefficient and penetration depth of ~0.1 and 11 μm, respectively. A good adherence was recorded for thin layers as no peeling off was noticed, which was confirmed by acoustic emission signals. The exposure of magnetron-sputtered + thermally treated alloy substrates to 70% $K_2SO_4$ + 30% KCl salts at 973 K in air revealed retention of surface oxide predominantly composed of Al–Fe–Cr–Ni type oxide layer indicating its good resistance to aggressive environment.

**Keywords** Alloy · Aluminium · Aluminides · EDS · Layers · Magnetron · Microhardness · Oxide · SEM

R. S. Dutta (✉) · V. Singh · K. Singh
Materials Science Division, Bhabha Atomic Research Centre, Trombay, Mumbai 400085, India
e-mail: rsdutta@barc.gov.in

P. Mishra
Materials Processing and Corrosion Engineering Division, Bhabha Atomic Research Centre, Trombay, Mumbai 400085, India



P. Ghosal et al. (eds.), *Applications of Microscopy in Materials and Life Sciences*, Springer Proceedings in Materials 11,
https://doi.org/10.1007/978-981-16-2982-2_2

## 1 Introduction

Intermetallic compounds have been quite extensively studied for last couple of decades for structural applications at elevated temperatures. The main reasons of attraction towards these intermetallics have been their low density (in general), high melting point, good resistance to wear as well as high temperature corrosion [1–6]. Among the intermetallic compounds, β-FeAl, $Fe_3Al$ and β-NiAl have exhibited promising results [2, 3, 7–10]. It is revealed that a continuous and adherent $Al_2O_3$ layer forms on aluminide surface on an exposure to oxygen/air atmosphere. This alumina layer imparts superior oxidation resistance acting as a barrier to diffusion of ions. That is why, this layer is known from its function itself as diffusion barrier coating [4, 7, 9, 11–14]. It is also indicated that the protectiveness of α-$Al_2O_3$ layer is superior to $Cr_2O_3$ layer at 1273 K onward and also in various environments having low partial pressure of oxygen [15, 16].

The major shortcoming of aluminides has been their poor ductility. Therefore, a composite structure comprising a metallic core with an aluminide layer on top is expected to overcome this deficiency to a considerable extent. This type of structure can be achieved by depositing a thin aluminium layer on metallic substrate that should be subjected to a standardized thermal treatment to form aluminide layers on metallic substrate through diffusion of elements. There are quite a good number of methods those can be employed for surface coatings. These include physical/chemical vapour deposition, thermal/plasma spraying, magnetron sputtering and many more those are discussed elsewhere [4, 17–29]. It can be understood that each method has its advantages as well as limitations.

Alloy 800 is basically a Fe–Ni–Cr containing austenitic, precipitation-hardening type alloy. The alloy is having extensive use as construction material for equipments, which require heat resistance, strength, stability up to $\sim$1073 K and resistance to corrosion. It exhibits good creep and rupture strength at high temperatures as well as resistance to sulfidation, carburization and oxidation. The alloy is also used as digester-liquor heaters in paper pulp industries, heat-exchanger in petrochemical and chemical industries and steam-generator (SG) tube material in nuclear industries [30, 31]. It is reflected in the literature that as compared to the number of studies dealing with the issues related to SG tubes, only a very few discusses on the development of aluminides on Alloy 800 substrates for high temperature applications [31–34]. Development of aluminides on Alloy 800 substrates could be of immense industrial importance as these can provide protection against aggressive environments at elevated temperatures. Therefore, an attempt has been made in the present investigation to explore this possibility. The first step of this exploration has been to deposit an aluminium-rich layer on the uppermost surface of Alloy 800 substrates using magnetron sputtering technique. Pre-heating of alloy substrates has been done at a standardized temperature during magnetron sputtering. This process is immediately followed by conversion of deposited layer to thin layers of aluminides by suitable thermal treatment under controlled atmosphere through diffusion of elements. Subsequently, microstructural

characterization, property as well as performance evaluation of thin-layered alloy substrates have been undertaken. Since magnetron sputtering is a versatile technique, the same has been chosen as a principal method to form an aluminium-rich uppermost layer on alloy substrates and also to form an aluminium-containing metastable phase just beneath it, which are subsequently converted to thin multilayer of aluminides. The novelty of this investigation lies in the fact that this kind of approach to form thin multilayer of aluminides on alloy substrates by magnetron sputtering with pre-heated substrates followed by suitable thermal treatment has not been explored earlier.

## 2 Experimental Method

Commercial Alloy 800 was available in the form of ~1 mm thick sheet under mill-annealed condition. This alloy sheet was used as substrate material in the present study. Table 1 shows typical chemical composition of the alloy. Metallographically polished alloy substrates of dimensions $\sim 25 \times 20 \times 1$ mm$^3$ were used during magnetron sputtering under controlled atmosphere.

Deposition parameters during DC magnetron sputtering have been given in Table 2. Magnetron sputtering was continued till a thickness of 4–5 µm layer formed on the alloy substrates. Preheating of alloy substrates during magnetron sputtering was standardized at 898 K, while subsequent thermal treatment of sputtered specimens was standardized at a temperature of 1273 K under controlled atmosphere. A soaking period in the range of 18–20 h has been found to be adequate to form a fairly continuous, thin multilayer of aluminides on the upper surface of the alloy substrates. However, in the present investigation, the sputtered samples were thermally treated at 1273 K for a duration of 18 h.

**Table 1** Typical chemical composition of Alloy 800 (wt%)

| Ni | Cr | Fe | C | Mn | Ti | Al | Si | S | P | N |
|---|---|---|---|---|---|---|---|---|---|---|
| 30.0 | 19.5 | Bal | 0.03 | 0.7 | 0.5 | 0.3 | 0.4 | 0.01 | 0.01 | 0.02 |

**Table 2** Deposition parameters during DC magnetron sputtering

| Parameter | Numerical value |
|---|---|
| Base pressure | $1.1 \times 10^{-5}$ mbar |
| Deposition pressure | $5 \times 10^{-3}$ mbar |
| Power density of cathode | 7.4 W/cm$^2$ |
| Substrate temperature | 898 K |
| Substrate rotation | 5 rpm |
| Target | Al (99.9% purity) |
| Target-to-substrate distance | 6.5 cm |
| Sputtering gas flow rate | 15 sccm Ar/min |

Magnetron-sputtered alloy substrates (having ~5 μm aluminium deposit) as well as sputtered + thermally treated (at 1273 K for 18 h) substrates were examined using scanning electron microscope (SEM) along their thickness. Elemental analysis (energy-dispersive X-ray spectroscopy; EDS) was also conducted on a number of locations. Despite analysing oxygen, no quantitative estimate of it has been shown in any analysis. Prior to SEM-EDS analysis, the specimens were metallographically polished and cleaned.

Microhardness measurements were taken at a number of locations on thin-layered alloy substrates. Prior to microhardness tests, sputtered + heat-treated alloy substrates were subjected to light metallographic polishing (800 grit emery paper onwards) followed by cleaning to remove the uppermost oxygen-containing aluminium-rich layer. Microhardness values were also measured for bare alloy substrates. At least two specimens were considered from either bare or heat-treated alloy substrates. Vickers microhardness number (VHN) was measured applying 1 g load for 5 s. At least, six readings were taken into consideration for the samples from each type and average values with the variations were recorded.

The scratch tests (adherence tests) were conducted at ambient temperature on thin-layered alloy substrates after light metallographic polishing and cleaning of the sputtered + thermally treated samples. The tests were performed under progressive mode of loading in the range of 1–10 N over a scratch length of 1 mm to evaluate the adherence of the layers. The tests were performed with CSM make scratch tester having a Rockwell indenter of 200 μm tip radius. The parameters those were recorded during the scratch tests were coefficient of friction, signals of acoustic emission and depth of penetration. Examination of scratched surface was also carried out using an optical microscope.

The sputtered + heat-treated alloy substrates of dimensions $\sim 10 \times 10 \times 1$ mm$^3$ were exposed to 70% $K_2SO_4$ + 30% KCl salts taken in an alumina crucible that maintained a temperature of 973 K inside a furnace for a duration of 3.5 h in air. After the exposure to salts, the cross-sections of both bare alloy substrate and thin multilayered alloy substrate were metallographically polished, cleaned and examined using SEM-EDS.

## 3 Results and Discussion

Figure 1 demonstrates X-ray diffraction pattern of mill-annealed Alloy 800 indicating primarily austenite phase. SEM examination as well as quantitative analysis along the thickness of the magnetron-sputtered Alloy 800 substrate indicated formation of an oxygen-rich Al–Fe–Ni–Cr containing layer having a thickness of ~1.0 μm just below the uppermost aluminium-rich deposited layer as shown in Fig. 2. Typical EDS analysis of oxygen-rich Al–Fe–Ni–Cr containing layer has been recorded as (in at.%): 41.4%Al–10.1%Fe–6.1%Ni–5.2%Cr–0.1%Ti. Elemental analysis indicated that the variation of aluminium content in the said

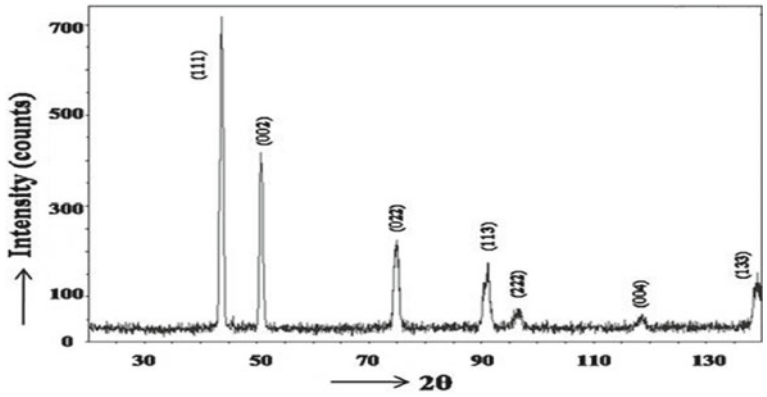


**Fig. 1** X-ray diffraction pattern of mill-annealed Alloy 800 indicating primarily austenite phase

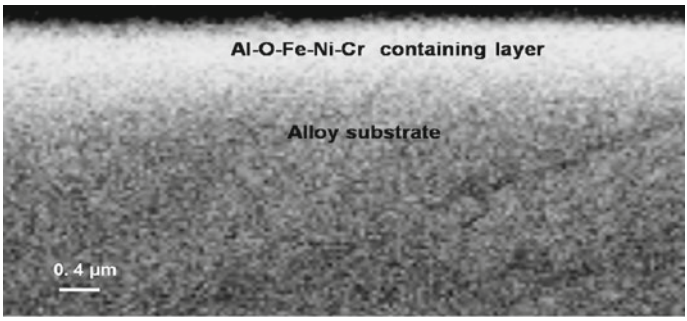


**Fig. 2** SEM-EDS analyses along the thickness of magnetron-sputtered Alloy 800 substrate revealing formation of an Al–O–Fe–Ni–Cr containing layer of thickness of around 1.0 µm just below the uppermost aluminium-rich deposited layer

layer has been in the range of 8–42 at.% showing a gradual decrease of its content towards the core.

SEM-EDS analysis of magnetron-sputtered + thermally treated alloy substrate has revealed formation of thin (∼5 µm) multilayer of aluminides at the upper surface of the alloy substrate through elemental diffusion. It is indicated that the multilayer comprising primarily Fe–Al rich layer (first one) followed by Fe–Ni–Cr–Al rich layer (second one) and Ni–Al rich layer (third one) adjacent to substrate as is evident from Fig. 3 and Table 3.

Based on Fe–Al, Ni–Al and Cr–Al phase diagrams [35–37], Fe–Al rich layer and Ni–Al rich layer can be designated as FeAl type and NiAl type phase, respectively, while the intermediate Fe–Ni–Cr–Al rich layer is a solid solution of Fe, Ni, Cr and Al. Vokál et al. [34] have carried out pack aluminization (cementation) of Alloy 800 substrate at 1223 K using a pack mixture composed of 5 wt% Al. According to the authors [34], (Ni, Fe)Al type and $Fe_2Al_5$ type phases with a

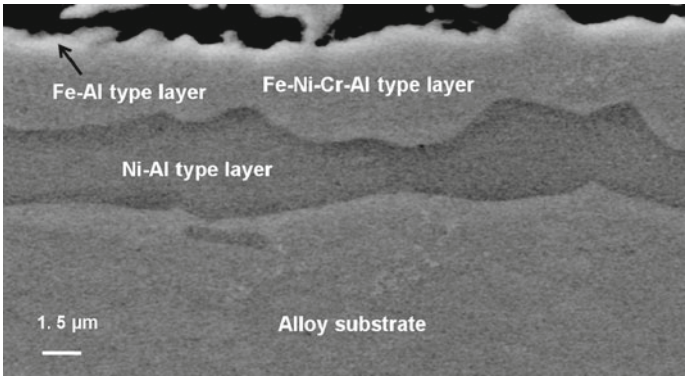


**Fig. 3** SEM-EDS analyses along the cross section of magnetron-sputtered + thermally treated Alloy 800 substrate revealing thin multilayer comprising Fe–Al rich, Fe–Ni–Cr–Al rich and Ni–Al rich layers

**Table 3** EDS analyses on magnetron-sputtered + heat-treated Alloy 800 substrate along the cross-section

| Analysis point | Elements, at.% | | | | Possible phase |
|---|---|---|---|---|---|
| | Fe | Al | Ni | Cr | |
| Fe–Al rich layer | 26.6 | 22.9 | 14.8 | 13.0 | Resembling FeAl type phase |
| Fe–Ni-Cr–Al rich layer | 43.4 | 7.6 | 25.0 | 19.7 | Fe–Ni–Cr–Al type phase |
| Ni–Al rich layer | 15.1 | 31.8 | 47.0 | 4.5 | Resembling NiAl type phase |
| Alloy substrate | 45.9 | 5.9 | 26.2 | 20.4 | Austenite phase |

thickness in the range of 15–20 µm have formed on top surface of the substrate. Dutta et al. [5] have conducted pack aluminization of substrates on Alloy 800 at 1273 K using a pack mixture containing 10 wt% Al. The authors [5] have observed that FeAl + $Fe_2Al_5$ type phases have formed on the outermost surface with an adjoining layer of FeAl type phase. Houngniou et al. [4] have performed pack cementation of Fe-30 wt% Cr alloy substrate at 1273 K using a pack containing 15 wt% Al. According to the investigators [4], FeAl and $Fe_3Al$ type phases formed as the first layer followed by an interdiffusion zone, which could be attributable to diffusion of aluminium towards inward direction with an outward diffusion of iron and chromium. In view of the above findings, the formation of thin multilayer consisting primarily of Fe–Al rich layer with adjoining Fe–Ni–Cr–Al rich intermediate layer followed by Ni–Al rich layer as observed in the present investigation can be manifested as follows. In magnetron sputtering with preheated alloy substrate followed by cooling, a metastable Al–O–Fe–Ni–Cr containing layer forms just below the aluminium-rich deposited layer. During subsequent thermal treatment of the sputtered substrate at a temperature of 1273 K for a duration of 18 h, the metastable phase equilibrates and also the uppermost aluminium-rich deposited

layer. This equilibration takes place by inward diffusion of aluminium with an outward diffusion of iron, nickel and chromium depending upon their diffusivities. This phenomenon results in formation of Fe–Al rich layer on the upper surface (of thin multilayer) with an Fe–Ni–Cr–Al type intermediate layer. The formation of Ni–Al rich layer adjacent to alloy substrate could be due to slightly higher atomic weight of nickel than either chromium or iron leading nickel marginally less favourable element for diffusion as compared to other two elements. The aluminium content and soaking period favour the formation of Fe–Al rich layer but not any other high aluminium-containing phase on the uppermost surface of thin multilayer.

In case of thin aluminide layers, the average value of microhardness has been obtained in the vicinity of 405 (±15) VHN, while the same for the alloy substrate has been recorded in the proximity of 310 (±10) VHN. For magnetron-sputtered + thermally treated alloy substrate, the average value of microhardness for thin multilayer has been found to be much higher as compared to that of the bare substrate. This finding appears to be consistent with the microstructures of substrate and multilayer. Higher microhardness values for aluminides than the alloy substrates have been obtained by Dutta et al. in their previous investigations on aluminides [5, 38]. According to the authors [5, 38], Fe-aluminides and Ni-aluminide, formed by pack aluminization of Alloy 800 [5] and Alloy 690 [38] substrates, respectively, exhibit higher microhardness values as compared to their respective alloy substrate.

The scratch test on thin multilayered alloy substrate under progressive mode of loading in the range of 1–10 N has exhibited friction coefficient in the proximity of 0.1 as shown in Fig. 4a. Kumar et al. [39] have performed scratch tests on iron-aluminide thermal spray coatings at 30 N and 90 N load levels. The authors [39] have obtained friction coefficient in the range of 0.19–0.28 those are higher than that obtained for magnetron-sputtered and thermally treated substrate in the present study. Dutta et al. [5] have conducted scratch tests under progressive mode of loading in the range of 1–10 N on pack aluminized Alloy 800 substrates. The authors [5] have reported the value of coefficient of friction in the range of 0.08–0.1 for aluminides while substrate has exhibited that in the range of 0.2–0.22. It appears that the value of friction coefficient that is obtained in the present study is consistent with the reported ones. Figure 4b, c demonstrates acoustic emission signals and appearance of scratched surface at the end of the scratch test, while Fig. 4d shows penetration depth during the scratch test. Magnetron-sputtered and heat-treated Alloy 800 substrate has shown good adherence of thin multilayer and absence of surface peeling off or formation of any crack as is evident from acoustic emission signals as well as appearance of the scratched surface. A maximum depth of penetration of around 11 μm has been measured for the multilayered substrate. Similar behaviour has also been noticed for pack aluminized Alloy 800 substrates under similar experimental conditions [5]. The aluminized alloy substrate has exhibited neither any peeling off at aluminides nor at substrate/layer interfaces and has shown a maximum depth of penetration in the proximity of 12 μm, which is indicative of good adherence of layers of aluminides [5].

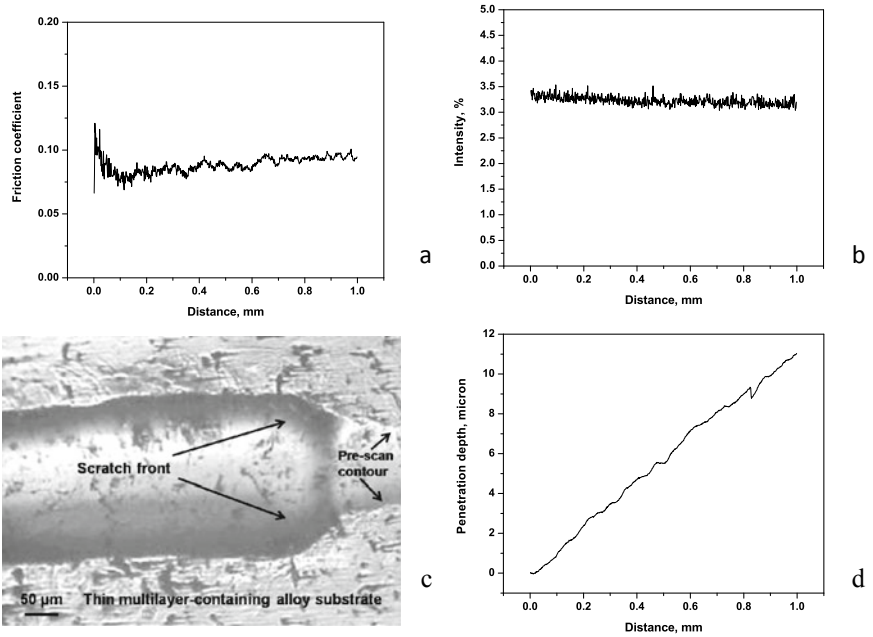


**Fig. 4** Variation of (a) coefficient of friction, (b) intensity of acoustic emission signal, with scratch length, (c) appearance of scratched surface at the end of the scratch test and (d) variation of penetration depth with scratch length, for magnetron-sputtered + thermally treated Alloy 800 substrate

SEM-EDS analysis of sputtered + thermally treated substrate has shown the existence of aluminium-oxide layer on the surface of thin multilayered substrate after the exposure to $K_2SO_4$–KCl salts at 973 K. Detailed elemental analyses have indicated that the surface layer is predominantly composed of Al–Fe–Cr–Ni type oxide layer having an average thickness in the vicinity of 4 µm with a variation of composition along its thickness. The maximum contents of the elements have been recorded as (in at.%): 39.5%Al–21.4%Fe–18.6%Cr–14.1%Ni–12.9%S–4.0%K–0.5%Cl. The salts used during the exposure are believed to be the main sources of sulphur, potassium and chloride. Figure 5 shows SEM micrograph along the thickness of the specimen on which quantitative point analyses using EDS have been performed. Haanappel et al. [33] have observed that the aluminide coatings, which formed on Alloy 800H during pack aluminization are resistant to sulphidation up to a temperature of 823 K. According to Vokál et al. [34], out of (Ni, Fe)Al and $Fe_2Al_5$ phases those formed on Alloy 800 surface during pack aluminization, degradation of (Ni, Fe)Al type phase takes place after the exposure to 50 mol% KCl + 50 mol% $K_2SO_4$ at 923 K. It is, therefore, indicative from the above discussion that the resistance of magnetron-sputtered + thermally treated Alloy 800 substrates to $K_2SO_4$–KCl salts at 973 K, which is indicative in the present study, could be attributable to retention of predominantly aluminium-oxide type surface layer.

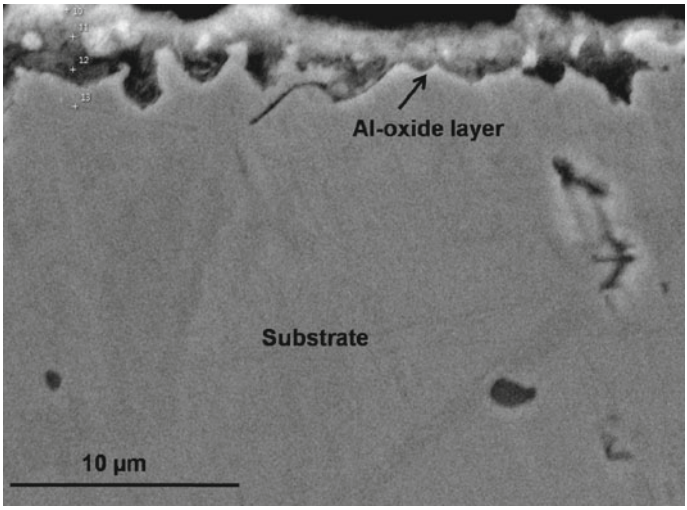


**Fig. 5** SEM-EDS analyses along the thickness of magnetron-sputtered + thermally treated Alloy 800 substrate after the exposure to $K_2SO_4$-KCl salts at 973 K indicating retention of predominantly aluminium-oxide type layer

## 4 Conclusions

1. Aluminization of substrates of Alloy 800 using magnetron sputtering in controlled atmosphere with properly preheated substrate followed by suitable thermal treatment in controlled atmosphere can form thin ($\sim$5 µm) multilayer of aluminides on the upper surface of alloy substrate.
2. Thin multilayer primarily composed of Fe–Al rich layer on the upper surface with adjoining Fe–Ni–Cr–Al rich intermediate layer followed by a Ni–Al rich layer.
3. In magnetron sputtering with preheated substrate, a metastable aluminium-containing phase forms below the uppermost aluminium-rich deposited layer. In the subsequent thermal treatment, equilibration of metastable layer takes place and also of the aluminium-rich deposited layer. This leads to formation of thin layers of aluminides by diffusion of aluminium towards inward direction with an outward diffusion of iron, chromium and nickel based on their diffusivities.
4. Thin multilayered alloy surface shows higher microhardness than bare substrate.
5. Adherence of multilayer has been found to be good under progressive mode of loading in the range of 1–10 N.
6. Retention of predominantly aluminium-oxide type layer on thin multilayered alloy surface after the interaction with sulphate-chloride salts at 973 K indicates its good resistance to aggressive environment.

**Acknowledgements** The authors wish to thank AD, Materials Group, Head, MSD, and Head, MP&CED, Bhabha Atomic Research Centre, Trombay, Mumbai, India, for their supports during this work.

**Funding** The work was funded by DAE, Government of India.

## References

1. Goward GW (1998) Progress in coatings for gas turbine airfoils. Surf Coat Technol 108–109:73–79
2. Sunder RR, Baligidad RG, Prasad YVRK, Sastry DH (1998) Processing of iron aluminides. Mater Sci Eng, A 258:219–228
3. Stoloff NS (1998) Iron aluminides: present status and future prospects. Mater Sci Eng, A 258:1–14
4. Houngniou C, Chevalier S, Larpin JP (2004) Synthesis and characterisation of pack cemented aluminide coatings on metals. Appl Surf Sci 236(1):256–269
5. Dutta RS, Majumdar S, Laik A, Singh K, Kulkarni UD, Sharma IG, Dey GK (2011) Formation and characterization of aluminide coatings on alloy 800 substrate. Surf CoatS Technol 205(19):4720–4725
6. Dutta RS, Singh K, Vishwanadh B, Dey GK (2017) Aluminide formation on Alloy 800 by plasma spraying and heat treatment. Mater Manuf Process 32(16):1845–1850
7. Deevi SC, Sikka VK (1996) Nickel and iron aluminides: an overview on properties, processing and applications. Intermetallics 4:357–375
8. Checchetto R, Tocello C, Miotello A, Principi G (2001) Structural evolution of Fe–Al multilayer thin films for different annealing temperatures. J Phys: Condens Matter 13:811–821
9. Xia J, Li CX, Dong H (2005) Thermal oxidation treatment of B2 iron aluminide for improved wear resistance. Wear 258:1804–1812
10. Chen Y, Wang HM (2006) Microstructure and wear resistance of laser-melted TiC reinforced nickel aluminide dual-phase matrix in situ composite. Intermetallics 14(3):325–331
11. Li D, Xu Y, Lin D (2001) Oxidation behavior of FeAl alloys with and without titanium. J Mater Sci 36:979–983
12. Tacikowski M, Sitek R, Sikorski K, Wierzchoń T (2009) Structure of Al–Ni intermetallic composite layers produced on the Inconel 600 by the glow discharge enhanced-PACVD method. Intermetallics 17(12):1098–1104
13. Kamal S, Jayaganthan R, Prakash S (2010) Hot corrosion behaviour of D-gun sprayed NiCoCrAlYTa coated superalloys at 900 °C in molten salt environment. Surf Eng 26:453–462
14. Mahesh RA, Jayaganthan R, Prakash S (2010) Evaluation of hot corrosion behaviour of HVOF sprayed Ni–5Al and NiCrAl coatings in coal fired boiler environment. Surf Eng 26(6):413–421
15. Klöwer J, Brill U, Heubner U (1999) High temperature corrosion behaviour of nickel aluminides: effects of chromium and zirconium. Intermetallics 7(10):1183–1194
16. Cho H, Lee BW (2015) High temperature stability of aluminide-coated Inconel 617. Modern Phy Lett B 29(6&7):1–5)
17. Bateni MR, Shaw S, Wei P, Petric P (2009) Deposition of Fe–Al intermetallic coatings on solid oxide fuel cell (SOFC) interconnects by pack cementation. Mat Manuf Proc 24(6): 626–632

18. Thirumalaikumarasamy D, Shanmugam K, Balasubramanian V (2012) Effect of atmospheric plasma spraying parameters on porosity level of alumina coatings. Surf Eng 28(10):759–766
19. Thiyagarajan TK, Anantha padmanabhan PV, Sreekumar KP, Chakravarthy Y, Das AK, Gantayet LM, Selvan B, Ramachandran K (2012) Experimental and simulation approach to plasma spray deposition of yttrium oxide. Surf Eng 28(9):646–656
20. Karaoglanli1 AC, Turk A, Ozdemir I, Ustel F (2015) Comparison of oxidation and thermal shock performance of thermal barrier coatings. Mat Manuf Proc 30(6):717–723
21. Chen QY, Li CX, Zhao JZ, Yang GJ, Li CJ (2016) Microstructure of YSZ coatings deposited by PS-PVD using 45 kW shrouded plasma torch. Mat Manuf Proc 31(9):1183–1191
22. Stanciu EM, Pascu A, Ţierean MH, Voiculescu I, Roată IC, Croitoru C, Hulka I (2016) Dual Coating Laser Cladding of NiCrBSi and Inconel 718. Mat Manuf Proc 31(12):1556–1564
23. Murtaza Q, Pandey SM, Niranjan SM (2016) A novel manufacturing route for automobile parts through two-wire-arc thermal spray process. Mat Manuf Proc 31(11):1424–1432
24. Dhineshkumar SR, Duraiselvam MM, Natarajan S, Panwar SS, Jana T, Khan MA (2017) Effect of laser glazing on the thermo-mechanical properties of plasma-sprayed LaTi2Al9O19 thermal barrier coatings. Mat Manuf Proc 32(14):1573–1580
25. Vinoth E, Gowrishankar S, Gopalakrishnan N (2017) RF magnetron sputtered Cd doped ZnO thin films for gas-sensing applications. Mat Manuf Proc 32(4):377–382
26. Ashja M, Verdian MM (2017) Al–Cu–Fe coatings manufactured by the flame spraying process. Mat Manu Proc 32(4):383–388
27. Ghadai RK, Kalita K, Mondal SC, Swain BP (2018) PECVD process parameter optimization: towards increased hardness of diamond-like carbon thin films. Mat Manu Proc 33(16):1905–1913
28. Vetrivendan E, Madhura B, Rao CJ, Ningshen S (2019) Pack cemented silicon carbide interlayer for plasma sprayed yttria over graphite. Mat Manu Proc34(6):681–688
29. Goud V, Ramasamy A, Das A, Kalyanasundaram D (2019) Box-Behnken technique based multi-parametric optimization of electrostatic spray coating in the manufacturing of thermoplastic composites. Mat Manu Proc 34(14): 1638–1645
30. Special Metals, Alloy 800, Retrieved from www.specialmetals.com
31. Dutta RS (2009) Corrosion aspects of Ni–Cr–Fe based and Ni–Cu based steam generator tube materials. J Nuclear Mat 393(2):343–349
32. Miller DM, Kung SC, Scarberry SD, Rapp RA (1988) Simultaneous Chromizing-Aluminizing Coating of Austenitic Stainless Steels. Oxidation of Metals 29(3):239–254
33. Haanappel VAC, Geerdink B, Fransen T, Gellings PJ (1991) The corrosion and mechanical behaviours of aluminide, FeCrA1Y and CoCrA1Y coatings in aggressive environments. Mat Sci Engi A 148(1):131–139
34. Vokál V, Rohr V, Pomeroy MJ, Schütze M (2008) Corrosion of alloys and their diffusion aluminide coatings by KCl: $K_2SO_4$ deposits at 650 °C in air. Mat Corr 59(5):374–379
35. Kattner UR, Burton BP (1993) In: Okamoto H (ed) Phase Diagrams of Binary Iron Alloys. ASM International, Materials Park, OH, pp 12–28
36. Okamoto H (1993) J Phase Equlibria 14(2):257–259
37. Murray JL (1998) J Phase Equlibria 19(4):368–375
38. Dutta RS, Arya A, Yusufali C, Vishwanadh B, Tewari R, Dey GK (2013) Formation of aluminides on Ni-based superalloy 690 substrate, their characterization and first-principle Ni (111)/NiAl(110) interface simulations. Surf Coat Technol 235:741–747
39. Kumar S, Selvarajan V, Padmanabhan PVA, Sreekumar KP (2006) Characterization and comparison between ball milled and plasma processed iron-aluminium thermal spray coatings. Surf Coatings Tech 201(3–4):1267–1275

# Structural Characteristics of Cr-Doped $In_2O_3$ Thin Films Grown by Pulsed Laser Deposition


**Y. Veeraswamy, R. J. Choudhary, D. Shobharani, S. Vinoth, and M. V. Ramana Reddy**

**Abstract** The pulsed laser deposition technique is employed to deposit undoped and Cr-doped $in_2O_3$ thin films on Si (100) substrate. The obtained undoped and Cr-doped $In_2O_3$ thin film samples were systematically investigated by using XRD, XPS, VBS-RPES and SEM-EDX. SEM micrographs revealed that the deposited films showed flake-like structures and Cr-doped $In_2O_3$ showed well-separated columnar morphology. X-ray photo electron spectroscopy reveals ionization states of the elements present in the films. Cr-core level spectra showed two ionic states $3^+$ and $4^+$. Valence band spectroscopy measurements divulge that doping Cr ions create an additional state close to Fermi level in the valence band spectra of $In_2O_3$. Using resonant photoemission spectroscopy, it is confirmed that the additional state is due to Cr-3d and O-2p hybridized state.

**Keywords** Dilute magnetic semiconducting oxides · Valence band structure and resonant · X-ray photoemission spectroscopy

## 1 Introduction

The transparent metal oxide with higher carrier mobility has a magnetic property, then this property attracts very much like a miniature robust device for spintronic applications. Such materials are known as diluted-magnetic metal oxide semiconductors (DMOS). If carrier-mediated magnetization can be induced in transparent

Y. Veeraswamy (✉) · D. Shobharani
Institute of Aeronautical Engineering, Dundigal, Hyderabad 500043, Telangana, India

R. J. Choudhary
UGC-DAE Consortium for Scientific Research, Indore 452017, Madhya Pradesh, India

M. V. Ramana Reddy
Department of Physics, Osmania University, Hyderabad 500007, Telangana, India

S. Vinoth
Department of Electronics and Communication Engineering, Manakula Vinayagar Institute of Technology, Puducherry 605107, India



P. Ghosal et al. (eds.), *Applications of Microscopy in Materials and Life Sciences*, Springer Proceedings in Materials 11,
https://doi.org/10.1007/978-981-16-2982-2_3

semiconducting oxides such as $In_2O_3$, ZnO, $TiO_2$, etc., it is predicted that such DMOS will exhibit coupling among electrical, optical and magnetic properties, further boosting the prospects of devices emanating from such materials. Among various transparent conducting oxide materials, $In_2O_3$ is a versatile material with a huge collection of applications in optoelectronics, gas sensors, solar cells, etc. $In_2O_3$ is an n-type semiconducting material with a wide optical energy band gap with a cubic bixbyite crystal structure. In past, a few attempts were made to probe the magnetic properties of transition metal-doped $In_2O_3$. However, the origin of magnetism in such a system is always a mystery. In that Philip et al. [1] reported that ferromagnetic ordering in Cr-doped $In_2O_3$is due to carrier mediation. O. D Jayakumar et al. suggested that defects in the synthesis may cause the magnetism in Iron-doped $In_2O_3$ thin films [2]. N. B. Ukah et al. described the structural and electrical transport properties of Cr-doped $In_2O_3$ films, and they have suggested that pulsed laser deposition technique (PLD) is more advantageous than other deposition techniques [3]. From the above discussions, it is evident that the properties of $In_2O_3$ based DMOS depend on the dopant and defects which would alter the electronic structure of such materials. However, change in the electronic structure of $In_2O_3$ occurring by defects or dopants is not well-understood. Probing the electronic structure will be key to understand the underlying mechanism responsible for the coupled electrical, optical and magnetic properties of $In_2O_3$ based DMOS and accordingly design the material for device application. In this article, we have probed the valence band structure of pulsed laser deposited $In_2O_3$ thin films and its modification resulted due to the environment of Cr-doping. Resonant photoemission spectroscopy (RPES) was employed to study the characteristics of valence band spectra (VBS). The fabricated undoped $In_2O_3$ and Cr-doped $In_2O_3$ thin films are characterized by different analytical techniques like GIXRD, SEM, EDAX and XPS.

## 2 Experimental

In the present investigation, we have deposited undoped $In_2O_3$ and Cr-doped $In_2O_3$(i.e. $In_{2-x}Cr_xO_3$(x = 0.06)) thin films on Si (100) substrate. To deposit the films, a well-sintered target of undoped $In_2O_3$ and Cr-doped $In_2O_3$($In_{2-x}Cr_xO_3$(x = 0.06)) for pulsed laser deposition technique targets were prepared by the solid-state process. The high purity $In_2O_3$ (99.99%) and $Cr_2O_3$ (99.99%) powders (purchased from Sigma-Aldrich) are the precursor chemicals to synthesize the $In_{2-x}Cr_xO_3$ (x = 0.06) powder sample by solid-state reaction shown in Fig. 1a. The grounded mixture was annealed at 800 °C in air for 10 h. The prepared high purity $In_2O_3$and Cr-doped $In_2O_3$(i.e., $In_{2-x}Cr_xO_3$(x = 0.06)) powders were cold-pressed at 10 ton load and pellets with a diameter of 1-inch and thickness of 2 mm was made. The as-made pellets were sintered at 900 °C for 12 h. Si (100) is used as substrates and the films were grown by pulsed laser deposition (PLD) (Lambda physic complex 201 model) system. Depositions were carried out

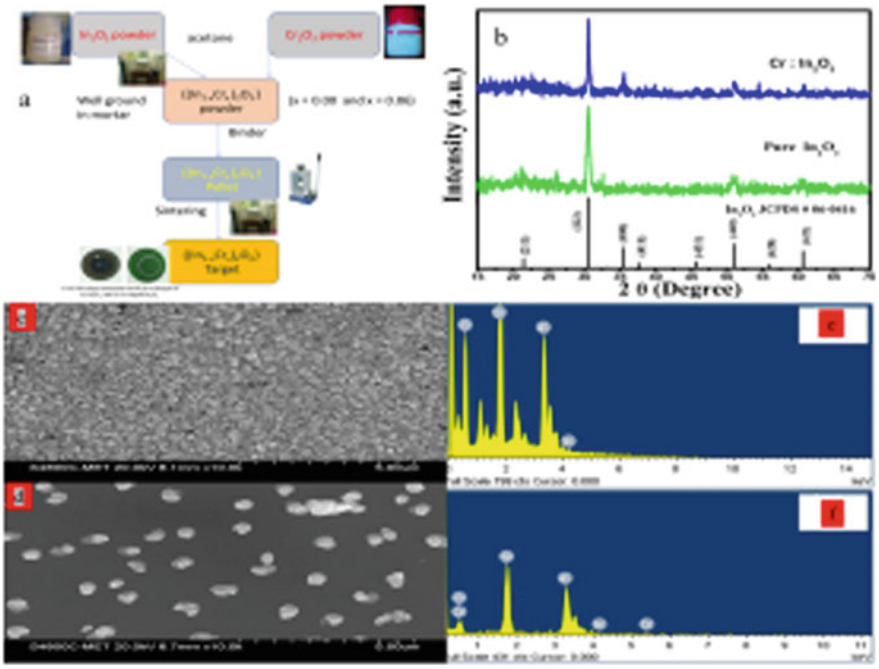


**Fig. 1** **a** Flowchart of PLD target preparation and **b** GIXRD of undoped and Cr-doped $In_2O_3$ thin film **c** and **e** are SEM and EDS of undoped $In_2O_3$, **d** and **f** SEM of Cr-doped $In_2O_3$ thin film

at a laser energy of 200 mJ/pulse for the deposition of 15 min. During the deposition, the distance between target to the substrate was adjusted to 6 cm and the substrate temperature was sustained at 673 °C. Formerly, the deposition chamber was evacuated to a base pressure better than $10^{-6}$Torr. During the deposition, oxygen partial pressure was maintained at 0.1 mTorr. The structural and crystallographic phases of the deposited films were analyzed using GIXRD (D8-Discover system of M/s Bruker) furnished with CuKα. The XPS analysis was recorded in vacuum in the order of $10^{-10}$ Torr using the Omicron energy analyzer (EA-125) with the Al Kα (1486.6 eV) X-ray source. The photoemission experiments were carried out after cleaning the deposited films using 500 eV Ar ions. The resonant photoemission spectroscopy (RPES) and valence band photoemission (VBS) measurements of the film were performed at the angle-integrated PES beamline on the Indus-1 synchrotron radiation source at RRCAT, Indore, India. The valence band photoemission spectra were carried out in the photon energy range of 44–57 eV and were recorded by an Omicron (EA-125) energy analyser. The position of the Fermi levels ($E_F$) of the samples was determined by measuring PES spectra of gold which was electrically in contact with the samples.

# 3 Result and Discussion

## 3.1 Glancing Incidence X-Ray Diffraction (GIXRD)

In the present investigation, we have deposited pure $In_2O_3$ and Cr-doped $In_2O_3$(i.e., $In_{2-x}Cr_xO_3$(x = 0.06)) thin Fig. 1(b) presents the GIXRD patterns of the pure $In_2O_3$ and Cr-doped $In_2O_3$(i.e. $In_{2-x}Cr_xO_3$(x = 0.06)) thin films on Si (100) substrate. From Fig. 1b, the observed XRD peaks compared with the JCPDS (card no. 06-0416) standard data file of indium oxide, which confirms the formation of the phase of pure bixbyite cubic crystal structure of $In_2O_3$with the Ia-3(206) space group. No extra characteristic peaks were observed in the films that can be related to any metal chromium, indium metal and chromium-based compounds. The pure $In_2O_3$ and Cr-doped $In_2O_3$ thin film samples show prominent (2 2 2) peak that confirms polycrystalline structure. Besides, the (222) peak position shifted toward a higher angle for Cr-doped $In_2O_3$ thin film. The lattice parameters of the pure $In_2O_3$ and Cr-doped $In_2O_3$ thin film samples were evaluated by analysing the observed XRD patterns using the celref3 software and are found to be 10.11 and 10.12 Å, respectively.

XRD results confirm the formation of the nanocrystalline pure bixbyite cubic phase of pure $In_2O_3$ and Cr-doped $In_2O_3$ thin film samples.

## 3.2 Scanning Electron Microscopy (SEM)

Figure 1c, d presents the SEM micrographs of undoped $In_2O_3$ and Cr-doped $In_2O_3$ thin film samples, respectively. Figure 1e, f, represents energy dispersive spectroscopy of undoped and Cr-doped $In_2O_3$ thin films. The flake like morphology applies in case of undoped indium oxide and well-separated spherical morphology is observed for Cr-doped $In_2O_3$ thin film. The mean grain size ranges from 200–300 to 300–500 nm, respectively. It is also observed that the average grain size is more in case of pure $In_2O_3$ thin films compared with the Cr-doped $In_2O_3$ thin films. Figure 1e, f shows the EDS spectra of undoped $In_2O_3$ and Cr-doped $In_2O_3$ thin film samples, respectively. From the EDS plot Figs. 1e and 2f, we could observe the peaks of In and O and the peaks of In, Cr and O elements, respectively, without any additional peaks, which suggests the purity of the $In_2O_3$ and Cr-doped $In_2O_3$ thin film samples, respectively.

## 3.3 X-Ray Photoelectron Spectroscopy (XPS)

Figure 2i(a) depicts the X-ray photoelectron survey scan spectrum of the undoped $In_2O_3$ thin film. It shows all the intense peaks related to Indium (In) and Oxygen

(O) electronic states and there are no extra peaks related to any impurity. Figure 2i (b) represents the X-Ray photoelectron survey scan of Cr-doped $In_2O_3$ thin film. From Fig. 2i(b), the several intense peaks observed in the survey scan spectrum represent the different electronic states of Indium (In), Chromium (Cr) and Oxygen (O). The detailed survey scan spectrum has been performed to determine the ionic state of In, Cr, and O in the deposited undoped and Cr-doped $In_2O_3$ thin films.

Figure 2ii(a) shows the core-level fine spectra of Carbon (C) core and its shifting correction. Figure 2ii(b) shows the deconvolution of the core-level fine spectra of O–1 s of Cr-doped $In_2O_3$. From this the observed spectra show the presence of three features in the spectrum. The feature around 528.4 eV is related to the lattice oxygen, while the feature appearing at higher binding energy 531.2 eV is due to the presence of surface hydrocarbon over the sample surface. The feature around 529.6 eV is due to the presence of oxygen vacancy in our sample. A similar spectrum is observed for pure $In_2O_3$ thin film also. Oxygen vacancy in the film is rather a familiar occurrence in transparent oxide films due to the loss of oxygen during the synthesis process. The presence of oxygen vacancy state can be understood from the Cr core-level spectra. From Fig. 2ii(c), it is observed that In-3d core-level spectra contain two peaks which are due to spin-orbit splitting and

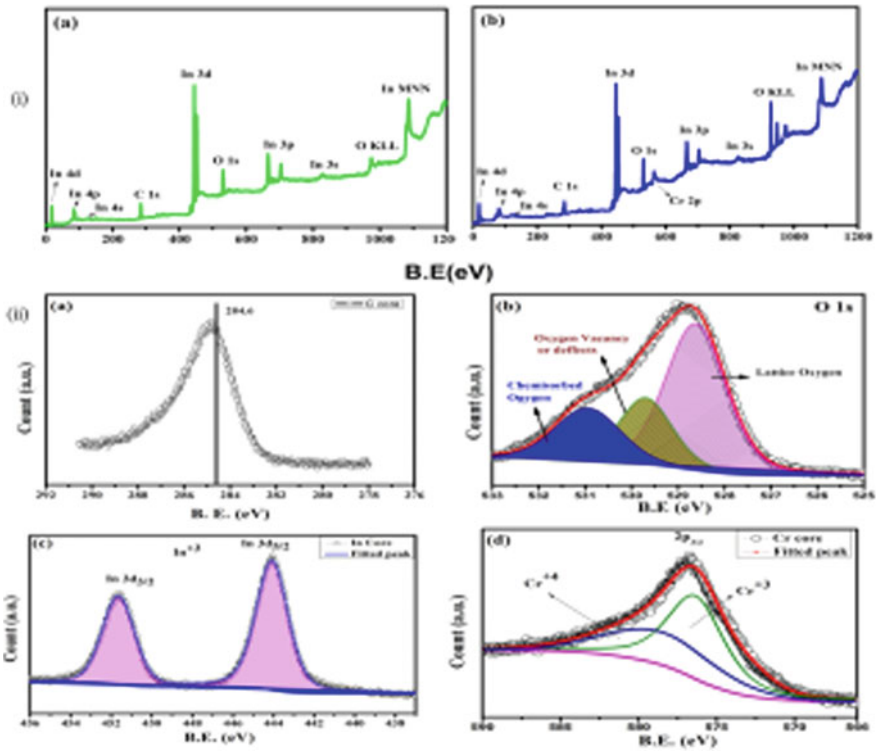


**Fig. 2** XPS study of undoped and Cr-doped $In_2O_3$ thin films

separated by 7.6 eV. Features of In-3d core-level spectrum were fitted with combined Gaussian-Lorentzian function and the observed features corresponding to In $3d_{3/2}$ and In $3d_{5/2}$ states were observed at 451.6 eV and 444 eV, respectively [4]. This is consistent with the expected $3^+$ state of $In_2O_3$. A similar spectrum was also observed for the pure $In_2O_3$thin film.

Figure 2ii(d) shows the Cr $2p_{3/2}$core level spectrum of Cr: $In_2O_3$ thin film. The spectrum was corrected with Shirley background approximation and fitted with the Gaussian-Lorentzian function. The fitted spectrum reflects the presence of $Cr^{3+}$ state along with the $Cr^{4+}$ state. The most intense peak at 576.3 eV is assigned as $Cr^{3+}$ state and a hump at higher energy tail of $Cr^{3+}$ state reflects the presence of higher oxidation state $Cr^{4+}$. The hump cannot be a satellite feature due to $Cr^{3+}$ state since its position should appear at 11 eV higher in binding energy from the Cr-$2p_{3/2}$ feature. A small feature of 572.7 eV is due to the multiple splitting of Cr-2p energy levels [5]. The occurrence of $3^+$ and $4^+$ states of Cr ions suggests its substitutional character and excludes the possibility of Cr clusters in the studied films. The hetero valence of Cr ion can be explained by the occurrence of oxygen vacancy in the studied films.

## *3.4 Valence Band Spectroscopy*

After ensuring the ionic state of Cr in $In_2O_3$ matrix, we now probe the change in the valence band spectra of $In_2O_3$ thin films due to Cr-doping. In Fig. 3a valence band spectra obtained at 44 eV photon energy of pure $In_2O_3$ and Cr-doped $In_2O_3$ thin films close to Fermi edge is shown. Zero energy corresponds to the Fermi level. It is observed that there is hardly any density of states available at Fermi level in both the films and it remains unaltered by doping suggesting their semiconducting nature [6]. It is also observed that there is a shift in the valence band maxima by 0.9 eV toward Fermi level due to Cr-doping in $In_2O_3$ illustrated in Fig. 3b. It also appears that an additional feature is emerging close to $E_F$ in Cr-doped $In_2O_3$thin film sample [7]. Valence band modification graphical illustration is shown in Fig. 3b.

To better understand the modification of electronic structures due to Cr-doping in $In_2O_3$ thin films, we analyse the VBS in detail. Figure 3c, d simultaneously shown the normalized VBS of undoped $In_2O_3$ and Cr-doped $In_2O_3$ thin films at the photon energy of 44 eV. The spectra were analyzed by with Shirley background approximation and fitted with the combined Gaussian-Lorentzian function. The pure $In_2O_3$ VBS consists of four features indicated as B (4 eV), C (5.7 eV), D (7.6 eV) and E (9.9 eV). But in Cr-doped $In_2O_3$ thin film, an additional feature at 2.6 eV labeled as a feature A is observed. By comparing these spectra with the previously reported theoretical calculations on the valence band structure of $In_2O_3$, features C and D are assigned to O-2p occupied states [8] and feature D is due to oxygen-indium hybridization states. Feature C at 5.7 eV is mainly O-2p bonding states. Feature E at 9.9 eV appears due to adsorbed CO or OH on the surface [9]. Feature B arises due to In-O bonding states [10]. The additional feature, labeled as

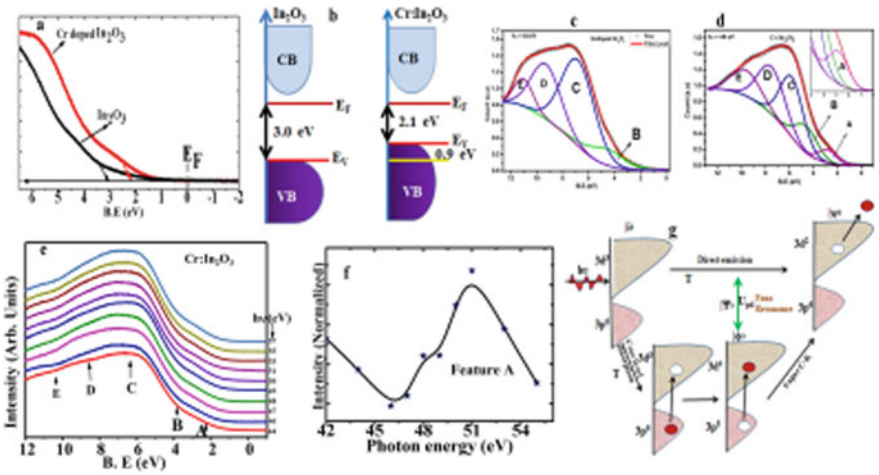


**Fig. 3** VBS spectral analyses of Cr-doped $in_2o_3$ thin film

A, appearing in the VBS spectrum of Cr-doped thin film suggests the modification in the electronic structure of $In_2O_3$ and to reveal its origin, we performed resonant photoemission spectroscopy measurements.

## 3.5 *Resonance Photoemission Spectroscopy*

RPES is performed by measuring VBS at different photon energies. In Fig. 3e, VBS taken at various photon energies ranging from 44 to 57 eV is shown. The above-selected energy range extends the photo-absorption energy from 3p to 3d transition of Cr ions. The spectra were normalized with the beam current. CIS spectra of feature A is plotted and presented in Fig. 3f. CIS intensity graph is observed by plotting the normalized intensity of various features at their respective binding energies with photon energy. From the CIS plot, resonant enhancement in intensity is shown at the photon energy of 51 eV. The origin of the resonance feature at 51 eV, can be justified based on the interference of two ways for photoemission. One of the photoemission ways is caused by the direct photoemission from the 3d state explained in Eq. (1).

$$\mathrm{Cr}: 3p^6 3d^3\left(t_2g^3 : d_{xy}^1 d_{xz}^1 d_{yz}^1\right) + h\nu \rightarrow \mathrm{Cr}\ 3p^6 3d^2\left(t_2g^2 \cdot d_{xy}^1 \cdot d_{yz}^1\right) + e^{-1} \qquad (1)$$

The other way of photoemission is due to absorption of the photon at the resonant photon energy by 3p state accompanied by super Coster-Kronig decay. In the atomic level, the intra-atomic excitation process followed by Super Coster-Kronig transition is represented as Eq. (2)

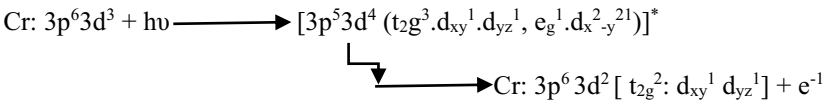


(2)

The last state is identical in both the cases and this kind of mechanism ascribes to a Fano-type profile for the photoemission intensity and Coster-Kroning transition illustrated in Fig. 3g. This confirms that feature A arises due to chromium 3d derived states. A minimum in the CIS plot is also observed at 46 eV kin to anti-resonance. Such feature in the CIS plot suggests the feature A to be because of hybridized states of Cr-3d and O-2p states [11].

## 4 Conclusion

In the present work, we deposited undoped $In_2O_3$ and Cr-doped $In_2O_3$ thin films on Si (100) substrate by using PLD technique. The deposited films are crystalline and grown in a single phase without any impurity. XPS studies highlight that the grown films have oxygen vacancies, which also lead mixed oxidations states of Cr in $3^+$ and $4^+$ states. The valence band edge is observed to shift toward to Fermi level after Cr-doping. Cr-doping also gives rise to an additional state close to the Fermi level. Using RPES studies, it is revealed that the Cr-3d derived states are hybridized with O-2p states. Cr-doping in the $In_2O_3$ thin film results in the magnetic ordering in the film. It has possible applications in DMOS and spintronic as a material for spin injectors.

**Acknowledgements** The authors are grateful to Dr. V. R. Reddy for GIXRD, Mr. Anupam Jana, Mr. Anup Kumar Mr. Manoj Kumar, Sharad karwal and A. Wadikar for helping in PLD and XPS and VBS measurements. The authors thank to Center director UGC-DAE CSR Indore experiment facility. One of the author (MVRR) thanks DST-SERB (file. No. EMR/2017/002651) for financial support to carryout this work.

## References

1. Philip J, Punnoose A, Kim BI, Reddy KM, Layne S, Holmes JO, Satpati B, Leclair PR, Santos TS, Moodera JS (2006) Nat Mater 5:298
2. Jayakumar OD, Gopalakrishnan IK, Kulshreshth K, Rao KV, Louzguine Luzgin DV, Inoue A, Glans A, Guo JH, Samanta K, Sing MK, Katiyar RS (2007) Appl Phys Lett 91:052504
3. Ukah NB, Gupta RK, Kahol PK, Ghosh K (2009) Appl Surf Sci 255:9420–9424
4. KJ Beera, Lethy R, Vinod Kumar VP, Mahadevan Pillai V, Ganesan, Phase DM, Sudheer SK (2009) Effect of substrate temperature on structural, optical and electrical properties of pulsed laser ablated nanostructured indium oxide films. Appl Surf Sci 255:8334–8342

5. Tripati M, Choudhary RJ, Phase DM (2016) RSC Adv 6:90255
6. King PDC, Veal TD, Payne DJ, Bourlange A, Erdell RG (2008) Conville, PRL.101: 116808
7. Gassenbauer Y Schafranek R, Klein A, Zafeiratos S, Havecker M, Knop–Gericke A, Schlogi R (2006) Surface states, surface potentials, and segregation at surfaces of tin-doped $In_2O_3$. Phys Rev B 73:245312
8. Vagadia M, Ravalia A, Katba S, Solanki PS, Bopana K, Kumar M, Choudhary RJ, Phase DM, Kuberkar DG (2014) J Alloys and Compounds 610:113–117
9. Hou T, Mao J, Pan H, Tu M (2006) J. Nano Particle Res 8:293–297
10. Piper LFJ, Demasi A, Cho SW, Smith KE, Fuchs F, Bechstedt F, Korber C, Klein A, Payne DJ, Egdell RG (2009) Appl Phys Lett 94: 022105
11. Zhou A, Alonso V, Omjakushin JB, Goodenough Y, Ren JQ, Yan JG (2010) Phys Rev B 81: 214115

# Estimation of Dislocation Density Using Electron Channelling Contrast Imaging in Ti-Hastelloy-N


**Harish Donthula, K. V. Manikrishna, B. Vishwanadh, and R. Tewari**

**Abstract** In the present study, using electron channelling contrast imaging (ECCI) technique dislocation densities were estimated in Ti-modified Hastelloy-N deformed to a nominal strain of 0.1. These dislocations were imaged using the backscattered electrons signal under controlled two beam diffraction conditions in SEM. To obtain such a condition, the crystallographic orientation of the grain is evaluated from the electron backscattered diffraction (EBSD) patterns. The grain is then oriented to a desired diffracting condition w.r.t electron beam using the tilt and rotation angles of the SEM stage. For this purpose, a software has been developed which helps in manoeuvring the crystal to different diffracting conditions by estimating the permissible tilt and rotation angles of the SEM stage due to its geometry. The dislocation densities obtained from this technique are corroborated with that of TEM.

**Keywords** Electron channelling contrast imaging · Dislocation density · Electron backscattered diffraction

## 1 Introduction

Researchers, from past to present, have characterized and quantified crystallographic defect densities (mainly dislocation density) using different methods, broadly classified as direct and indirect techniques [1–4]. The direct techniques are visual-based techniques, while the indirect techniques adopt a mathematical model to estimate the defect densities. Both these techniques have their inherent limitations and uncertainties in measurement of dislocation densities. For example, XRD and TEM, which are widely used to estimate the dislocation densities, probe dif-

H. Donthula (✉) · B. Vishwanadh · R. Tewari
Material Science Division, Bhabha Atomic Research Centre, Mumbai 400088, India
e-mail: dharish@barc.gov.in

K. V. Manikrishna
Mechanical Metallurgy Division, Bhabha Atomic Research Centre, Mumbai 400088, India



P. Ghosal et al. (eds.), *Applications of Microscopy in Materials and Life Sciences*,
Springer Proceedings in Materials 11,
https://doi.org/10.1007/978-981-16-2982-2_4

ferent length scales in a material; former in micrometres while the latter in nanometres [2, 3]. XRD estimates average defect densities by employing mathematical models based on the broadening of diffraction peak profiles obtained from a bulk specimen [3, 4]. However, this technique cannot visualize and characterize individual dislocations. On the other hand, TEM can quantify and characterize the dislocations based on the invisibility criterion by imaging at specific diffracting conditions [1]. The localized dislocation density can be quantifying by measuring the number of the lattice defects in a bright/dark field TEM micrographs. But TEM techniques are limited to low dislocation densities, and the margin of error increases substantially when the contrast of dislocations is lost due to overlapping defects and artefacts.

Microstructural features in deformed specimens such as slip bands, nano-twins, dislocation cells and domains are also distributed in the microstructure at various length scales [5, 6]. For example, depending on the alloy systems and deformation parameters these features can vary from few nanometres to hundreds of nanometres. As XRD and TEM probe different length scales in a material, it is highly likely that the former calculates the average densities due to overall deformation and the latter due to localized deformation. The length scales and the probing volume for different techniques are listed in Table 1.

In this regard, SEM-based ECCI can be of a great help, as it can probe the intermediate length scales between XRD and TEM. Also, this technique can image the distribution of various microstructural features and lattice defects without vigorous sample preparation [5–8]. The differential channelling of the electrons due to the misorientations caused by defects in a crystal generates a spatial variation of BSE yield, thereby generating a high contrast image of the defects from a bulk specimen near two-beam diffracting condition. To image lattice defects using ECCI, the crystal must be navigated to different diffracting conditions w.r.t electron beam. However, unlike TEM, kikuchi diffraction patterns are not available for the navigation of the crystal to different diffracting conditions. In the regard, the major challenges are the following:

- Generation of selected area channelling patterns (similar to kikuchi patterns) for a crystal of specific orientation w.r.t electron beam.
- Obtaining the permissible tilt and rotation angles of the SEM stage to orient the crystal into a near two beam diffracting conditions. It is observed that for the

**Table 1** Probing volumes and length scales for different techniques

| Technique | Length scale and probing volume |
|---|---|
| XRD | Few microns along thickness direction; *probe volume > $10^{-3}$ $mm^3$ |
| ECCI | Less than hundred nanometres along thickness direction with higher field of view; *Probe volume ($10^{-9}$ to $10^{-8}$ $mm^3$) |
| TEM | <100 nm along thickness direction; *Probe volume ($10^{-12}$ to $10^{-11}$ $mm^3$) |

*indicates an approximate estimate, as the probe volume depends on beam size, sample dimension and magnification

positive values of deviation parameter ($w$), product of extinction distance ($\xi_g$) and excitation error ($S_g$), a sharp bright contrast of defects is obtained against the dark matrix [9].

In this study, a software has been developed to simulate the diffraction patterns obtained from a crystal oriented with respect to electron beam. Based on the orientation of the crystal, the software estimates the permissible tilt and rotation angles of the stage to attain the desired two beam diffracting conditions. Using this approach, the defect densities in Hastelloy-N which was deformed to a nominal strain of 0.1 are estimated. The obtained dislocation densities from this approach are corroborated with those obtained from TEM analysis.

## 2 Experimental

In the study, an as-cast Hastelloy-N block was solutionized at 1200 °C for 2 h to dissolve the carbides into matrix and subsequently forged into a bar of 6 mm × 6 mm in cross section [10]. The forged bar is then held at 1200 °C for an hour to obtain a recrystallized microstructure and avoid the precipitation of secondary carbides at the grain boundaries. Cylindrical samples of 4.5 mm × 6 mm ($\phi$) samples were fabricated from the recrystallized bar and compressed uniaxially to a nominal deformation of 10% at a strain rate of $10^{-3}$ $s^{-1}$. The compressed samples were then cut across the axis and mechanically polished until mirror finish is obtained. Further, chemo-mechanical polishing was carried out with 40 nm colloidal silica suspension to eliminate the deformed layer from the surface generated during sample polishing. TEM samples were prepared from the centre region of the deformed sample by twin jet electropolishing the mechanically thinned down samples using a mixture of 90 parts of methanol and 10 parts perchloric acid as electrolyte at −35 °C and 20 V. Electron channelling contrast imaging is performed in backscattered imaging mode in Carl Zeiss Auriga FESEM attached with oxford Nordlys EBSD detector. Defect analysis was carried out using Carl Zeiss Libra 200FE microscope. Foil thickness of the TEM sample was estimated using electron energy loss spectroscopy using an omega filter attached with the TEM.

## 3 Achieving the Necessary Diffracting Condition for ECCI

D.G. Coates [11] had first observed selected area channelling patterns, similar to kikuchi pattern, on a single crystal of GaAs with (111) orientation in backscattering imaging mode by rocking the stage in two orthogonal directions in a conventional SEM. Later Crimp et al. [12] based on the invisibility criteria used ECCI to characterize the nature of the dislocations in Fe–Al alloys. The earlier ECCI studies used rocking beam method to image dislocations at a specific diffracting condition

where the sample stage was tilted/rotated by following a specific diffraction band in the channelling pattern to achieve near two beam condition, an approach similar to that followed in TEM [11–13]. However, this method could not extensively explored as (i) most SEMs are not equipped with additional deflector coils to allow rocking of beam and (ii) poor spatial resolution due to rocking beam or stage was not suitable for polycrystalline samples.

To overcome the above-mentioned limitations, ECCI is carried out by integrating EBSD with backscattered electron imaging in SEM [14]. In this approach, the orientation of a crystal/grain w.r.t global reference frame obtained from EBSD is used to simulate the channelling pattern of the crystal w.r.t electron beam. Using the appropriate set of tilt and rotation operations of the SEM stage obtained by the software, the chosen crystal/grain can be navigated to desired diffracting conditions ($w > 0$). A detailed flowchart of the software is shown in Fig. 1. At such diffracting conditions, due to higher channelling of electrons in the perfect crystal (matrix) than the regions with defects, a spatial variation of backscattered electron yield is obtained. Therefore, the defects appear brighter contrast against the dark matrix, similar to a weak beam TEM image as shown in Fig. 2. The contrast generation mechanism for lattice defects at different diffracting conditions is theoretically explained by using Bloch wave method [15, 16].

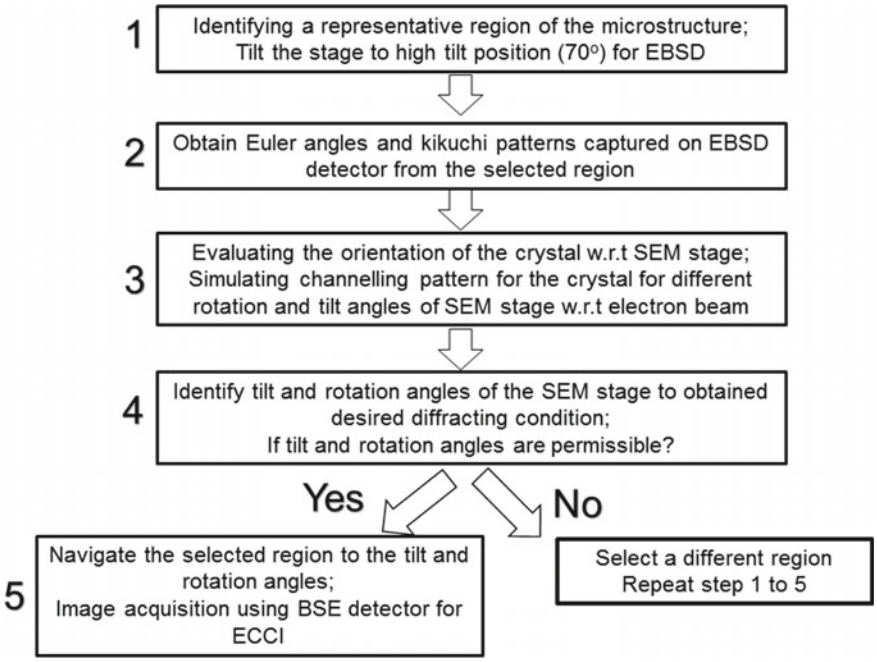


**Fig. 1** Flowchart for carrying out ECCI in SEM using the EBSD-based crystallographic software

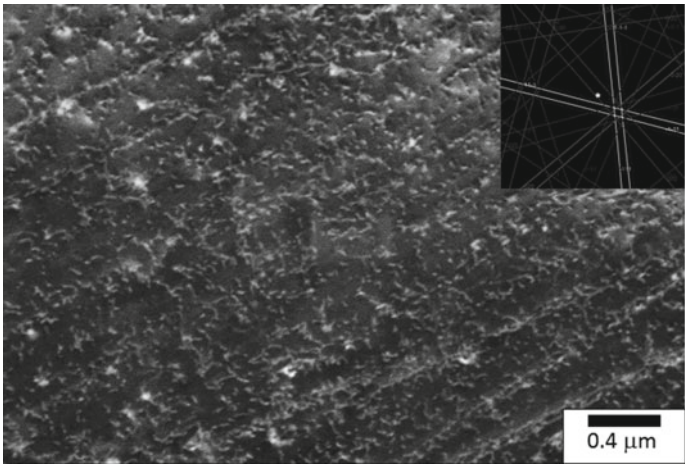


**Fig. 2** Microstructure of Hastelloy N deformed to a nominal strain of 0.1, showing the presence of dislocations captured using ECCI at $(\bar{2}02)$ diffracting condition. The simulated diffraction pattern of the crystal at diffracting condition is shown in inset

## 4 Results and Discussion

The microstructure of the 10% deformed Hastelloy-N specimen is shown in Fig. 3a. Consider the region marked as 'A' whose orientation $((\phi_1, \phi, \phi_2) = (343, 42, 10.3))$ is determined by EBSD w.r.t the global reference frame. By choosing the correct set of tilt (preferably lower tilt angles) and rotation angles for the SEM stage obtained from the software, the chosen grain can be navigated to different diffracting conditions. For example, three diffracting conditions are chosen to measure the dislocation density near (011) zone axis, namely $g_{200}$, $g_{0\bar{2}2}$ and $g_{1\bar{1}1}$. Figure 3c shows the simulated kikuchi pattern w.r.t electron beam at $g_{1\bar{1}1}$ two-beam condition by using the rotation and tilt angles of the stage (tilt = 8° rot = 340°). At such diffracting condition, due to greater electron channelling the grain marked as 'A' appears darker than other grains in the microstructure as shown in Fig. 3a. At higher magnifications, the dislocation structure can be observed as shown in Fig. 3b. The distribution of defects in the microstructure at similar diffracting conditions in TEM is also captured as shown in Fig. 3d.

The dislocation density is estimated using the following expression, $= \frac{2N}{Lt}$, where $N$ is the total number of intersection of dislocations with the grid of length '$L$' on the micrograph and '$t$' is the probe depth/foil thickness [17]. The probe depth in the expression is the length to which electrons channel into the material at a specific diffracting condition. The typical thickness to which electrons channel at a specific diffracting condition is in the order of $5\xi_g$ [16]. The probe depth calculated using extinction distance for different family of atomic planes in nickel is given in Table 2 [18]. Similarly, the foil thickness in TEM is calculated using electron

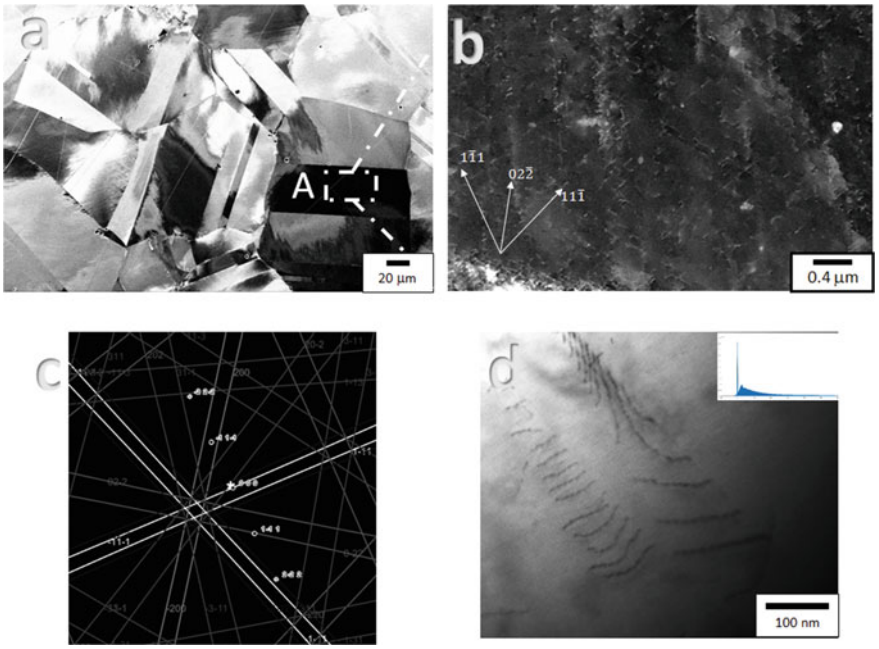


**Fig. 3** **a** Low magnification image highlighting the region A, which exhibit maximum electron channelling. **b** High magnification image of region 'A' showing the dislocation structure at (1$\bar{1}$1) diffracting condition superimposed with the traces of different crystallographic directions. **c** Simulated kikuchi pattern and spot pattern at (1$\bar{1}$1) diffracting condition. **d** Bright field TEM image showing the presence of dislocations at (1$\bar{1}$1) diffracting condition. Inset shows the EELS pattern obtained from the region

energy loss spectroscopy [1]. Therefore, using the above expression the dislocation density calculated at different diffracting conditions from ECCI and TEM are given in Table 2. The dislocation densities estimated by this method are of the similar order then the densities estimated by TEM. Both techniques TEM and ECCI can estimate the dislocation density provided its contrast is discernible. Therefore, this limits the estimation of defect densities in highly deformed samples due to overlapping lattice defects in the microstructure. The uncertainties in measurement of

**Table 2** Dislocation densities calculated at different diffraction conditions using TEM and ECCI. Probe depths in ECCI at these diffracting conditions are also listed

| Diffracting condition | Probe depth (in nm) in ECCI | Dislocation density ($m^{-2}$) using ECCI | Dislocation density ($m^{-2}$) estimated using TEM |
|---|---|---|---|
| 1$\bar{1}$1 | 42 | $1.75 \pm 0.9 \times 10^{14}$ | $1.67 \pm 0.5 \times 10^{14}$ |
| 200 | 48 | $2.11 \pm 0.5 \times 10^{14}$ | $1.96 \pm 0.7 \times 10^{14}$ |
| 0$\bar{2}$2 | 70 | $1.71 \pm 0.4 \times 10^{14}$ | $1.61 \pm 1.1 \times 10^{14}$ |

defect densities by TEM are subjected to the presence of artefacts such as bend contours, thickness fringes and annihilation of dislocations into the free surface near the hole generated during sample preparation. However, such artefacts do not affect the estimation of dislocation densities in ECCI. Unlike TEM, ECCI does not demand a vigorous sample preparation and is a robust technique for estimation of defect densities in a material. Also, ECCI is an effective tool to understand in-situ deformation/hardening phenomenon such as nano-indentation, irradiation and deformation induced transformations which is otherwise not possible with conventional techniques. However, this technique being a largely depended on the surface topology, utmost care has to be taken in eliminating the deformed layer due to mechanical polishing from the surface of the specimen.

## 5 Summary

The major challenge of obtaining channelling pattern from a crystal w.r.t electron beam is circumvented by using EBSD-based crystallographic approach to simulate these patterns at different tilt and rotation angles. This EBSD approach, unlike rocking beam method, has a better spatial resolution and can be integrated to conventional SEM's with greater ease. As the latter require tweaking the current of the deflector coils to rock the beam w.r.t optic axis. The current work has demonstrated that EBSD-based crystallographic approach for ECCI as a robust technique for measurement of dislocation densities on a bulk specimen. The dislocation densities obtained by ECCI in SEM is captured by probing the material at higher length scales (sub-micron) than TEM with a greater field of view. Therefore, ECCI can complement the conventional characterization techniques to estimate lattice defect densities at multiple length scales.

## References

1. Williams DB, Carter CB (1996) Transmission electron microscopy a textbook for materials science. Springer, USA
2. Griffiths M, Winegar JE, Mecke JF, Holt RA (1991) Determination of dislocation densities in hexagonal close-packed metals using X-ray diffraction and transmission electron microscopy. Adv X-Ray Anal 35:593–599. https://doi.org/10.1154/S0376030800009290
3. Karri M, Singh JB, Manikrishna KV, Kumawat BK, Kumar N, Srivastava D (2017) On the suitability of peak profile analysis models for estimating dislocation density. Mater Sci Eng, A 700:75–81. https://doi.org/10.1016/j.msea.2017.05.103
4. Williamson GK, Hall WH (1953) X-ray line broadening from filed aluminium and wolfram. Acta Metall 1:22–31. https://doi.org/10.1016/0001-6160(53)90006-6
5. Sulzer S, Li Z, Zaefferer S, Hafez Haghighat SM, Wilkinson A, Raabe D, Reed R (2020) On the assessment of creep damage evolution in nickel-based superalloys through correlative HR-EBSD and cECCI studies. Acta Mater 185:13–27. https://doi.org/10.1016/j.actamat.2019.07.018

6. Gutierrez-Urrutia I, Zaefferer S, Raabe D (2009) Electron channeling contrast imaging of twins and dislocations in twinning-induced plasticity steels under controlled diffraction conditions in a scanning electron microscope. Scr Mater 61:737–740. https://doi.org/10.1016/j.scriptamat.2009.06.018
7. Ahmed J, Wilkinson AJ, Roberts SG (1997) Characterizing dislocation structures in bulk fatigued copper single crystals using electron channelling contrast imaging (ECCI). Philos Mag Lett 76:237–245. https://doi.org/10.1080/095008397178986
8. Gutierrez-Urrutia I, Zaefferer S, Raabe D (2010) The effect of grain size and grain orientation on deformation twinning in a Fe-22wt.% Mn-0.6wt.% C TWIP steel. Mater Sci Eng A 527:3552–3560. https://doi.org/10.1016/j.msea.2010.02.041
9. Gutierrez-Urrutia I (2019) Quantitative analysis of electron channeling contrast of dislocations. Ultramicroscopy 206. https://doi.org/10.1016/j.ultramic.2019.112826
10. Braski DN, Leitnaker JM (1977) Production of homogeneous titanium-Hastelloy N alloys, ORNL/TM-56
11. Coates DG (1967) Kikuchi-like reflection patterns obtained with the scanning electron microscope. Philos Mag 16:1179–1184. https://doi.org/10.1080/14786436708229968
12. Crimp MA, Simkin BA, Ng BC (2001) Demonstration of the g b × u = 0 edge dislocation invisibility criterion for electron channelling contrast imaging. Philos Mag Lett 81:833–837. https://doi.org/10.1080/09500830110088755
13. Mansour H, Crimp MA, Gey N, Maloufi N (2015) Accurate electron channeling contrast analysis of a low angle sub-grain boundary. Scr Mater 109:76–79. https://doi.org/10.1016/j.scriptamat.2015.07.023
14. Gutierrez-Urrutia I, Zaefferer S, Raabe D (2013) Coupling of electron channeling with EBSD: Toward the quantitative characterization of deformation structures in the sem. JOM 65:1229–1236. https://doi.org/10.1007/s11837-013-0678-0
15. Zaefferer S, Elhami NN (2014) Theory and application of electron channelling contrast imaging under controlled diffraction conditions. Acta Mater 75:20–50. https://doi.org/10.1016/j.actamat.2014.04.018
16. Spencer JP, Humphreys CJ, Hirsch PB (1972) A dynamical theory for the contrast of perfect and imperfect crystals in the scanning electron microscope using backscattered electrons. Philos Mag 26:193–213. https://doi.org/10.1080/14786437208221029
17. Ham RK (1961) The determination of dislocation densities in thin films. Philos Mag 6:1183–1184. https://doi.org/10.1080/14786436108239679
18. Reimer L, Kohl H (2008) Transmission electron microscopy. Springer, Cham

# Efficiency of the Solid Oxide Cell (SOC) Using Nanocrystalline Mixed Ionic and Electronic Conducting (MIEC) Oxides as Air Electrode Materials in Conjunction with Doped Ceria-Based Interlayers


**Shoroshi Dey, Jayanta Mukhopadhyay, and Abhijit Das Sharma**

**Abstract** Nanocrystalline MIEC air electrodes, viz., La-Sr-Co-Fe and Ba-Sr-Co-Fe (6482) and nano-Gd-doped ceria (GDC) are synthesized using solution combustion technique and hydroxide co-precipitated route, respectively. Synthesized calcined nanopowders are characterized for phase purity using X-ray diffraction showing rhombohedral lattice for LSCF and cubic lattices for BSCF and GDC. Detailed transmission electron microscopy (TEM) reveals a near-net shape nanoparticles of MIEC perovskites and agglomerate free nanoparticles for GDC, and thus a composite functional layer was formulated in combination with MIEC and GDC to adhere in between electrolyte/interlayer and electrodes. Lower electrode polarizations of 0.017 $\Omega.cm^2$ and 0.17 $\Omega.cm^2$ with high exchange current density prove better electrode kinetic phenomena @850 °C for both LSCF-6482 and BSCF-6482 with sufficiently high current densities for both SOFC and SOEC modes of operation with the highest hydrogen generation rate of 0.62 $Nl.cm^{-2}.h^{-1}$. Cell performances are clinically correlated with the cell microstructure.

## 1 Introduction

Solid oxide cell (SOC) is considered as one of the most efficient energy conversation devices which can play the most vital part for a socio-economic development in near future [1, 2]. During the past few decades, tremendous efforts have been devoted toward the development of the air electrode to suppress the delamination and degradation issues. Mixed ionic and electronic conducting (MIEC) perovskite

S. Dey (✉) · J. Mukhopadhyay · A. Das Sharma
Fuel Cell and Battery Division, CSIR-Central Glass and Ceramic Research Institute, Kolkata 700032, India

S. Dey · J. Mukhopadhyay · A. Das Sharma
Academy of Scientific and Innovative Research (AcSIR), Ghaziabad 201002, India



P. Ghosal et al. (eds.), *Applications of Microscopy in Materials and Life Sciences*, Springer Proceedings in Materials 11,
https://doi.org/10.1007/978-981-16-2982-2_5

oxides, viz., $La_{1-x}Sr_xCo_yFe_{1-y}O_3$ (LSCF), $Sm_{0.5}Sr_{0.5}Co_{0.5}O_3$ (SSC), $Ba_{1-x}Sr_xCo_{1-y}Fe_yO_3$(BSCF), etc., have recently drawn much attention to encounter such problems [3, 4]. However, the application of such MIEC perovskites as air electrodes faces a problem with solid-state unwanted reaction with that of the conventional yttria-stabilized-zirconia (YSZ) electrolyte, and thus the application of doped ceria as an interlayer and the composite layer of MIEC mixed with doped ceria as a buffer layer lowers the interfacial polarization resistances with layer-wise minimization of the thermal expansion coefficient mismatches from the air electrodes to the electrolyte [5]. Researchers have shown that doping with aliovalent cations like $Gd^{3+}$, $Sm^{3+}$, $Eu^{3+}$, $La^{3+}$, etc., can enhance the electrocatalytic activity by increasing the oxygen vacancy in the ceria lattice [6]. Among the MIECs, $La_{1-x}Sr_xCo_yFe_{1-y}O_3$ (LSCF) and $Ba_{1-x}Sr_xCo_yFe_{1-y}O_3$ (BSCF)-based oxides have been widely reported as an efficient air electrode for SOC because of the extended triple phase boundary (TPB) for oxygen reduction or evaluation reaction through the bulk path [7, 8]. Doped ceria having an excellent solid solubility of the diffused 'Sr' from the air electrodes of such MIEC classes can further increase the stability of the materials while using for longer time of operation [5]. Comparison of the partial molar free energy change $(\Delta G_{O_2}^{-})$ associated with the oxygen reduction/evolution process for $Ba_{0.6}Sr_{0.4}Co_{0.8}Fe_{0.2}O_3$ (BSCF-6482) and $Ba_{0.5}Sr_{0.5}Co_{0.8}Fe_{0.2}O_3$ (BSCF-5582) in the temperature regime 650–950 °C shows high values for BSCF-6482 system and thus has been taken for the present investigation with the state-of-the-art $La_{0.6}Sr_{0.4}Co_{0.8}Fe_{0.2}O_3$ based MIEC [9]. It has further been shown by many groups of researchers that the structural property of the doped ceria has a strong correlation with processing techniques and thus correlates with the efficacy of using in conjunction with the air electrodes [10].

Under this present study, $La_{0.6}Sr_{0.4}Co_{0.8}Fe_{0.2}O_3$ (LSCF-6482) and $Ba_{0.6}Sr_{0.4}Co_{0.8}Fe_{0.2}O_3$ (BSCF-6482)-based multicomponent mixed ionic and electronic conducting (MIEC) ceramic oxides were synthesized using combustion technique which is believed to be a modified Pechini process. Gel combustion characteristics with detail crystallographic structural analyses have been investigated thoroughly. Detailed electron microscopic analyses both for MIEC electrodes and Gd-doped ceria, which is synthesized by simple, cost-effective and up scalable co-precipitation method were carried out. Electrode polarizations for LSCF-6482 and BSCF-6482 system in combination with buffer layers of Gd-doped ceria (GDC) and MIEC on the top of GDC-based electrolyte were studied through impedance spectroscopic analyses in the symmetric cell configuration. The single cell (NiO-YSZ/YSZ/GDC/LSCF-6482:GDC/LSCF-6482 and NiO-YSZ/YSZ/GDC/BSCF-6482:GDC/BSCF-6482) configurations were fabricated and tested for the electrochemical performances of such MIEC air electrodes in association with the interlayers and buffer layers through I-V characteristics both under the SOFC and SOEC modes. The detail results have been presented in corroboration with synthesized particle size, morphology, electrode, and cell performance both in SOFC and SOEC modes of operation.

## 2 Experimental Procedure

Self-heat sustainable solution autocombustion technique was used for the synthesis of LSCF-6482 and BSCF-6482 MIEC powders by using nitrate salts of lanthanum, barium, strontium, iron, and cobalt-based precursors and reported in our previous articles [11, 12]. L-alanine and citric acid-glycine were used to serve as a metal complexing fuel agent for such multicomponent perovskites as schematically shown in Fig. 1a. Schematic representation for synthesizing Gd-doped ceria (GDC) powder for the interlayer and buffer layers by co-precipitation technique using nitrate salts as the precursors of cerium and gadolinium is given in Fig. 1b. Ammonium hydroxide was added to the solution for the complete precipitation with constant measuring of pH. The detailed procedure for the synthesis with the rate determining steps and optimized parameters has already been discussed in our previous communication [13].

Thermal analyses of the precursor gels of LSCF-6482 and BSCF-6482 and dried GDC powder were carried out using differential thermal and thermogravimetric analyses (DTA, TGA) using simultaneous thermal analyzer (NETZSCH, STA 449 F3, Jupiter). The samples were tested from room temperature to 1000 °C in air at a specified heating rate of 5 °C/min. Phase purity of the synthesized materials, calcined at 850 and 1000 °C for LSCF-6482 and BSCF-6482 respectively and at 750 °C for GDC was checked by X-ray diffractometer in the 2θ range of 10°–80° with X'Pert Pro software using (PANalytical, Philips, Holland) X'Celerator operating at 40 kV and 40 mA with CuKα ($\lambda$ = 1.5406Å) radiation. The morphology of the powders was characterized using transmission electron microscopy (TEM, Tecnai G230ST) and the lattice spacing was determined using high resolution TEM (HRTEM) operating at an accelerated voltage of 300 kV. Detail impedance studies were carried

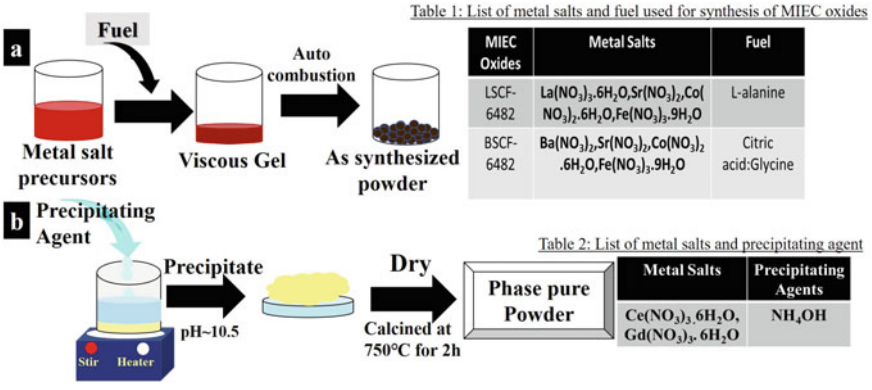


Table 1: List of metal salts and fuel used for synthesis of MIEC oxides

| MIEC Oxides | Metal Salts | Fuel |
|---|---|---|
| LSCF-6482 | $La(NO_3)_3.6H_2O$,$Sr(NO_3)_2$,$Co(NO_3)_2.6H_2O$,$Fe(NO_3)_3.9H_2O$ | L-alanine |
| BSCF-6482 | $Ba(NO_3)_2$,$Sr(NO_3)_2$,$Co(NO_3)_2.6H_2O$,$Fe(NO_3)_3.9H_2O$ | Citric acid:Glycine |

Table 2: List of metal salts and precipitating agent

| Metal Salts | Precipitating Agents |
|---|---|
| $Ce(NO_3)_3.6H_2O$, $Gd(NO_3)_3.6H_2O$ | $NH_4OH$ |

**Fig. 1** **a** Schematic representation of synthesis procedure for LSCF-6482 and BSCF-6482; **b** Scheme for GDC synthesis by using co-precipitation technique

out using symmetric cell configuration, viz., BSCF-6482/BSCF-6482:GDC(1:1)/GDC/BSCF-6482:GDC(1:1)/BSCF-6482 and LSCF-6482/LSCF-6482:GDC(1:1)/GDC/LSCF-6482:GDC(1:1)/LSCF-6482 onto sintered GDC-disks. The interlayer and buffer layers made of GDC and BSCF-6482/LSCF-6482:GDC (1:1wt ratio) were prepared by screen printing techniques of the thick pastes of the respective formulations and subsequently heat treated in the temperature range of 1300 °C–1100 °C for 4 h. The impedance spectra for such symmetrical cells were captured with AC frequency, i.e., $10^{-1}$ Hz $\leq$ f $\leq$ $10^{6}$ Hz from Solartron frequency response analyzer (Modulab). Cyclic voltammetry by using potentiostat-galvanostat (PGSTAT302N, Autolab, The Netherlands) was also used for measuring the exchange current densities of such MIEC air electrodes. For the single cell fabrication of configurations Ni-YSZ/YSZ/GDC/LSCF-6482:GDC/LSCF-6482 and Ni-YSZ/YSZ/GDC/BSCF-6482:GDC/BSCF-6482 tape cast, laminated and sintered half cells [14] were screen printed with interlayer, buffer layer, and final MIEC air electrode layers in a subsequent intervals and sintered. I-V characterizations for the single cell were measured both in SOFC and SOEC mode in the temperature range 800–850 °C in an indigenously made electrochemical testing assembly. While 3% moist hydrogen was fed in the SOFC mode, a mixture of $H_2O$–$H_2$ (1:1) was pumped into the fuel electrode during SOEC mode of operation. Oxygen is being fed at the air electrode side during both the operational modes. Cross-sectional micrograph of the single cell with GDC interlayer was obtained using field emission scanning electron microscope [FESEM] (Gemini Supra 35, Zeiss) at 10 kV accelerated voltage in a polished section of an epoxy mounted sample.

## 3 Results and Discussion

### *3.1 Characteristics of Precursors and Synthesized Powders*

Thermal analysis of the gels of LSCF-6482, BSCF-6482 and dried powder sample of GDC in the temperature range of 25–1000 °C reveals highly exothermic combustion process that starts with the decomposition of the trapped water molecules from the metal complexes in the temperature range of 150–180 °C and is reflected by the endothermic peak in the DTA curve at 118 °C and 133 °C for LSCF-6482 and BSCF-6482 sample, respectively. Metal-fuel complex decomposition was initiated at the temperature regime of 150–270 °C as observed from the TG plot for both the samples which correspond to the exothermic peaks at 269 °C and 238 °C for LSCF-6482 and BSCF-6482. In this regard, a major weight loss is found in the temperature range of 300–420 °C with the exothermic peaks at 383 °C for BSCF-6482 and at 415°C for LSCF-6482, respectively. For GDC, sample as shown in Fig. 2b exhibits the initial mass loss for the structural water at 183°C which is reflected by the endothermic peak at 278°C in the DTA. A sharp exothermic peak at 323°C reflects the decomposition of the metal-hydroxide precursor. No considerable amount of weight loss was observed after 600°C for all the samples indicates

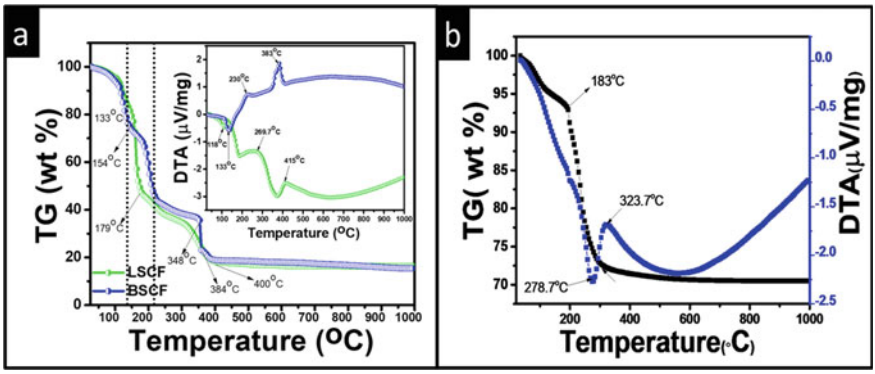


**Fig. 2** Thermogravimetric and differential thermal analysis plot of **a** LSCF-6482 and BSCF-6482; **b** GDC

the complete decomposition of the metal-ligand complexes. Figure 3a, b depicts the X-ray diffractograms for the calcined BSCF-6482, LSCF-6482, and GDC, wherein cubic, rhombohedral, and cubic phases are indexed for BSCF, LSCF, and GDC, respectively, by using ICDD-JCPDS database (JCPDS card no-34-394, 82-1961, and 000 055563). No additional secondary peaks are found, demonstrating that phase pure crystalline samples have been successfully prepared which is also confirmed from the existing literatures [11, 13, 15]. Transmission electron microscopic analysis (Fig. 4) revealed soft agglomerates of size in the range of 100–150 nm with embedded primary nanoparticle (in the range of 20–50 nm) for air electrode materials LSCF and BSCF synthesized by solution combustion technique, wherein agglomerate free nanoparticle of size $\sim$25 nm was observed for the nanocrystalline GDC, synthesized by co-precipitation method. The crystallite sizes for these nanocrystalline materials are calculated using Scherer's equation (Eq. 1). While the crystallite sizes for BSCF and LSCF were found to be $\sim$80 nm and $\sim$56 nm, respectively, the same for GDC (used as a buffer layer) was found to be $\sim$24 nm;

$$D = \frac{0.94\lambda}{\beta cos\theta} \tag{1}$$

where $D$ is the crystallite size, $\lambda$ is the wave length of radiation, $\beta$ is the full peak width at the half maxima (FWHM) and $\theta$ is the peak position. HRTEM for both LSCF-6482 and BSCF-6482 have revealed 'd' spacing of 0.277 nm and 0.283 nm for the crystal planes (104) and (110) that corroborate well with the crystallographic findings from XRD as rhombohedral and cubic perovskites for LSCF an BSCF systems, respectively. The interpenetrating angles, calculated from the fast fourier transformation (FFT) pattern of the two adjacent lattice planes of the synthesized LSCF-6482 and BSCF-6482 are found to be 29.81° and 19.44°, respectively. The highly ordered crystal lattice planes and the induced crystal strain as observed from

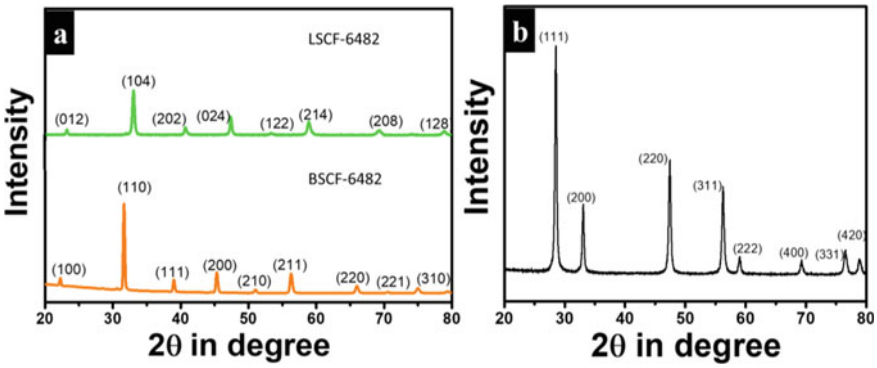


**Fig. 3** X-ray diffractograms of **a** BSCF-6482 and LSCF-6482; **b** GDC

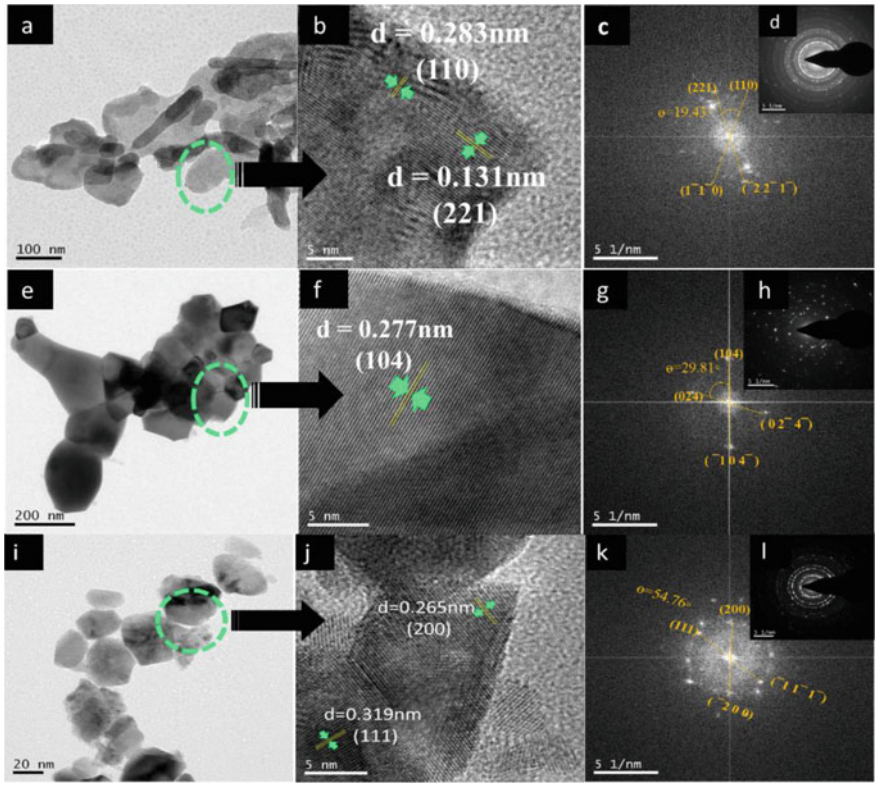


**Fig. 4** TEM micrographs (**a**, **e**, **i**); high resolution TEM images (**b**, **f**, **j**); FFT pattern (**c**, **g**, **k**) with SAD pattern in the inset (**d**, **h**, **l**) of BSCF-6482, LSCF-6482 and GDC, respectively

the HRTEM and FFT pattern may be effective for the electrocatalytic oxygen redox reaction. HRTEM images have revealed that both (111) and (200) planes corresponding to 'd' spacing of 0.319 nm and 0.265 nm are exposed for the nanocrystalline GDC powder having good resemblance with the corresponding XRD data and FFT pattern exhibits the interpenetrating angle of 54.7°. Formation of oxygen vacancy at (200) plane is higher than that of the stable least reactive (111) plane and hence enhance the catalytic activity [12]. Thus, the well-defined nanocrystalline particle of Gd-doped ceria formed by co-precipitation methodology may also responsible for the higher electrocatalytic activity when used as the interlayers and buffer layers.

## 3.2 Characteristics of MIEC Air Electrodes with GDC Based Inter and Buffer Layers

In order to establish the efficacy of the MIEC perovskite as air electrode material in conjunction with the GDC interlayer, impedance spectroscopic analysis has been carried out by using the symmetric cells of configuration as described in the experimental section in the temperature range of SOC operation (800–850 °C). The electrode polarization losses involving the diffusion are primarily being represented in the lower frequency region, wherein the higher frequency region attributed to the overall bulk impedance associated with electron transfer through grain interior and ion transfer process throughout defects in the grain boundaries [5]. From the temperature dependent Nyquist plot, as shown in Fig. 5a, it is further observed that with increase in temperature from 800 °C to 850 °C, ohmic resistance ($R_0$) and interfacial polarization resistance ($R_p$) of BSCF electrode are found to reduce from 8.94 Ω.cm$^2$ and 0.22 Ω.cm$^2$ to 6.86 Ω.cm$^2$ and 0.17Ω.cm$^2$ and the same $R_0$ and $R_p$ values of LSCF electrode are reduced from 1.63 Ω.cm$^2$ and 0.02 Ω.cm$^2$ to 1.37 Ω.cm$^2$ and 0.017 Ω.cm$^2$ (Table 1). It is also observed that $R_0$ of LSCF is much smaller than that of BSCF in both the temperature. This should be attributed to the presence of aliovalent substitution of $Sr^{2+}$ in the A site of $La^{3+}$creating sufficient metal ion pairs of $Co^{3+}/Co^{4+}$ and thus optimizing the disproportionation reactions of $Co^{3+}$ rather than BSCF [8]. The lower values of $R_p$ for both the electrodes at 800–850 °C dictate their effective application as an air electrode in conjunction with the GDC interlayer for SOCs. Tafel's plot as shown in Fig. 5b is the most convenient way for the measurement of exchange current density ($i_o$) to evaluate the electrode activation mechanism for both oxygen reduction reaction (ORR) and oxygen evaluation reaction (OER). The activation overpotential for the air electrode is defined as;

$$\eta_{act} = \pm A \log\left(\frac{i}{i_0}\right) \tag{2}$$

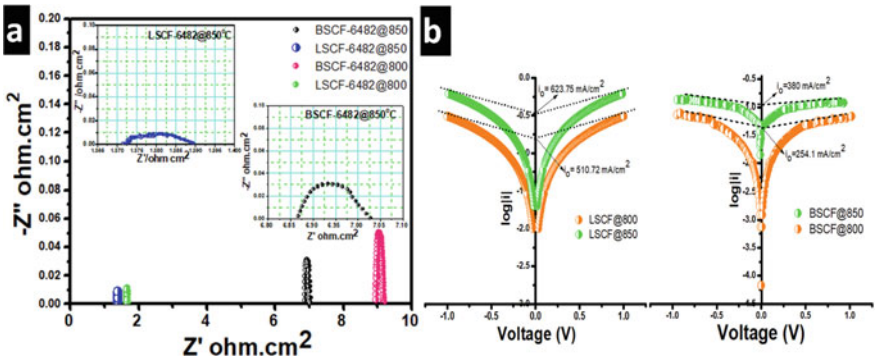


**Fig. 5** **a** Temperature dependent Nyquist plot of the symmetric cells of configuration BSCF-6482/BSCF-6482:GDC(1:1)/GDC/BSCF-6482:GDC(1:1)/BSCF-6482 and LSCF-6482/LSCF-6482:GDC(1:1)/GDC/LSCF-6482:GDC(1:1)/LSCF-6482; **b** Tafel's Plot of log|i| vs V

**Table 1** Interfacial resistances for MIEC air electrodes in symmetric cells

| Cell configuration | Temperature (°C) | $R_0$ (ohm.cm$^2$) | $R_{CT}$ (ohm.cm$^2$) | $R_p$ (ohm.cm$^2$) |
|---|---|---|---|---|
| LSCF-6482/LSCF-6482:GDC/GDC/ LSCF-6482:GDC/LSCF-6482 | 800 | 1.63 | 1.65 | 0.02 |
| | 850 | 1.37 | 1.387 | 0.017 |
| BSCF-6482/BSCF-6482:GDC/GDC/ BSCF-6482:GDC/BSCF-6482 | 800 | 8.943 | 9.17 | 0.22 |
| | 850 | 6.86 | 7.03 | 0.17 |

where, $\eta_{act}$ is the overpotential, $\pm A$ is Tafel's slope, i and $i_o$ are being the measured current density and the exchange current density. For both the electrodes, exchange current density ($i_o$) increases to 623.75 mA/cm$^2$ and 380 mA/cm$^2$ from 510.72 mA/cm$^2$ and 254.1 mA/cm$^2$ with increasing the temperature from 800$^o$ to 850 °C for the electrodes LSCF-6482 and BSCF-6482, respectively. Higher value of exchange current density reflects the better electrochemical reaction and easier charge transfer reaction at the electrode/electrolyte interface and being MIEC also through the bulk.

I-V characteristic of the single cells of configuration as mentioned in the experimental section with various MIEC air electrodes was investigated both in SOFC and SOEC modes at 800 °C and 850 °C as shown in Fig. 6a. For the electrodes LSCF-6482 and BSCF-6482, maximum current densities of 0.71 A.cm$^{-2}$ and 1.4 A.cm$^{-2}$ are observed at 1.3 V in SOEC mode, whereas current densities of 0.95A.cm$^{-2}$ and 0.77A.cm$^{-2}$ are measured at 0.5 V and at 800 °C in SOFC mode. It has also been observed that with increasing the operational temperature to 850 °C, the hydrogen generation rate for both the electrodes increases as shown in Fig. 6b. Hydrogen generation rate of 0.58 Nl.cm$^{-2}$.h$^{-1}$ and 0.30 Nl.cm$^{-2}$.h$^{-1}$ is obtained at 800 °C@1.3 V for BSCF and LSCF compositions with an increasing trend with increase in temperature. Irrespective of the temperature of operations, BSCF is found to have

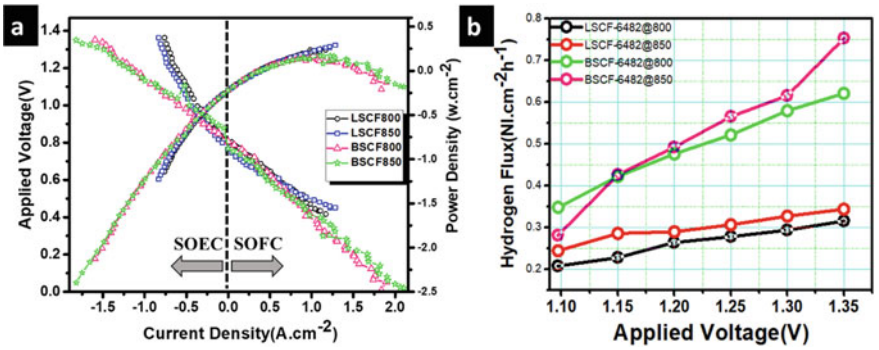


**Fig. 6** **a** I-V characteristics of the single cells with LSCF-6482 and BSCF-6482 as air electrode; **b** hydrogen flux of the single cells in SOEC mode of operation

higher hydrogen flux because of the intrinsically higher charge transfer reaction for OER as indicated by the presence of higher oxygen vacancies in the reaction:

$$O_2 + 2\,V_0^{\cdot\cdot} + 4e^- = 2O_0^x \tag{3}$$

Figure 7 shows the characteristic cross-sectional micrograph for the single cell of configuration Ni-YSZ/YSZ/GDC/BSCF-6482:GDC (1:1)/BSCF-6482 after I-V testing which reveals a strong coherence of the interlayer and buffer layers with that

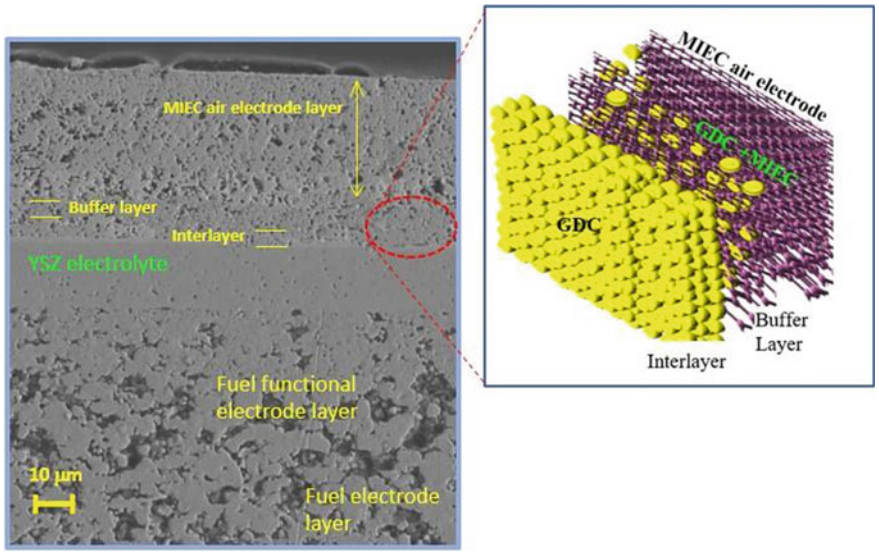


**Fig. 7** Cross-sectional micrograph for the single cell of configuration Ni-YSZ/YSZ/GDC/BSCF-6482:GDC(1:1)/BSCF-6482 with schematic representation of importance of GDC and GDC + MIEC-based interlayer and buffer layers

of the YSZ electrolyte and MIEC air electrode. Extended lengths of TPB in the MIEC air electrodes synthesized using solution combustion resulting in a near-net shape nanocrystalline particulates help in easy penetration of agglomerate free GDC nano-particulates synthesized using sol-gel route. Thus, the functionalization in the buffer layer is established during high temperature sintering of GDC and MIEC air electrodes ensuring easy charge transfer reactions to happen both for ORR and OER in SOFC and SOEC modes of operation and inhibition of layer-wise Sr diffusion.

## 4 Conclusion

Synthesized nanocrystalline MIEC oxides BSCF/LSCF-6482 by solution combustion and GDC nanoparticles by co-precipitation technique reveal phase purity through X-ray crystallographic study and MIEC air electrodes show rhombohedral and cubic lattices for LSCF and BSCF systems, respectively, and cubic for GDC. TEM analysis for MIEC oxides revealed that primary nanoparticles of size $\sim$20–50 nm are embedded into the agglomerate of size $\sim$100 nm while agglomerate free nanoparticles are obtained for GDC nano-powder. Interplanar distance of 0.277 nm and 0.283 nm obtained from HRTEM for planes (104) and (110) resembles with the XRD data for LSCF-6482 and BSCF-6482, respectively with desired interpenetrating angles for effective electrocatalytic activities in SOCs. Lower polarization values of 0.017 $\Omega.cm^2$ and 0.17 $\Omega.cm^2$ with higher exchange current densities of 623 mA/cm$^2$ and 380 mA/cm$^2$at 850 °C for LSCF & BSCF electrodes reflect the effective electrode activity. Current densities of 1.48 A.cm$^{-2}$ and 0.79 A.cm$^{-2}$ @ 1.3 V in SOEC mode with hydrogen generation rate of 0.62 Nl.cm$^{-2}$.h$^{-1}$ and 0.33 Nl.cm$^{-2}$.h$^{-1}$ are obtained at 850 °C for the cells with BSCF and LSCF electrodes, respectively. Cell performances with MIEC air electrodes in SOC application clearly indicate the efficacy of the nanocrystalline GDC interlayer and GDC and MIEC-based buffer layer by enhancing the bulk TBP length with layer-wise inhibition of Sr.

**Acknowledgements** Authors would like to acknowledge Director CSIR-CGCRI for his kind permission to publish this work and also BRNS and ONGC Energy Trust for the financial support.

## References

1. Addo PK, Sanchez BM, Chen M, Paulson S, Birss V (2015) CO/$CO_2$ study of high performance $La_{0.3}Sr_{0.7}Fe_{0.7}Cr_{0.3}O_3$ reversible SOFC electrodes. Fuel Cells 5:689–696
2. Zhang Y, Han M, Sun Z (2020) High performance and stability of nanocomposite oxygen electrode for solid oxide cells. Int J Hydrog Energy 8:5554–5564
3. Wang W, Huang Y, Jung S, Vohs JM, Gorte RJ (2006) A comparison of LSM, LSF and LSCO for solid oxide electrolyzer anodes. J Electrochem Soc 153:A2066–A2070

4. Li S, Xie K (2013) Composite oxygen electrode based on LSCF and BSCF for steam electrolysis in a proton-conducting solid oxide electrolyzer. J Electrochem Soc 160:224–233
5. Ghosh KB, Mukhopadhyay J, Basu RN (2016) Functionally graded doped lanthanum cobalt ferrite and ceria-based composite interlayers for advancing the performance stability in solid oxide fuel cell. J Power Sources 328:15–27
6. Wang Z, Quan Z, Lin J (2007) Remarkable Changes in the Optical Properties of $CeO_2$ Nanocrystals Induced by Lanthanide Ions Doping. Inorg Chem 46:5237–5242
7. Qiu L, Ichikawa T, Hirano A, Imanishi N, Takeda Y (2003) $Ln_{1-x}Sr_xCo_{1-y}Fe_yO_{3-\delta}$ (Ln = Pr, Nd, Gd; x = 0.2, 0.3) for the electrodes of solid oxide fuel cells. Solid State Ion 158:55–65
8. Zhang X, Zhang W, Zhang L, Meng L, Meng F, Liu X, Meng J (2017) Enhanced electrochemical property of $La_{0.6}Sr_{0.4}Co_{0.8}Fe_{0.2}O_3$ as cathode for solid oxide fuel cell by efficient in situ polarization-exsolution treatment. Electrochim Acta 258:1096–1105
9. Tanasescu S (2013) Effects of A-site composition and oxygen non stoichiometry on the thermodynamic stability of compounds in the Ba–Sr–Co–Fe–O system. J Solid State Chem 200:354–362
10. Fadzil N, Rahim M, Maniam GP (2018) Brief review of ceria and modified ceria: synthesis and application. Mater. Res. Express 5:085019
11. Dey S, Mukhopadhyay J, Lenka RK, Patro PK, Sharma AD, Mahata T, Basu RN (2020) Synthesis and characterization of nanocrystalline $Ba_{0.6}Sr_{0.4}Co_{0.8}Fe_{0.2}O_3$ for application as an efficient anode in solid oxide electrolyser cell. Int J Hydrog Energy 7:3995–4007
12. Dutta A, Mukhopadhyay J, Basu RN (2009) Combustion synthesis and characterization of LSCF-based materials as cathode of intermediate temperature solid oxide fuel cells. J Eur Ceram 29:2003–2011
13. Dey S, Choudhury D, Choudhuri M, Bhattacharya A, Mukhopadhyay J, Sharma AD, Mukhopadhyay M (2020) Facile synthesis of doped ceria-based oxide by co-precipitation technique and performance evaluation in solid oxide fuel cell. Int J Appl Ceram Technol 17:1769–1784
14. Basu RN, Sharma AD, Dutta A, Mukhopadhyay J (2008) Processing of high-performance anode-supported planar solid oxide fuel cell. Int J Hydrog Energy 33:5748–5754
15. Shen F, Lu K (2015) Comparative study of $La_{0.6}Sr_{0.4}Co_{0.2}Fe_{0.8}O_3$, $Ba_{0.5}Sr_{0.5}Co_{0.2}Fe_{0.8}O_3$ and $Sm_{0.5}Sr_{0.5}Co_{0.2}Fe_{0.8}O_3$ cathodes and the effect of $Sm_{0.2}Ce_{0.8}O_2$ block layer in solid oxide fuel cells. Int J Hydrog Energy 40:16457–16465

# Role of Second-Phase Particles on *In Situ* Deformation of an AZ80 Mg Alloy


**R. Sarvesha, W. Alam, J. Jain, and S. S. Singh**

**Abstract** *In situ* tensile testing was performed to examine the second-phase particle's role in crack initiation and propagation in the as-cast AZ80 alloy. The crack propagation predominantly occurred through the $Mg_{17}Al_{12}$ precipitates. Further, *in situ* tensile testing, in assistance with EBSD, delineated the strain partitioning between the matrix and $Mg_{17}Al_{12}$ precipitate. Besides, two-dimensional microstructure-based modeling was performed to understand the stress distribution in the alloy.

**Keywords** *In situ* tensile testing · Electron backscattered diffraction (EBSD) · Microstructure-based modeling

## 1 Introduction

Magnesium alloys exhibit a high strength-to-weight ratio, making them potential structural materials in the automobile and space industries [1]. Mg–Al-Zn alloys, which are designated as AZ series alloys, are a vital class of Mg alloys. As AZ series alloys mainly constitute aluminum (Al) and zinc (Zn) as alloying elements, they form non-equilibrium $Mg_{17}Al_{12}$ precipitates during casting. Apart from the major alloying elements (i.e., Al and Zn), a small quantity of Mn is also added to remove Fe from the Mg matrix by forming Al–Mn inclusions, which improves the overall corrosion resistance of the alloy [2].

The second-phase particles, i.e., $Mg_{17}Al_{12}$ and Al–Mn inclusions, have been observed to affect the AZ alloy's deformation behavior. Lü et al. [3] studied the

R. Sarvesha (✉) · W. Alam · S. S. Singh
Department of Materials Science and Engineering, Indian Institute of Technology Kanpur, Kanpur 208016, Uttar Pradesh, India
e-mail: sarvesha@iitk.ac.in

J. Jain
Department of Materials Science and Engineering, Indian Institute of Technology, Delhi, New Delhi 110016, India



P. Ghosal et al. (eds.), *Applications of Microscopy in Materials and Life Sciences*, Springer Proceedings in Materials 11,
https://doi.org/10.1007/978-981-16-2982-2_6

fracture behavior of the AZ91 alloy under tensile loading. Secondary crack growth in the alloy suggested that the cracks propagate near $Mg_{17}Al_{12}$ and α-Mg grain boundaries. Further, it was hypothesized that the crack initiates at the interface of Mg and $Mg_{17}Al_{12}$. Yakubtsov et al. [4] studied the tensile behavior of the AZ80 alloys, solutionized at different durations. It was found that the stress-strain behavior of the alloy strongly depends on the volume fraction of the $Mg_{17}Al_{12}$ phase. The dissolution of the $Mg_{17}Al_{12}$ precipitate, with time, during the solutionization increased the ductility.

Additionally, the eutectic $Mg_{17}Al_{12}$ phase has been believed to strongly influence the alloy's work hardening behavior, which is attributed to the high dislocation density at the interface between the matrix and the $Mg_{17}Al_{12}$ phase. Recently, it has been established that both the $Mg_{17}Al_{12}$ and $Al_8Mn_5$ particles in the AZ alloy deform considerably before fracture [5]. It should be noted that all the above findings are based on the post-mortem investigation of the fractured samples.

In the present work, we have systematically characterized the microstructure of the as-cast AZ80 magnesium alloy. For the first time, the effect of the $Mg_{17}Al_{12}$ precipitates on the fracture process, i.e., crack initiation and propagation, has been investigated using *in situ* tensile testing in a scanning electron microscope (SEM). Besides, two-dimensional microstructure-based modeling has been performed to understand the stress distribution in the alloy during tensile loading.

## 2 Experimental Procedure

Direct chill (DC) cast samples were cut into 5 mm × 9 mm × 8 mm blocks, using electrical discharge machining (EDM), to characterize the sample. The alloy's bulk composition was measured using optical emission spectroscopy (OES) (SPECTROMAXx, AMETEK). Further, the samples were polished till P4000 emery paper, using ethanol as a lubricant, followed by polishing a vibratory polisher (Buehler, VibroMet™ 2) in 0.05 μm alumina dispersed in ethanol. Final chemical polishing was carried out by agitating in 10% Nital for 10 s. Optical micrographs (OM) in different modes (bright and dark fields) were obtained using an optical microscope (Olympus, BX53M).

Secondary electron (SE) and backscattered electron (BSE) images were acquired using a scanning electron microscope (SEM) (JEOL, JSEM–7100F). EDS elemental maps were obtained using an EDS detector (Oxford, X-max50) attached to SEM. *In situ* tensile testing was carried out using a Gatan 2kN tensile stage at a crosshead velocity of 0.4 mm/min in an SEM (JEOL, JSEM–7100F). Electron backscattered diffraction (EBSD) using the EBSD detector (Oxford, Nordlys) was scanned with an accelerating voltage of 20 kV and a probe current of ∼13 nA. AZtec Crystal Version 1.1 was used for the post EBSD data analysis.

# 3 Results and Discussion

## *3.1 Microstructure of As-Cast Sample*

The composition from OES (Table 1) confirms it to be an AZ80 type magnesium alloy (as per the ASTM B275 standard) [6]. The optical micrograph (Fig. 1a), at low magnification, of an as-cast sample, shows that the precipitates have a network-like structure. The magnified image (Fig. 1b) indicates Mg–Al precipitates and Al–Mn inclusion. Yellow arrows (in Fig. 1b) indicate the additional dark regions in the optical micrograph, which will be identified shortly. Further, magnified optical bright-field image shows these eutectic precipitates contain porosities, which are prevalent in the optical dark-field micrograph (Fig. 1d). The formation of porosities is attributed to the selective dissolution of α-Mg during chemical polishing.

The BSE and SE micrographs of the same regions are shown in Fig. 2a, b, respectively. The BSE micrograph indicates that the Al–Mn particle is bright, and the Mg–Al precipitates are gray. The magnified SE image (Fig. 2c) shows continuous precipitates (arrows) adjacent to the large eutectic precipitate. Note that these regions appeared darker in the optical micrograph (Fig. 1b). The continuous precipitates exhibit rod and spherical morphologies (indicated in Fig. 2c). EDS elemental maps show that Zn is segregated in Mg–Al precipitate, whereas Fe is segregated in Al–Mn inclusion. The segregation of Zn in Mg–Al precipitate and Fe in Al–Mn inclusion is further confirmed by the presence of their peaks in the EDS spectra (Fig. 2f). Segregation of Fe in Al–Mn inclusion indicates that it acts as an effective scavenger for removing Fe from the α-Mg.

**Table 1** OES composition of the as-cast Mg alloy

| Al | Zn | Mn | Fe | Si | Mg |
|---|---|---|---|---|---|
| 9.1 ± 0.3 | 0.43 ± 0.06 | 0.16 ± 0.04 | 0.008 ± 0.005 | 0.025 ± 0.009 | Remaining |

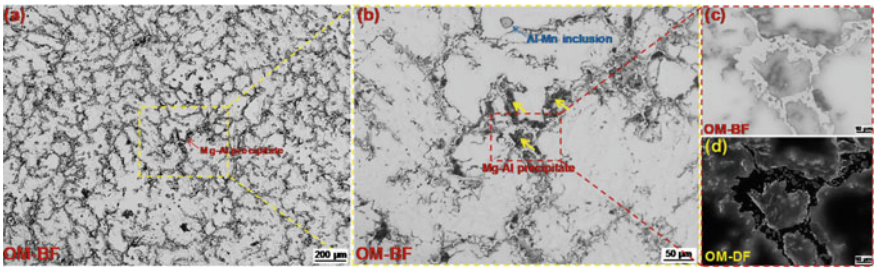


**Fig. 1** **a**, **b** As-cast optical micrographs (OM) in bright-field (arrows indicate Al–Mn inclusion and Mg–Al precipitates), **c**, **d** magnified images of a Mg–Al precipitate in bright-field (BF) and dark-field (DF), respectively

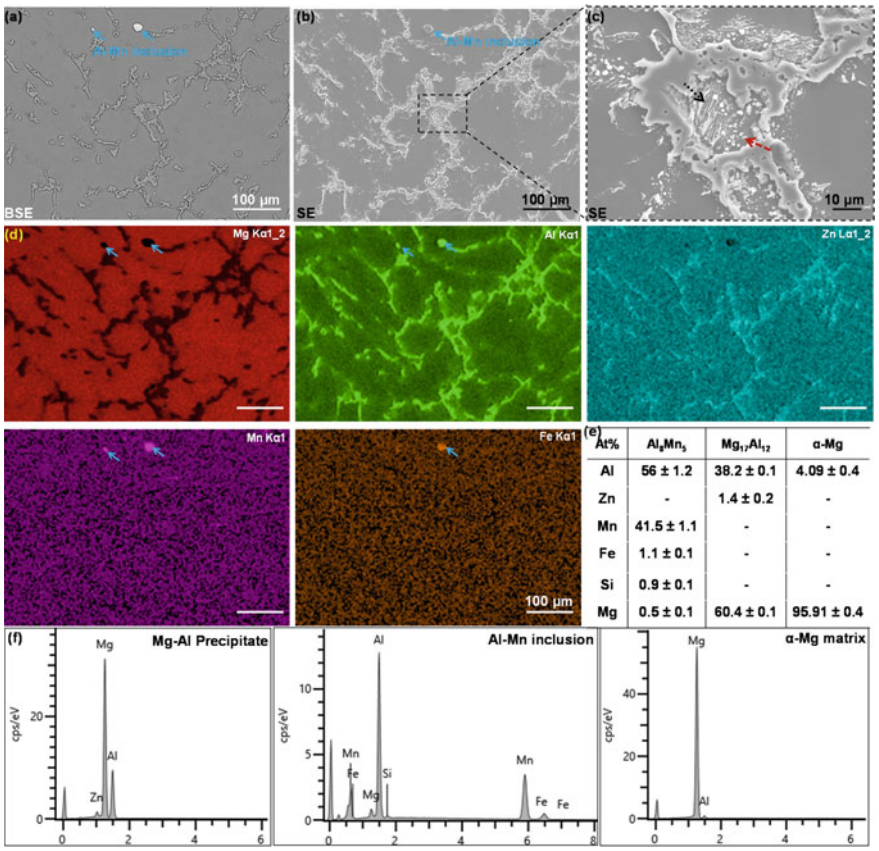


**Fig. 2** **a** BSE micrograph and **b**, **c** SE micrographs, **d** corresponding area EDS map, **e** composition of the constituent particles ($Al_8Mn_5$ and $Mg_{17}Al_{12}$) and α-Mg matrix, (f) EDS spectra of the $Mg_{17}Al_{12}$, $Al_8Mn_5$, and α-Mg matrix (solid blue color arrows in **a**, **b** and **d** show Al–Mn inclusion, whereas dotted black and red arrows indicate rod and spherical type $Mg_{17}Al_{12}$ principate, respectively.)

Further, EBSD maps of constituent particles are shown in Fig. 3. During EBSD scanning, a Truphase routine (AZtec, Oxford instruments) was used, where EDS data is simultaneously collected with EBSD data and the solution for the Kikuchi patterns was obtained. The hit rate during scanning was around 85%, and the un-indexed points were cleaned up by removing wild spikes and extrapolating to five nearest neighbors. The Mg–Al precipitates, as shown in Figs. 1 and 2, correspond to the $Mg_{17}Al_{12}$ eutectic precipitate having space group $I\bar{4}3m$. They form along the grain boundaries of the α-Mg matrix and are poly-crystalline (Fig. 3a, b), and grains are randomly oriented. The Al–Mn inclusions correspond to the $Al_8Mn_5$ phase having space group R3m. They constitute only twin boundaries which twinned along $\langle 10\bar{1}2 \rangle$ direction with dis-orientation of 90.66 ± 5° These constituent particles have also been identified through transmission electron microscopy (TEM) for the alloy of approximately similar composition [10].

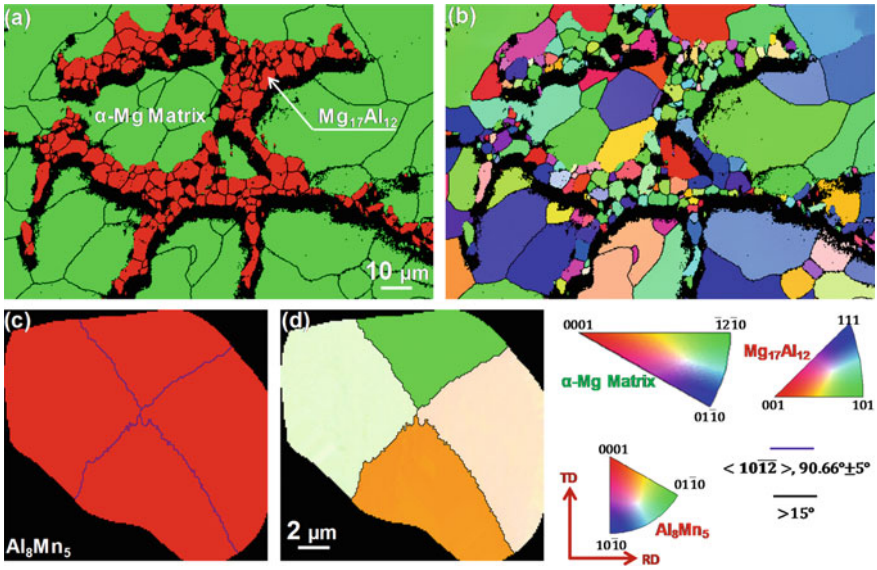


**Fig. 3** **a** Phase map and **b** EBSD map of the $Mg_{17}Al_{12}$ eutectic precipitate and α-Mg matrix. **c**, **d** are the phase map and EBSD map of the $Al_8Mn_5$ particle, respectively ($Mg_{17}Al_{12}$ eutectic precipitate is indicated in **a**)

## 3.2 In Situ *Tensile Testing in SEM*

The sample dimension and the as-cast microstructure of complete gauge length are shown in Fig. 4a, b, respectively. The as-cast SE micrograph is similar to the optical micrograph as shown in Fig. 1a. The SE micrograph at different strain (ε) levels is shown in Fig. 5. No significant microstructural changes were observed with an increase in strain until a strain of 0.021 (Fig. 5). When the strain reaches 0.033, microcrack is evident on the surface, as shown in Fig. 5. The stress reaches

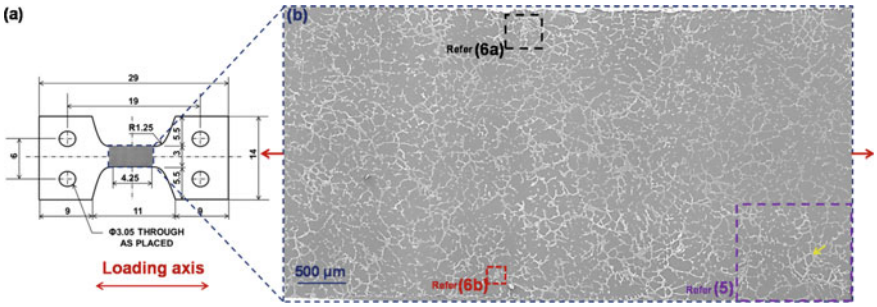


**Fig. 4** **a** In situ tensile testing sample dimension, **b** SE micrograph of the gage length of the sample (arrows at the end indicates loading direction)

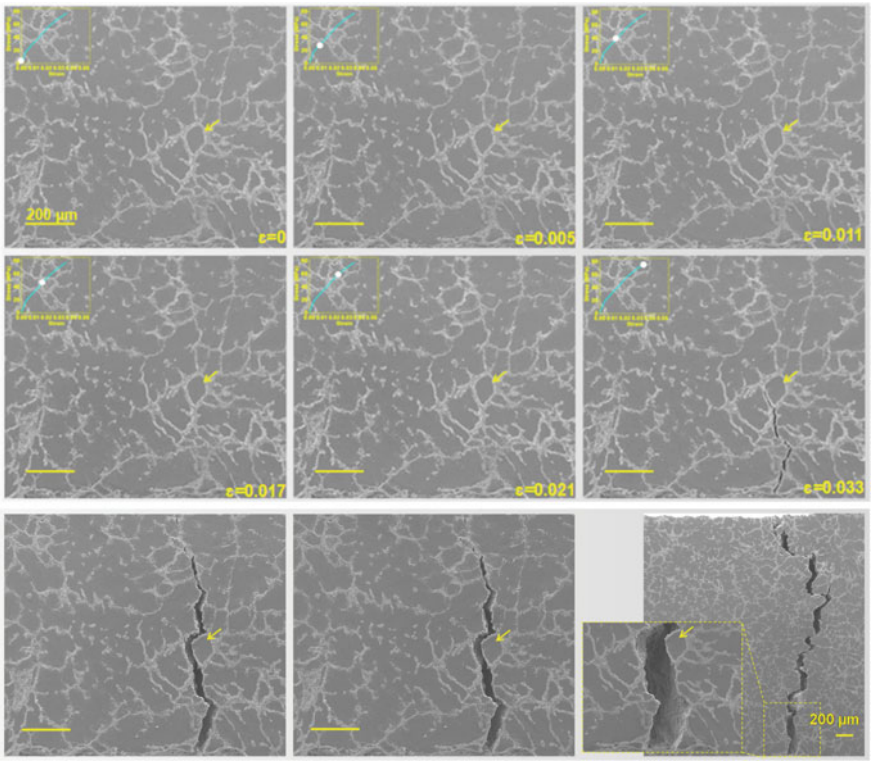


**Fig. 5** In situ SE micrographs showing the crack propagation at different strain levels in the as-cast AZ80 alloy (arrow indicates a reference feature in the SE micrograph)

the maximum value at this stage, as shown in the stress-strain diagram (refer to inset in Fig. 5). With the infinitesimal increase in strain, the crack was observed to propagate predominantly through the $Mg_{17}Al_{12}$ eutectic precipitates (Fig. 5).

Further, the magnified images from Fig. 4, as shown in Fig. 6a, b, indicate the evolution of damage in the $Mg_{17}Al_{12}$ and $Al_8Mn_5$ phases at different strain levels. It is evident from Fig. 6a, b that at the strain (ε) of 0.021, the cracks initiate in both the $Mg_{17}Al_{12}$ and $Al_8Mn_5$ particles. Further, increase in the strain resulted in the multiple cracks perpendicular to the loading direction (indicated by arrows in Fig. 6). Besides, the width of the cracks was observed to increase with an increase in strain. From Fig. 6, it is clear both particles, i.e., $Mg_{17}Al_{12}$ and $Al_8Mn_5$, contribute toward the crack initiation process. However, the crack propagation was predominantly observed to occur through the $Mg_{17}Al_{12}$ particles.

Further, to understand the strain partitioning between the $Mg_{17}Al_{12}$ precipitate and α-Mg, an *in situ* test was carried out in assistance with EBSD on the solutionized sample. Solutionization (420 °C, 3 h) was performed to avoid continuous precipitate interference during EBSD. Details of the solutionization treatment and respective microstructure have been discussed elsewhere [7].

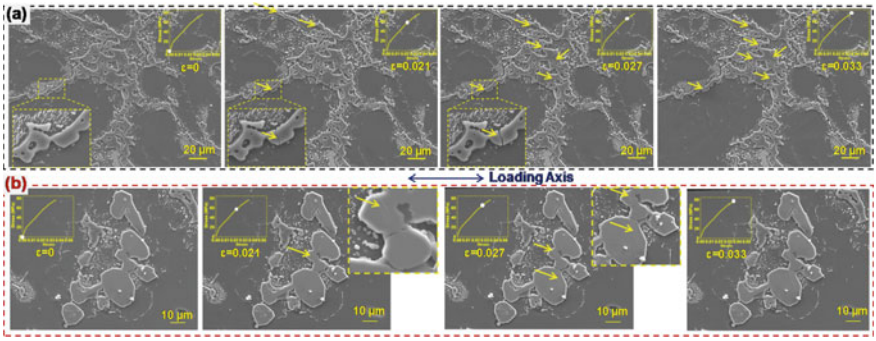


**Fig. 6** In situ SE micrographs (at higher magnification) showing the crack initiation in **a** $Mg_{17}Al_{12}$ precipitate, and **b** $Al_8Mn_5$ inclusion (arrow indicates the formation of crack in the $Mg_{17}Al_{12}$ and $Al_8Mn_5$ particle)

The band contrast map and EDS maps of the solutionized alloy, at $\varepsilon = 0$, are shown in Fig. 7a, b, respectively. IPF-X and grain reference orientation deviation (GROD)-Angle of the same region, at different strain levels, are shown in Fig. 7c, d, respectively. GROD-Angle map provides the misorientation angle relative to the average orientation of the grain. Due to the presence of low angle grain boundaries, a couple of grains are showing higher GROD value at $\varepsilon = 0$. With an increase in the strain (at $\varepsilon = 0.024$), twins are observed to form majorly in the basal and pyramidal oriented grains (w.r.t loading direction). Additionally, twins were also observed to originate in the prismatic-oriented grains adjacent to the basal and pyramidal grains. The formation of twin's re-orient grains by $\sim 86°$ about $\langle 11\bar{2}0 \rangle$ direction [8]. With

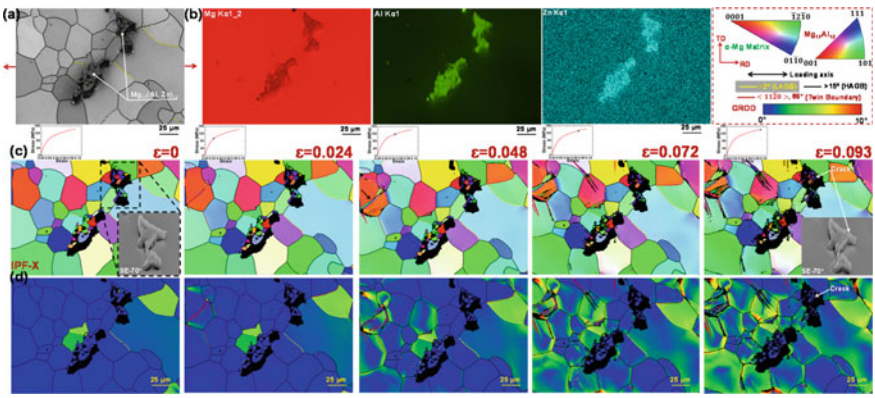


**Fig. 7** **a** Band contrast (arrow indicates the loading direction), **b** EDS, **c** IPF-X, and **d** GROD-Angle are the maps of the solutionized AZ80 alloy at different strain levels (Inset SE micrographs (70° tilt) in IPF-X at $\varepsilon = 0$ and 0.093 show the $Mg_{17}Al_{12}$ precipitate before loading and after fracture)

further increase in strain, width, and length of the twins increase, double twinning is observed at $\varepsilon = 0.024$. The GROD value of the matrix grains was also observed to increase with increasing the strain. Note that the GROD value of the $Mg_{17}Al_{12}$ precipitates is zero till fracture (shown by an arrow in Fig. 7d, $\varepsilon = 0.093$), which indicates that the precipitates fracture in a brittle manner. Furthermore, SE micrographs at 70° tilt (insets in Fig. 7c) and corresponding IPF-X suggest the fracture to be transgranular as the crack is observed to propagate through the grain.

From the *in situ* EBSD GROD map, it is evident with an increase in the strain, the increase in the GROD is mainly observed in the regions away from the precipitate. This suggests deformation was concentrated only in the matrix regions and away from the precipitate, which could be attributed to the relief in the strain accumulation near the precipitate after it fractures.

## 3.3 Microstructure-Based Modeling

As fracture was observed to propagate majorly through the $Mg_{17}Al_{12}$ precipitates, the microstructure-based modeling was performed to understand the stress distribution near the $Mg_{17}Al_{12}$ precipitate. The SE micrograph of the $Mg_{17}Al_{12}$ precipitate at $\varepsilon = 0$ is shown in Fig. 8a. The micrograph was segmented into two different phases, i.e., $Mg_{17}Al_{12}$ and α-Mg, using an image processing software (ImageJ) (Fig. 8b). The segmented image was converted to vector format (Fig. 8c) using Rastervect software, which was then imported to a commercial ABAQUS finite element software.

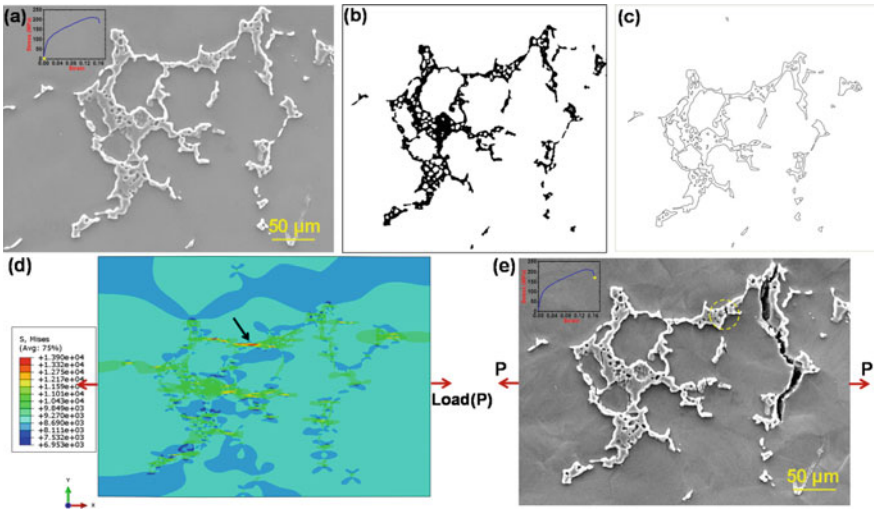


**Fig. 8** **a** SE micrograph of the $Mg_{17}Al_{12}$ precipitate, **b** binary image of the $Mg_{17}Al_{12}$ and α-Mg matrix, **c** vector image, **d** von Mises stress distribution, and **e** fractured $Mg_{17}Al_{12}$ precipitate

The elastic properties of the $Mg_{17}Al_{12}$ precipitate and α-Mg matrix were taken from [9]. This model highlights only the maximum elastic stress distributed due to the morphology of the $Mg_{17}Al_{12}$ particle. Loading was applied along the *x*-direction. Figure 8d shows the stress distribution in the $Mg_{17}Al_{12}$ and Mg matrix. It is evident that the maximum stress is generated near the $Mg_{17}Al_{12}$ particle, as indicated by the arrow (in Fig. 8d). This high-stress concentration region has been shown (dotted circle in Fig. 8e) in the corresponding SE micrograph.

Interestingly, the final fracture does not form in this high-stress concentration region but is far away from it, where the stress is much smaller. This indicates that the cracks in the $Mg_{17}Al_{12}$ precipitate would have initiated below the surface due to the complex morphology of precipitate in 3D [9, 10], which then appeared as the final fracture surface with an increase in strain. Further, it can be noticed from Fig. 8e that the crack formed in the $Mg_{17}Al_{12}$ precipitate is perpendicular to the loading axis. This also suggests that 2D microstructure-based modeling is inadequate to capture the real stress distribution in the alloy. The 3D microstructure-based modeling is necessary, which will be dealt with in future.

## 4 Conclusions

The present study indicates that the $Mg_{17}Al_{12}$ eutectic precipitates play a vital role in the crack initiation and propagation during tensile loading of an as-cast AZ80 alloy. From *in situ* tensile test, the cracks were observed to initiate in the $Mg_{17}Al_{12}$ eutectic precipitate at low strain ($\varepsilon$) of 0.021 and then propagate predominantly through the $Mg_{17}Al_{12}$ precipitates. Further, the IPF-Z and GROD maps indicate that the precipitates fracture in a brittle and transgranular manner. In addition, the cracks in the precipitate are observed to the perpendicular to the loading direction.

**Acknowledgements** Authors acknowledge the Electron Microscopy Facility support at Advanced Center of Materials Science (ACMS) at IIT Kanpur for characterization and in situ testing in SEM. The authors are also grateful to Prof. Warren Poole of the University of British Columbia for providing the AZ80 Mg alloy.

## References

1. Kulekci MK (2008) Magnesium and its alloys applications in automotive industry. Int J Adv Manuf Technol 39:851–865
2. Hillis J, Corrosion HE, Friedrich BL, Mordike (Eds) (2006) Magnesium technology: metallurgy, design data, applications. Springer-Verlag, Berlin Heidelberg, pp 469–497
3. Lü YZ, Wang QD, Ding WJ, Zeng XQ, Zhu YP (2000) Fracture behavior of AZ91 magnesium alloy. Mater Lett 44:265–268
4. Yakubtsov IA, Diak BJ, Sager CA, Bhattacharya B, MacDonald WD, Niewczas M (2008) Effects of heat treatment on Microstructure and tensile deformation of Mg AZ80 alloy at room temperature. Mater Sci Eng, A 496:247–255

5. Sarvesha R, Ghori U-R, Chiu YL, Jones IP, Singh SS, Jain J (2020) Mechanical property evaluation of second phase particles in a Mg–8Al-0.5Zn alloy using micropillar compression. Mater Sci Eng A 775:138973
6. ASTM Standard B275, 2005 (2005) Standard Practice for Codification of Certain Nonferrous Metals and Alloys, Cast and Wrought. ASTM International, West Conshohocken, PA
7. Kadali K, Dubey D, Sarvesha R, Kancharla H, Jain J, Mondal K, Singh SS (2019) Dissolution Kinetics of Mg17Al12 Eutectic Phase and Its Effect on Corrosion Behavior of As-Cast AZ80 Magnesium Alloy. JOM 71:2209–2218
8. Barnett MR (2007) Twinning and the ductility of magnesium alloys: Part I: "Tension" twins. Mater Sci Eng, A 464:1–7
9. Sarvesha R, Alam W, Gokhale A, Guruprasad TS, Bhagavath S, Karagadde S, Jain J, Singh SS (2019) Quantitative assessment of second phase particles characteristics and its role on the deformation response of a Mg-8Al-0.5Zn alloy. Mater Sci Eng A 759:368–379
10. Sarvesha R, Bhagyaraj J, Bhagavath S, Kargadde S, Jain J, Singh SS (2020) 2D and 3D characteristic of intermetallic particles and their role in fracture response of AZ91 magnesium alloy. Mater Characterization:110733

# Imaging Dislocation Cores in Severe Plastically Deformed Nanocrystalline CP-Ti Alloy Through Geometrical Phase Analysis of Spherical Aberration-Corrected HRTEM Images


**Chanchal Ghosh and Arup Dasgupta**

**Abstract** An attempt has been made here to map localized strain (lattice distortion) by means of interpretation of direct contrast of high-resolution aberration-corrected TEM images. The technique is intriguing since the atom column contrast is governed by several parameters viz., thickness, defocus, and drift apart from localized strain. An observed localized linear contrast in the experimental image of bulk nanocrystalline CP-Ti was attributed to a fluctuation of tensile and compressive strain along atomic columns. In addition, strain map generated through geometrical phase analysis quantifies the strain distribution in and around the defect cores.

**Keywords** Strain · HRTEM · Lattice deformation · Nanocrystalline metals · Dislocation core · Geometrical phase analysis

## 1 Introduction

Microscopic and functional manifestations of strains in materials originate from the existence of local strain at atomic scale levels. This is essentially manifestation of the shift of atoms from their mean equilibrium positions [1, 2]. These atomic shifts could be result of several factors, including existence of intrinsic defects, introduction of defects by means of deformation and exposure to irradiation, and presence of alloying elements or even impurity atoms in trace levels. The microstructural understanding of the local strain is of immense importance to assess the properties of the material in the in-service conditions [3, 4]. In material-related research, X-ray diffraction analysis (XRD) and electron back scattered diffraction (EBSD) studies can provide the information of the lattice strain quite efficiently.

C. Ghosh · A. Dasgupta (✉)
Materials Characterization Group, Metallurgy & Materials Group, Indira Gandhi Centre for Atomic Research, Kalpakkam 603102, Tamil Nadu, India
e-mail: arup@igcar.gov.in



P. Ghosal et al. (eds.), *Applications of Microscopy in Materials and Life Sciences*, Springer Proceedings in Materials 11,
https://doi.org/10.1007/978-981-16-2982-2_7

However, direct mapping of extremely localized deformation fields spreading across few atomic columns is next to impossible without the help of techniques such as high-resolution TEM (HRTEM). To measure the local strain by HRTEM, the positions of the atomic columns need to be compared to a reference region (unstrained or relaxed structure) within the same image. It is then theoretically possible to measure the strain at atomic level [5]. The information of the atomic position is averaged over at least 1 nm to improve the strain precision and accuracy of the technique. In case of SiGe layers the strain, precision has been reported in the literature to be $\sim 1.5 \times 10^{-3}$ and $\sim 1 \times 10^{-3}$ in the HRTEM profiles from the substrate and middle of the SiGe layers, respectively, which were in very good agreement with the simulation results [6].

While HRTEM may be the most useful technique here, interpretation of the high-resolution phase contrast TEM images seems to be most intriguing, since these images are formed by interference of the direct beam with the diffracted beams and the phase part is lost at the image plane. Although aberration correction of lenses improves the resolution, it is nontrivial to derive additional information because of the indirect nature of phase contrast images. The high-resolution images are also affected by channeling which occurs when the crystal is imaged along a low index plane [7]. The quantification of images is further complicated by the presence of drift, localized strain, or the alloyed interstitials which in turn distort the atomic column projections. Hence, understanding of the atom column contrast necessarily demands quantitative HRTEM analysis involving the simulation of structures with localized strains, drifts, and variation in chemistry [8]. The contrast due to a strain field at an amorphous silicon/crystalline silicon (*a*-Si/*c*-Si) interface relative to the bulk crystal has been studied using a scanning transmission electron microscope equipped with a low angle annular dark field (LAADF) and a HAADF detector [9]. In some cases, particularly the severe plastically deformed (SPD) materials, the strain fields may also manifest through the generation of moiré contrast arising from a high density of overlapping irregular structured grain boundaries or through the segregation of alloying elements at the grain boundaries or even through the formation of new phases in metallic alloys [10–12]. In another studies from the author's group, the quantitative investigation of induced localized strain in the Laves phase lattice through a combination of zero-loss phase contrast imaging and quantitative HRTEM by means of atomic structure modeling and phase retrieval analysis using multislice image simulation reveals the site substitution behavior of V in V-$TiCr_2$ Laves phase [13].

In recent years, bulk nanocrystalline titanium and its alloys have drawn considerable attention as one of the major engineering alloys finding a variety of applications in chemical, aerospace, biomedical, and nuclear industries [14–17]. The combination of high strength to weight ratio and excellent corrosion resistance in hostile environments makes this family of alloys more attractive than their bulk counterparts [18–22]. Equal channel angular pressing (ECAP) and severe cold rolling (SCR) at ambient and cryogenic temperatures are the predominant SPD methods adopted for producing bulk nanocrystalline (BNC) materials for

commercial applications [4, 23, 24]. However, the extent of the grain refinement predominantly depends on the imposed strain, processing routes as well as on the deformation mechanism of the applied process. Grain refinement is achieved in SCR method by suppression of dynamic recovery at cryogenic temperatures resulting in higher defect densities [25]. The yield and tensile strengths of various metals and alloys, such as Al, Al alloys, Cu alloys, CP-Ti, Zircaloy, and Ni,, have been reported to have significantly improved by this method [26–29].

In earlier studies from the author's group, formation of bulk nanocrystalline grains (~20 nm) was established during cryo-rolling of coarse grained Ti-5Ta-1.8Nb alloy. This structure is attributed to the severe plastic deformation of the grains during cryo-rolling [30]. The nanocrystalline grains appeared to be defect-free under diffraction contrast imaging conditions. Based on the above, a defect-free grain structure and well-defined atomic columns were expected under phase contrast imaging conditions. Contrary to the expectations, a delocalized contrast in aberration-corrected phase contrast images was observed [23]. In the present study, an attempt has been made to investigate the possible causes for the delocalized contrast. Toward this purpose, bulk nanocrystalline CP-Ti synthesized by cryo-rolling was studied in place of Ti–Ta-Nb alloy, so as to eliminate the effect of alloying elements on the contrast of aberration-corrected images. The different features observed in the aberration-corrected HRTEM images were analyzed through quantitative HRTEM and image simulation. The simulated images were obtained by using the experimental imaging conditions as input in the different software packages. The experimental images have been interpreted by comparison with the simulated images, under similar imaging conditions. The drift and the strain accumulation in the localized scale have been estimated through quantitative analysis of phase contrast images. The findings have further been evaluated with the aid of geometrical phase analysis (GPA). GPA provides a fingerprint of the manifestation of the local strain in the phase contrast images and also quantifies the strain fields.

## 2 Materials and Methods

CP-Titanium was subjected to a stress-relieving treatment at 650 °C for 2 h (denoted as ST) and then cryo-rolled to 90% (denoted as CR 90) in 11 passes by equilibrating in liquid nitrogen between each pass. Electron-transparent specimens of ST and CR 90 were prepared by grinding and polishing the 3 mm TEM disk with successively finer grades of SiC emery sheets followed by dimple grinding and Ar-ion milling. High-resolution images were taken with a spherical aberration-corrected FEI Titan 80–300 electron microscope. Phase contrast imaging was carried out in a negative $C_s$-imaging (NCSI) condition ($C_s$ = −13.56 µm). In this particular condition, atomic columns in thin crystalline samples appear as bright dots on a dark background generating an image, which closely resembles the projected crystal structure [31]. Multislice image simulation was performed using

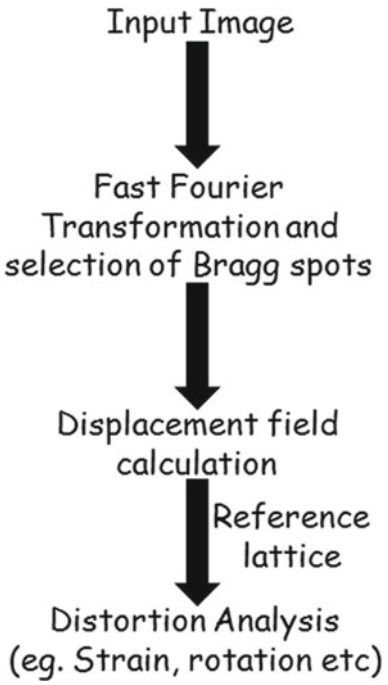


**Fig. 1** Schematic of the process flow of geometric phase analysis (GPA) for strain mapping

Java-based EMS (jEMS) and SimulaTEM image simulation software to simulate the high-resolution images of annealed and cold worked CP-Ti [32, 33]. Prior to the simulation, the hexagonal crystal input file (.cif) was transformed into orthogonal coordinates using the inbuilt orthogonal transformation matrix in jEMS simulation package. Qantitative strain mapping from the HRTEM images has been attempted using the geometrical phase analysis algorithm as developed by Hÿtch and core-searchers [34]. In GPA, displacement field calculation was carried out for selected Bragg diffraction spots in the power spectra of the HRTEM image. This displacement field would then compare with an unstrained region (reference region) of the image to generate the strain map. Details of the schematic for the GPA calculation analogy are presented in Fig. 1.

## 3 Results and Discussion

Effect of severe plastic deformation in the atomic domain was studied through comparing phase contrast microscopy results of both ST and CR 90 samples of CP-Ti. HRTEM characterization was carried out in the aberration-corrected mode to precisely locate the atomic columns which is otherwise quite difficult in the case of a metallic specimen having a significant amount of free electron cloud. Relatively low-magnification bright-field images of the ST and CR 90 samples of CP-Ti are

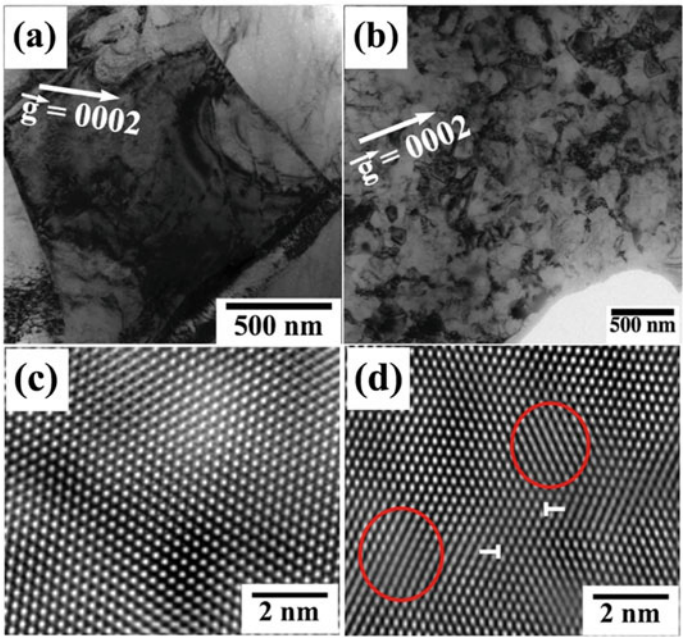


**Fig. 2** Relatively low-magnification bright-field images from **a** ST **b** CR 90. Aberration-corrected high-resolution images of ST and CR90 specimen are shown in **c** and **d**, respectively. The linear delocalized contrast can be seen in different locations in the HRTEM micrograph from CR 90. Specimen

shown in Fig. 2a, b respectively. In the ST sample, the grain sizes are significantly higher than that of CR-90 specimen. While the grain size of the ST sample is of the order of ~1−2 μm, the grain size of CR 90 sample is of the order of ~80 −100 nm. Aberration-corrected HRTEM images of ST and CR 90 samples are displayed in Fig. 2c, d, respectively. In both the images, bright atomic contrast is observed in dark background. However, in Fig. 2d, certain regions are observed to have a linear bright contrast compared to the surrounding regions. This localized contrast can be attributed either to the defocus used for the imaging or to the change in the position of the atoms. To eliminate the former cause, phase contrast images were recorded at different defocus values (Δf) raging from +30 nm to −26 nm keeping the other imaging parameters unchanged for CR-90 specimen, as shown in Fig. 3. Two important observations are made in the experimental focal series. First, contrast reversal is observed in few of the atomic columns, which is expected for a series of phase contrast images with varying defocus. Secondly, it is observed that the delocalization contrast is present throughout the series and is not an attribute of a specific value of defocus (Δf). Present observation confirms that the observed contrast is not due to change in defocus. A change in the overall background

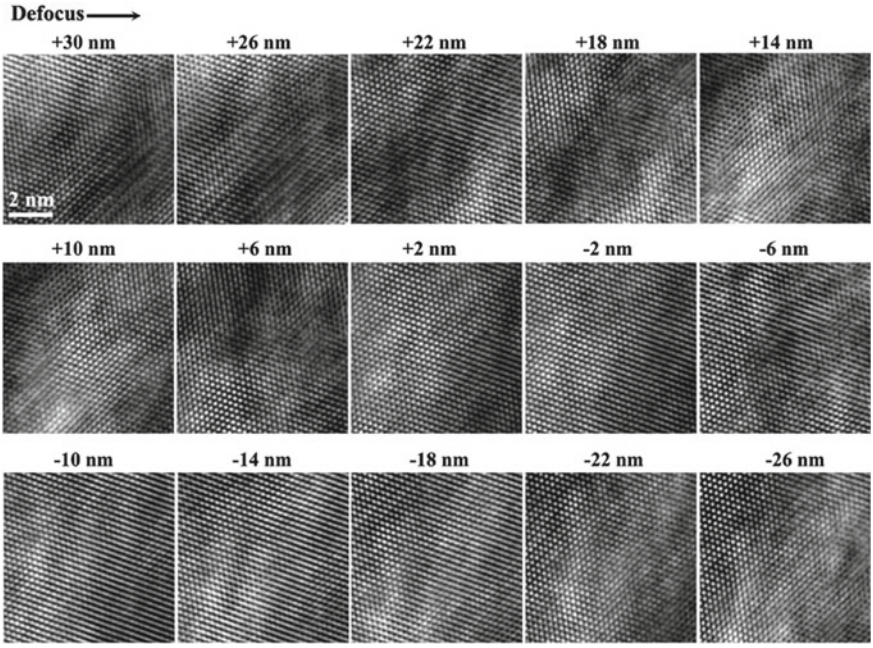


**Fig. 3** Experimental images of CR 90 sample at Cs = −0.01356 mm and defocus range of +30 nm to −26 nm

intensity is observed in the phase contrast image which is mainly attributed to the presence of diffraction-controlled parameters and partial non-satisfaction of weak phase object approximation (WPOA).

## *3.1 Effect of Imaging Parameters*

The present observations warrant further investigation to identify the cause of the linear contrast in the aberration-corrected image of bulk nanostructured metal. The effect of drift and the effect of localized strain in the atomic columns is also reported to generate similar types of delocalization of the bright contrast in aberration-corrected images [35, 36]. In the present section, a systematic analysis has been provided to identify the cause of the linear contrast—whether it is caused by drift or strain or a combined effect of both. In an earlier work from the author's laboratory, significantly higher grain sizes, of the order of few μm, have been reported in ST specimen as compared to 80–100 nm in CR-90 specimen [23]. This is attributed to the suppression of dynamic recovery during cryo-rolling. Moreover, the microstrain is observed to increase initially from ST to 50% cryo-rolling and then reduce with further increase in cryo-rolling to 90%. Additionally, the nanograins in CR 90

specimen are observed to be recrystallized [30]. This is because of the higher stored energy accumulated in the specimen as a result of extreme amount of cold work and thus a higher driving force of recrystallization. Having observed a decrease in microstrain in 90% cryo-rolled sample, in addition to recrystallized nanograins, the detection of localized strain is quite intriguing and demands further quantitative understanding. However, it should also be noted that the lattice strains cannot be removed completely as the lattice defects, in particular dislocations and interstitials (e.g., O, N, C) are responsible for some amount of lattice strain in the system. Moreover, most of the bulk nanocrystalline grains experienced plastic deformation mediated by dislocation slip rather than deformation twinning. As already discussed, the appearance of delocalized linear contrast in the phase contrast micrographs can either be due to strain or a manifestation of the atomic level drift present during the experiment. However, the effect of drift can be ruled out in the present case because of the following reasons. First in Fig. 2d, the delocalization is observed in all directions, whereas in the presence of drift, the delocalization should be unidirectional in nature. Second, in the experimental image, the delocalization zones observed to have spread over a few atomic columns in some specific pockets. On the contrary, in the presence of drift, the delocalization should be uniform throughout the entire region of interest. In order to study the effect of thickness and defocus, the HRTEM micrographs of the ST and CR 90 are compared with the simulated images generated in similar imaging conditions and are shown in Fig. 4. It is further observed that in few locations, the atomic contrasts of the simulated

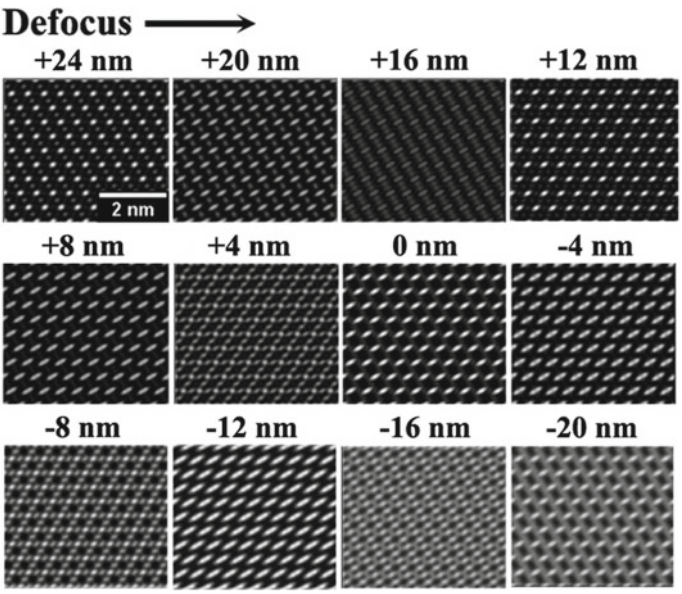


**Fig. 4** Simulated defocus series from hcp Ti structure with drift = 0.15 nm keeping other parameters same as of experimental imaging conditions

image are not comparable with the experimental focal series images of CR90 shown in Fig. 3. Having eliminated the possibility of defocus and drifting of images, the main focus shifts to the possibility of presence of strain in a few selected columns.

## 3.2 *Effect of Strain*

To introduce the effect of strain, it has been assumed that a sinusoidal wave passes through the atomic columns, where it alternatively introduces tensile and compressive strains in the lattice planes. The detail of the scheme for introducing the sinusoidal wave as well as the change in the relative atom column projection along the c-direction of hexagonal unit cell is shown as a schematic in Fig. 5a. This re-modified crystal file has now been used for simulating the phase contrast images in the multislice routine of SimulaTEM package. The simulated images ($C_s$ = −0.01356 mm; Δf = 3 nm) for different strain values are shown in Figs. 5b, d. The strain has been introduced in a few atomic columns in each case, marked in red. The delocalization of contrast is not observed at 5% strain (Fig. 5b). The change in the contrast started to appear at the introduction of 10% strain (Fig. 5c) and becomes more prominent at 15% strain (Fig. 5d). In these cases, the delocalization of contrast is observed at specific atomic columns where the strain was

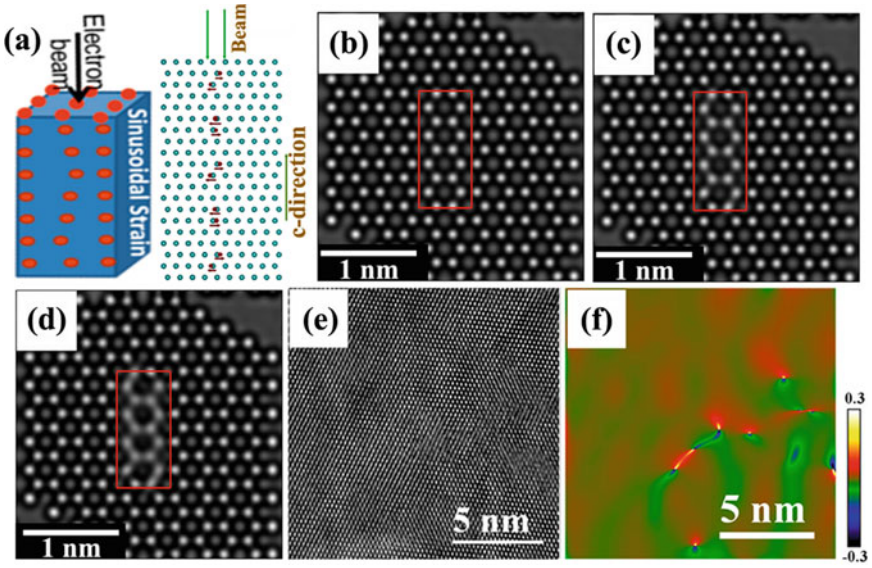


**Fig. 5** **a** Schematic indicating the method used to introduce strain in the atomic columns of synthetic hcp Ti unit cells. Simulated images with $C_s$ = −0.01356 mm and defocus 3 nm for different strain values of **b** 5% **c** 10% and **d** 15%. **e–f** Image-corrected HRTEM micrograph and the corresponding localized strain map ($\varepsilon_{xx}$ component) from a severely deformed CP-Ti specimen

introduced. This delocalization of contrast at specific atomic columns is comparable to the contrast observed in experimental image (Fig. 2d). In order to substantiate the presence of localized strain in the atomic scale, geometrical phase analysis (GPA) was carried out for an image-corrected HRTEM micrograph from CR90 CP-Ti specimen. Figure 5e, f displays the collage of an image-corrected HRTEM micrograph and corresponding $\varepsilon_{xx}$ component of the localized GPA strain map. Present analysis confirms that the linear delocalized contrast regions present in the HRTEM image (Fig. 5e) are always associated with an increase in the displacement field and subsequent strain concentration in the corresponding GPA map (Fig. 5f). The GPA calculation is carried out using the $01\bar{1}0$ and 0002 Bragg diffraction spots from the power spectrum generated from HRTEM micrograph shown in Fig. 5e. These reflections correspond to the 0.256 nm and 0.234 nm interplanar spacing from α-Ti, respectively. In addition, a mask size of the order $\sim|\frac{\vec{g}}{2}|$ is used in the frequency space for the present GPA calculation. The average displacement field measured from the strain map ranges ∼2–3 nm which encompasses 8–10 delocalized lattice planes as seen in the phase contrast images. In the present case, effect of strain has not been observed in the simulated image below 10% of applied strain value. Therefore, for a given $C_s$ and defocus condition, above a critical level, the strain in the atomic column is manifested as delocalization in the high-resolution images. No significant difference in the contrast is observed for any strain below that value. An in-depth analysis of the GPA map also provides an indication about the deformation behavior of cryo-rolled CP-Ti. Figure 6 shows aberration-corrected phase contrast micrograph along with the corresponding GPA map superimposed over it. The superimposed micrograph confirms that in the GPA map, the sharp changes from the tensile to the compressive component are always associated with a dislocation core [37]. The nearby strain field is generated because of the dislocation field corresponding to the dislocation core. Moreover, from the superimposed micrographs, it can be seen that the core of the dislocation is

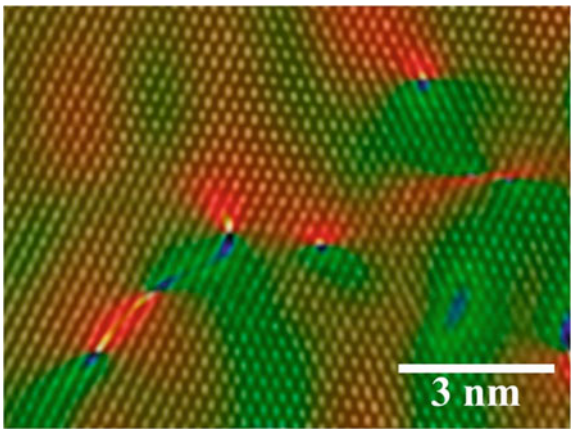


**Fig. 6** Superimposed image of the GPA strain map along with the atomic resolution phase contrast micrograph

comprised of a tensile and a compressive component coexisting over a distance of two atomic spacing [38]. This measured spacing is in support of the sinusoidal nature of lattice deformation wave discussed earlier.

## 4 Summary

Main findings of the work can be summarized as follows

i. The effect of deformation on the nature of phase contrast images has been studied in severely plastic deformed CP-Ti.
ii. Localized strain is identified as the cause of delocalization of contrast. The enhancement of localized strain in these delocalized regions has been further supported by the geometrical phase analysis (GPA) studies.
iii. A critical value of strain localized over only a few rows of atomic columns is present in the alloy even after it formed a nanocrystalline structure through the grain fragmentation mechanisms. This strain is manifested as delocalized contrast in aberration-corrected HRTEM image at a given $C_s$ and defocus condition. In the present study, it was observed that the said atomic contrast would appear if the localized strain present in the material was 10% or higher.

**Acknowledgements** The authors gratefully acknowledge Ms. Pragna Bhaskar, Dr. Joysurya Basu, and Dr. Saroja Saibaba (formerly at IGCAR) for many useful discussions at different occasions. The authors would also like to acknowledge Dr. Martina Luysberg for helping in carrying out the aberration-corrected microscopy at the Ernst Ruska-Center for Microscopy and Spectroscopy with Electrons, Forschungszentrum, Jülich. The authors hereby gratefully acknowledge Dr. A K Bhaduri, Director, IGCAR, Dr. Shaju K Albert, Director, Metallurgy and Materials Group, Dr. S. Raju, Associate Director, Materials Characterization Group, and Dr. P. Parameshwaran, Head, Physical Metallurgy Division for their encouragement and support.

## References

1. Cherkashin N, Denneulin T, Hÿtch M (2017) Sci Reports 7:12695–12698
2. Neumann W, Kirmse H, Häusler I, Otto R (2006) J Microscopy 223(3):200–204
3. Sabirov I, Perez-Prado MT, Molina-Aldareguia JM, Semenova IP, Salimgareeva GK, Valiev RZ (2011) Scripta Mater 64:69–72
4. Xu W, Wu X, Calin M, Stoica M, Eckert J, Xia K (2009) Scripta Mater 60:1012–1015
5. Du K, Phillipp F (2006) J Microscopy 221(1):63–71
6. Béché A, Rouvière JL, Barnes JP, Cooper D (2013) Ultramicroscopy 131:10–23
7. Tillmann K, Thust A, Urban K (2004) Microsc Microanal 10:185–198
8. Grillo V, Rossi F (2011) J Cryst Growth 318:1151–1156
9. Yu Z, Muller DA, Silcox J (2004) J Appl Phys 95:3362–3371
10. Rentenberger C, Waitz T, Karnthaler HP (2004) Scripta Mater 51:789–794
11. Basha DA, Sahara R, Somekawa H, Rosalie JM (2016) Scripta Mater 124:169–173
12. Zafari A, Xia K (2016) Scripta Mater 124:151–154

13. Ghosh C, Sharma V, Basu J, Divakar R, Mohandas E (2015) Philos. Mag. 95(22):2403–2426
14. Zhu YT, Lowe TC, Langdon TG (2004) Scripta Mater 51:825–830
15. Eylon D (1990) Titanium and Titanium Alloy Castings. ASM International, USA
16. Preetham K, Chakkingal U (2008) Mat Sci Forum 584–586:275–280
17. Terry CL, Yuntian TZ (2003) Adv Eng Mater 5:373–378
18. Wang Y, Chen M, Zhou F, Ma E (2002) Nature 419:912–915
19. Chookajorn T, Murdoch HA, Schuh CA (2012) Science 337:951–954
20. Tonpe S, Saibaba N, Jayaraj RN, Ravi Shankar A, Kamachi Mudali U, Raj B (2011) Energy Proc 7:459–467
21. Sano Y, Takeuchi M, Nakajima Y, Hirano H, Uchiyama G, Nojima Y, Fujine S, Matsumoto S (2013) J Nucl Mater 432:475–481
22. Yuntian TZ, Varyukhin V (eds) (2006) Nanostructured materials by high-pressure severe plastic deformation. Springer
23. Dasgupta A, Murugesan S, Saroja S, Vijayalakshmi M, Luysberg M, Veron M, Rauch E, Jayakumar T (2013) J Mater Sci 48:4592–4598
24. Valiev RZ, Islamgaliev RK, Alexandrov IV (2000) Prog Mater Sci 45:103–189
25. Shanmugasundaram T, Murty BS, Sarma VS (2006) Scripta Mater 54:2013–2017
26. Niranjani VL, Hari Kumar K, Sarma VS (2009) Mater Sci Eng A 515:169–174
27. Sarma VS, Sivaprasad K, Strum D, Heilmaier M (2008) Mater Sci Eng, A 489:253–258
28. Lee TR, Chang CP, Kao PW (2005) Mater Sci Engg A 408:131–135
29. Goel S, Keskar N, Jayaganthan R, Singh IV, Srivastava D, Dey GK, Saibaba N (2014) Mater Sci Engg A 603:23–29
30. Pragna B, Dasgupta A, Sarma VS, Kamachi Mudali U, Saroja S (2014) Mater Sci Engg A 616:71–77
31. Spiecker E, Garbrecht M, Jäger W, Tillmann K (2010) J Microscopy 237(3):341–346
32. Stadelmann PA (1987) Ultramicroscopy 21(2):131–145
33. Gómez-Rodríguez A, Beltrán-Del-Río LM, Herrera-Becerra R (2009) Ultramicroscopy 110 (2):95–104
34. Hÿtch MJ, Snoeck E, Kilaas R (1998) Ultramicroscopy 74:131–146
35. Hÿtch MJ, Planmann T (2001) Ultramicroscopy 87:199–212
36. Hüe F, Hÿtch M, Bender H, Houdellier F, Claverie A (2008) Phys Rev Lett 100:156602–156604
37. Turner S, Idrissi H, Sartori AF, Korneychuck S, Lu YG, Verbeeck J, Schreck M, Tendeloo GV (2016) Nanoscale 8:2212–2218
38. Nabarro FRN, Hirth JP (2007) Dislocation in solids Vol-13. North-Holland, Amsterdam

# Growth of Spheroidal Silicon Carbide by Arc Plasma Treatment


**R. K. Sahu, T. Dash, V. Mukherjee, S. K. Pradhan, and B. B. Nayak**

**Abstract** Spheroidal growth of silicon carbide (SiC) was observed by treating SiC grain in thermal arc plasma reactor/furnace followed by 4 h of in situ cooling under argon atmosphere. The plasma treatment of samples was carried out between 5 and 15 min. under Ar atmosphere. High microhardness and Young's modulus values were found for plasma-treated SiC with spheroidal structure. Materials were evaluated by employing techniques such as XRD, XPS, micro Raman, FTIR, FESEM, TEM, EDS, microhardness, and Young's modulus. Typical 15 min. plasma-treated SiC shows relatively high microhardness and Young's modulus values of 3680 VHN and 470 GPa, respectively, than that of untreated one.

**Keywords** Arc plasma reactor · Spheroids · Microscopy · Hardness

## 1 Introduction

Silicon carbide (SiC) has potential application in the area of material science and engineering. It is used for anode material for Li-ion batteries, electrochemical performance, increase ductility, durability of high carbon steel, and better catalytic behavior (hydrogen storage) [1–5]. SiC replaces Si for high temperature semiconductor application [2–6]. The carbide exhibits very high hardness, high chemical resistance, excellent refractory, and ceramic properties [2, 7]. The high fracture strength properties of SiC are suitable for ultra-high nanocomposite fiber, polymer, metals composites, ceramic matrices, etc. for ballistic, armor, and personal safety equipment [8–10]. Silicon carbide possess high melting temperature, i.e., around

R. K. Sahu · V. Mukherjee
Sambalpur University, Sambalpur 768019, India

R. K. Sahu · S. K. Pradhan · B. B. Nayak
CSIR-Institute of Minerals and Materials Technology, Bhubaneswar 751013, India

T. Dash (✉)
Centurion University of Technology and Management, Bhubaneswar, Odisha, India
e-mail: tapan.dash@cutm.ac.in



P. Ghosal et al. (eds.), *Applications of Microscopy in Materials and Life Sciences*,
Springer Proceedings in Materials 11,
https://doi.org/10.1007/978-981-16-2982-2_8

2200 °C which makes it a better field emitter for high power applications [10]. Silicon carbide is a support for improvements in sulfur recovery as well $H_2S$ oxidation [11]. Silicon carbide tips are promising material for atomic force microscopy and/or scanning tunneling microscopy [12]. SiC spheroids and nanostructure are at present synthesized by arc plasma [13], hydro-thermal method [14], chemical vapor deposition and growth [15], microwave and RF sputtering [16], etc. Out of these methods, arc plasma synthesis methods are fast and amiable for bulk production of SiC spheroids and nanorods with a decent amount of purity in the outcomes. Thermal plasma has high charge density, energy density, and ion temperature [17]. It can be considered as a suitable source for heat treatment of silicon carbide which is high melting point material. The SiC with spheroidal microstructure developed in this work has the scope to be used as a heat radiating material for higher thermal conductive performance in terms of high filling and fluidity (for use in heat dissipation sheets, thermal grease, heat dissipation tape, and thermal compounds) and filling material in composite for developing abrasion resistance. Spheroidal-based SiC has excellent characteristics of repletion because of its round shape. It can also be used for corrosion resistance coating, enhancement of heat resistance, abrasion resistance, high strength, and sliding properties of automobile and aircraft components. In this work, *in situ* growth of novel spheroidal structure was optimized keeping in view its various applications. Since sample synthesis has vital role in terms of fabrication and purity, arc plasma processing proofs as a fast and energy saving technique for spheroidal growth of silicon carbide. The arc plasma-treated SiC with spheroidal structure shows better mechanical and microstructural properties than untreated one.

## 2 Experimental

A 50 kW dc arc plasma reactor/furnace having in situ cooling facility has been used for growing of spheroids in silicon carbide. Argon of 2 lt/min was used during plasma treatement. 5–15 min of the plasma treatment of samples was carried out. Silicon carbide kept in graphite crucible which acts as the anode during plasma operation. Water continuously supplied for colling down of reactor after plasma reactor. Electrode spacing of about 0.7 cm was maintained for developing stable arc condition. *In situ* cooling of 4 h was carried out after plasma treatment. Even during cooling for around 3 h, the materials were maintained under Ar atmosphere ($\sim$1.5 lit. per min) to prevent oxidation of the product. The plasma experiment conditions are given in Table 1. Then plasma-treated samples were taken for various characterizations as follows: X-ray diffraction (XRD) was done by "PANalytical X'Pert Pro diffractometer, microstructural behavior of the samples was done by field emission scanning electron microscopy (FESEM), ZEISS SUPRA 55 and transmission electron microscope (TEM) (TECNAI $G^2$ (200 kV)), FEI (Netherland). EDS spectrum was taken to know the elements present in the samples. X-ray photoelectron spectroscopy (XPS) was done out by using the S/N-10001 (Project

**Table 1** Typical arc plasma-treated experimental conditions opted for silicon carbide

| Sample ID | Arc length (in cm) | Argon gas flow rate (Lit/min) | Current (A) | Voltage (V) | Yield (wt%) | Hardness (VHN) | Young's modulus (GPa) |
|---|---|---|---|---|---|---|---|
| SiC (Untreated) | – | – | – | – | – | 2540 ± 6 | 402 + 09 |
| SiC-1 (5 min plasma treatment) | 0.7 | 2 | 100 | 60 | 90 | 2850 ± 12 | 415 ± 06 |
| SiC-2 (10 min plasma treatment) | 0.7 | 2 | 120 | 45 | 93 | 3206 ± 16 | 435 ± 09 |
| SiC-3 (15 min plasma treatment) | 0.7 | 2 | 145 | 45 | 91 | 3680 ± 11 | 470 ± 10 |

no. 251, Prevac, Poland). Microhardness and Young's modulus values of typical samples were measured by a UMIS nanoindentation system (Fisher-Cripps, Australia)."

## 3 Results and Discussion

The plasma treatment of SiC samples was carried out under the argon flow rate of 2 ltr/min. The current and voltage used as 100–145 A and voltage 45–60 V, respectively. The yield recovery of samples was obtained above 90 wt%. XRD analysis (Fig. 1) of untreated and plasma-treated SiC exhibit both SiC (cubic) [18] and small amount of free carbon (C). The intensity of C (002) peak was varied between before and after plasma treatment. The plasma-treated samples show less intense peak of SiC. The structural modification and new microstructure developed in the sample caused because of plasma treatment. Such result is obvious in material synthesis due to reorientation and growth of planes formed during processing conditions adopted. The shift of peaks may be due to non-equilibrium plasma treatment of SiC, which can affect its crystal behavior. Peaks are shifted to lower two theta values up to 10 min of plasma treatment and found shifted to higher values beyond 10 min of plasma treatment. The irregular peak shift trend could be attributed to non-equilibrium reaction kinetics taking place in the plasma melt-casting operation because of instability of energy transformation for phase transformation. In fact, plasma is very much well popular for such peculiar behavior. It is a matter of further study for the near coming future research work.

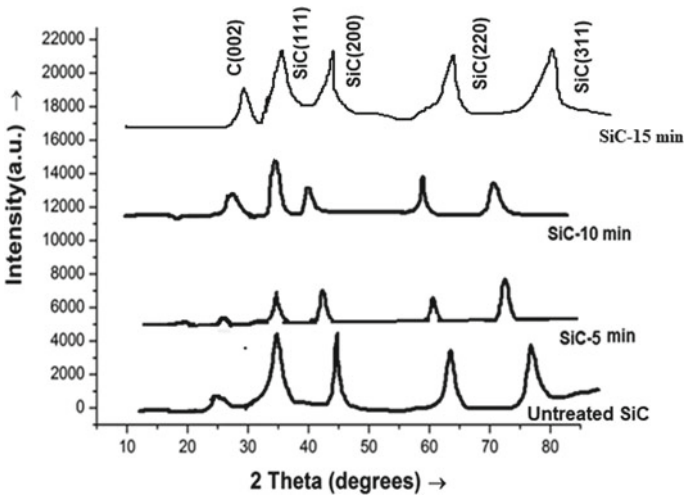


**Fig. 1** XRD results of the SiC samples

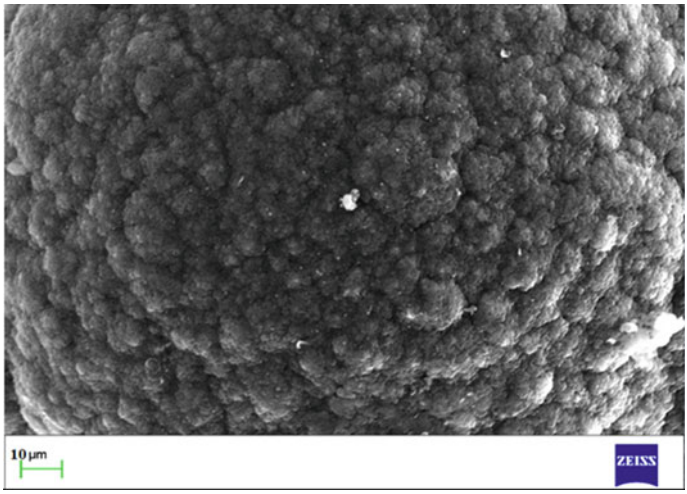


**Fig. 2** FESEM microstructure of untreated silicon carbide

FESEM analysis for the untreated and the typical 10- and 15-min arc plasma-treated SiC are shown in Figs. 2, 3 and 4 respectively. Irregular type of plates was found in the untreated SiC. In plasma-treated SiC, it was found that microstructure changed to spherical form. The microstructure with grain size round 700 µm for 10 min arc plasma-treated SiC was observed in Fig. 3. But when plasma melting time is improved to 15 min, it is observed that almost plasma energy optimization occurred and the microstructure with grain size of 2–5 µm was

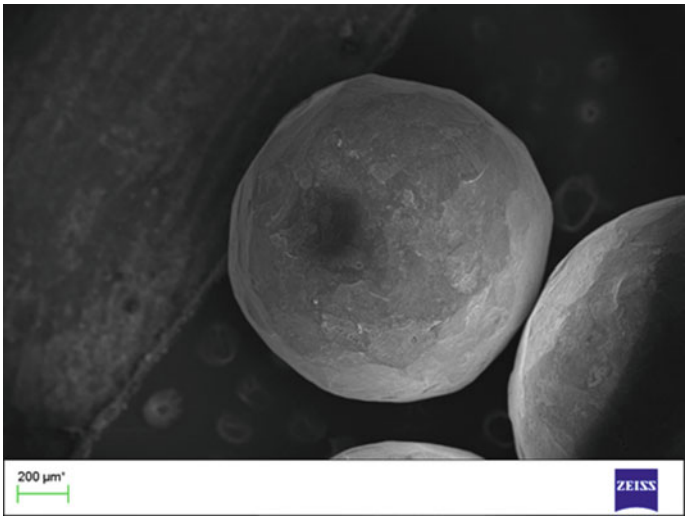


**Fig. 3** FESEM image of plasma-treated SiC (10 min plasma treatment)

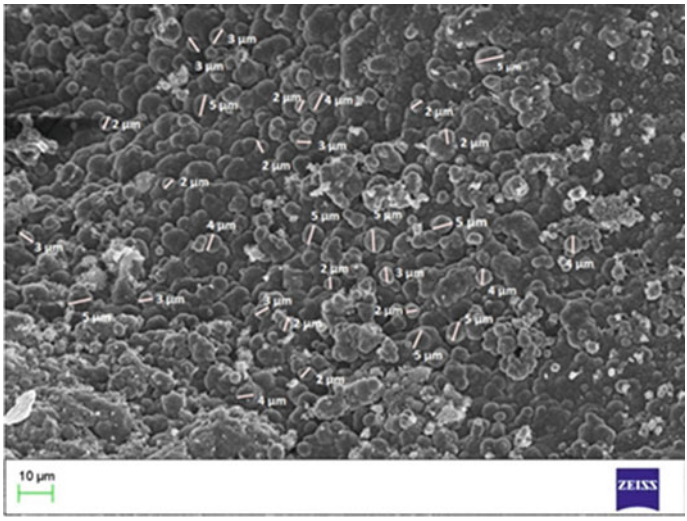


**Fig. 4** FESEM microstructure of plasma-treated silicon carbide (15 min plasma treatment (∼2–5 µm diameter spheroids)

observed in Fig. 4. The microstructure was found almost uniform. No defect or surface irregularly was marked in the FESEM. The spherical microstructure may be due to the top view of bundle of nanotubes. The higher magnification FESEM of 15 min plasma-treated SiC is shown in Fig. 4 which clearly represents spheroidal

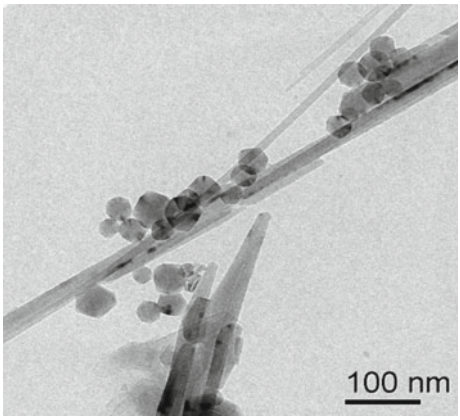


**Fig. 5** TEM microstructure of 15 min plasma-treated silicon carbide

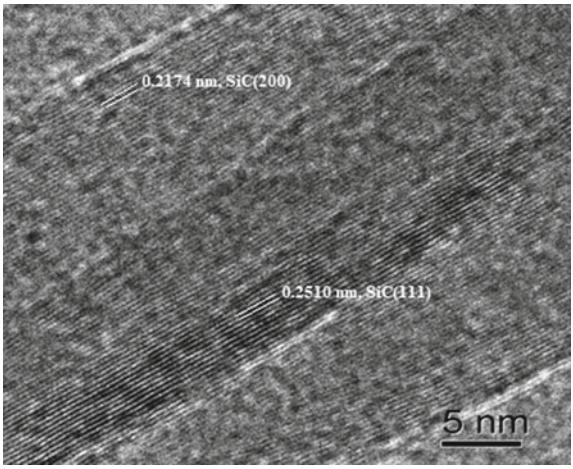


**Fig. 6** TEM microstructure of 15 min plasma-treated silicon carbide showing lattice fringes

growth in the microstructure. TEM microstructure of 15 min plasma-treated SiC is shown in Figs. 5 and 6. Figure 5 confirms the development nanotube of dia. ~20–39 nm in the melt cast SiC. High-resolution TEM is taken on selected phase/area of Fig. 5 and lattice fringes are clearly observed (Fig. 6) which confirms crystallinity nature of the plasma-treated SiC. The *d*-spacing between lattice atomic layers is measured and corresponding phases of SiC are assigned. Hence, the plasma treatment was found efficient technique for developing the novel structures of nanotube and explore the properties of SiC. The elemental identification of 15 min plasma-treated SiC sample was done by EDS analysis as shown in Fig. 7. It shows peaks of Si, C, O, and Cu. The minor peak of O is due to the preparation of sample in a semi-open-type furnace. The appearance of Cu is because of using carbon coated Cu grids in TEM analysis. No impurity phase was detected in the plasma-treated SiC. Hence, the plasma treatment of SiC not only changes structures

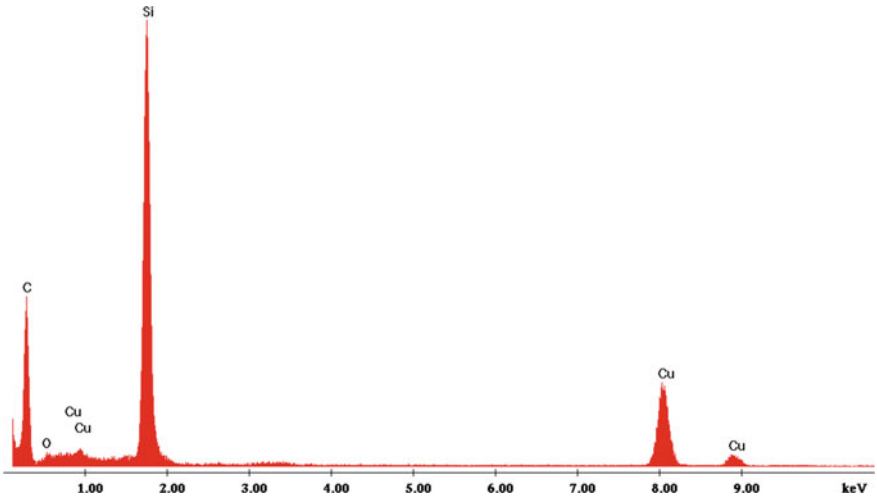


**Fig. 7** EDS study of 15 min plasma-treated silicon carbide

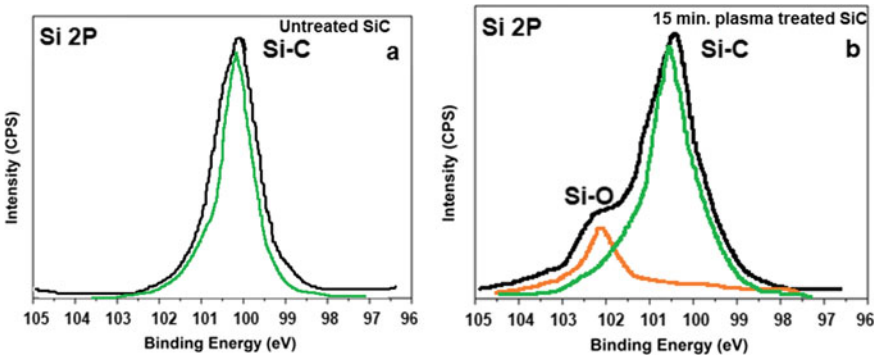


**Fig. 8** XPS spectra of SiC sample: **a** untreated and **b** 15 min plasma-treated

but also develops nanotubes in random direction which in fact is essential to enhance the properties of SiC.

XPS Si2p core-level spectra for untreated and 15 min plasma-treated SiC samples are shown in Fig. 8a, b respectively. The untreated one only shows peak of SiC. 15 min plasma-treated SiC sample shows two peaks, i.e., for major peak SiC and minor peak Si-O. Because of trace amount of presence Si-O, it could not observed in XRD spectra. The incipient oxidation observed may be due to sample preparation in semi-open type of plasma furnace. The microhardness and Young's modulus of untreated and plasma-treated SiC are shown in Table 1. The microhardness and Young's modulus values were found to be improved after plasma treatment. The typical 15 min arc plasma-treated SiC sample shows 3680 VHN and

470 GPa values for microhardness and Young's modulus, respectively. The improvement of microhardness of plasma-treated sample may be attributed to the development of nanotubes grown in the sample. The reported work is the *first* in kind in literature.

## 4 Conclusion

FESEM study of typical 15 min. arc plasma-treated SiC shows spheroidal growth of microstructure. The microstructure of 15 min plasma-treated SiC observed in TEM exhibits random growth of nanotubes (20–30 nm). From FESEM and TEM results, it may be concluded that mixed type of morphology involving nanotubes (which are observed in TEM) as well as spheroidal (as seen in FESEM) is developed in the plasma-treated SiC. The above structural modification developed in plasma-treated SiC can be attributed to the uniqueness of plasma treatment. Plasma-treated samples show peaks of SiC and C in XRD analysis. The presence of major SiC and minor Si-O bands was confirmed by XPS analysis. 15 min plasma-treated SiC exhibits high microhardness and Young's modulus values of 3680 VHN and 470 GPa, respectively, than that of untreated SiC.

**Acknowledgements** The authors acknowledge the help and support received from their respective institutes.

## References

1. Barghi SH, Tsotsis TT, Sahimi M (2015) Hydrogen absorption in silicon carbide nanotubes doped with potassium and titanium. AIChE Annual Meeting; 8–3 November, Salt Lake City, UT, USA
2. Harris GL (1995) Properties of silicon carbide. Iet
3. Lee JT et al (2013) Sulfur-infiltrated micro-and mesoporous silicon carbide-derived carbon cathode for high-performance lithium sulfur batteries. Adv Mater 25(33):4573–4579
4. Sahu RK et al (2019) Production of C/SiC nanotubes by arc Plasma treatment. Mat Today: Proc 18:575–581
5. Nayak BB et al (2018) Growth of silicon carbide nanotubes in arc plasma treated silicon carbide grains and their microstructural characterizations. Ceram Int 4:1512–1517
6. Son IH et al (2015) Silicon carbide-free graphene growth on silicon for lithium-ion battery with high volumetric energy density. Nature Comm 6:7393
7. Petrovic J et al (1985) Tensile mechanical properties of SiC whiskers. J Mat Sci 20(4):1167–1177
8. Brennan JJ, Prewo KM (1982) Silicon carbide fibre reinforced glass-ceramic matrix composites exhibiting high strength and toughness. J Mat Sci 17(8):2371–2383
9. Pham-Huu C et al (2001) The first preparation of silicon carbide nanotubes by shape memory synthesis and their catalytic potential. J Catal 200(2):400–410
10. Yang W et al (2004) Synthesis of silicon carbide nanorods by catalyst-assisted pyrolysis of polymeric precursor. Chem Phys Lett 383(5–6):441–444

11. Keller N, et al (2005) New catalysts based on silicon carbide support for improvements in the sulfur recovery. Silicon carbide as support for the selective $H_2S$ oxidation. J Brazilian Chem Soc 16(2):202–209
12. Mavrandonakis A et al (2006) Silicon carbide nanotube tips: promising materials for atomic force microscopy and/or scanning tunneling microscopy. Appl Phys Lett 89(12): 123126
13. Nayak BB, Mohanty BC, Singh SK (1996) Synthesis of silicon carbide from rice husk in a dc arc plasma reactor. J Am Ceram Soc 79(5):1197–1200
14. Pei L et al (2006) Preparation of silicon carbide nanotubes by hydrothermal method. J Appl Phys 99(11): 114306
15. Xie Z, Tao D, Wang J (2007) Synthesis of silicon carbide nanotubes by chemical vapor deposition. J Nanosci Nanotechnol 7(2):647–652
16. Tony V et al (2006) Characterization of silicon carbide nanotube synthesized using microwave heating
17. Conrads H, Schmidt M (2000) Plasma generation and plasma sources. Plasma Sources Sci Technol 9(4):441
18. Iwanowski R et al (1999) XPS and XRD study of crystalline 3C-SiC grown by sublimation method. J Alloy Compd 286(1–2):143–147

# Deformation Behavior of Inconel 617 Alloy Under Monotonic and Cyclic Loading


**N. C. Santhi Srinivas, Ch. Visweswara Rao, G. V. S. Sastry, and Vakil Singh**

**Abstract** Inconel 617 alloy is used in important power plant applications involving steam generation equipment such as boiler superheaters and reheaters. Deformation behavior of the IN 617 alloy under monotonic and cyclic loading at room temperature, 750 and 850 °C at strain rate of 0.005 $s^{-1}$ was studied in the present investigation. Under tensile loading, decrease in strength was observed at 750 and 850 °C compared to the value observed at RT. Transmission electron microscopy (TEM) studies revealed traces of slip bands whereas precipitation of carbides and γ′ at 750 and carbides at 850 °C. Formation of slip bands suggests slip as the primary mechanism of deformation under tensile loading at RT. Continuous cyclic hardening under cyclic loading was observed, at all the three temperatures and at all the strain amplitudes. Cyclic hardening was noticed till peak hardening at 750 and 850 °C at all the strain amplitudes. Increase in temperature of testing had deleterious influence on fatigue life. Cyclic hardening at RT was attributed to, the existence of pile up of dislocations in planar array in slip bands, the interaction of dislocations with the fine carbide and γ′ particles at 750 °C and with the carbides particles at 850 °C.

## 1 Introduction

Enhancement of thermal efficiency and reduction in $CO_2$ emissions in Advanced Ultra-Super Critical (A-USC) power plants need steam with inlet temperature more than 700 °C, for which materials with good strength and oxidation resistance at elevated temperatures are essential. Materials used for these applications need to withstand steam at high temperatures (700–780 °C) and pressures up to 35 MPa. Among nickel-based superalloys, Inconel 617 (IN617) alloy is a promising material for the applications such as super heater, reheater and other steam generating

N. C. Santhi Srinivas (✉) · Ch.Visweswara Rao · G. V. S. Sastry · V. Singh
Department of Metallurgical Engineering, Indian Institute of Technology (Banaras Hindu University), Varanasi 221005, India
e-mail: ncssrinivas.met@iitbhu.ac.in



P. Ghosal et al. (eds.), *Applications of Microscopy in Materials and Life Sciences*, Springer Proceedings in Materials 11,
https://doi.org/10.1007/978-981-16-2982-2_9

components in power plants [1]. IN617 alloy is known to have good oxidation and corrosion resistance along with exceptional creep strength at temperatures above 950 °C [2, 3].

Study of tensile and low cycle fatigue (LCF) behavior of IN617 and deformation behavior at room temperature and high temperatures is important as the components made of IN617 experience monotonic and cyclic stresses during their service. Roy et al. [4] studied this alloy under tensile loading from RT to 1000 °C and found a sudden increase in yield strength (yield strength anomaly) at 800 °C. Kauomi et al. [5] investigated tensile behavior at RT as well as high temperatures at 600, 800 and 950 °C. They observed precipitation and recrystallization at higher temperatures under tensile loading. Strizak et al. [6] investigated the influence of environment on LCF behavior and found negligible effect on its fatigue life in air and impure helium in solution annealed and aged conditions. Rao et al. [7] studied LCF behavior of IN617 at 750,850 and 950 °C and found reduction in number of cycles for macro crack initiation with increase in temperature and decrease in strain rate. In this investigation, the deformation and fracture behavior of IN617 under monotonic and cyclic loading at RT, 750 and 850 °C was studied.

## 2 Materials and Methods

The material of the present investigation, IN 617, alloy has the chemical composition as given in Table 1. It was subjected to solution annealing at 1175 °C for 40 min and was quenched in water. Tensile testing was done at room temperature, 750 and 850 °C using a strain rate of $5 \times 10^{-3}s^{-1}$ [8].

ASTM E 606 standard cylindrical specimens having gauge section of 5.5 mm diameter, length of 15 mm length were prepared for LCF studies and tested at three different temperatures, RT, 750 and 850 °C, at strain amplitudes ranging from ±0.20% to ±0.50% at a constant strain rate of 0.005 $s^{-1}$ [9]. TEM foils were sectioned from tested specimens for deformation studies.

## 3 Results and Discussion

### *3.1 Deformation Behavior Under Monotonic Loading*

Figure 1 shows engineering stress–strain curves at three temperatures in comparison. It is obvious from the curves that typical ductile behavior is observed for this

**Table 1** Analysis of chemical composition of the alloy IN617 (wt%)

| C | Fe | B | Al | Mn | Ti | Si | Cu | S | Cr | Mo | Co | Ni |
|---|---|---|---|---|---|---|---|---|---|---|---|---|
| 0.066 | 0.77 | 0.002 | 0.81 | 0.019 | 0.38 | 0.26 | 0.023 | <0.003 | 20.61 | 8.92 | 11.11 | Bal |

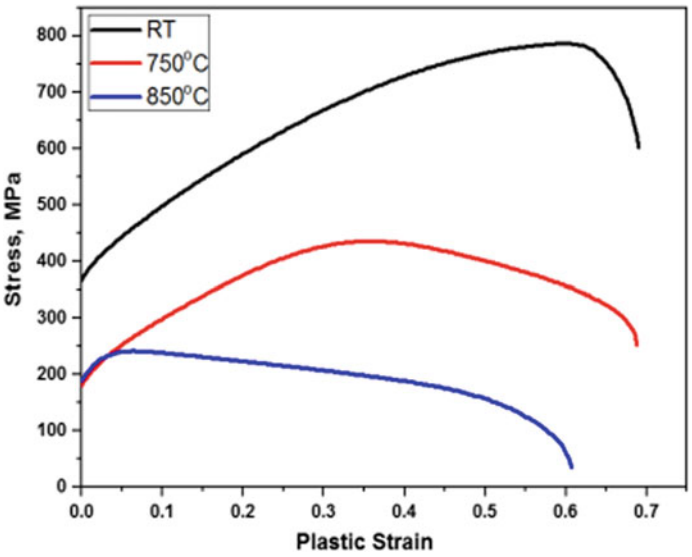


**Fig. 1** Stress-plastic strain plots of IN 617 under monotonic loading at different temperatures

alloy at all the three temperatures. Table 2 shows the tensile properties obtained from the tests conducted at 0.005 $s^{-1}$ strain rate. Reduction in ultimate tensile strength was observed with increase in the temperature. However, no difference is observed in the values of yield strength at 850 °C in comparison to the value of yield strength at 750 °C. A reverse trend in values of ductility was found which decreased with increase in temperature. Similar results were observed by Mo et al. [10]. The ratio of $S_{UTS}/S_{YS}$ often referred as degree of work hardening was more at 750 °C compared to that at RT. However, it showed decrement again at 850 °C.

Figure 2a shows the microstructure of the tensile tested specimen at RT as revealed by TEM, containing traces of slip bands formed during deformation. Tangles of dislocations were observed within the slip bands. This confirms the deformation process is through slip at RT under monotonic tensile loading. The high density of dislocations is due to pileup of dislocations during deformation.

Figure 2b shows the microstructure of the tensile tested specimen at 750 °C. Formation of carbides as well as $Ni_3$(Al, Ti) precipitates referred as $\gamma'$ is observed at this temperature (inset image). The precipitates are fine and uniformly distributed through the microstructure. The high degree of work hardening noticed at this temperature can be attributed to the evolution of carbides and $\gamma'$ precipitates and their interaction with dislocations. Micro-twins were also observed in the dislocation substructure at this temperature which indicates that the deformation process is by slip as well as micro-twinning. Figure 2c shows the microstructure of specimen tested under monotonic loading at 850 °C. Carbides can be observed throughout the matrix and the carbides are bigger in size. Formation of sub-grains is also observed at this temperature. The decrease in elongation values at this temperature can be

**Table 2** Effect of monotonic loading on properties of IN617 at different temperatures

| Temperature (°C) | 0.2% Y.S, MPa ($S_{YS}$) | U.T.S, MPa ($S_{UTS}$) | Elongation, % ($e_f$) | R.A % | Degree of work hardening ($S_{UTS}/S_{YS}$) |
|---|---|---|---|---|---|
| RT | 372 | 785 | 73 | 52 | 2.11 |
| 750 | 180 | 435 | 71 | 50 | 2.41 |
| 850 | 189 | 240 | 63 | 55 | 1.45 |

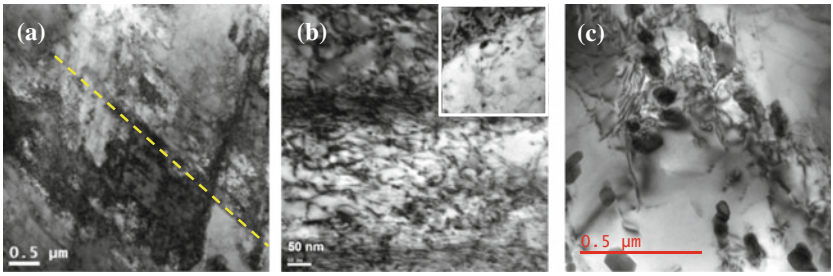


**Fig. 2** Microstructure of the specimen tested under monotonic loading: **a** at RT showing traces of slip bands (dashed line) and dislocation tangles with in slip bands **b** at 750 °C showing formation of fine precipitates, micro-twins present in the substructure and dislocation–precipitate interaction **c** at 850 °C showing formation of coarse carbide precipitates and sub-grains

attributed to the formation the bigger size carbides which acted as nucleation sites for the formation of voids which led to premature failure of the samples.

## *3.2 Deformation Behavior Under Cyclic Loading*

Table 3 shows the summary of the data obtained for IN617 tested under cyclic loading at three temperatures namely room temperature, 750 and 850 °C.

It can be seen from Table 3 that the temperature has adverse effect on fatigue life of the IN617 alloy. Fatigue life was found to be reduced with rise in temperature and strain amplitude. Run out was noticed at room temperature at ±0.18% strain amplitude, i.e., no failure of the sample was observed. Decrease in life was observed at 750 °C with rise in strain amplitude. Decrement in life was drastic at above ±0.375% strain amplitude. Nearly similar trend was detected at 850 °C at strain amplitudes of similar magnitude.

The strain amplitude (plastic) ($\Delta\varepsilon_p/2$) and average stress amplitude ($\Delta\sigma/2$) determined from the hysteresis loops at $0.5N_f$ often referred as half life cycle, are also presented in Table 3. It is evident that the value of $\Delta\varepsilon_p/2$ increased with increase in strain amplitude as well as temperature. Increase in strain amplitude also affected the stress amplitude which exhibited rise in the values. However at 750 °C,

**Table 3** Data for IN617 tested under cyclic loading at different temperatures

| $\Delta\varepsilon_t/2$ | $N_f$ (Cycles) | $\Delta\varepsilon_p/2$ | $\Delta\sigma/2$ (MPa) | *H* % |
|---|---|---|---|---|
| *Room temperature* | | | | |
| 0.0018 | Run out[a] | 0.00011 | 322 | 19.5 |
| 0.0020 | 95,931 | 0.00043 | 369 | 21.5 |
| 0.0025 | 35,329 | 0.00079 | 377 | 22.6 |
| 0.00375 | 13,239 | 0.00168 | 441 | 26.8 |
| 0.0042 | 6994 | 0.00198 | 452 | 30.0 |
| 0.0050 | 5743 | 0.00253 | 505 | 25.6 |
| *750 °C* | | | | |
| 0.0020 | 6926 | 0.00051 | 286 | 88.2 |
| 0.0025 | 6237 | 0.00,054 | 319 | 120.7 |
| 0.00375 | 945 | 0.00120 | 454 | 126.1 |
| 0.0050 | 405 | 0.00219 | 531 | 103.5 |
| *850 °C* | | | | |
| 0.0020 | 2600 | 0.00035 | 260 | 29.0 |
| 0.0025 | 1190 | 0.00095 | 272 | 48.3 |
| 0.00375 | 973 | 0.00175 | 295 | 45.8 |
| 0.0050 | 435 | 0.00290 | 350 | 39.2 |

[a]Run out at 1,82,000 cycles

the values of stress amplitude observed at higher strain amplitudes were higher compared to those at RT. The stress amplitude values at 850 °C followed similar trend as that of the RT. Degree of hardening was increased with increase in temperature from RT to 750 °C; however, it was again decreased at 850 °C.

Figure 3 depicts the variation of stress amplitude with fatigue cycles at two strain amplitudes studied at three temperatures. Cyclic hardening is observed at all the strain amplitudes and temperatures, except at ±0.5% strain amplitude. The tested specimen at this strain amplitude showed cyclic hardening initially upto100 cycles and then exhibited cyclic softening at RT. At higher temperatures, continuous cyclic hardening is observed and dual slope behavior is visible from Figs. 3a, b. It can be concluded that from these curves, that Inconel 617 alloy exhibits mostly cyclic hardening behavior at the three temperatures studied. This behavior is in line with the hypothesis that cyclic hardening is expected in the materials with $S_{UTS}/S_{YS}$ ratio greater that 1.4 (Table 2) and monotonic strain hardening exponent ($n$) values greater than 0.15 [9].

Figure 4 shows plots of the plastic strain amplitude and $2N_f$ often referred as number of reversals to failure, at three different temperatures clearly depicting the validity of Coffin–Manson (C-M) relationship. C-M plot at 750 °C can be seen in the left to that of the 850 °C due to sudden decrease in life at higher strain amplitudes at 750 °C.

Figure 5a and b show microstructures of the samples tested under cyclic loading at RT and at two strain amplitudes (±0.2% and ±0.5%) as revealed by TEM. The sample at low strain amplitude shows traces of slip bands, micro-twins and

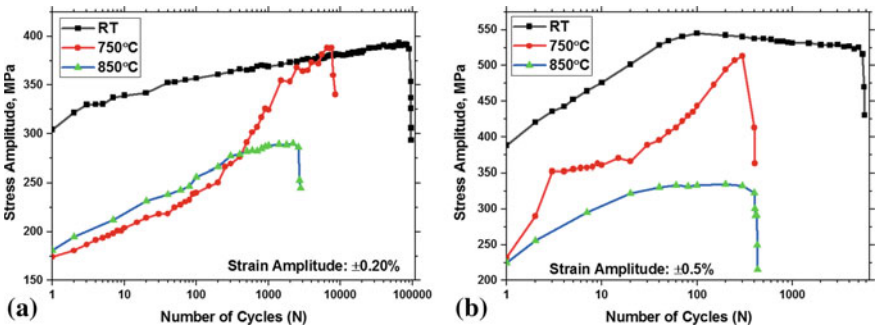


**Fig. 3** Stress response curves under cyclic loading at RT, 750 °C and 850 °C at two strain amplitudes: **a** ±0.2% and **b** ±0.5%

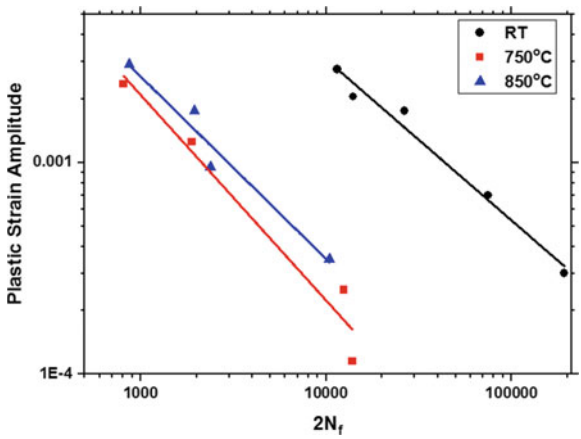


**Fig. 4** Coffin–Manson plots of the IN 617 alloy at RT, 750 °C and 850 °C

dislocations within micro-twins. The dislocation pile ups are also more within the slip bands. It clearly shows the deformation process is through slip and twinning at this temperature and strain amplitude. At higher strain amplitude, there was reduction in dislocation density and tangles of dislocations were less. There was no evidence of precipitation of second phase particles. The annihilation of dislocations might have occurred at this strain amplitude which caused the absence of the pileups of dislocations at this strain amplitude.

Figure 6a and b show microstructures of the samples tested under cyclic loading at 750 °C and at two strain amplitudes (±0.2% and ±0.5%) by TEM clearly indicating precipitation of carbides and γ′ particles. This can be confirmed from the analysis of diffraction patterns presented in our previous publication [9]. These precipitates are fine and uniformly distributed throughout the structure. These precipitates were found to form at tangles of dislocations. The interaction of dislocations with the precipitates also can be evidenced from the micrographs. The dislocation density was found to be less than that at RT. At high strain amplitude,

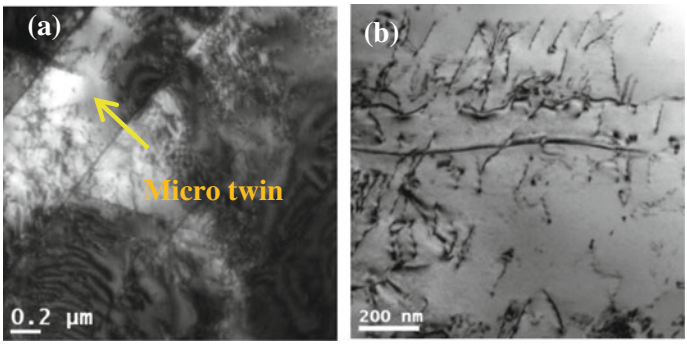


**Fig. 5** Microstructure of the samples tested under cyclic loading at RT at two strain amplitudes: **a** at ±0.20% revealing traces of slip bands and dislocations within micro-twins (shown by arrow) **b** at ±0.50% revealing less number of dislocation tangles

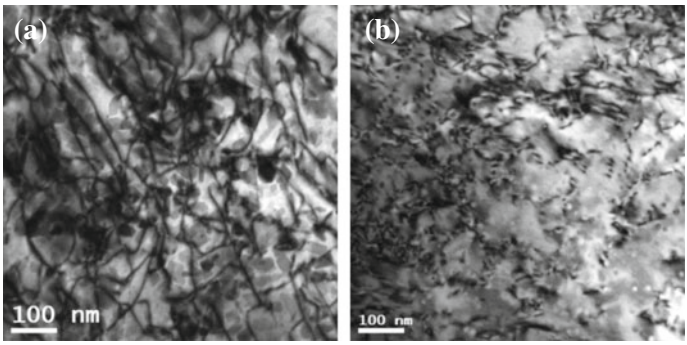


**Fig. 6** Microstructure of the samples tested under cyclic loading at 750 °C at two strain amplitudes: **a** at ±0.20% revealing precipitates formed and their interaction with dislocations **b** at ±0.50% revealing evolution of precipitates and dislocation interaction

precipitates formed were less in number and smaller in size due to decrease in cyclic fatigue life observed at this strain amplitude. Formation of the precipitates increased the stress amplitude continuously for the subsequent cycles. The degree of hardening also increased due to the precipitates which increase in number and size with rise in strain amplitude.

Figure 7a and b show microstructure of the samples tested under cyclic loading at 850 °C and at two strain amplitudes (±0.2% and ±0.5%) which clearly depict precipitation of carbides which are bigger in size and randomly distributed in the microstructure. The absence of γ′ particles at 850 °C is also reported by Mankins et al. [2] as the γ′ solvus line lies in the temperature range of 760 °C and 816 °C. Sub-grain formation can also be visualized. The precipitates contributed for increase in stress amplitude for the subsequent cycles. Number of precipitates was found to decrease with increase in strain amplitude. The degree of work hardening

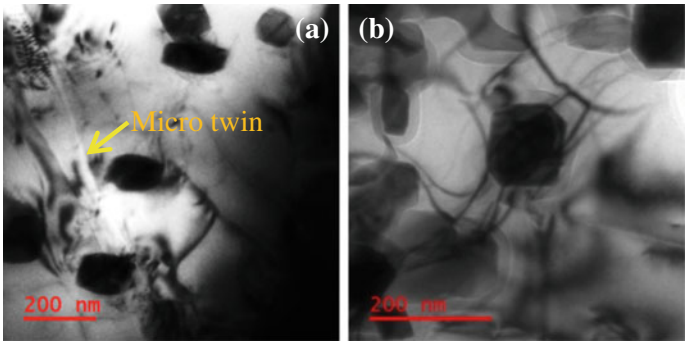


**Fig. 7** Microstructure of the samples tested under cyclic loading at 850 °C at two strain amplitudes: **a** at ±0.20% revealing precipitates formed which are bigger in size compared to that formed at 750 °C **b** at ±0.50% revealing precipitate formation and their interaction with dislocations

(Table 3) at 850 °C was low compared to that at 750 °C due to the absence of γ′ particles and decrease in number of carbides. At low strain amplitude, micro-twins were observed (shown by arrow) in which aligned dislocations can also be seen. Dislocation density was low compared to that at RT and 750 °C. The precipitation behavior of the alloy at high temperature is observed to be same under monotonic and cyclic loading, i.e., formation of γ′ particles and carbides at 750 °C whereas only formation of carbides at 850 °C.

## 4 Conclusions

1. Tensile properties of IN617 alloy showed that the temperature had adverse effect on strength parameters. Also, ductility parameters decreased at 750 °C and 850 °C compared to the values of RT due to precipitation of carbides.
2. Deformation mechanism under monotonic loading is observed to be slip at RT. Precipitation of carbides and γ′ particles, and their interaction with dislocations at 750 °C contributed to high degree of work hardening. Deformation process is by slip as well as micro-twinning. Precipitation of coarse carbides and sub-grain formation was observed at 850 °C. Low density of dislocations was found at higher temperatures.
3. Cyclic deformation studies revealed cyclic hardening at RT which was attributed to the existence of pile up of dislocations in planar array in slip bands, and to the interaction of dislocations with to fine carbide and γ′ particles at 750 °C. The hardening at 850 °C is attributed to the interaction of dislocations with the carbides particles.
4. Coffin–Manson relationship was found to be valid at the three temperatures explored.

## References


1. Klöwer J, Husemann RU, Bader M (2013) Development of nickel alloys based on alloy 617 for components in 700 °C power plants. Procedia Eng 55:226–231
2. Mankins WL, Hosier JC, Bassford TH (1974) Microstructure and phase stability of Inconel alloy 617. Metallurgical Trans 5(12):2579–2590
3. Hosier JC, Tillack DJ (1972) Inconel alloy 617—new high temperature alloy. Metals Eng Quar 12:51–55
4. Roy AK, Marthandam V (2009) Mechanism of yield strength anomaly of Alloy 617. Materials Sci Eng A 517 1–2:276–280
5. Kaoumi D, Hrutkay K (2014) Tensile deformation behavior and microstructure evolution of Ni-based superalloy 617. J Nuclear Mat 454(1–3):265–273
6. Strizak JP et al (1981) High temperature low cycle fatigue and tensile properties of Hastelloy X and Alloy 617 in air and HTGR Helium. Proceedings of the IAEA Specialists meeting, "High temperature metallic materials for applications in gas cooled reactors", Oak Ridge National Laboratory, Vienna, Austria, May 1981, OEFZS-Report No. 4086
7. Rao KBS, Schiffers H, Schuster H, Nickel H (1988) Influence of time and temperature dependent processes on strain controlled low cycle fatigue behavior of alloy 617. Metallurgical Trans A 19(2):359–371
8. Rao CV, Srinivas NCS, Sastry GVS, Singh V (2019) Dynamic strain aging, deformation and fracture behavior of the nickel base superalloy Inconel 617. Mater Sci Eng, A 742:44–60
9. Rao CV, Srinivas NCS, Sastry GVS, Singh V (2019) Low cycle fatigue, deformation and fracture behavior of Inconel 617 alloy. Mater Sci Eng, A 765:
10. Mo K, Lovicu G, Chen X, Tung HM, Hansen JB, Stubbins JF (2013) Mechanism of plastic deformation of a Ni-based superalloy for VHTR applications. J Nucl Mater 441(1–3): 695–703

# A Study on the Active Eutectoid Phase Transformations of Ti/Zr–Cu Alloys


**Harish Donthula, R. Tewari, B. Vishwanadh, R. Banerjee, and S. Banerjee**

**Abstract** In this paper, the insupressible eutectoid transformations in Ti–Cu and Zr–Cu alloys are studied. Under non-equilibrium cooling conditions, the parent β (bcc) phase decompose into several fine colonies of lamellar eutectoid of α (hcp) and $M_2Cu$ (tetragonal) phases (M = Ti/Zr) nucleated within the grain. The resultant lamellar eutectoid microstructures in both these alloy systems show a finer lamellar spacing and orientation relationship between the product phases. This article discusses the favourable conditions during non-equilibrium conditions that helps in maintaining the integrity of transformation front between the parent and product phases during the transformation resulting in lamellar morphology.

**Keywords** Active eutectoid decomposition · Orientation relationship · Lattice site correspondence · Transformation front

## 1 Introduction

In general, eutectoid transformation involves decomposition of a parent phase into two product phases which evolve cooperatively, sharing a common growth front with the parent phase resulting in a lamellar morphology. However, the lamellar morphology of eutectoid products is not always maintained. In certain conditions, when the advancing front where three phases come in contact, cannot maintain its integrity, the two-phase product degenerates into a non-lamellar morphology. Under such non-equilibrium cooling conditions facilitated by higher cooling rates,

H. Donthula (✉) · R. Tewari · B. Vishwanadh
Material Science Division, Bhabha Atomic Research Centre, Mumbai 400085, India
e-mail: dharish@barc.gov.in

R. Banerjee
Department of Materials Science and Engineering, University of North Texas, Denton, TX 76203, USA

S. Banerjee
Homi Bhabha National Institute, Mumbai 400085, India



P. Ghosal et al. (eds.), *Applications of Microscopy in Materials and Life Sciences*, Springer Proceedings in Materials 11,
https://doi.org/10.1007/978-981-16-2982-2_10

the transformation of parent phase into the lamellar eutectoid products is suppressed and partition less transformation is favoured which results in the formation of metastable phases, like martensite and bainite [1, 2]. However, some eutectoid transformations in titanium and zirconium alloys cannot be suppressed by rapid cooling and the formation of lamellar eutectoid product is insuppressible. Such transformations are categorized as "active eutectoid" transformations.

Preliminary studies on eutectoid transformations in titanium alloys were pioneered by Jaffee [3], who classified these eutectoid transformations into two categories: namely, sluggish and active. Most of the eutectoid transformations in titanium alloys fall into the category of sluggish. On the other hand, there are few eutectoid transformations encountered in Ti–Cu, Ti–Ni and Ti–Si alloys, are so rapid that they cannot be suppressed even by rapid quenching and hence classified as active eutectoid transformations. This phenomenon of active eutectoid transformation is not confined only to Ti based alloys, but also found in Zr based alloys such as Zr–Cu, Zr–Ni and Zr–Fe, which exhibit non-suppressible eutectoid transformation [4–8]. The following are some of empirical observations in different alloy systems which exhibit active eutectoid transformations:

(i) eutectoid transformation temperature is high,
(ii) eutectoid composition is lean in solute and
(iii) intermetallic product phase is rich in the base metal.

However, the studies on microstructural evolution and phase transformations in active eutectoid transformations are limited. In the current work, the active eutectoid transformation is studied from the view point of Ti–Cu and Zr–Cu alloys. The details of the different phases involved in these active eutectoid transformations are tabulated in Table 1.

In these alloy systems, the microstructures of hypo-eutectoid and near eutectoid alloys showed evidences of martensitic, bainitic and eutectoid transformations [9–11]. It is found that there exists a competition amongst these transformations due to which retained β is absent in these of the microstructure, even in those samples subjected to higher cooling rates, was observed. In order to suppress the formation of the metastable phases and understand the active eutectoid decomposition from

**Table 1** Details of the eutectoid transformations in Ti–Cu, Zr–Cu and U-Mo alloys

| Alloy system | Eutectoid composition (at.%) | Eutectoid temperature (°C) | Details of product phases |
|---|---|---|---|
| Ti–Cu | 12 | 798 | β - Ti (BCC) → α - Ti (HCP) + $Ti_2Cu$ (BCT - $MoSi_2$) |
| Zr–Cu | 2.2 | 810 | β - Zr (BCC) → α - Zr (HCP) + $Zr_2Cu$ (BCT - $MoSi_2$) |
| *U–Mo | 20 | 500 | γ - U (BCC) → α - U (orthorhombic) + $U_2Mo$ (BCT - $MoSi_2$) |

* is a sluggish eutectoid but with similar crystallography as Ti/Zr–Cu eutectoids

the super saturated parent phase, hyper-eutectoid alloy compositions (Ti-15wt%Cu and Zr-2.5wt%Cu) are chosen. The higher density of interfaces ($\alpha/M_2Cu$) per unit volume due to fine intermetallic plates (20–30 nm thick) and inter lamellar spacing (40–50 nm) formed as a result of active eutectoid transformation [4, 5], makes these is alloy systems a potential candidate for higher strength applications.

## 2 Experimental

The hyper-eutectoid compositions of Ti–Cu (Ti-15wt%Cu) and Zr–Cu (Zr-2.5wt% Cu) alloys were produced by arc melting using a non-consumable tungsten electrode and water cooled copper crucible in an argon atmosphere. These alloy samples were produced from high purity titanium, zirconium and copper (99.99%). To ensure their chemical homogeneity in these dilute alloys, master alloys of Zr-10wt %Cu and Ti-25wt%Cu were diluted to the required compositions by addition of solvent element. The as-cast arc melted buttons are shrouded and sealed in mild steel capsules under vacuum and hot rolled into sheets at a temperature of 1000 °C. The specimens of Ti-15wt%Cu and Zr-2.5wt%Cu fabricated from the hot-rolled sheets are glass sealed in argon atmosphere to prevent oxidation during the subsequent heat treatments. The glass sealed specimens of these alloys were then solutionized in β-phase (1000 °C in Ti-15wt%Cu and 950 °C in Zr-2.5wt%Cu) for an hour and subsequently water quenched.

Specimens for scanning electron microscopy were polished using emery sheets of different grit sizes, followed by diamond polishing using 1-μm suspension to obtain a mirror finish surface. The specimens are then chemically etched for microstructural characterization under SEM. For TEM, the pre-thinned foils made by mechanical polishing of the heat treated specimens were electro-polished using a mixture of 90 parts of methanol and 10 parts perchloric acid as electrolyte at −35 °C and 20 V. SEM specimens were examined under FEI and Auriga Carl Zeiss FESEM instruments. TEM examination was carried out in Technai F-30 microscope with an accelerating voltage of 200KV.

## 3 Results and Discussion

The microstructures of the β quenched Ti–Cu and Zr–Cu specimens are shown in Fig. (1a & b). The microstructures showed the distribution of several lamellar eutectoid colonies (longest dimension being 2–3 μm) nucleated within a prior β grain. Unlike conventional eutectoid decomposition resulting in nodular eutectoid colonies, these lamellar eutectoid colonies have uni-directional growth. One such colony is marked in Fig. 1a. In Ti–Cu, the arrangements of the lamellae in a colony (feathery structure) show as if these lamellae are fanning out from the point of origin (Fig. 1b). In contrast, the lamallea in Zr–Cu eutectoid are parallel, straight

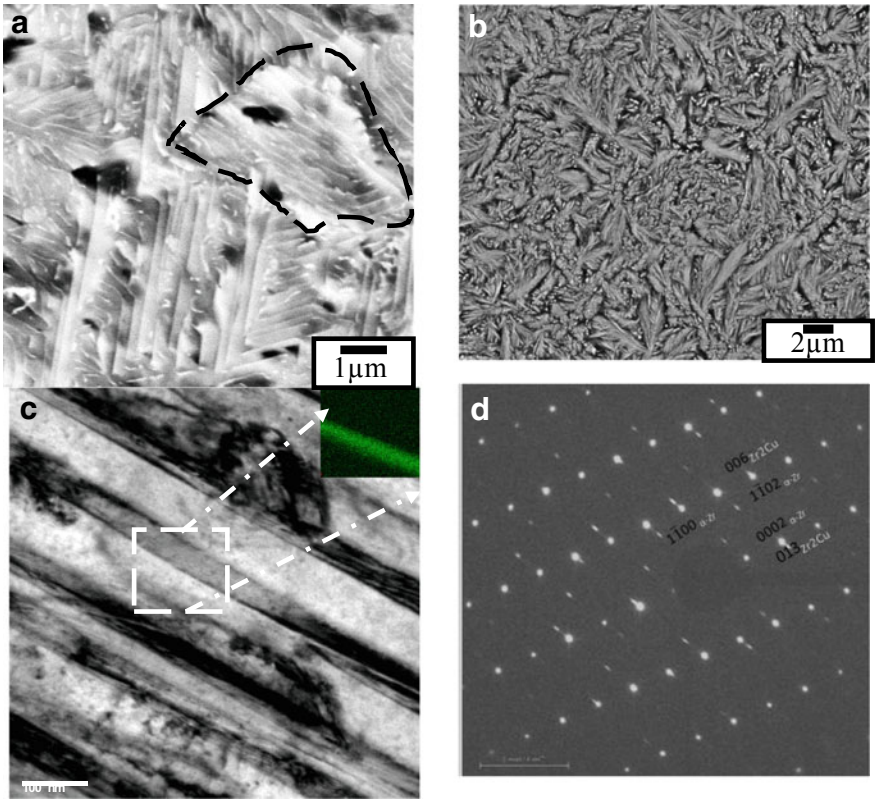


**Fig. 1** **a–b** The microstructure of the water quenched Ti–Cu and Zr–Cu hyper eutectoid alloys. **c** TEM micrograph of an eutectoid colony in showing the presence of α-Zr and $Zr_2Cu$. Inset shows EDS map of copper enrichment and depletion in $Zr_2Cu$ and α-Zr phases, respectively. **d** SAD pattern from the colony indexed in terms of α-Zr and $Zr_2Cu$

and does not fan out from the point of origin suggest a possibility crystallographic habit plane between the two phases. The TEM micrograph from an individual colony of Zr–Cu is shown in Fig. 1c. The compositional analysis by EDS showed the copper in the intermetallic region is close to 33 at.% Cu in both these alloys, indicating that the solute separation has reached equilibrium limits. However, the microstructure did not show the presence of any retained β phase in the microstructure. The composite selected area diffraction pattern from one such colony is indexed in term of $\left[11\bar{2}0\right]_{\alpha}$ and $[100]_{Zr_2Cu}$ zone axes as shown in Fig. 1d. The matching of diffraction spots and the parallelity of the crystallographic zone axis between the two phases indicate the presence of an orientation relationship between them, which can be expressed as:

$$[11\bar{2}0]_{\alpha-Zr}//[100]_{Zr_2Cu};\ (0002)_{\alpha-Zr}//(013)_{Zr_2Cu}.$$

A similar orientation relationship is also observed in the eutectoid decomposition of hyper-eutectoid Ti–Cu alloy [12, 13]. Based on orientation relationships obtained between the product phases and their crystallography, following observations could be made:

(i) The unit cell of $Ti_2Cu/Zr_2Cu$ can be visualized as stacking of three unit cells of parent β phase along any of the <001> β directions with specific atomic sites decorated by copper and titanium atoms as shown in the Fig. 2. The crys-

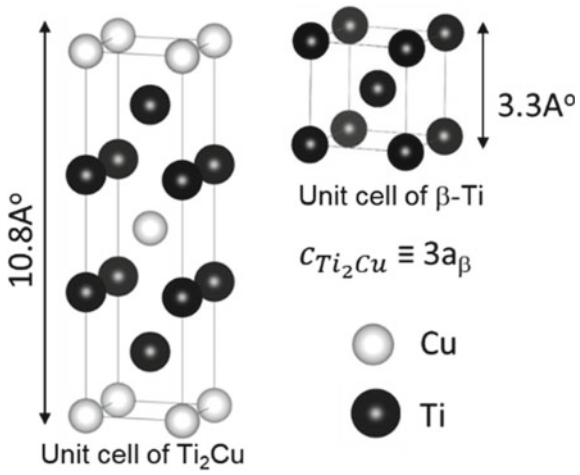


**Fig. 2.** The unit cells of the intermetallic phase ($Ti_2Cu$) and β phase

**Table 2** The crystallographic information of the phases involved in eutectoid transformation and the three phase crystallography between the parent and product phases

| Alloy system | Parent β phase | Product phases | |
|---|---|---|---|
| | | α-phase | Intermetallic |
| Ti–Cu | Space group: $Im\bar{3}m$ (BCC, $a$ = 3.31 Å) | Space group: $P6_3/mmc$ (Hexgonal, $a$ = 2.95 Å; $c$ = 4.68 Å) | Space group: I4/mmm (Tetragonal, $a$ = 2.94 Å; $c$ = 10.78 Å) |
| Zr–Cu | Space group: $Im\bar{3}m$ (BCC, $a$ = 3.63 Å) | Space group: $P6_3/mmc$ (Hexgonal, $a$ = 3.22 Å; $c$ = 5.14 Å) | Space group: I4/mmm (Tetragonal, $a$ = 3.2204 Å; $c$ = 11.1832 Å) |
| Three phase crystallography | Burgers OR | | |
| | | Crystallographic OR deduced from the study | |
| | Lattice correspondence between β and $M_2Cu$ constructed | | |

tallographic details of the parent and product phases involved in the eutectoid transformation are tabulated in Table 2.

(ii) Based on the observed OR between α and $M_2Cu$ and the Burgers OR between α and β, a three phase crystallographic relationship between α, β and $M_2Cu$ can be constructed [7, 12, 13] as shown in Table 2.

The absence of any pro-eutectoid features in the microstructure suggested that the alloy systems have unequivocally showed that the direct eutectoid decomposition of the β phase on water quenching. Such a condition in a hyper-eutectoid alloy can be attained when the parent phase is undercooled into the direct eutectoid umbrella formed by extension of solvus curves of β/α and β/$M_2Cu$ below transformation temperature as shown in Fig. 3. The thermodynamic feasibility of direct eutectoid transformation is discussed in detailed by Donthula et al. [12].

It is evident from Fig. 1c that the inter lamellar spacing of the active eutectoid decomposed products is close to 80 nm. The time required ($t = x^2/D$) for diffusion of impurity solute atoms [14] in the bcc lattice along the interface to a characteristic length of half lamellar spacing ($\lambda/2 \sim 40$ nm) at direct eutectoid transformation temperature is close to 0.01 s and 0.02 s for Zr–Cu and Ti–Cu eutectoid, respectively. In addition, the contribution due to anamolous diffusion and the interfacial effects further reduce the time required for solute partitioning along the interface [12]. The presence of lattice site registry between the parent and the product phases suggests that short range diffusion of solute atoms across the transformation front by few unit cells (minimum of three) is sufficient for solute rich β phase ($\sim$33 at.% Cu) to transform to intermetallic and solute lean β into α. It is also reported that the velocity of transformation front during the active eutectoid transformation is few orders higher than that of the conventional eutectoid [12].

The finer lamellar spacing and the higher diffusivity of the diffusional species makes the solute segregation along the transformation front to solute rich and solute

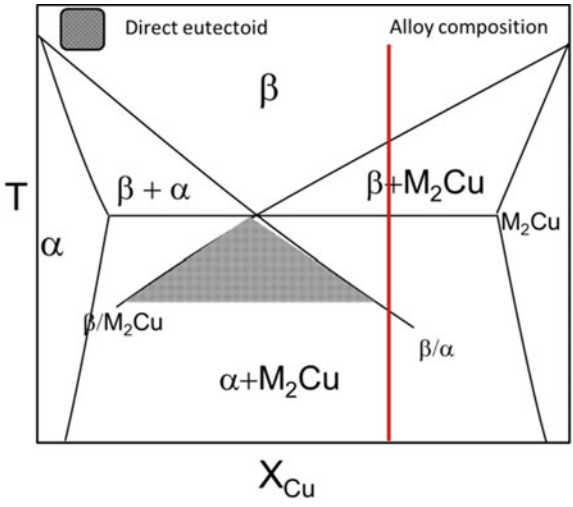


**Fig. 3.** Schematic of phase diagram showing the region of direct eutectoid transformation for a hyper-eutectoid alloy

lean region feasible at such a short timer intervals. Therefore, due to the finer lamellar spacing and higher diffusivity of the solute atoms along the transformation front, the integrity of the transformation front under non-equilibrium cooling conditions is uncompromised. Also, the lattice site registry between the parent and product phases reduces the length scale of atomic shuffle to few unit cells ahead of the transformation front resulting in greater velocity of the transformation front. In this regard, it is worthwhile to discuss the eutectoid transformation in U–Mo alloy system (refer Table 1). Due to lower transformation temperature and the slothy diffusional species (molybdenum) makes the solute segregation ahead of the transformation front unfeasible, thereby degenerating into a non-lamellar morphology. Though a crystallographic relationship exists between β-U & α-U and α-U & $U_2Mo$, transformation is suppressed due to poor diffusional kinetics [15]. In contrast to U–Mo system, it is the synergy of higher diffusional kinetics for solute segregation along the transformation front and the presence of lattice registry which can quickly transform the solute rich and depleted regions of parent phase into product phases leading to insuppressible lamellar eutectoid.

## 4 Summary

Some of the observations based on the study on the active eutectoid transformations in Ti–Cu and Zr–Cu alloy systems are the summarised as the following:

- The lamellar structure showed the presence of α-Ti/Zr and the $M_2Cu$ (M = Ti/Zr) with a finer lamellar spacing. The parent phase is not retained in any of the non-equilibrium cooled samples.
- Unlike the conventional lamellar eutectoid colonies which nucleate at the grain boundaries, the lamellar colonies can nucleate within the grain in active eutectoid transformation.
- The lattice site correspondence between the parent and product phases, because of the orientation relationship, and the rapid kinetics are the solute species are the characteristic features of the active eutectoid transformation.

## References

1. Banerjee S, Mukhopadhyay P (2007) Phase transformations examples from Titanium and Zirconium alloys, 1st edn. Pergamon, Amsterdam
2. Froes FH (2015) Titanium physical metallurgy processing and applications. ASM International, Ohio
3. Jaffee RI (1958) The physical metallurgy of titanium alloys. Prog Met Phys 7:65–106
4. Krishnamurthy S, Jackson AG, Jones H, Froes EH (1988) Beta-eutectoid decomposition in rapidly solidified titanium-nickel alloys. Metall Trans A 19(1):23–33

5. Kumar L, Ramanujan RV, Tewari R, Mukhopadhyay P, Banerjee S (1999) Active eutectoid decomposition in Zr-3 wt% Fe. Scripta Mater 40(6):723–728
6. Brice DA, Samimi P, Ghamarian I, Liu Y, Mendoza MY, Kenney MJ, Reidy RF, Garcia-Avila M, Collins PC (2017) On the eutectoid transformation behaviour of the Ti–Zn system and its metastable phases. J Alloy Comp 718:22–27
7. Mukhopadhyay P, Menon SK, Banerjee S, Krishnan R (1979) Active eutectoid decomposition in a near-eutectoid zirconium-copper alloy. Metall Trans A 10:1071–1079
8. Franti GW, Williams JC, Aaronson HI (1978) A survey of eutectoid decomposition in ten Ti–X systems. Metall Trans A 9:1641–1649
9. Souza SA, Afonso CRM, Ferrandini PL, Coelho AA, Caram R (2009) Effect of cooling rate on Ti–Cu eutectoid alloy microstructure. Mater Sci Eng C 29:1023–1028
10. Lee HJ, Aaronson HI (1988) Eutectoid decomposition mechanisms in hypo eutectoid Ti–X alloys. J Mater Sci 23:150–160
11. Devaraj A, Nag S, Muddle BC, Banerjee R (2011) Competing martensitic, Bainitic, and Pearlitic transformations in a hypo-eutectoid Ti–5Cu alloy. Metall Mater Trans 42:1139–1143
12. Donthula H, Vishwanadh B, Alam T, Borkar T, Contieri RJ, Caram R, Banerjee R, Tewari R, Dey GK, Banerjee S (2019) Morphological evolution of transformation products and eutectoid transformation(s) in a hyper-eutectoid Ti-12 at.% Cu alloy. Acta Mater 168(63):63–75
13. Dong Q, Yu H, Yao Z, Long F, Balogh L, Daymond MR (2016) Study of microstructure and precipitates of a Zr–2.5Nb–0.5Cu CANDU spacer material. J Nucl Mater 481:153–163
14. Neuman G, Tuijn C (2009) Self diffusion and impurity diffusion in pure metals. In: Pergamon material series, vol 14
15. Neogy S, Saify MT, Jha SK, Srivastava D, Hussain MM, Dey GK, Singh RP (2012) Microstructural study of gamma phase stability in U–9wt.% Mo alloy. J Nucl Mater 422(1–3): 77–85

# TEM Studies of Segregation in a Ge–Sb–Te Alloy During Heating


**Manish Kumar Singh, Chanchal Ghosh, Shalini Tripathi, Paul Kotula, Gokhan Bakan, Helena Silva, and C. Barry Carter**

**Abstract** Phase-change materials are important for optical and electronic computing memory. Ge–Sb–Te (GST) is one of the important phase-change materials and has been studied extensively for fast, reversible, and non-volatile electronic phase-change memory. GST exhibits structural transformations from amorphous to metastable fcc at ~150 °C and fcc to hcp at ~300 °C. The investigation of the structural, microstructural, and microchemical changes with high-temporal resolution during heating is crucial to gain insights on the changes that materials undergo during phase transformations. The as-deposited GST film has amorphous island morphology which transform to the metastable fcc phase at ~130 °C. The second-phase transformation, from fcc to hexagonal, is observed at ~170 °C. While the as-deposited amorphous islands show a homogeneous distribution of Ge, Sb and Te, these islands boundaries become Ge-rich after heating. Morphological and structural evolutions were captured during heating inside an aberration corrected environmental TEM equipped with a high-speed camera under a low-dose conditions to minimize beam-induced changes in the samples. Microchemical studies were carried out employing ChemiSTEM technique in probe-corrected mode with a monochromated beam.

**Keywords** GST-225 · Island morphology · Oxidation · Low-dose imaging · Crystallization · Chemical segregation

M. K. Singh (✉) · C. Ghosh · S. Tripathi · H. Silva
Electrical and Computer Engineering, University of Connecticut, Storrs, CT 06269, USA
e-mail: manish.singh@uconn.edu

P. Kotula
Materials Science and Engineering Center, Sandia National Lab, Albuquerque, NM 87123, USA

G. Bakan
National Graphene Institute, The University of Manchester, Manchester M13 9PL, UK

C. B. Carter
Chemical and Biomolecular Engineering, University of Connecticut, Storrs, CT 06269, USA

C. B. Carter
Center for Integrated Nanotechnologies (CINT), Albuquerque, NM 87123, USA



P. Ghosal et al. (eds.), *Applications of Microscopy in Materials and Life Sciences*, Springer Proceedings in Materials 11,
https://doi.org/10.1007/978-981-16-2982-2_11

## 1 Introduction

Phase-change materials are important class of materials for their usage in optical and electronic memory applications including phase change random access memory (PCRAM). The PCRAM relies upon the heating induced amorphous to crystalline phase transformation wherein materials exhibit a large change in electrical resistance [1, 2]. Germanium-Antimony-Tellurium (GST) based alloys have attracted considerable attention of the scientific community owing to their rapid switching time (∼nanoseconds) and high cyclic endurance. There are three stoichiometric GST alloys namely, $GeSb_2Te_4$, $Ge_2Sb_2Te_5$, and $GeSb_2Te_7$ lying on the pseudobinary tie line joining GeTe and $Sb_2Te_3$. Among them $Ge_2Sb_2Te_5$ (GST-225) alloy is most promising due to its better stability at room temperature, fast crystallization, and good reversible transformation between amorphous and crystalline states [3]. The physical and crystallization properties of phase change materials to a large extent determine the performance of these memories. One of the issues with GST-225 has been the requirement of large reset current to melt-quench the materials, followed by rapid quenching to room temperature. To circumvent this, strategies were adopted to dope GST-225 with light elements including N and O to increase the resistance of the crystalline phase which in turn reduces the reset current [4–6]. Moreover, delayed crystallization has also been observed which further improves the room temperature stability of GST-225. The role of capping on the crystallization temperature of GST-225 film has significant effect. For the 100-nm thick films, the non-oxidized films crystallize at ∼170 °C, whereas uncapped films show amorphous to crystalline phase transformation at ∼150 °C. The early transition observed in uncapped films has been attributed to the surface oxidation and have been demonstrated previously in several reports [7, 8]. A reduction of 50 °C in the crystallization temperature of 10 nm GeTe film has been reported, when exposed to atmosphere for 2 months. Kooi and coworkers reported the complete crystallization of the GST-225, 10 nm film at room temperature upon exposure to atmosphere for 2 months [9]. We have recently reported the crystallization temperature of ∼130 °C, in an uncapped Ge-rich GST-225 film of thickness 30 nm exposed to atmosphere for 4 months [10]. The observed depression in crystallization temperature as well as chemical segregation was ascribed to the presence of oxygen in the film. It has been demonstrated that chemical composition of the GST-225 remains unchanged after the amorphous to crystalline transformation. However, situation may change if composition deviates from the standard one caused by film deposition conditions such as nature of substrates and protective layers, exposure to atmosphere and so on. For instance, Ge-rich GST-225 film was reported to grow when sputtered from a target of a $Ge_2Sb_2Te_5$ [10]. This film exhibited chemical segregation among Ge, Sb, and Te in as-deposited film at room temperature which increases further at elevated temperatures. The increased crystallization temperature observed in thickness of the films less than 10 nm have been attributed to interface energy/stress between the active films and protective layers [11]. However, the effect on crystallization and chemical

changes of uncapped film of thickness less than 10 nm exposed to air has not been explored in detail. The crystallization behavior of the amorphous GST-225 thin films have been investigated through X-ray diffraction, temperature dependence of electrical resistivity, calorimetric, spectroscopic, and electron microscopy [12–19]. The investigation of phase transformation of GST-225 at high spatial and temporal resolutions in *real time* using in-situ TEM is required to determine the transformation temperature precisely [20, 21]. However, amorphous GST can transform to crystalline with the exposure of electron beam and impair the determination of crystallization temperature [22, 23]. To minimize the e-beam effect on sample, investigation using a low-electron dose is required. The images acquired using a low dose possess a low SNR thereby makes the image interpretation difficult. This can be even more challenging for GST, as the chemistry of the transformed phase and the amorphous matrix remain nearly same. The present work deals with the study of structural transformations and chemical segregation in uncapped $Ge_2Sb_2Te_5$ thin film sputtered directly on $SiN_x$ support of the protochips. The structural transformation was followed in-situ using an aberration corrected environmental TEM.

## 2 Materials and Methods

The GST-225 film of a thickness 40 nm was deposited directly on $SiN_x$ support film of a protochips using magnetic sputtering from $Ge_2Sb_2Te_5$ target [10, 24, 25]. The details of deposition condition of the film have been reported elsewhere. The in-situ heating of the film was carried out employing an Aduro 300 heating holder in a FEI image-corrected Environmental TEM (ETEM). Dynamics of the crystallization process were captured using a low-electron-dose with a large-field-of-view direct electron detection camera (Gatan K3 IS). The film was heated at a ramp rate of 5 °C/s from room temperature 25 to 200 °C. Microchemical studies were carried out employing a FEI G2 80–200 kV ChemiSTEM in probe-corrected mode with a monochromated beam and the chemical distribution within the specimen was determined using four quadrant X-ray energy dispersive spectrometry (XEDS) detectors.

## 3 Results and Discussion

The bright-field TEM micrographs of as-deposited and after exposure of e-beam for about 30 min and their corresponding selected area electron diffraction (SAD) patterns are shown in Fig. 1. The islands morphology of the as-deposited 40 nm GST-225 film was observed. Average size of the islands was measured to be ~15 nm. The SAD pattern is devoid of any distinct spot or rings leading us to conclude that the as-deposited film is amorphous in nature. However, there might

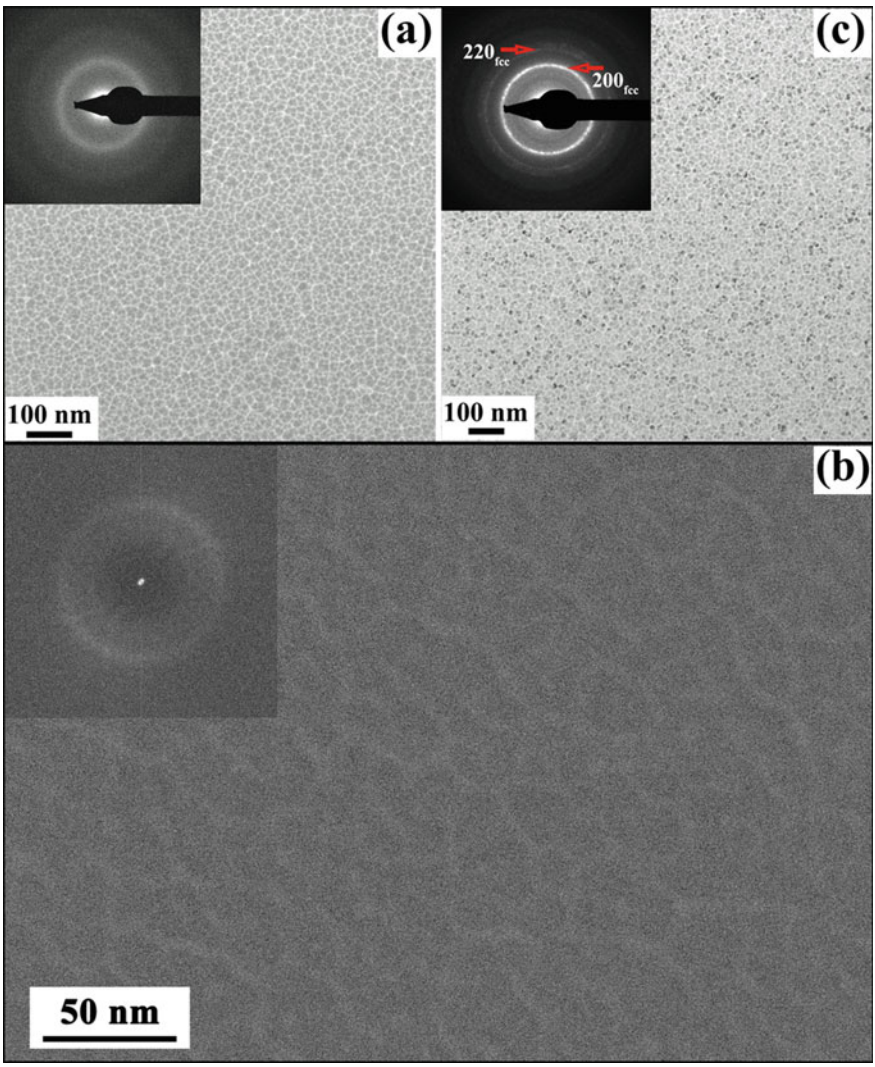


**Fig. 1** BF-TEM micrographs and their corresponding SAD patterns (insets) of as-deposited GST-225 film of thickness 40 nm **(a)** at the beginning and **(c)** after 30 min of e-beam. Exposure. **(b)** shows a low-dose and large field of view image with FFT as inset

be weak reflections which are masked by the amorphous matrix. A low-dose and large field of view micrograph along with corresponding power spectrum as inset is shown in Fig. 1b. The absence of lattice periodicity in the power spectrum confirms the amorphous nature of the film. After 30 min of exposure with e-beam (300 kV), a few islands with dark contrast were observed in the BF image indicating the crystallization of the film. This is further evidenced by the presence of rings in the

corresponding SAD pattern. The rings in the SAD pattern are indexed to (200) and (220) of fcc-GST-225 phase. The e-beam has triggered amorphous to crystalline transformation in GST-225 film suggests that GST is extremely sensitive to the radiation (e-beam) and requires an alternate imaging technique, e.g., low-electron dose imaging, cryo-TEM. To minimize the effect of e-beam, a low-electron dose rate (6.67 e. $Å^{-2}$. $s^{-1}$) was used to record the images, while heating the film inside the aberration corrected TEM. Structural transformation was recorded using a high-speed camera. The morphology of the film at 130 °C during heating is shown in Fig. 2. The onset of the crystallization was observed at 130 °C which is about 20 °C less than the reported value in the literature. The contrast in the image has been reduced due to low-dose imaging and has been enhanced through integration of in-situ video data set. Nevertheless, the presence of a faint ring in the power spectrum (inset-top left) revealed the early stages of crystallization and indexed as fcc phase of GST-225. One such crystallite at a very early stage is marked in a red square in the micrograph and is digitally zoomed, as shown in bottom right inset. The lattice spacing ~0.34 nm has been marked in the image which corresponds to (111) of fcc-GST-225 phase. The similar amorphous to crystalline transformation studies in an uncapped 30 nm GST-225 film on $SiN_x$ support membrane on Protochips have been reported previously [10].

With further heating at 150 °C, crystals corresponding to $Sb_2Te_3$ phase was also observed as shown in Fig. 3, where three different regions marked as 1, 2, and 3 along with corresponding power spectra as well as digitally zoomed images are also shown. Figure 4 depicts a low-dose image showing the microstructural nature of

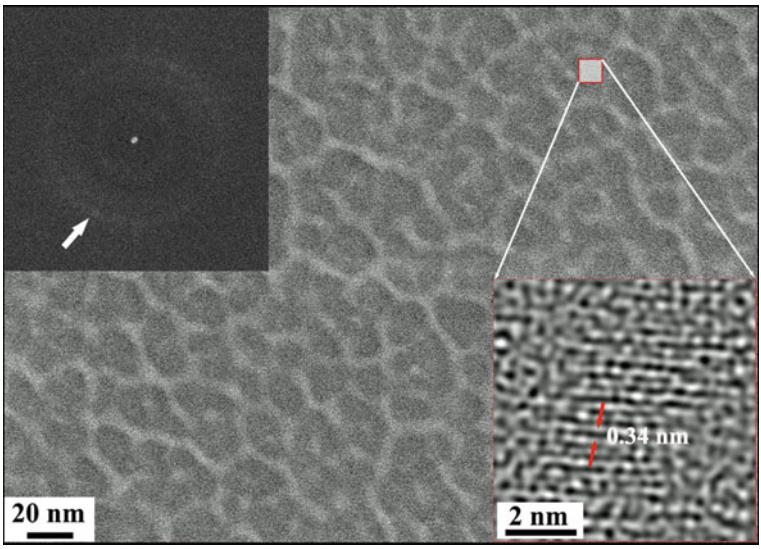


**Fig. 2** Low-electron-dose micrograph of GST-225 film heated at 130 °C. Power spectrum and a zoomed image of a crystalline domain as insets showing onset of crystallization

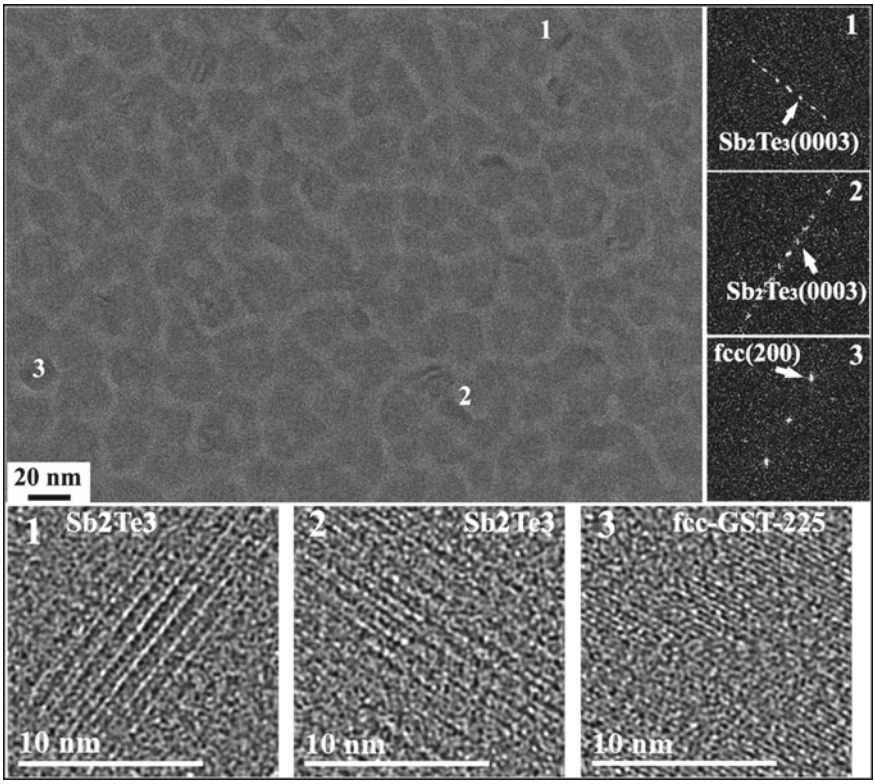


**Fig. 3** Low-electron-dose micrograph of GST-225 film heated at 150 °C showing three different regions 1, 2, and 3. Power spectra and digitally zoomed images corresponding to regions 1, 2, and 3 are also shown. The spots in the power spectra corresponding to $Sb_2Te_3$ and fcc-GST-225 phases are marked

the film heated at 170 °C. With the increase in temperature, crystallinity of the film increases, and the presence of crystalline domains are visible even in a low-dose condition (Fig. 4a). Power spectrum (shown as inset) exhibits increased number of spots conforming to a greater degree of crystallization in the film. Periodicities corresponding to fcc-GST-225, hex-GST-225, and $Sb_2Te_3$ phases are marked in the power spectrum. Emergence of newer crystallites can also be observed in the low-dose HRTEM micrograph and two such crystallites are marked with red squares. The magnified view of them is displayed in Fig. 4b, c, respectively, where lattice fringe spacings correspond to (200) of fcc-GST-225 and (0003) of $Sb_2Te_3$ are presented. It is noteworthy to mention that the crystalline domains are observed within the islands and inter-island regions remain devoid of long-range order.

The chemical nature of the film heated at 100 °C is shown in Fig. 5a. This figure comprised of the STEM-HAADF image and the corresponding STEM-XEDS maps of Ge, Sb, Te, O, and their composite from the same region. It is apparent that the

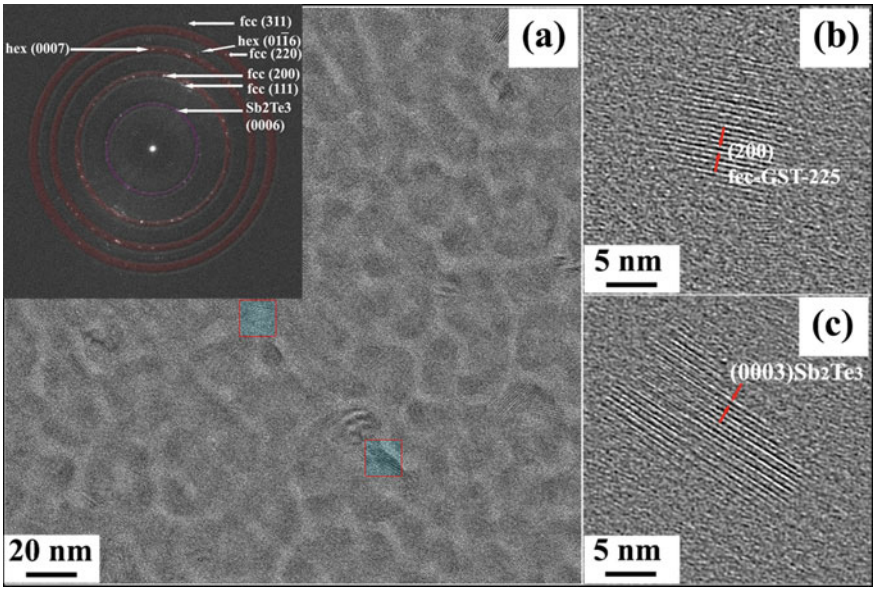


**Fig. 4** **(a)** A low dose image of GST-225 film heated at 170 °C along with power spectrum showing periodicities corresponding to fcc and hexagonal GST-225 and $Sb_2Te_3$ phases. The false color rings are inserted for the visibility of spots. The magnified images from selected square regions in **(a)** showing lattice fringe spacings correspond to fcc-GST-225 and $Sb_2Te_3$ phases in Figures **(b)** and **(c)**, respectively

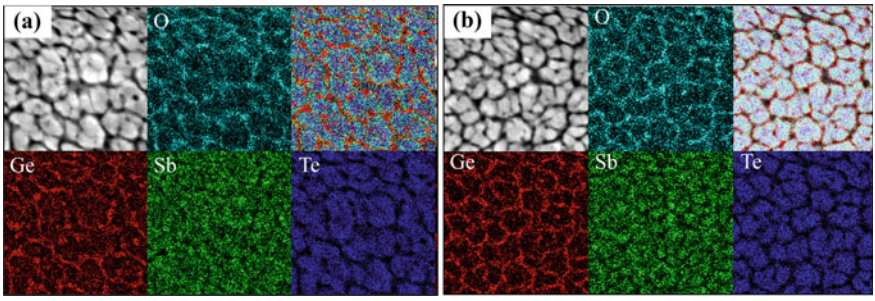


**Fig. 5** STEM-HAADF image and STEM-XEDS maps of Ge, Sb, Te, and O along with their composite images acquired from the in-situ heated GST-225 film at **(a)** 100 °C and **(b)** 150 °C. The field of view for all the images is 125 nm.

distribution of the elements is not homogeneous where Ge and O are rich in the inter-island regions, whereas the islands consist of Sb and Te. The composite map clearly depicts the distribution of the elements. It is evident that a chemical segregation is taking place resulting a partition of Ge–O and Sb–Te at this temperature. However, there can be a few nanostructural domains of GST-225 over the islands.

With the increase in temperature, this partition becomes prominent as shown in the element maps acquired at 150 °C (Fig. 5b). This chemical segregation can be attributed to the following: (i) The uncapped nature of the film which promotes the oxidation with a long exposure to the atmospheric conditions and (ii) island morphology of the film. The oxidized GST-225 film promotes the chemical segregation into Ge–O and $Sb_2Te_3$ over crystallization into the *fcc* and subsequent *hexagonal* phase. In the previous communication from author's group [10], it was shown that Ge segregates toward island boundaries even in as-deposited film based on room temperature STEM-XEDS maps.

Of the elements present in the $Ge_2Sb_2Te_5$, Ge is more prone to oxidation owing to its affinity toward oxygen, leading to preferential oxidation of Ge. The remaining film is then rich in Sb and Te. The bond-dissociation energy for Ge–O (657.5 kJ/mol) is much higher than that of the Ge-Te (396.7 kJ/mol), Te–O (377 kJ/mol) and Sb-O (434 kJ/mol) [26]. The Ge–O compound is thermodynamically more favorable than Sb-O or Te–O compounds. This explains the preferential oxidation of Ge over Sb, and Te with long term atmospheric exposure. The microchemical nature of the similar film at room temperature has been reported earlier [10]. Moreover, in the same communication the STEM-XEDS line profiles at 200 °C, the stoichiometry of the island was estimated close to $Sb_2Te_3$.

Oxygen can play a very different role depending on the nature of its presence in the system. The increase in the crystallization temperature from 150 to 200 °C was observed when 16.7 and 21.7 wt% oxygen was incorporated into GST-225 [6]. Moreover, in the presence of oxygen, the onset of amorphous to crystalline transformation is significantly delayed due to hindrance in the cubic atomic arrangement [8]. Contrary to this, in the oxidized film the crystallization is observed at relatively lower temperature. The Sb diffuses faster than those of Ge and Te in Ge–Sb–Te, however, in the presence of oxygen, Ge moves out from the Ge–Sb–Te matrix [27] and segregates toward the island boundaries in the present study. The similar results were observed in the case of $Ge_1Sb_2Te_4$ system where oxygen influenced the formation of Ge–O and $Sb_2Te_3$ phases [28]. They act as a heterogeneous nucleation sites for the FCC and HCP phase transformations.

## 4 Conclusions

The following conclusions can be drawn from the present work.

1. The amorphous to crystalline transformation temperature in an uncapped GST-225 film of thickness 40 nm has been observed at ~130 °C using a low-electron dose and large field of view direct detection camera. The observed reduction in the crystallization temperature is attributed to oxidation of the film.
2. At 170 °C, crystallites correspond to fcc and hexagonal GST-225 along with $Sb_2Te_3$ phases are observed.

3. The island morphology and oxidized nature of the film promotes chemical segregation resulting into formation of Ge–O and Sb–Te rich phases.
4. The current study can be extended to investigate the phase transformation behavior of GST-based films in the presence of O and other interstitials.

**Acknowledgements** This research is supported by NSF under award DMR-1710468. The TEM studies were carried out at the Center for Integrated Nanotechnologies, an Office of Science User Facility operated for the U.S. Department of Energy (DOE) Office of Science, and in the Materials Characterization Department, Sandia National Laboratories. The GST films were deposited at the Institute of Materials Science and Nanotechnology (UNAM) at Bilkent University, Turkey. The authors thank Drs. John Watt, Matthew T. Janish and Ali Gokirmak for helpful discussions. Use of the K3 IS camera was provided courtesy of Gatan. The Sandia National Laboratories are managed and operated by National Technology and Engineering Solutions of Sandia, LLC., a wholly owned subsidiary of Honeywell International, Inc., for the U.S. DOE's NNSA under contract DE-NA-0003525. The views expressed here do not necessarily represent the views of the U.S. DOE or the U.S. Government.

## References

1. Raoux S (2009) Phase change materials. Annu Rev Mater Res 39:25–48
2. Wuttig M, Yamada N (2007) Phase-change materials for rewriteable data storage. Nat Mater 6 (11):824–832
3. Yamada N (2012) Origin, secret, and application of the ideal phase-change material GeSbTe. Phys Status Solidi (b) 249(10):1837–1842
4. Agati M, Renaud F, Benoit D, Claverie A (2018) In-situ transmission electron microscopy studies of the crystallization of N-doped Ge-rich GeSbTe materials. MRS Commun 8 (3):1145–1152
5. Golovchak R, Choi Y, Kozyukhin S, Chigirinsky Y, Kovalskiy A, Xiong-Skiba P, Trimble J, Pafchek R, Jain H (2015) Oxygen incorporation into GST phase-change memory matrix. Appl Surf Sci 332:533–541
6. Jang M, Park S, Lim D, Cho M-H, Do K, Ko D-H, Sohn H (2009) Phase change behavior in oxygen-incorporated $Ge_2Sb_2Te_5$ films. Appl Phys Lett 95(1):012102
7. Agati M, Gay C, Benoit D, Claverie A (2020) Effects of surface oxidation on the crystallization characteristics of Ge-rich Ge–Sb–Te alloys thin films. Appl Surf Sci 518:146227
8. Berthier R, Bernier N, Cooper D, Sabbione C, Hippert F, Noé P (2017) In situ observation of the impact of surface oxidation on the crystallization mechanism of GeTe phase-change thin films by scanning transmission electron microscopy. J Appl Phys 122(11):115304
9. Kooi B, Groot W, De Hosson JTM (2004) In situ transmission electron microscopy study of the crystallization of $Ge_2Sb_2Te_5$. J Appl Phys 95(3):924–932
10. Tripathi S, Kotula P, Singh MK, Ghosh C, Bakan G, Silva H, Carter CB (2020) Role of oxygen on chemical segregation in uncapped $Ge_2Sb_2Te_5$ thin films on silicon nitride. Ecs J Solid State Sc 9(5):054007
11. Wei XQ, Shi LP, Chong TC, Zhao R, Lee HK (2007) Thickness dependent nano-crystallization in $Ge_2Sb_2Te_5$ films and its effect on devices. Jpn J Appl Phys Part 1-Regular Papers Brief Commun Rev Papers 46(4b):2211–2214
12. Zhu Z, Liu FR, Yang JF, Fan ZK, Liu F, Sun NX (2016) A cross-sectional study on the crystallization of amorphous $Ge_2Sb_2Te_5$ films induced by a single-pulse ultraviolet laser. Opt Laser Technol 81:100–106

13. Chen B, ten Brink GH, Palasantzas G, Kooi BJ (2017) Crystallization kinetics of GeSbTe phase-change nanoparticles resolved by ultrafast calorimetry. J Phys Chem C 121(15):8569–8578
14. Shao R, Zheng K, Chen Y, Zhang B, Deng Q, Jiao L, Liao Z, Zhang Z, Zou J, Han X (2016) Direct observation of structural transitions in the phase change material $Ge_2Sb_2Te_5$. J Mater Chem C 4(39):9303–9309
15. Privitera S, Rimini E, Bongiorno C, Pirovano A, Bez R (2007) Effects of dopants on the amorphous-to-fcc transition in $Ge_2Sb_2Te_5$ thin films. Nucl Instrum Methods Phys Res, Sect B 257(1–2):352–354
16. Kooi BJ, Momand J (2019) High resolution imaging of chalcogenide superlattices for data storage applications: progress and prospects. Phys Status Solidi (RRL) 13(4):1800562
17. Song SA, Zhang W, Sik Jeong H, Kim JG, Kim YJ (2008) In situ dynamic HR-TEM and EELS study on phase transitions of $Ge_2Sb_2Te_5$ chalcogenides. Ultramicroscopy 108 (11):1408–1419
18. Laine B, Rivera-Rodrígues C, Morales-Sanchez E, Prokhorov E, Trapaga G, Gonzalez-Hernandez J (2004) Isothermal phase transformation kinetics in stoichiometric Ge–Sb–Te thin films. J Non-Cryst Solids 345:173–177
19. Naito M, Ishimaru M, Hirotsu Y, Takashima M (2004) Local structure analysis of Ge–Sb–Te phase change materials using high-resolution electron microscopy and nanobeam diffraction. J Appl Phys 95(12):8130–8135
20. Carter CB, Williams DB (2016) Transmission electron microscopy: diffraction, imaging, and spectrometry. Springer
21. Williams DB, Carter CB (2009) Transmission electron microscopy: a textbook for materials Sci. Springer
22. Jiang T-T, Wang X-D, Wang J-J, Zhou Y-X, Zhang D-L, Lu L, Jia C-L, Wuttig M, Mazzarello R, Zhang W (2020) In-situ study of vacancy disordering in crystalline phase-change materials under electron beam irradiation. Acta Mater 187:103–111
23. Tripathi S, Janish M, Dirisaglik F, Cywar A, Zhu Y, Jungjohann K, Silva H, Carter CB (2018) Phase-change materials; the challenges for TEM. Microsc Microanal 24(S1):1904–1905
24. Ghosh C, Singh M K, Watt J, Silva H, Carter C B (2020) Defect imaging and structure evolution in GST films during in-situ heating microscopy andmicroanalysis 26:1396–1398.
25. Singh M K, Ghosh C, Kotula P, Watt J, Silva H, Carter C B (2020) Direct observation of phase transformations in Ge-Sb-Te materials microscopy andmicroanalysis. 26:1418–1420.
26. Luo Y-R (2002) Handbook of bond dissociation energies in organic compounds. CRC Press
27. Akola J, Jones R (2008) Structural patterns in Ge/Sb/Te phase-change materials. NIC Series 39:169–176.
28. Rivera-Rodrıguez C, Prokhorov E, Trapaga G, Morales-Sanchez E, Hernandez-Landaverde M, Kovalenko Y, Gonzalez-Hernandez J (2004) Mechanism of crystallization of oxygen-doped amorphous $Ge_1Sb_2Te_4$ thin films. J Appl Phys 96(2):1040–1046

# Synergistic Effect of Cold Work and Annealing Temperature on Recrystallization and Texture of 18-Cr ODS


**Sumita Santra, S. V. Ramana Rao, and Komal Kapoor**

**Abstract** Synergistic effect of cold work and annealing temperature in recrystallization and texture was studied in an extruded and annealed 18-Cr oxide dispersion strengthened (ODS) steel bar. The study revealed that alpha and gamma fibre texture in deformed structure transforms to near Goss/Brass orientation at 1150 °C where substructure initiates. Misorientation between pre-existing matrix and nucleated grain orientation suggests texture transformation through high energy boundaries of high mobility with a misorientation range of 15–45°.

**Keywords** ODS · Texture · Recrystallization · Misorientation

## 1 Introduction

Oxide dispersion strengthened (ODS) steels are being proposed as candidate clad tube material in the future sodium-cooled fast reactor (SFRs). Typical fabrication process involves hot extrusion and multiple cold forming with intermediate heat treatments in order to reduce the anisotropy that is one of the major issues in the ODS fabrication which effects the service conditions [1]. These process parameters have substantial impact on alloy microstructure and texture. Study of the changes in microstructure and texture at each stage is essential to optimize the fabrication parameters to obtain the desired microstructure and texture. Several studies have been conducted, and reports are available on recrystallization behaviours of ferritic steels, like interstitial free (IF) steel [2–4] and silicon steel [5–8] for the immense industrial importance. Fewer works on recrystallization texture of cold-rolled ODS ferritic steels are available [9–12]. The present work focuses on studying the synergistic effect of cold work and temperature in texture evolution in 18-Cr ODS alloy.

S. Santra (✉) · S. V.R. Rao · K. Kapoor
Characterisation Lab, Quality Assurance, Nuclear Fuel Complex, Hyderabad 500 062, India



P. Ghosal et al. (eds.), *Applications of Microscopy in Materials and Life Sciences*,
Springer Proceedings in Materials 11,
https://doi.org/10.1007/978-981-16-2982-2_12

**Table 1** Chemical composition of the 18-Cr ODS alloy used in the present study

| Elemental composition (in Wt %) | | | | | | | | |
|---|---|---|---|---|---|---|---|---|
| Cr | Ti | W | Al | $Y_2O_3$ | O | C | N | Fe |
| 18 | 0.36 | 2.2 | 0.05 | 0.3 | 0.12 | 0.030 | 0.016 | Bal |

## 2 Experimental

18-Cr ODS steel bar after extrusion and annealing was sliced into sheets, and the sheets were subjected to cold rolling by 30, 40 and 50% (measured as a reduction in sheet thickness). Each sheet was further sliced into three pieces and annealed at 1050, 1150 and 1250 °C in vacuum for 30 min followed by furnace cooling (Table 1).

Electron backscattered diffraction technique (EBSD—make: Oxford Instruments, Nordlys Nano) was employed for orientation imaging microscopy (OIM). The samples were prepared through mechanical polishing followed by electropolishing in a solution of methanol, 2-butoxyethanol and perchloric acid in 7:2:1 ratio at 25 V, −35 °C.

## 3 Results

Figure 1a shows the OIM map of extruded and annealed bar of 18-Cr ODS alloy. Elongated grains were observed along the longitudinal direction with around 40% recrystallized fraction. Figure 1b shows the corresponding $\Phi_2 = 45°$ section of the orientation distribution function (ODF). In cubic materials, usually texture is described through $\Phi_2 = 0$ and 45° sections of ODF with ideal orientations as shown in Fig. 1c, d, respectively [13]. Same was used for the present study of texture in ODS. Complete alpha fibre texture was found ∼6.5 times random (tr). Only {111} <1−10> component of gamma fibre was present (6.9 tr).

OIM map of the 30% cold worked sheet after annealing at 1050 °C is shown in Fig. 2a. Fine deformed grains coexisted with some abnormally grown grain with 35% recrystallized. Figure 2b shows OIM map after annealing at 1150 °C, with 61% grains recrystallized and 16% in substructured form. Annealing at 1250 °C led to increase in recrystallized fraction and growth. Figure 2c shows the OIM map of the 50% cold worked and annealed sheet at 1050 °C with 35% recrystallization fraction. At 1150 °C, deformed fraction drastically reduced and recrystallized and substructured fraction was 85 and 9%, respectively (Fig. 2d). Annealing at 1250 °C increased recrystallized fraction of grains with growth. The recrystallization maps were generated from the OIM images through Channel-5 software. The critical misorientation of 1° and 7.5° was considered for subgrain and grain identification. Figure 3a shows the recrystallization map of 30% cold worked sample after

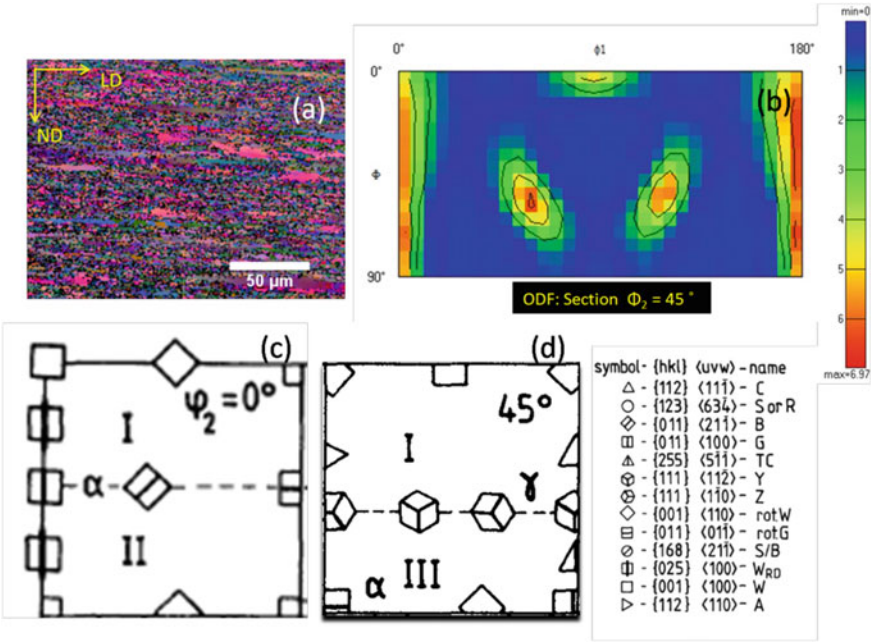


**Fig. 1** **a** OIM image of extruded and annealed 18-Cr ODS bar; **b** corresponding ODF; Orientation used for texture description in cubic materials plotted in **c** $\Phi_2 = 45°$ and **d** $\Phi_2 = 0°$ sections of the Euler space [13]

annealing at 1050 °C. The recrystallized, substructured and deformed parts are presented in blue, yellow and red colour, respectively. Figure 3b shows the recrystallization map of 30% cold worked sample after annealing at 1150 °C. Similarly, Fig. 3c, d shows the recrystallization map of 50% cold worked sample after annealing at 1050 °C and 1150 °C, respectively. The results obtained for 40% cold worked sheet with annealing were similar of course with varying amount of recrystallized grain fractions. The results related to recrystallization fraction study for all the samples are given in Table 2.

After 30% cold work, the complete alpha and gamma fibre was found but of less strength (Fig. 4a). $\Phi_2 = 45°$ and $\Phi_2 = 0°$ sections of ODF are presented for comparison and for studying the texture transition. After annealing at 1050 °C, partial alpha fibre {001} <110> to {111} <1−10> (max 6 tr) was observed (Fig. 4b). {111} <1−10> component of gamma fibre was also present (4tr). When annealed at 1150 °C, texture changed to Goss type (3 tr) as shown in Fig. 4c presenting $\Phi_2 = 0°$ and 45° of ODF. At 1250 °C, Brass component of texture was found with 7.6 tr strength (Fig. 4d).

After 40% cold work, complete alpha fibre was found but the components with orientation {001} <110> to {112} <110> became preferentially stronger 13 tr and gamma fibre component {111} <1−10> was present. At 1050 °C, alpha fibre

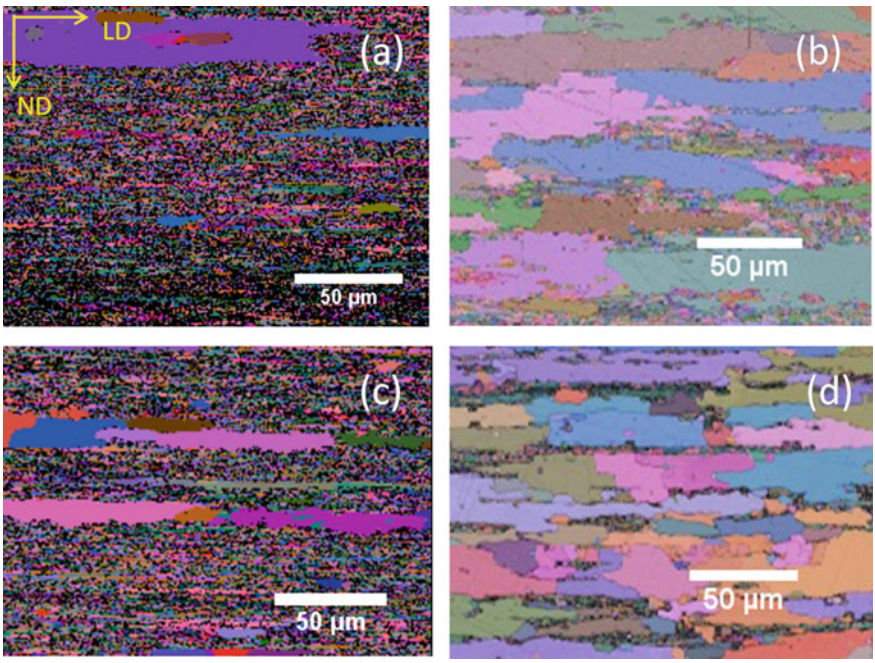


**Fig. 2** OIM image obtained from 30% cold worked 18-Cr ODS sheet annealed at **a** 1050 °C and **b** 1150 °C; from 50% cold worked 18-Cr ODS sheet annealed at **a** 1050 °C and **b** 1150 °C

became partial with strong {111} <1−10> component (12 tr) along with {111} <1 −10> component of gamma fibre (12.6 tr). At 1150 and 1250 °C, Goss and Brass components developed.

Figure 5a shows the $\Phi_2 = 0°$ and 45° section of ODF after 50% cold rolling. Partial alpha fibre formed (5 tr). Gamma fibre was complete with strong {111} <11 −2> (9 tr) component. Figure 5b shows the $\Phi_2 = 0°$ and 45° ODF section at 1050 ° C of 50% cold-rolled sample. Partial alpha fibre formed with strong (10 tr) orientation in between {112} <110> and {111} <1−10>. Gamma fibre was complete with strong {111} <1−10> component (7 tr). Figure 5c shows that Goss-type texture forms at 1150 °C (max. 9.6 tr). At 1250 °C, Goss texture intensity increased (11.4 tr) as can be seen from Fig. 5d.

## 4 Discussion

The extruded and annealed rod has dominant deformed structure with homogenous alpha fibre (6.9 tr) and {111} <1$\bar{1}$0> component of gamma. After 30% cold work, same exists. At 1050 °C, partial alpha ({001} <110> to {111} <1$\bar{1}$0>) was retained

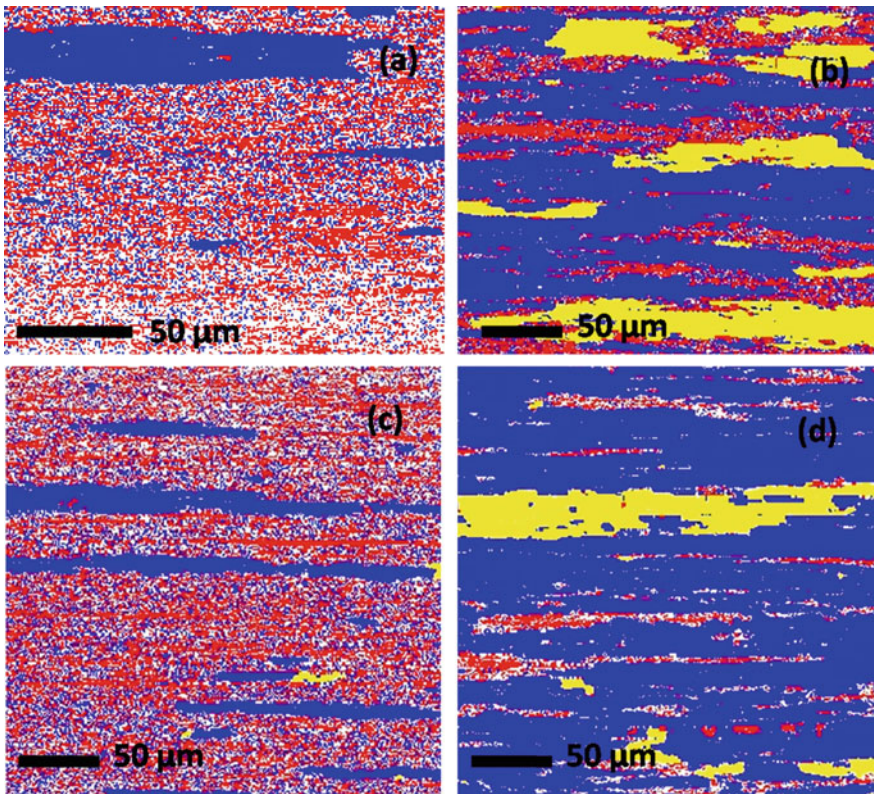


**Fig. 3** Recrystallization map of 30% cold worked 18-Cr ODS sheet annealed at **a** 1050 °C and **b** 1150 °C; from 50% cold worked 18-Cr ODS sheet annealed at **a** 1050 °C and **b** 1150 °C showing deformed structure in red, substructure in yellow and recrystallized part in blue

with increase in intensity. Weak Goss {101} <100> texture is formed at 1150 °C. At 1250 °C, Brass texture {011} <21$\bar{1}$> (7.6 tr) is developed. Correlation with Table 2 data suggests that deformed grains have alpha and gamma texture whereas substructure and recrystallization develops near Goss or Brass texture. To understand the process of texture transformation, misorientation angle between the growing grain and the major texture components of the consumed matrix was calculated. Table 3 shows that most of the transformations either perfectly or marginally (considering the deviation from ideal orientation in the practical ODS steel [14]) satisfies the criteria for high energy boundaries with high mobility having misorientation in the range of 15°–45° [15, 16]. Only misorientation between matrix {001} <110> to Goss is high 62.8°. But it is quite possible that matrix {001} <110> transformed to Brass grains at 1150 °C which were of much lesser intensity probably because of either small quantity or size.

**Table 2** Misorientation and recrystallization fraction obtained for different sample conditions

| Alloy | Condition | Fraction of grains with misorientation (0–15°) | Fraction (%) | | |
|---|---|---|---|---|---|
| | | | Deformed | Substructured | Recrystallized |
| 18-Cr ODS | As extruded | 42 | 60 | – | 40 |
| | 30% CW | 72 | 70 | – | 30 |
| | 40% CW | 68 | 85 | – | 15 |
| | 50% CW | 74 | 85 | – | 15 |
| | 30-1050 | 45 | 65 | – | 35 |
| | 30-1150 | 45 | 23 | 16 | 61 |
| | 30-1250 | 52 | 11 | 3 | 86 |
| | 40-1050 | 50 | 68 | – | 32 |
| | 40-1150 | 41 | 12 | 25 | 63 |
| | 40-1250 | 35 | 9 | 16 | 75 |
| | 50-1050 | 49 | 65 | – | 35 |
| | 50-1150 | 32 | 6 | 9 | 85 |
| | 50-1250 | 18 | 1 | 17 | 82 |

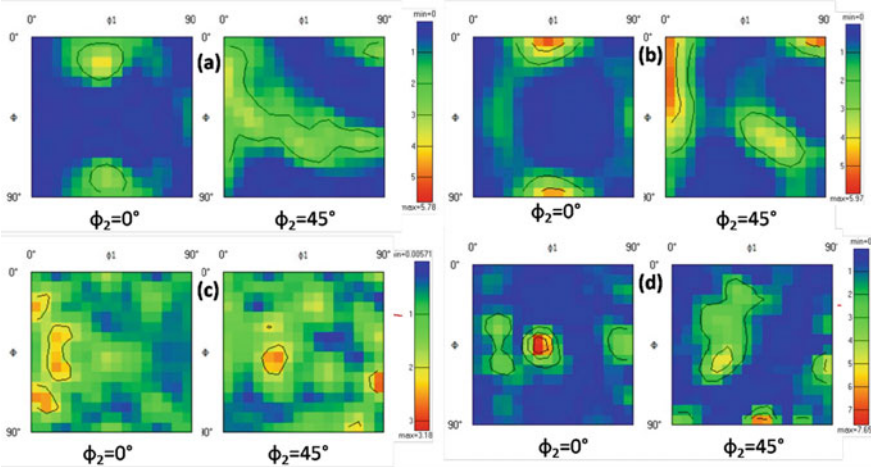


**Fig. 4** ODF $\Phi_2$ = 0° and 45° section of **a** 30% cold worked; annealed at **b** 1050 °C; **c** 1150 °C; **d** 1250 °C

Table 4 shows that matrix {112} <110> of 40% cold worked sample transformed into {111} <1$\bar{1}$0> energetically favoured through misorientation of 19.47° at 1050 °C. On the other hand, 54.74° misorientation inhibited transformation which is supported by the fact that he strength of the {001} <110> component

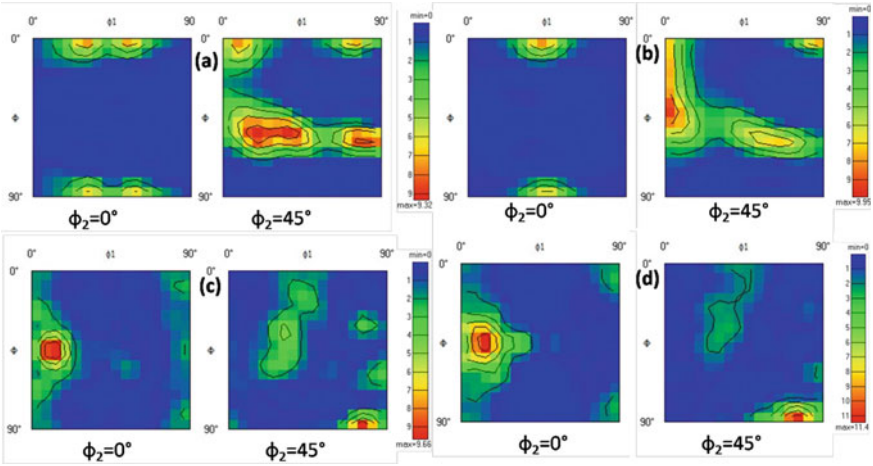


**Fig. 5** ODF $\Phi_2$ = 0° and 45° section of **a** 50% cold worked; annealed at **b** 1050 °C; **c** 1150 °C; **d** 1250 °C

**Table 3** Misorientation between nucleus and deformed grain of 30% CW and annealed samples

| Nucleus/growing grain | Deformed matrix | | |
|---|---|---|---|
| | {001} <110> | {112} <110> | {111} <1$\bar{1}$0> |
| {011} <21$\bar{1}$> (Brass) | 46° @[2 $\overline{24}$ $\bar{5}$] | 30° @[11 $\bar{1}$] | 35.6° @[16 1 $\overline{12}$] |
| {011} <100> (Goss) | 62.8° @[5 12 12] | 45.99° @[117 $\overline{10}$ 24] | 45.99° @[117 $\overline{10}$ 24] |

**Table 4** Misorientation between nucleus and deformed grain of 40% CW sample

| Temperature | Nucleus/growing grain | Deformed matrix | |
|---|---|---|---|
| | | {001} <110> | {112} <110> |
| 1050 °C | {111} <1$\bar{1}$0> | 54.74° @[$\bar{1}$ $\bar{1}$ 0] | 19.47° @[0 $\bar{1}$ 1] |
| 1150 and 1250 °C | {011} <21$\bar{1}$> (Brass) | 46° @[2 $\overline{24}$ $\bar{5}$] | 30° @[1 1 $\bar{1}$] |
| | {011} <100> (Goss) | 62.8 @ [5 12 12] | 45.99° @[117 $\overline{10}$ 24] |

before and after annealing remained same. Annealing at higher temperature, i.e. 1150 °C and 1250 °C produced near Goss/Brass texture. Brass nucleation from matrix {001} <110> is favourable through misorientation of 46° but nucleation of Goss grains overcoming 62.8° misorientation might have been possible through stored energy from increased amount cold work and higher temperature.

**Table 5** Misorientation between nucleus at 1050 °C and deformed grain of 50% CW sample

| Nucleus/growing grain | Deformed matrix |
|---|---|
| | {111} <11$\bar{2}$> |
| {111} <1$\bar{1}$0> | 30° @[1 1 $\bar{1}$] |
| {112} <110> | 35.64° @[66 88 $\bar{5}$] |

**Table 6** Misorientation between nucleus at higher temperature and deformed grain of 50% CW sample

| Nucleus/growing grain | Deformed matrix | | |
|---|---|---|---|
| | {001} < 110 > | {111} <1$\bar{1}$0> | {111} <11$\bar{2}$ > |
| {011} <100> (Goss) | 62.8° @[5 12 12] | 45.99° @[117 $\bar{1}$0 24] | 35.26° @[$\bar{1}$10] |

50% cold work produced {001} <110> and {111} <1$\bar{1}$0> component of alpha fibre and strong {111} <11$\bar{2}$> component of gamma. At 1050 °C, partial alpha from {001} <110> to {111} <1$\bar{1}$0> was developed with maximum in between {112} <110> and {111} <1$\bar{1}$0> via high mobility boundaries as shown in Table 5. Annealing at 1150 °C and 1250 °C transformed the texture to strong near-Goss orientation with much higher intensity (Table 6).

## 5 Conclusions

Deformed structure in 18-Cr ODS develops alpha and gamma fibre texture with excitation of different components with different amount of cold work. Substructure initiates at 1150 °C with texture transformation from alpha/gamma fibre to near Goss/Brass orientation. It is suspected that the texture transforms through high energy boundaries of high mobility associated with a misorientation range of 15–45°.

## References

1. Toualbi L, Cayron C, Olier P, Logé R, De Carlan Y (2013) Relationships between mechanical behavior and microstructural evolutions in Fe 9Cr-ODS during the fabrication route of SFR cladding tubes. J Nucl Mater 442(1–3):410–416
2. Jonas TU, Jonas JJ (1994) Modeling texture change during the recrystallization of an IF steel. ISIJ Int 34(5):435–442
3. Bocos JL, Novillo E, Petite MM, Iza-Mendia A, Gutierrez I (2003) Aspects of orientation-dependent grain growth in extra-low carbon and interstitial-free steels during continuous annealing. Metall Mater Trans A Phys Metall Mater Sci 34(3):827–839
4. Jonas JJ, Kestens L (1996) Modelling the effects of nucleation and growth on texture formation in commercial steels. Mater Sci Forum 204–206:155–168

5. Jirou B, Shimizu R (1988) Distribution of {110} 001 oriented grains in the primary recrystallized 3% Si–Fe Alloy CSL. Trans JIM 29(5):388–398
6. Ushigami Y, Kubota T, Takahashi N (1998) Mechanism of orientation selectivity of secondary recrystallization in Fe-3% Si alloy. ISIJ Int 38:553–558
7. Hayakawa Y, Szpunar JA (1997) A new model of Goss texture development during secondary recrystallization of electrical steel. Acta Mater 45:4713–4720
8. Hayakawa Y, Szpunar JA (1997) The role of grain boundary character distribution in secondary recrystallization of electrical steels. Acta Mater 45:1285–1295
9. Chou TS, Bhadeshia HKDH (1993) Crystallographic texture in mechanically alloyed oxide dispersion-strengthened MA956 and MA957 steels. Metall Trans A 24:773–779
10. Capdevila C, Chen YL, Lassen NCK, Jones AR, Bhadeshia HKDH (2001) Heterogeneous deformation and recrystallisation of iron base oxide dispersion strengthened PM2000 alloy. Mater Sci Technol 17:693–699
11. Okada H, Ukai S, Inoue M (1996) Effects of grain morphology and texture on high temperature deformation in oxide dispersion strengthened ferritic steels. J Nucl Sci Technol 33:936–943
12. Regle H, Alamo A (1993) Secondary recrystallization of oxide dispersion strengthened ferritic alloys. J Phys IV C7:727
13. Hirsch J, Lücke K (1988) Description and presentation methods for textures. Textures Microstruct 8:131–151
14. Leng B, Ukai S, Sugino Y, Tang Q, Narita T, Hayashi S, Wan F, Ohtsuka S, Kaito T (2011) Recrystallization texture of cold-rolled oxide dispersion strengthened ferritic steel. ISIJ Int 51:951–957
15. Titorov DB (1973) Orientational relationship between the textured matrix in the alloy Fe-3% Si, and grains growing into it. Phys Met Met 35:165–168
16. Titorov DB (1973) Prediction of recrystallization texture. Phys Met Met 36:82–87

# Nucleation of Precipitates on Multiple Habit Planes in an Artificially Aged AA2618 Alloy


**Rajdeep Sarkar, A. K. Mukhopadhyay, Partha Ghosal, Vipin S. Ramteke, and Deepak Kumar**

**Abstract** The aim of this investigation is to study precipitation behavior in an aluminum alloy AA2618, based on Al–Cu–Mg–Si–Ni–Fe system. The as-received extruded alloy was solution treated and independently aged at ambient temperature as well as aged for various times at 193 ± 1 °C, and at 275 ± 1 °C for 5 h. TEM revealed that the microstructure developed due to prolonged natural aging consisted of a fine distribution of Guinier–Preston–Bagaryatski (G-P-B) zones. During artificial aging, the sample aged for as low as 1 h revealed the presence of very fine precipitates on both $\{220\}_{Al}$ and $\{420\}_{Al}$ planes. With increasing artificial aging hours, widespread precipitation occurred on both $\{220\}_{Al}$ planes, and, of course, on $\{420\}_{Al}$ planes that are known to be due to the S′/S ($Al_2CuMg$) phase. The corresponding selected area diffraction patterns confirmed the presence of G-P-B zones and S phase in the microstructure. Preliminary high-resolution transmission electron microscopy (HRTEM) did confirm the presence of precipitates on $\{220\}_{Al}$ planes in the artificially aged samples of AA2618.

**Keywords** Aluminum alloy AA2618 · Natural and artificial aging · Precipitates · Multiple habit planes · Transmission electron microscopy (TEM) · High-resolution transmission electron microscopy (HRTEM)

## 1 Introduction

The precipitation behavior during aging of 2xxx series Al–Cu–Mg alloys of commercial interest, wherein the alloy composition lies in the α(Al) + S($Al_2CuMg$)-phase field in Al–Cu–Mg phase diagram [1], is commonly described as: supersaturated solid solution ($\alpha_{SS}$) → G-P(Cu, Mg) zones, i.e., G-P-B zones → S′($Al_2CuMg$) → S($Al_2CuMg$) [2]. Silcock [3] pointed out that the distinction between S′ and S is very slight and somewhat arbitrary. In this communication, no distinction will, therefore, be made between S′ and S. Wilson and

R. Sarkar · A. K. Mukhopadhyay (✉) · P. Ghosal · V. S. Ramteke · D. Kumar
Defence Metallurgical Research Laboratory, Kanchanbagh, Hyderabad 500 058, India



P. Ghosal et al. (eds.), *Applications of Microscopy in Materials and Life Sciences*, Springer Proceedings in Materials 11,
https://doi.org/10.1007/978-981-16-2982-2_13

Partridge [4], using an Al—2.5 wt% Cu—1.2 wt% Mg alloy aged at 190 °C, observed that small rod-shaped S precipitates initially nucleated on dislocation loops and helices formed during quenching. As aging progressed, the rods grew in the $<100>_{Al}$ directions and widened to form laths lying on $\{420\}_{Al}$ [4].

The G-P-B zones consisting of "groups of Mg and Cu atoms" are cylindrical and form as rods along $<100>_{Al}$ directions [2]. The G-P-B zones are typically identified by the presence of diffuse streaks (superimposed on diffuse G-P-B spots) along $<100>_{Al}$ directions through the forbidden $\{110\}_{Al}$ reflections [5, 6] in selected area electron diffraction patterns. A recent work by the present authors [7] did establish the formation of precipitates on $\{220\}_{Al}$ planes in over aged AA2618 and AA8090 alloys [7], wherein (i.e., under such aging conditions), the S phase is known to be present as the prime rather the only strengthening precipitate in constituent ternary Al–Cu–Mg system [8]. However, our previous studies [7] did not verify whether the precipitation on $\{220\}_{Al}$ planes could also occur early in the artificial aging cycle coincident with the presence of G-P-B zones as the major precipitate in the microstructure. It is the purpose of the present work, using transmission electron microscopy, to examine the formation of precipitates on $\{220\}_{Al}$ in addition to S phase known to be forming on $\{420\}_{Al}$ in an artificially aged AA2618 aluminum alloy.

## 2 Experimental Procedure

The AA2618 alloy was supplied by Century Extrusions Limited (CEL), Kharagpur [7] in the form of extrusions. The composition (wt%) of the alloy is: 2.4% Cu, 1.4% Mg, 0.19% Si, 0.96% Fe, 1.0% Ni, 0.04% Ti, and balance Al. The artificial aging treatment consisted of heating the material to the solutionizing temperature of 530 °C for 2 h, quenching in water at ambient temperature followed by aging at 193 °C for 1 to 20 h, and at 275 °C for 5 h. The 275 °C sample was examined because, under this aging condition, the microstructure consists only of S phase. Following solution treatment, the alloy was further natural aged for times up to 8 weeks to detect and study the formation of G-P-B zones.

The TEM, using a 200 kV Tecnai 20 T $G^2$ (FEI make) microscope, was used to characterize the phases present in naturally aged and artificially aged microstructure. Samples for TEM studies were prepared using standard metallographic techniques [7]. Preliminary HRTEM studies were carried out on the artificially aged samples of the alloy, using a Themis Z TEM (FEI make) at 300 kV. Plasma cleaning of the TEM foils was carried out 2 min before the HRTEM experimentation. Vickers hardness measurements, using a 10 kg load, were taken following various stages of natural and artificial aging to monitor the progress of precipitation hardening in the AA2618 alloy.

## 3 Results and Discussion

A transmission electron micrograph obtained from the as-quenched alloy using a two-beam orientation near $<100>_{Al}$ zone is shown in Fig. 1a. The as-quenched materials were, however, unavoidably naturally aged for about 2 h before the specimens for TEM could be prepared and examined. Figure 1b represents a selected area electron diffraction pattern (SAEDP), obtained from the same region of the TEM thin foil as that of Fig. 1a but the electron beam is now approximately parallel to $<001>_{Al}$. Bright field image obtained from the naturally aged alloy (for 8 weeks) using a two-beam orientation ($g_{200}$) near $<001>_{Al}$ zone is shown in Fig. 1c.

Figure 1d represents an SAEDP, obtained from the same region of the thin foil as that of Fig. 1c but the electron beam is now approximately parallel to $<001>_{Al}$. The noticeable features of Fig. 1a, c are the absence of dislocation loops. This is known to be due to both Si and Mg having a strong affinity to bind vacancies in Al

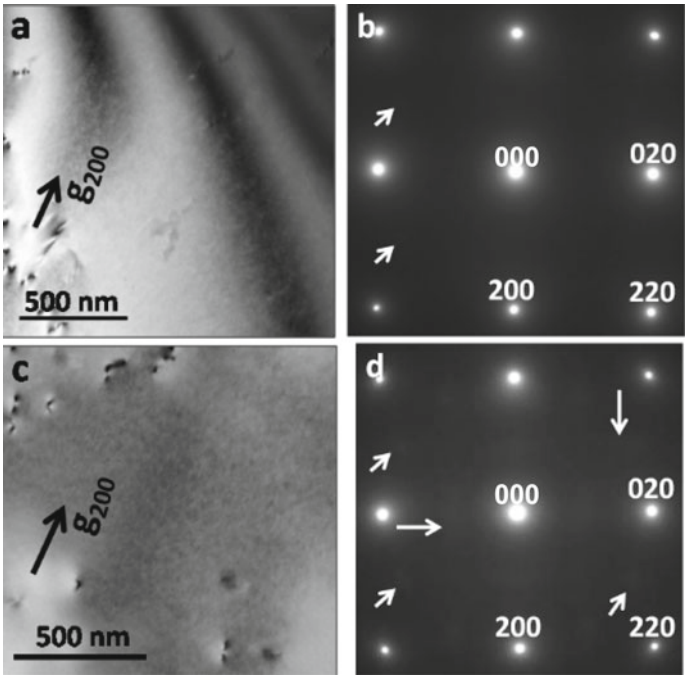


**Fig. 1** **a** Transmission electron micrograph obtained from the alloy when naturally aged for 2 h: the two-beam orientation ($g_{200}$) was obtained near $<001>_{Al}$ zone, **b** SAEDP corresponding to the same region of the thin foil as that of (**a**) but the electron beam is approximately parallel to $<001>_{Al}$ **c** Transmission electron micrograph obtained from the alloy when naturally aged for 8 weeks; the two-beam orientation ($g_{200}$) was obtained near $<001>_{Al}$ zone, and **d** SAEDP corresponding to the same region of the thin foil as that of (**c**), when the electron beam is approximately parallel to $<001>_{Al}$

[9]. Both the micrographs, on the other hand, contain a few dislocations in the matrix. The microstructure, naturally aged for 2 h, further showed the presence of fewer fine precipitates that could be viewed with a better visibility within or in proximity to the thickness fringes, as shown in Fig. 1a. Such fine precipitates were detected relatively more in numbers in the alloy naturally aged for 8 weeks, as shown in Fig. 1c.

The SAEDP presented in Fig. 1b shows the presence of very faint, diffuse spots (a couple marked by short arrows) in locations that are known to be occupied by the G-P-B zones [5–7]. On the other hand, in Fig. 1d, the characteristic continuous, diffuse streaks (marked by *long arrows*) through the forbidden $\{110\}_{Al}$ locations are further present along with the diffuse spots (marked by short arrows) due to G-P-B zones [5–7]. From the as-quenched hardness value of 69 VHN, the hardness of the alloy also increased to 105 VHN following 8 weeks of natural aging. This shows that the G-P-B zones continually developed during natural aging and the formation of such G-P-B zones is associated with appreciable hardening of the alloy. In

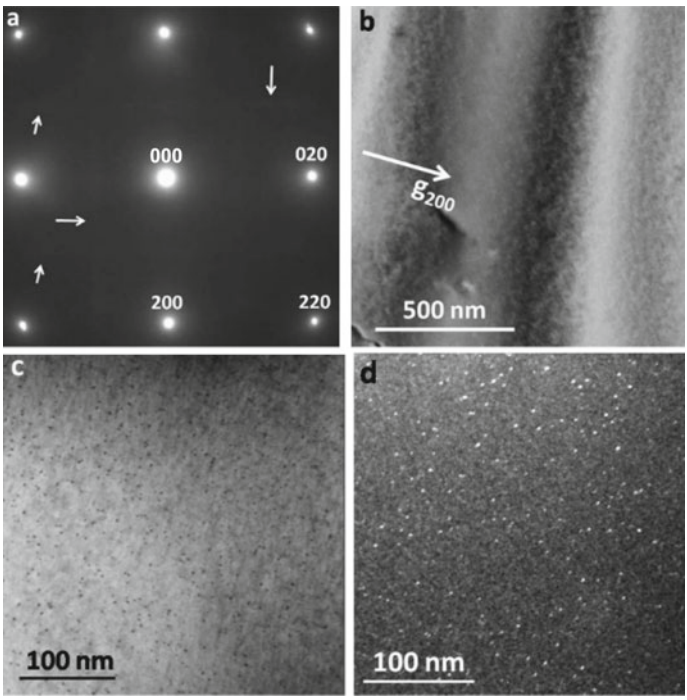


**Fig. 2** **a** SAEDP obtained from the alloy when artificially aged for 1 h; the electron beam is approximately parallel to $<001>_{Al}$, **b** transmission electron micrograph obtained from the alloy when artificially aged for 1 h; the two-beam orientation was obtained near $<001>_{Al}$ zone, **c** transmission electron micrograph obtained from the region from where the SAEDP in **a** was obtained, **d** dark field image obtained using the cross-streak region, i.e., the position of the forbidden $\{110\}_{Al}$ reflection [refer to (**a**)]

Si-bearing Al–Cu–Mg alloys, the G-P-B zones contain Si [10], and Si additions cause a refinement of the S phase morphology during artificial aging [4, 10].

TEM results for the alloy artificially aged at 190 °C for 1 h are shown in Fig. 2. The characteristic *continuous* diffuse streaks in the SAEDP (shown by long arrows in Fig. 2a) along $<100>_{Al}$ directions *through* the forbidden $\{110\}_{Al}$ reflections together with the characteristic diffuse spots (a couple shown by short arrows)due to the G-P-B zones could now be observed with more clarity. Figure 2b, c represents transmission electron micrographs obtained using two-beam orientation (i.e. $g_{200}$ near $<001>_{Al}$ zone) and near on-zone (i.e., when the electron beam is approximately parallel to $<001>_{Al}$) conditions, respectively. A dark field image obtained using the cross-streak region (i.e., the forbidden $\{110\}_{Al}$ reflection position) illuminating the aging products is shown in Fig. 2d. Transmission electron micrographs in Fig. 3a, b are showing the presence of fine precipitates on both $\{220\}_{Al}$ and $\{420\}_{Al}$ planes in the alloy when artificially aged for 1 h and 3 h, respectively. It follows that these rod-like precipitates grow along $<100>_{Al}$ directions and, as a result, they are viewed end-on when imaged with the electron beam being approximately parallel to $<001>_{Al}$. It is, therefore, safe to conclude that either the entire aging product or a majority of the aging product observed in the 1 h sample (refer to Figs. 2d and 3a) must represent the G-P-B zones. *It further follows that the G-P-B zones in this alloy system either form only on* $\{220\}_{Al}$ *planes or on both* $\{220\}_{Al}$ *and* $\{420\}_{Al}$ *planes.* The present results are not adequate to distinguish between these possibilities.

The streaks were subsequently developed along $<220>_{Al}$ and $<042>_{Al}$ directions [refer to Fig. 4] with artificial aging hours reaching 10 h and more. Figure 4a, c and b, d represents SAEDPs obtained from the alloy when the electron beam is

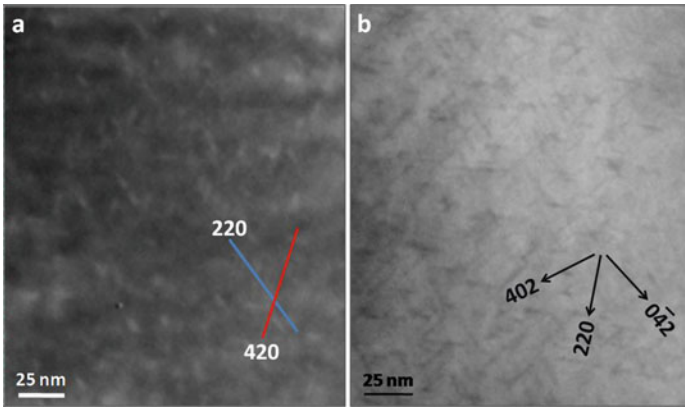


**Fig. 3** **a** Transmission electron micrographs [imaged in $<112>_{Al}$ orientation] obtained from the alloy when artificially aged for (a) 1 h and (b) 3 h, respectively. Note the nucleation of fine precipitates on $\{220\}_{Al}$ and $\{420\}_{Al}$ planes, and an increase in the number density and size of such precipitates with increasing aging hours. The $\{220\}_{Al}$ and $\{420\}_{Al}$ planes are indicated in (**a**) while, the directions are shown in (**b**)

approximately parallel to $<111>_{Al}$ and $<112>_{Al}$, respectively. Figure 4a, b and c, d corresponds to the alloy when artificially aged for 10 h and 20 h, respectively. The most noticeable features of these SAEDPs are the presence of streaks along $<042>_{Al}$ directions (marked by short arrows) as well as $<220>_{Al}$ directions (marked by long arrows). These diffraction features suggest the presence of fine precipitates on $\{420\}_{Al}$ and $\{220\}_{Al}$ planes. It may be noted that the alloy attained a peak hardness value of 134 VHN after aging for 16 h, and the hardness value decreased to 122 VHN following aging for 20 h.

Bright field images, corresponding to the SAEDPs in Fig. 4c, d, are shown in Fig. 5a, b, wherein the electron beam is approximately parallel to $<111>_{Al}$ and $<112>_{Al}$, respectively. In Fig. 5a, b, the formation of precipitates parallel to $\{220\}_{Al}$ planes [Fig. 5a] and $\{420\}_{Al}$ and $\{220\}_{Al}$ planes [Fig. 5b], respectively,

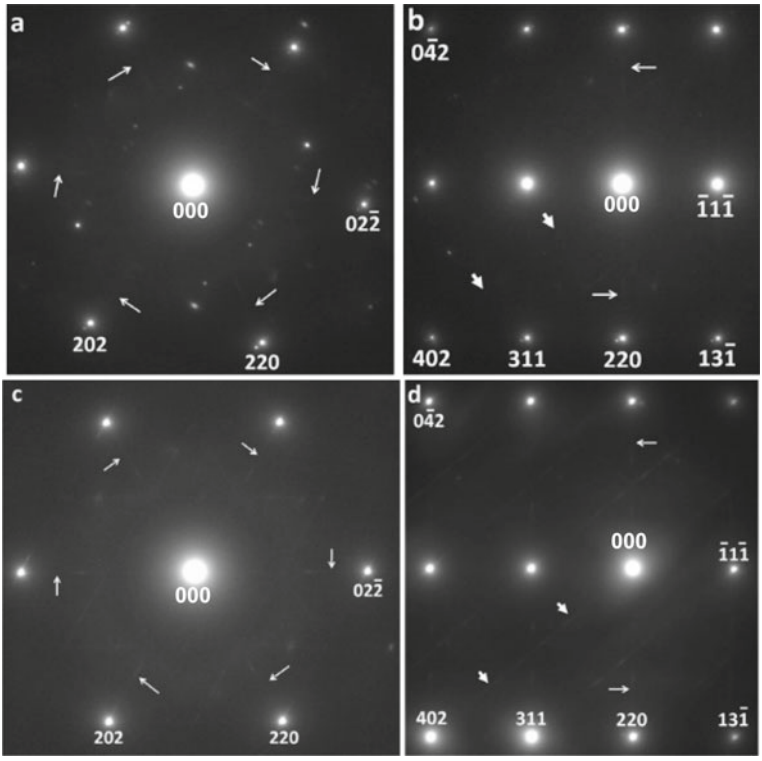


**Fig. 4** **a** and **b** SAEDPs, when the electron beam is approximately parallel to $<111>_{Al}$ and $<112>_{Al}$, respectively, obtained from the alloy when artificially aged for 10 h. **c** and **d** SAEDPs, when the electron beam is approximately parallel to $<111>_{Al}$ and $<112>_{Al}$, respectively, obtained from the alloy when artificially aged for 20 h. In Fig. 4a, c, the arrows show streaks along $<220>_{Al}$ directions. In Fig. 4b, d, the short arrows show the streaks along $<042>_{Al}$ directions and the long arrows show streaks along $<220>_{Al}$ directions. The streaks in Fig. 4 suggest the formation of fine precipitates on $\{420\}_{Al}$ and $\{220\}_{Al}$ planes

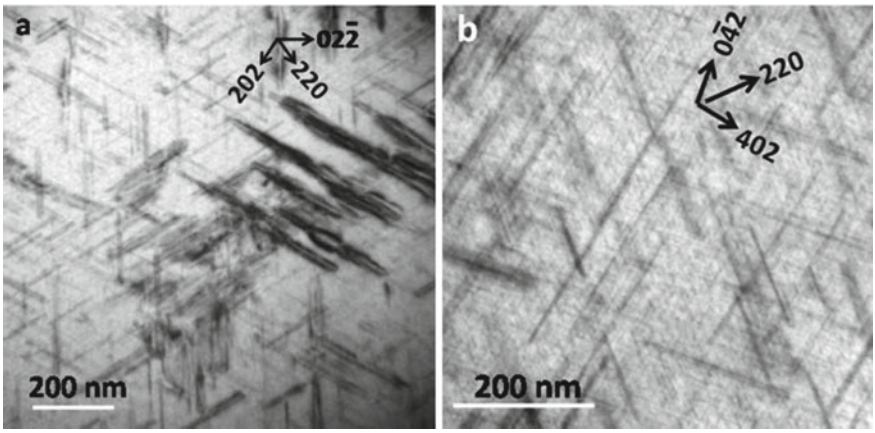


**Fig. 5** **a** and **b** Transmission electron micrographs obtained from the alloy when artificially aged for 20 h. The electron beam is approximately parallel to (a) $<111>_{Al}$ and (b) $<112>_{Al}$, respectively

may be observed. TEM image in Fig. 6a [imaged in $<112>_{Al}$ orientation] is showing a region of the thin foil from where Fig. 5b was obtained. Figure 4d represents the corresponding SAEDP. Figure 6b represents a two-beam ($g_{220}$) electron diffraction pattern corresponding to the transmission electron micrograph shown in Fig. 6c. Figure 6d represents a dark field image obtained using the streak located at 2/3 $<220>_{Al}$ position [marked by an arrow in Fig. 6b]. Consideration of Figs. 5 and 6 does indeed demonstrate the formation of precipitates parallel to $\{220\}_{Al}$ planes in the alloy.

Bright field image (in $<112>_{Al}$ orientation) of the alloy, artificially aged for 5 h at 275 °C, is shown in Fig. 7a. The figure shows presence of coarse precipitates on $\{220\}_{Al}$ and $\{420\}_{Al}$ planes in the alloy (having a hardness value of 97 VHN). The corresponding SAEDP of Fig. 7a is shown in Fig. 7b. These results indicate that the phase precipitates forming on $\{220\}_{Al}$ planes co-exist together with the S phase known to be forming on $\{420\}_{Al}$ planes.

Figure 8 represents a high-resolution transmission electron micrograph in <001> Al orientation showing the nucleation of precipitates along $\{220\}_{Al}$ and $\{420\}_{Al}$ planes in the alloy aged for 20 h at 190 °C.The present results and interpretations demonstrate that during artificial aging of the alloy AA2618, the nucleation of precipitates occurs parallel to $\{220\}_{Al}$ planes apart from the known habit planes of $\{420\}_{Al}$ due to S phase. Such a trend is observed very early in the aging cycle when the microstructure is known to be consisting of G-P-B zones, as well as in over aged conditions when only S phase is known to dominate the microstructure in Al–Cu–Mg–Si alloys having similar Si content [10]. Preliminary HRTEM studies carried out on slightly over aged AA2618 alloy do show the nucleation of precipitates on $\{220\}_{Al}$ planes. Further, HRTEM studies involving different stages of artificial aging of the alloy are planned to conclusively know the details of the precipitates forming on $\{220\}_{Al}$ planes.

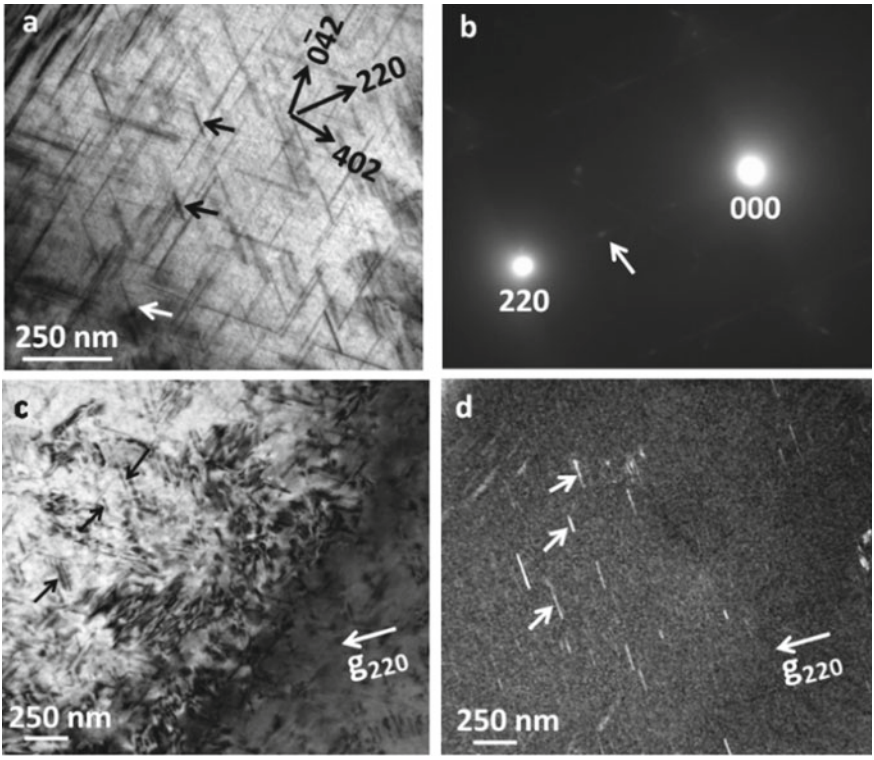


**Fig. 6** **a** Transmission electron micrograph [imaged in <112>$_{Al}$ orientation] representing a wider and an enlarged view of the region of the thin foil from where Fig. 5b was obtained. Figure 4d represents the corresponding SAEDP. **b**, **c** represent a two-beam ($g_{220}$) electron diffraction pattern and the corresponding micrograph, respectively. **d** represents a dark field image obtained using the streak located at 2/3 <220>$_{Al}$ position [marked by an arrow in (**b**)]. Consideration of Fig. 5 and this figure does indeed demonstrate the formation of precipitates parallel to {220}$_{Al}$ planes in the alloy

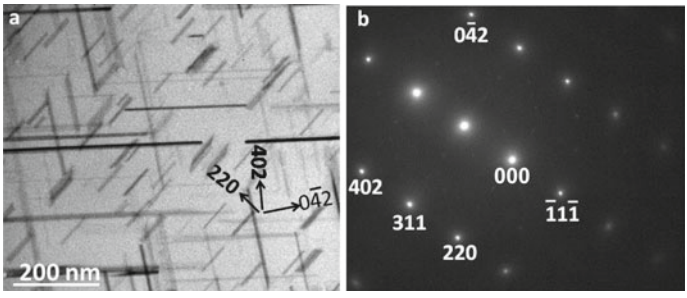


**Fig. 7** **a** Transmission electron micrograph [in <112>$_{Al}$ orientation] showing the presence of coarse precipitates on {220}$_{Al}$ and {420}$_{Al}$ planes in the alloy when artificially aged for 5 h at 275 °C; the corresponding SAEDP is shown in (**b**)

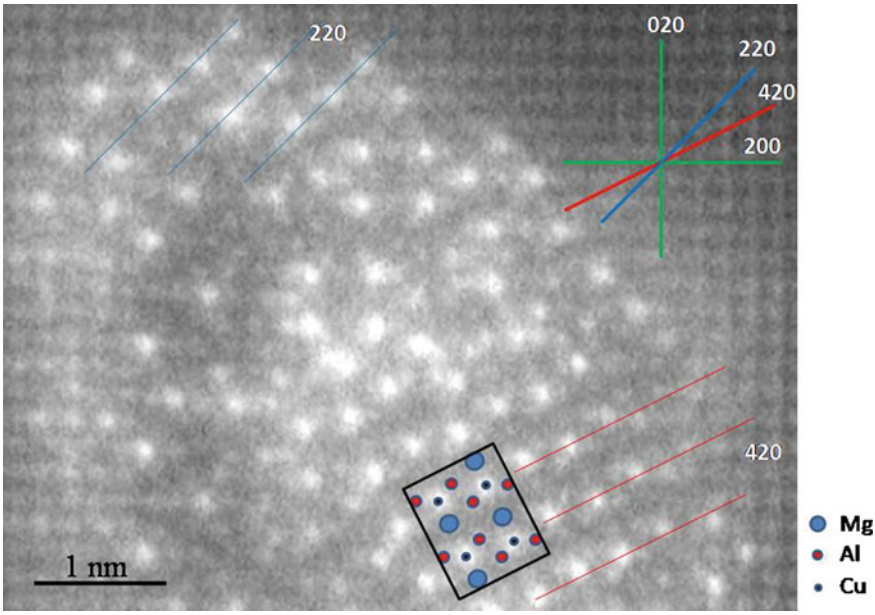


**Fig. 8** High-resolution transmission electron micrograph (imaged in $<001>_{Al}$ orientation) showing the formation of precipitates on $\{220\}_{Al}$ and $\{420\}_{Al}$ planes in the alloy when artificially aged at 190 °C for 20 h

## 4 Conclusions

1. In an AA2618 alloy, the G-P-B zones form during natural aging and it causes considerable hardening of the alloy.
2. Following 1 h of aging at 190 °C, the nucleation of very fine precipitates is detected on both $\{220\}_{Al}$ and $\{420\}_{Al}$ planes. The number density and the size of such precipitates grow with aging times. The precipitation continues to occur on both the habit planes, albeit with coarser morphology, even following over aging at 275 °C.

**Acknowledgements** The authors wish to acknowledge the financial support of Defence Research and Development Organization (DRDO), Government of India. One of the authors (AKM) is now with Hindalco Innovation Centre, Hindalco Industries Limited, Navi Mumbai. The HRTEM work carried out at the Thermo Fisher Scientific Centre at Eindhoven, the Netherlands is gratefully acknowledged.

## References

1. Silcock JM, Parsons BA (1958) The structural aging characteristics of some ternary Al–Cu–Mg alloys. Fulmer Research Institute Report No. R10/67, United Kingdom

2. Hatch JE (1984) Aluminium: properties and physical metallurgy. Am Soc Metals:144
3. Silcock JM (1961) The structural aging characteristics of Al–Cu–Mg alloys with copper: magnesium weight ratios of 7:1 and 2.2:1. J Inst Metals 89:203
4. Wilson RN, Partridge PG (1965) The nucleation and growth of S' precipitates in an Aluminium-2.5% Copper-1.2% Magnesium Alloy. Acta Metall 13:1321
5. Mukhopadhyay AK (2002) Co-precipitation of Ω and σ phases in Al–Cu–Mg–Mn alloys containing Ag and Si. Metall Mater Trans A 33:3635
6. Mukhopadhyay AK, Eggeler G, Skrotzki B (2001) Nucleation of Ω phase in an Al–Cu–Mg–Mn–Ag alloy aged at temperatures below 200 °C. Scripta Mater 44:545
7. Mukhopadhyay AK, Sarkar R, Kumar D, Ghosal P (2019) On the phases present in artificially aged AA2618 extrusions. Mater Perform Charact 8:946
8. Wang SC, Starink MJ, Gao N (2006) Precipitation hardening in Al–Cu–Mg alloys revisited. Scripta Mater 54:287
9. Takamura J, Koike M, Furukawa K (1978) The vacancy-solute interaction in aluminium. J Nucl Mater 69, 70:738
10. Hutchinson CR, Ringer SP (2000) "Precipitation processes in Al–Cu–Mg alloys micro-alloyed with Si." Metall Mater Trans A 31:2721

# Hot Deformation Behavior of $\gamma$-TiAl-Based Ti–45Al–8Nb–6Cr–0.2B Alloy in the $\gamma + \beta$ Phase Field


**Vajinder Singh, Chandan Mondal, Aditya R. Sharma, Atul Kumar, P. P. Bhattacharjee, and Partha Ghosal**

**Abstract** The hot deformation behavior of a cast Ti–45Al–8Nb–6Cr–0.2B (at.%) alloy has been investigated in the temperature and strain rate range of 1000–1200 °C and 0.5–0.005 $s^{-1}$, respectively, using a Gleeble thermo-mechanical simulator. The as-cast pancake shows a coarse distribution of $\gamma$-TiAl laths with irregular $\beta$(B2)-phase structure (average volume fraction: $\gamma = 0.75$ and $\beta = 0.23$). Characteristics of hot deformation have been evaluated through the correlation between Arrhenius type constitutive models, processing maps, and microstructural evolution. The apparent activation energy, measured through the hyperbolic-sinusoidal relationship between flow stress, temperature, and strain rate, has been found to be 282.90 kJ/mol. The significantly low activation energy is attributed to the absence of lamellar microstructure and high volume fraction of $\beta$(B2)-phase which aids deformation at higher temperatures. Microstructural evolution of the deformed samples indicates that the flow softening corresponds to the dynamic recrystallization (DRX). DRX has been found to occur preferentially in the coarse lath boundary of the TiAl phase and also within elongated $\beta$(B2)-grains. It has been shown that extensive DRX as a result of morphological characteristics of $\gamma$-phase together with a high volume fraction of $\beta$-phase facilitates high hot workability of the present alloy.

**Keywords** TiAl-based alloy · Hot compression · Process maps · Microstructure · EBSD

V. Singh · C. Mondal (✉) · A. R. Sharma · A. Kumar · P. Ghosal
Defence Metallurgical Research Laboratory (DMRL),
Kanchanbagh, Hyderabad 500058, India
e-mail: c_mondal@dmrl.drdo.in

P. P. Bhattacharjee
Department of Materials Science and Metallurgical Engineering, Indian Institute of Technology, Kandi, Hyderabad 502285, India



P. Ghosal et al. (eds.), *Applications of Microscopy in Materials and Life Sciences*,
Springer Proceedings in Materials 11,
https://doi.org/10.1007/978-981-16-2982-2_14

## 1 Introduction

Gamma TiAl-based alloys are an emerging class of materials for high-temperature aerospace applications due to their high specific strength, oxidation resistance (800–900 °C), and excellent structural stability. Applications of γ-TiAl-based alloys are now realized in the manufacturing of gas turbine components such as disks, blades, valves, and spacer rings [1] as well as automobile engine parts such as cast turbocharger rotors and valves [2, 3]. However, one of the major obstacles in these γ-TiAl alloys which limit their applications is the poor workability at industrially acceptable high temperatures [4, 5].

In recent years, significant advancements have been made to enhance the hot processing capability through the development of the so-called β-solidifying TiAl alloys [6]. Solidification of TiAl alloys through β-Ti phase field containing high Nb and other β-stabilizers (e.g., Mo, W, Cr, Mn, Ta) results in not only retained β-phase which improves hot formability but also more chemical uniformity and reduced dendrite segregation [5]. However, the beneficial effects of retained β-phase on the hot workability come at the expense of high-temperature creep resistance. Hence, the optimization of β(B2) phase fraction with respect to acceptable levels of creep resistance and hot workability is essential. The addition of Cr to the high Nb-containing γ-TiAl-based alloys has recently been explored [7]. Cr decreases the α-transus (∼15 °C per at.%) in Ti-48Al-based alloys. It not only widens the α-phase field toward higher Al content but also tends to lower the γ solvus [8]**.** Further, an increase in Cr addition lowers the volume fraction of the transformed $\alpha_2$ phase by stabilizing the α-phase at high temperatures and promotes the formation of thermal twins in the γ-phase [8]. These factors together with the weakening of Ti–Al bond covalency in Cr alloyed TiAl-based alloys lead to the enhancement in ductility due to Cr in duplex alloys [8]. Although Cr addition (∼2 at.%) to high Nb-containing TiAl alloys has shown improvement in hot deformability [7], it will be interesting to examine whether workability further improves with higher levels of Cr additions.

In the present study, the hot workability of a Ti–45Al–8Nb–6Cr–0.2B alloy having a significant amount of retained β-phase in the as-cast condition has been explored.

## 2 Experimental Procedure

The experimental alloy having a nominal composition of Ti–45Al–8Nb–6Cr–0.2B (at.%) was melted in a vacuum arc melting furnace using a non-consumable tungsten electrode in the form of pancake ($\phi$100 mm × 15 mm; 450 g). The pancake was re-melted six times by flipping over to ensure chemical homogeneity. The analyzed alloy chemistry of the pancake was found to be in good agreement with the desired nominal composition. Hot compression tests were carried out using

Gleeble-3800 thermo-simulator at the temperature range of 1000–1200 °C and strain rates in the range of 0.5–0.005 $s^{-1}$ followed by forced air quenching. Cylindrical specimens ($\phi$8 mm × 12 mm) machined from the pancake were used and specimen surfaces were polished, and parallelism of top and bottom ends was ensured. The true stress-true strain curves have been calculated from the load-extension data using a standard module available in Gleeble data processing software. The microstructure evaluation was carried out in the cast condition and also after hot compression by scanning electron microscopy (SEM), X-ray diffraction analysis (XRD), and electron backscatter diffraction (EBSD). For the EBSD study, after standard metallographic polishing, the final polishing was carried out in Buehler vibratory polisher (Vibromet 2) for 8–12 h using non-crystallize colloidal silica (0.05 µm) in dilute solution. The EBSD scans had been performed using Zeiss FEG-SEM (model: Supra55) with the attached *Oxford Nordlys* EBSD detector. Data analysis had been carried out in TSL 8.0 software. The raw data were cleaned using a pseudo-symmetry module in TSL software to remove the pseudo-twins of 60° <−11−1>, 90° <010>, and 70° <1−10> [9]. This is essential as the pseudo-symmetry-related indexing problem in $\gamma$-TiAl arises due to its close tetragonal **c**:**a** ratio of 1.018. X-ray diffraction (XRD) studies were carried out using a PHILIPS PW 1710 automatic diffractometer.

## 3 Results and Discussion

### *3.1 Initial Microstructure*

Characterization of the initial microstructure from the mid-region of the pancake in the as-cast condition is shown in Fig. 1. Figure 1a represents a low magnification BSE image showing acicular laths of $\gamma$-TiAl phase (dark contrast) with a network of the remnant $\beta$(B2)-phase (bright contrast). Laths of $\gamma$-TiAl have both fine and

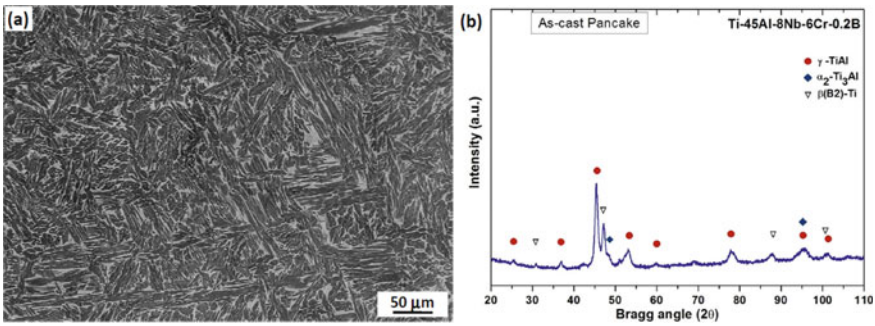


**Fig. 1** **a** Back-scattered SEM image showing microstructural development in the as-cast condition. **b** A representative XRD pattern of the as-cast alloy

coarse morphology and are found to originate from prior $\beta$ grain boundaries. Quantitative phase estimation has been carried out by EBSD phase analysis and the average volume fraction of $\gamma$, and $\beta$-phases are 76%, and 23%, respectively. In addition, a very small amount of long needle-shaped TiB phase has been identified (mostly found at colony boundaries visible only at higher magnifications). The presence of constituent phases is further established by X-ray diffraction study as shown in Fig. 1b. The as-solidified microstructure corresponds to the $\beta + \gamma$ phase field in a highly $\beta$-stabilized TiAl-based alloy [10]. It is to be noted that the microstructure of the present alloy is substantially different from the typical lamellar colony structure comprising of ($\alpha_2 + \gamma$)-phases.

## 3.2 Hot Deformation Flow Behavior

The high-temperature flow behavior of the alloy has been studied by the hot compression tests in the temperature range of 1000–1200 °C and strain rate range of 0.5–0.005 $s^{-1}$. The true stress-true strain curves obtained through hot compression tests up to 50% reduction in heights are shown in Fig. 2. As observed by previous studies [7, 11], both temperature and strain rate significantly affect the flow stress of the material. At lower temperature and higher strain rates, the flow curves are characterized by the initial rapid work hardening stage, followed by dynamic softening stage and steady-state regime at higher strains. On the other hand, at higher temperatures and slower strain rates, the flow curves are increasingly dominated by the steady-state (flow stress saturation). The shape of the flow curves is a typical characteristic of the hot deformation dominated by the dynamic recrystallization processes. The flow behavior of the alloy is representative of a low stacking fault energy (SFE) material [5, 12].

During hot deformation, the combined effect of temperature and strain rate on flow behavior can be expressed in terms of the Zener–Hollomon parameter (Z) [13]. Sellars and McTegart [14] first proposed a constitutive equation that relates the flow stress and the deformation parameters. The equation has been shown to yield satisfactory results even for $\gamma$-TiAl alloys [7]. It considers the flow behavior of materials during deformation as a thermally activated process and is expressed as

$$Z = \dot{\varepsilon} \exp\left(\frac{Q}{RT}\right) = A[\sinh(\alpha\sigma)]^n \tag{1}$$

where $A$, $n$, and $\alpha$ are material constants and $Z$, $\dot{\varepsilon}$, $\sigma$, $Q$, $R$, $T$ have their usual meaning. The apparent activation energy ($Q$) can be calculated by partial differentiation of Eq. (1).

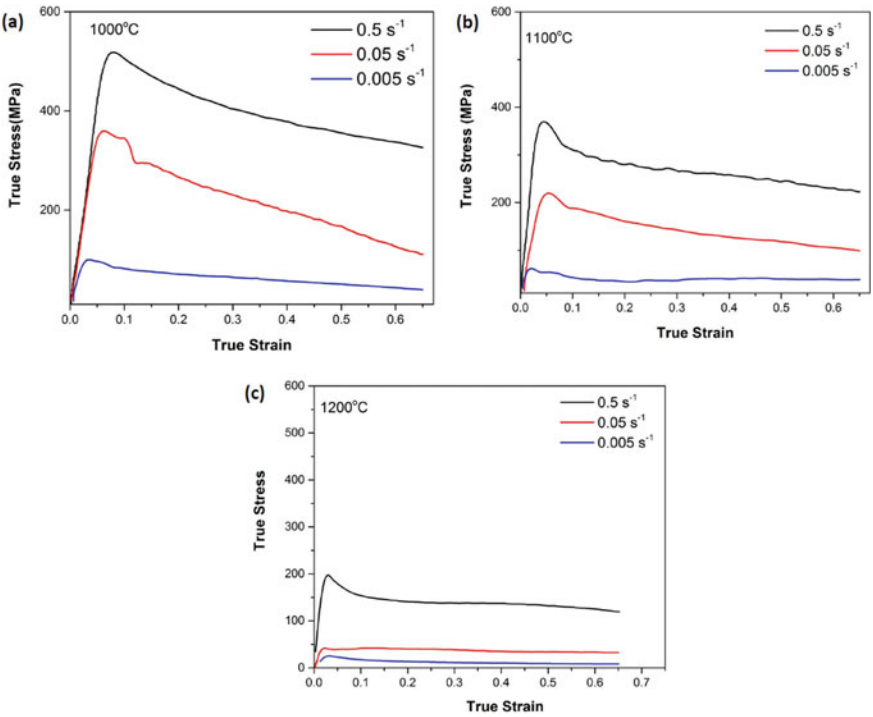


**Fig. 2** True stress-true strain curves of the experimental alloy deformed at **a** 1273 K, **b** 1373 K, and **c** 1473 K as a function of strain rates

$$Q = R\left\{\frac{\partial \ln \dot{\varepsilon}}{\partial \ln[\sinh(\alpha\sigma)]}\right\}_T \left\{\frac{\partial \ln[\sinh(\alpha\sigma)]}{\partial(1/T)}\right\}_{\dot{\varepsilon}} \tag{2}$$

Figure 3 displays the pertinent plots showing linear relationships between appropriate forms of peak stress, strain rate, and deformation temperatures. The average apparent activation energy for hot deformation obtained through the mean slopes of $\ln[\sinh(\alpha\sigma)]$ versus $1/T$ (Fig. 3c) is found to be 282.9 kJ/mol and the value of $\alpha$ is obtained as 0.007 $MPa^{-1}$. Figure 3d shows a good linear relationship and from linear regression, the values of $A$, $n$ are estimated to be $1.55 \times 10^9$ $s^{-1}$ and 1.565, respectively. Therefore, the constitutive equation of hot deformation of Ti–45Al–8Nb–6Cr–0.2B alloy at peak stress can be expressed as

$$\dot{\varepsilon} = 1.55 \times 10^9 [\sinh(0.007.\sigma)]^{1.56} \exp\left(-\frac{289200}{RT}\right) \tag{3}$$

The calculated value of apparent activation energy for the present alloy is close to the activation energy of Ti–Al interdiffusion (298 kJ/mol), and Ti self-diffusion (260 kJ/mol) in single-phase γ-TiAl alloys [15]. It indicates that the dominant hot

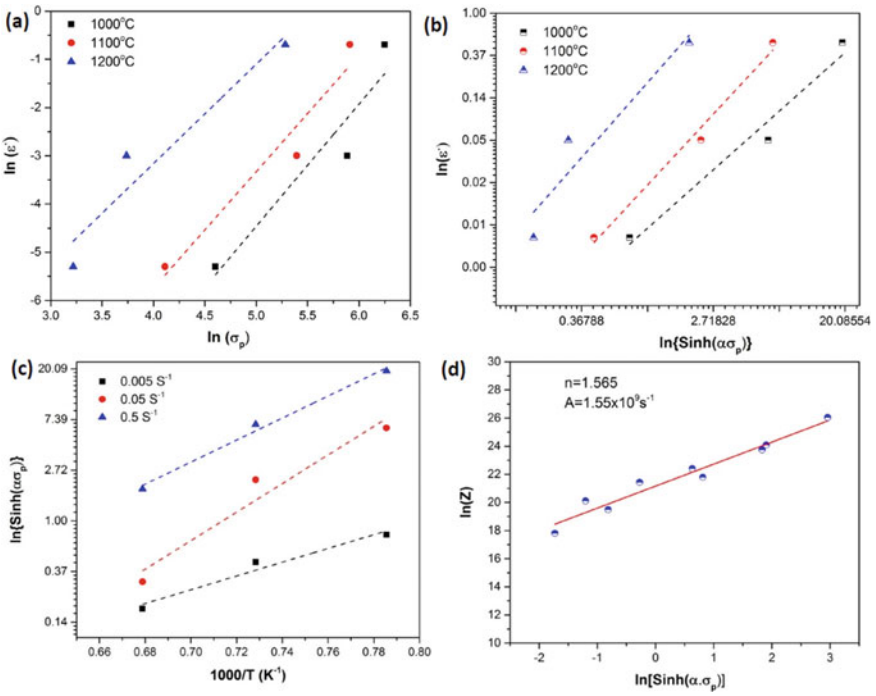


**Fig. 3** Determination of constants of constitutive behavior (Eq. 1) from the linear relationships of **a** $\ln(\dot{\varepsilon})$ verus $\ln(\sigma_p)$, **b** $\ln(\dot{\varepsilon})$ versus $\ln[\sinh(\alpha.\sigma_p)]$, **c** $\ln[\sinh(\alpha.\sigma_p)]$ versus 1000/T, and **d** $\ln(Z)$ versus $\ln[\sinh(\alpha.\sigma_p)]$

deformation mechanism is DRX. It should be noted that the apparent activation energy of Ti–45Al–8Nb–2Cr–0.2B alloys has a significantly higher value (429.4 kJ/mol) [7] similar to Ti–45Al–5Nb–0.2B–0.2C, Ti–45Al–8Nb–0.2C, and Ti–45Al–10Nb alloys having initial near-lamellar microstructure [5]. It is evident that the hot deformation behavior of the TiAl alloy is controlled by microstructural features. The significantly higher values of activation energies mainly can be attributed to lamellar $\alpha_2 + \gamma$ microstructures since $\alpha_2/\gamma$ interfaces act as a strong barrier to the mobile dislocation motion [5]. The absence of lamellar structures, as well as the high volume fraction of highly deformable B2-phase, could possibly account for the very low apparent activation energy of the present alloy.

## *3.3 Microstructure After Deformation*

Development of microstructures imaged at the longitudinal cross-section of deformed specimens over the entire processing parameter range is summarized in Fig. 4. It is evident that the development of microstructures is strongly affected by

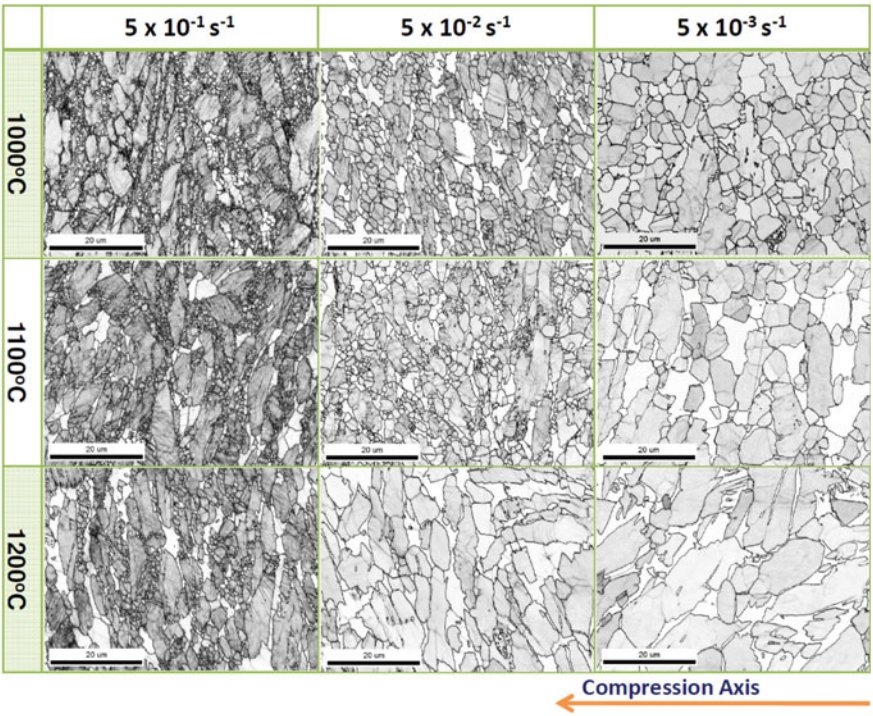


**Fig. 4** Matrix of post-deformation microstructures imaged by EBSD band contrast mode as a function of deformation temperature and strain rates

both temperature and strain rate. From the EBSD band contrast images of 50% deformed samples, $\gamma$-TiAl phase carries most of the deformation (darker contrast implies more lattice strain), whereas $\beta$-phases are recovered/recrystallized. At high strain rate (0.5 $s^{-1}$), the $\gamma$-grains are highly deformed with lots of deformation bands and kink band formation. Very fine, dynamically recrystallized (DRX) grains at the inter-phase boundaries indicate the initiation of DRX processes. With the increase in temperature and decreasing strain rate, the extent of DRX of $\gamma$-grains increases significantly. Coarsening of both $\gamma$- and $\beta$-phases can be observed at higher temperatures and lower strain rates. It is thus evident from the microstructures presented here that the significant flow softening observed in this alloy at higher temperatures and lower strain rates can be attributed to the occurrence of DRX as concluded by Seetharaman and Lombard [16] in Ti–49.5Al–2.5Nb–1.1Mn alloy.

## *3.4 Hot Deformability and Processing Map*

The hot deformability of the present alloy has been analyzed through a processing map using the dynamic material model (DMM) approach pioneered by Prasad et al.

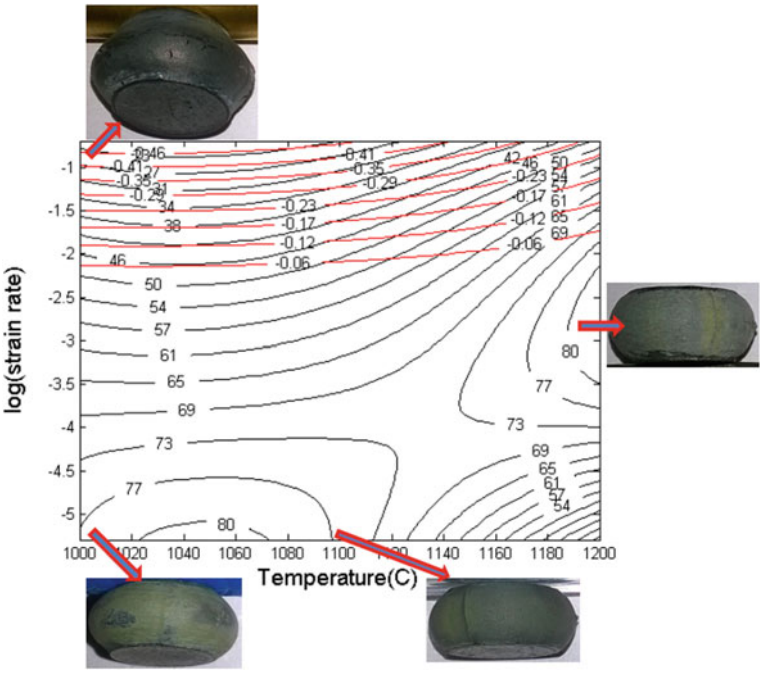


**Fig. 5** **a** Contour plot of power dissipation efficiency as a function of temperature and strain rates at a true strain of 0.4. Insets: Photographs of deformed samples tested using parameters corresponding to locus of the indicated points

[17]. The power dissipation efficiency map constructed at a strain of 0.4 (at the near steady-state condition) is shown in Fig. 5, showing iso-efficiency lines directly related to microstructural evolution. It is evident from the figure that the peak efficiency of about 80% can be found near 1100 °C/0.005 $s^{-1}$ and 1200 °C/0.05 $s^{-1}$, whereas the dissipation efficiency is considerably lower toward a higher strain rate regime for the entire temperature range. This unstable deformation condition is marked as the cross-hatched region. The area below the red cross-hatched mark corresponds to the stable flow area implying that defect-free deformation can be carried out at this zone. Indeed, it has been found that experimental deformation behavior corroborates well with the trend predicted by the process map (refer to the actual photograph of deformed samples in Fig. 5). It is believed that DRX plays a critical role in facilitating higher dissipation efficiency during deformation in agreement with the microstructural features as shown in Fig. 4.

In this context, the deformability of the present alloy should be compared with the Ti–45Al–8Nb alloy having a fully lamellar structure [11] and Ti–45Al–8Nb–2Cr–0.2B alloy having a mixed lamellar and remnant $\beta$-phase (vol. fraction $\sim$10%) [7]. Macroscopic surface morphologies of the deformed samples and processing maps indicate that the present alloy clearly offers a much wider hot-working

window to achieve "sound" quality wrought products. This is mainly attributed to the large volume fraction of $\beta$-phase and absence of lamellar structure.

As pointed out previously [7], at higher strain rates and lower temperatures presence of $\beta$-phase has a major influence on the hot workability of γ-TiAl-based alloys. Although brittle at room temperature, the $\beta$-phase becomes relatively more deformable compared to the $\gamma$- and $\alpha_2$-phases at elevated temperatures. Consequently, the preferential deformability of $\beta$-phase absorbs the stress concentration which is generated by lamellar colony boundary sliding during deformation. It is well established that such a process can lead to the minimization of cavitation at triple junctions as noticed by Nieh et al. [18]. It is to be further noted that hot deformation, being a typical thermally activated process, depends heavily on dislocation glide and climb processes at a given temperature and strain rate. It has been commonly observed that owing to their lower SFE and poor mobility of the dislocations across the lamellar ($\alpha_2$ + $\gamma$) structure, $\gamma$-TiAl-based alloys are prone to DRX during hot deformation [19]. In presence of high content of Nb-solutes which further reduce diffusivity (hence mobility of dislocations), the deformability of the lamellar structure plays a critical role as demonstrated through very high-value activation energy of lamellar or near-lamellar alloys [7, 11].

It is evident from the foregoing discussion that the amount of retained $\beta$-phase along with the absence of lamellar morphology of microstructure facilitates the improvement in hot workability of $\beta$-modified $\gamma$-TiAl alloys containing high niobium and chromium.

## 4 Conclusions

(1) High-temperature flow behavior of the Ti–45Al–8Nb–6Cr–0.2B alloy displays typical strain rate and temperature-sensitive flow softening. The apparent activation energy of hot deformation ($Q$) and the stress exponent are found to be 282.9 kJ/mol and 1.565, respectively. The significantly low activation energy is attributed to the absence of lamellar microstructure and high volume fraction of $\beta$-phase.

(2) The present experimental alloy demonstrates a much improved hot workability window as evidenced by the processing map and macroscopic observation of actual deformed samples in the temperature range of 1373–1473 K and strain rate range of 0.05–0.005 $s^{-1}$.

(3) Significantly high hot workability of the present alloy is attributed to the high volume fraction of $\beta$-phase and morphological characteristics of γ-phase (i.e., absence of lamellar morphology).

**Acknowledgements** The authors wish to acknowledge the financial support from Defence Research and Development Organization (DRDO), Government of India.

## References


1. Sauthoff G (1995) Intermetallics. VCH Verlagsgesellschaft, Weinheim, New York
2. Lütjering G, Williams JC (2007) Titanium: engineering materials and processes. Springer, New York
3. Westbrock JH, Fleischer RL (1995) Intermetallic compounds: principles and practice—vol 2 practice. John Wiley & Sons Ltd, West Sussex
4. Toshimitsu T, Kentaro S, Satoshi K, Satoru K, Masao T (2005) Fabrication of TiAl components by means of hot forging and machining. Intermetallics 13:971–978
5. Appel F, Paul JDH, Oehring M (2011) Gamma titanium aluminide alloys: science and technology. Wiley-VCH Verlag GmbH & Co, Weinheim, Germany
6. Clemens H, Smarsly W (2011) Light-weight intermetallic titanium aluminides–status of research and development. Adv Mater Res 278: 551–556
7. Singh V, Mondal C, Kumar A, Bhattacharjee PP, Ghosal P (2019) High temperature compressive flow behavior and associated microstructural development in a β-stabilized high Nb-containing γ-TiAl based alloy. J Alloys Compd 788:573–585
8. Niu HZ, Chen YY, Xiao SL, Kong FT, Zhang CJ (2011) High temperature deformation behaviors of Ti-45Al-2Nb-1.5 V-1Mo-Y alloy. Intermetallics 19:1767–1774
9. http://ww.ebsd.com/solving-problems-with-ebsd/ebsd-advancement
10. Singh V (2020) PhD thesis, microstructure, phase stability and high temperature deformation behavior in γ-TiAl based (Ti-45Al-8Nb-xCr-0.2B) alloys. Indian institute of technology hyderabad
11. Singh V, Kumar A, Mondal C, Bhattacharjee PP, Ghosal P (2019) Hot deformation of high-Nb-containing γ-TiAl alloy in the temperature range of 1000–1200 °C: microstructural attributes to hot workability. SN Appl Sci 1:366
12. Clemens H, Kestler H (2000) Processing and applications of intermetallic γ-TiAl-based alloys. Adv Eng Mater 2(9):551–570
13. Zener C, Hollomon JH (1944) Effect of strain rate upon plastic flow of steel. J Appl Phys 15:22–27
14. Sellers CM, McTegart WJ (1966) Acta Metall 14(9):1136–1138. https://doi.org/10.1016/0001-6160(66)90207-0
15. Herzig C, Przeorski T, Mishin Y (1999) Self-diffusion in γ-TiAl: an experimental study and atomistic calculations. Intermetallics 7(3–4):389–404
16. Seetharaman V, Lombard CM (1991) Microstructure property relationships in Titanium Aluminides and alloys. In: Kim YW, Boyer RR (eds), TMS, Warrendale, p 237
17. Prasad YVRK, Seshacharyulu T (1998) Modelling of hot deformation for microstructural control. Int Mater Rev 43(6):243–258
18. Nieh TG, Hsiung LM, Wadsworth J (1999) Superplastic behavior of a powder metallurgy TiAl alloy with a metastable microstructure . Intermetallics 7(2):163–170
19. Zhang WJ, Appel F (2002) Effect of Al content and Nb addition on the strength and fault energy of TiAl alloys. Mater Sci Eng A 329–331:649–652

# In-Situ Dissolution Behavior of Secondary Alloy Phases in Al–Zn–Mg–Cu-Base AA7055 Aluminum Alloy


**Renu Ghanghas, Chandan Mondal, Deepak Kumar, and Partha Ghosal**

**Abstract** The present study reports the dissolution behavior of the secondary alloy phases of an Al–8.3Zn–2Mg–2.4Cu–0.15Zr alloy (AA7055) during in-situ heating within a scanning electron microscope operating under highly evacuated condition. It has been shown that the dissolution of the major secondary alloy phases (i.e., η ($MgZn_2$)-base and T ($Al_2Mg_3Zn_3$)-base phases present in the inter-dendritic channels) is initiated at a substantially low temperature (∼300 °C) under SEM operating condition. It is to be contrasted with the fact that the typical homogenization temperature of 7xxx series Al alloys is always greater than 450 °C under atmospheric pressure. Characterization of morphological changes during the in-situ heating to different predetermined temperatures reveals that the dissolution process occurs by the *thinning*, *discontinuation*„ *and spheroidization* (TDS) mechanism which encompasses spheroidization and thinning processes. In addition, the dissolution kinetics of the fine eutectic phases have been found to be significantly accelerated compared to that under atmospheric pressure. The results are further augmented by conventional ex-situ homogenization experiments. The compositional variations of secondary phases have been investigated as a function of time and temperature. The result shows that elemental compositions of Fe-bearing phases vary marginally, whereas that of Zn, Cu-rich phases move from non-equilibrium to equilibrium values.

**Keywords** Al alloy · Microstructure · Scanning electron microscopy · Homogenization · Dissolution · In-situ microscopy

R. Ghanghas · C. Mondal (✉) · D. Kumar · P. Ghosal
Defence Metallurgical Research Laboratory (DMRL), Kanchanbagh, Hyderabad 500058, India
e-mail: c_mondal@dmrl.drdo.in



P. Ghosal et al. (eds.), *Applications of Microscopy in Materials and Life Sciences*, Springer Proceedings in Materials 11,
https://doi.org/10.1007/978-981-16-2982-2_15

## 1 Introduction

Al–Zn–Mg–Cu-based 7xxx series aluminum alloys are widely used for structural applications in aerospace industries due to their superior combination of properties encompassing a high strength-to-weight ratio, good fracture toughness, moderate fatigue resistance [1–2]. The processing of these alloys is quite challenging because of substantial alloying contents. During casting, solute redistribution leads to the segregation of a large fraction of alloying elements at the grain boundaries and forms secondary phases at inter-dendritic channels [3–4]. Homogenization treatment of the as-cast structure is required to remove chemical inhomogeneities and stabilize the microstructure. The homogenization time and temperature play a vital role in the evolution of secondary phases in 7055 alloys [5–6]. The alloys are precipitation hardenable, and follow a precipitation sequence of *super-saturated solid solution* $\rightarrow$ *GP zones* $\rightarrow \eta' \rightarrow \eta$ ($MgZn_2$) [7]. The $\eta$-phase has a quaternary phase composition containing Al, Zn, Mg, and Cu [8]. AA7055 alloy represents the highest strength wrought aluminum alloy through the ingot metallurgical route. The attractive mechanical properties of AA7055 alloy are dependent mainly on the nature, stability, morphology, and distribution of the strengthening precipitates and other constituent phases which, in turn, depend on the availability of alloying elements present in the form of a super-saturated solid solution of alloy [9]. The presence of coarse secondary phase at inter-dendritic channel deteriorates the toughness and fatigue performance of these alloys [10–11]. Hence, dissolution of the secondary phases present at inter-dendritic channels during homogenization assumes greater significance [12–13].

Over the last few decades, considerable work has been done to understand the evolution of secondary phases such as eutectic and divorced eutectic $MgZn_2$-base and *T*-base phases located at the inter-dendritic channels (IDC) [14–15]. In this study, series of experiments have been carried out to visualize the dissolution mechanism of the secondary alloy phase employing an in-situ technique inside the scanning electron microscope chamber [15] and analyze compositional variation as a function of time and temperature.

## 2 Experimental Procedure

The 7055 aluminum alloy used in the present study was prepared via an ingot metallurgical route. The details of the alloy preparation are reported elsewhere [8]. The analyzed chemical composition of the alloy is shown in Table 1. The as-cast

**Table 1** Chemical composition of the alloy

| Elements | Zn | Cu | Mg | Zr | Fe | Si | Al |
|---|---|---|---|---|---|---|---|
| Wt. % | 8.3 | 2.4 | 2 | 0.15 | 0.09 | 0.06 | Balance |

samples were homogenized both in an air furnace (ex-situ) and inside the scanning electron microscope (SEM) chamber (in-situ) at different temperatures for different durations. The characterization of the as-cast and homogenized samples were carried out using ZEISS EVO 18 SEM equipped with Oxford energy dispersive spectroscopy (EDS). The micro-chemical analyses of the secondary phases were evaluated with EDS. An average of 10 readings has been reported for compositional analysis of secondary phases. X-ray diffraction (XRD) study was undertaken in order to identify the alloy phases on a PHILIPS PW 1710 automatic diffractometer. The quantitative analysis (i.e., area fraction) of secondary phases visible in the microstructure was carried out by using *ImageJ software*. The analysis of a minimum of 10 images from different locations at 100× magnification pictures has been considered for area fraction measurement. An advanced microscopy technique, i.e., in-situ heating in SEM was used to visualize the dissolution mechanism of the secondary alloy phase as a function of time and temperature. In-situ heating of the as-cast sample was performed inside the SEM (ZEISS EVO 18) chamber using GATAN hot stage (H1004 Heating Module).

## 3 Results

### *3.1 Microstructural Characterization of the As-Cast Material*

Typical microstructures of the as-cast alloy are shown in Fig. 1. The as-cast microstructure consists of α-Al solid solution surrounded by the secondary alloy phases situated at the inter-dendritic channels (IDC). The IDC phases, appearing with brighter contrast in BSE images, are semi-continuous and are distributed uniformly throughout the alloy. The BSE images reveal that there are two contrasts

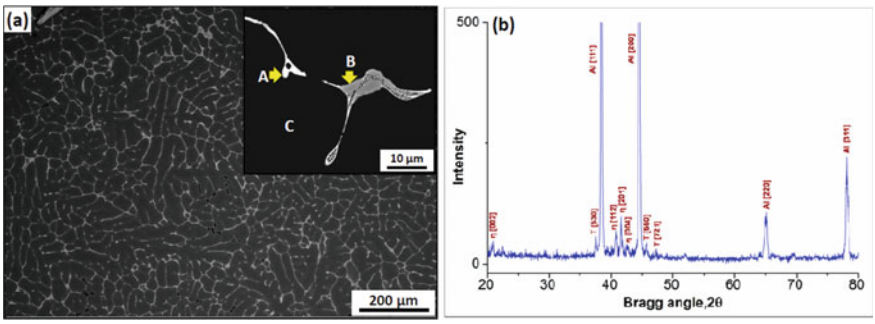


**Fig. 1** **a** Typical BSE image of the as-cast sample showing the dendritic microstructure, **b** corresponding X-ray diffraction pattern. Inset **a**: Higher magnification image of secondary phases and positions of EDS analyses

**Table 2** EDS analysis of secondary phases of the as-cast alloy

| Phase | Al | Zn | Mg | Cu | Fe |
|---|---|---|---|---|---|
| A | 37.88 | 31.24 | 12.13 | 18.75 | – |
| B | 58.14 | 3.93 | – | 20.30 | 17.63 |
| C | 90.43 | 7.72 | 1.85 | – | – |

of secondary alloy phases in the as-cast microstructure (Fig. 1a: inset). The EDS analyses show the presence of Cu, Zn, Mg elements in regions having bright contrast (point A) and Cu, Fe elements in regions having gray contrast (point B). Only Al, Zn, and a marginal amount of Mg elements were present in the matrix region (point C). Table 2 shows the micro-chemical analysis of the secondary phases. The gray region represents the presence of Cu and Fe-bearing particle (i.e., $Al_7Cu_2Fe$) and the brighter regions indicate the presence of either $\eta$ or $T$ containing higher atomic number elements (i.e., Zn, Mg, Cu). A typical XRD pattern of the as-cast sample (Fig. 1b) reveals the presence of two secondary phases, i.e., $\eta$ ($MgZn_2$) and $T$ ($Al_2Mg_3Zn_3$) in the as-cast alloy [8]. In addition to these phases, a Fe-rich phase (possibly $Al_7Cu_2Fe$ type) is identified by EDS compositional analysis, although the same could not be detected by XRD due to its low volume fraction.

## *3.2 Morphological Changes of Secondary Alloy Phases*

### 3.2.1 In-Situ Heating at 300 °C

The morphological changes of the secondary phase have been monitored in-situ at regular intervals during soaking inside the SEM chamber to 300 °C for a total time period of 40 h. The results are summarized in Fig. 2a–f showing the sequence of secondary phase dissolution occurring in the eutectic and divorced eutectic regions of the microstructure as a function of soaking time. During the initial period of soaking, it has been observed that the secondary phase dissolution process started with the inhomogeneous coarsening in the eutectic region (Fig. 2b). It is followed by discontinuous thinning of the divorced eutectic at the IDC by the formation of perturbation (Fig. 2c, d).

Initially, the eutectic phase starts coarsening with time which leads to a decrease in the interfacial energy (between the α-Al solid solution and the secondary phase) by the reduction in the interface area and the divorced eutectic regions start becoming thinner. The thinning process continues till the IDC (divorced eutectic) regions become discontinuous at some regions. In-situ experimentation reveals that the presence of shape irregularity at the interface accelerates the dissolution by perturbation mechanism. The discontinuities or perturbations continue to increase with time (Fig. 2e, f).

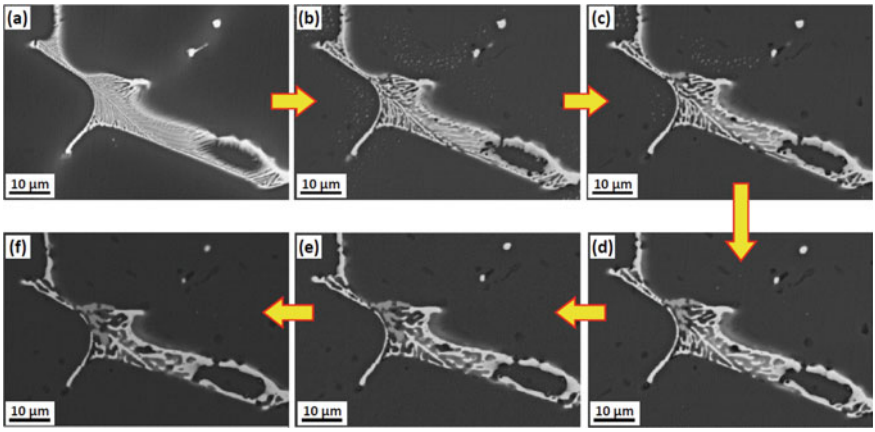


**Fig. 2** BSE images captured during in-situ heating: **a** at RT, soaking at 300 °C for **b** 1 h, **c** 3 h, **d** 10 h, **e** 35 h, and **f** after cooling to RT

### 3.2.2 In-Situ Heating at 350 °C

The in-situ experiment has also been conducted at 350 °C for about 5 h. Figure 3 shows the microstructural evolutions of eutectic and divorced eutectic phases at IDC as a function of soaking time at 350 °C. Figure 3a shows the starting microstructure at room temperature. On reaching and stabilizing the temperature at 350 °C Fig. 3b, one can see the perturbations developing in divorced eutectic regions. Thinning can also be seen in confined regions in the divorced eutectic phase. As the soaking time at 350 °C increases (Fig. 3c), it has been observed that thinning is no longer confined, rather it extends to other divorced eutectic regions. Perturbations continue to develop in the microstructure. Coarsening can be observed in the eutectic phase. After 1 h, the microstructure shows the onset of discontinuity in grain boundary channels (Fig. 3d). As the soaking time increases further the discontinuity in the divorced eutectic regions grows further with the partial dissolution of the grain boundary phase. With further increase in soaking time, extensive dissolution of the secondary phase is seen along with considerable coarsening (and spheroidization) of the eutectic phase. After 5 h of soaking at 350 °C (Fig. 3e), a significant amount of spheroidization of divorced eutectic occurs in some regions. It is to be noted that the simultaneous occurrence of dissolution and coarsening could be associated with two different phases (i.e., $\eta$ and $T$ phases) coexisting at the IDC eutectic structures. However, due to compositional similarity, they can not be distinguished easily through BSE images. Further studies involving the phase-resolved dissolution phenomenon need to be undertaken to resolve the issue.

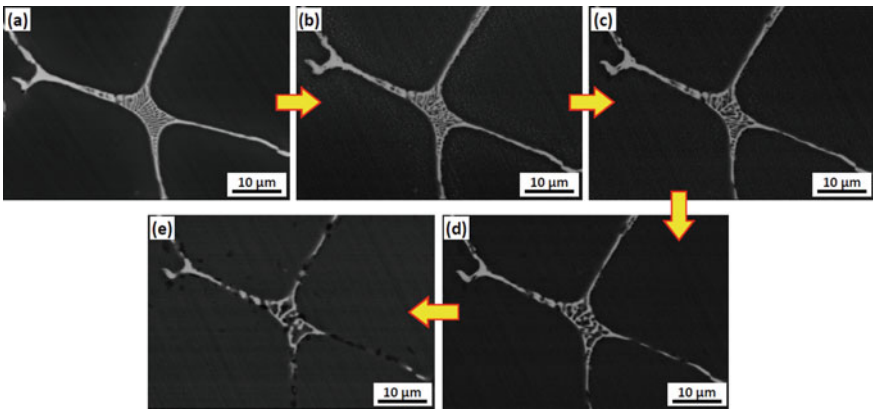


**Fig. 3** BSE images captured during in-situ heating of Al–Zn–Mg–Cu alloy at **a** RT, **b** 350 °C/30 min, **c** 350 °C/60 min, **d** 350 °C/105 min, **e**, while cooling

### *3.3 Conventional (Ex-Situ) Homogenization Experiments*

Another set of as-cast specimens have been subjected to a conventional homogenization treatment in an air furnace at 400 and 450 °C. For 400 °C soaking, it has been observed that after 1 h, the microstructure remains essentially unaltered compared to the as-cast microstructure. After 6 h, both the coarsening of eutectic and thinning of the GB phase can be noticed in the microstructure indicating the initiation of the TDFD mechanism as reported by Eivani et al. [16, 17, 18]. After 12 h, the continued thinning of the GB phase has led to discontinuity in the divorced eutectic. The spheroidization process is prominently visible after 26 h and it continues along with a partial dissolution of secondary phases with further increase in homogenization for 34 and 50 h. In contrast, spheroidization could be noticed even after 1 h at 450 °C. After 6 h, partial dissolution can be observed along with spheroidization of the IDC phase which is observed toward the later stages at 400 °C. It can be inferred that the dissolution rate is much higher at 450 °C leading to the observation of partial dissolution of secondary phases even at short soaking duration. This shows that such a high temperature is very effective for the dissolution of secondary phases. The microstructural developments after 26 h of soaking are compared in Fig. 4.

Micro-chemical analyses of the secondary phases that survive the homogenization soaking of 50 h indicate the identity of such phases. The results are compiled in Tables 3 and 4. EDS analysis (Table 3) of the secondary phase (marked as $A_1$ in Fig. 4a) shows the possible presence of the S ($Al_2CuMg$) phase. Fe-rich particle is also present in the grain boundary region (location $B_1$). The presence of $\eta$-base phase $Mg(Zn,Cu,Al)_2$ is also indicated at location $C_1$ (Fig. 4a, b) as remnants of partially dissolved divorced eutectic structure. EDS analysis (Table 4) of

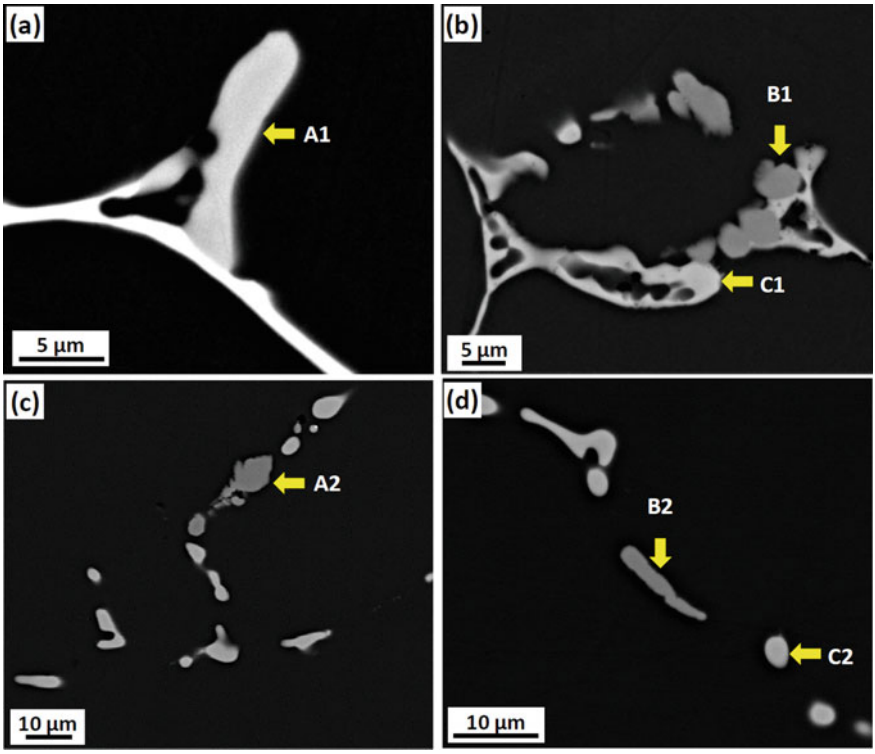


**Fig. 4** The presence of different intermetallic phases after 26 h of homogenization at **a**, **b** 400 °C, **c**, **d** 450 °C

**Table 3** EDS analysis of phases after 26 h at 400 °C

| Phase | Al | Zn | Mg | Cu | Fe |
|---|---|---|---|---|---|
| $A_1$ | 44.51 | – | 16.79 | 38.70 | – |
| $B_1$ | 56.40 | – | – | 29.52 | 14.08 |
| $C_1$ | 19.63 | 41.12 | 17.02 | 22.23 | – |

**Table 4** EDS analysis of phases after 26 h at 450 °C

| Phase | Al | Zn | Mg | Cu | Fe |
|---|---|---|---|---|---|
| $A_2$ | 53.05 | – | – | 32.87 | 14.09 |
| $B_2$ | 58.77 | – | – | 28.93 | 12.30 |
| $C_2$ | 27.62 | 33.12 | 17.15 | 22.11 | – |

the alloy after 26 h of homogenization shows the presence of η phase at location $C_2$ (Fig. 4d). The Fe-rich phase is also present in the IDC region (location $A_2$ and $B_2$) as shown in Fig. 4a, b.

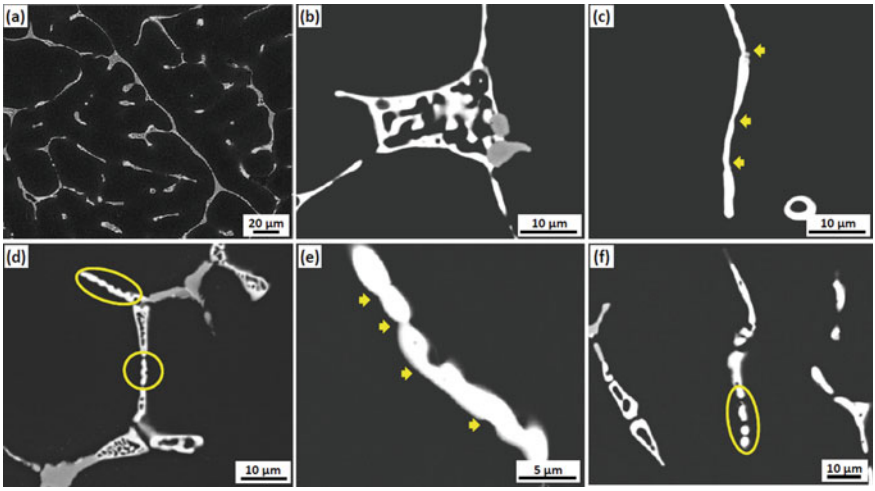


**Fig. 5** BSE morphologies of the IDC phase after homogenization in air furnace at 450 °C: **a** initial, **b** eutectic coarsening, **c** thinning of GB phase, **d** perturbation formation, **e** spheroidization initiation, **f** spheroidization

### *3.4 Observation of Different Stages of Dissolution*

Using the in-situ heating technique in SEM, we have already visualized the TDFD mechanism (as it occurred during homogenization) which was earlier proposed by Eivani et al. based on ex-situ experiments [17, 18]. The evidence of this mechanism can also be observed through the samples homogenized for different durations using the ex-situ experiments (Fig. 5). Coarsening of the IDC phase can be seen in (Fig. 5b). Figure 5c shows the thinning process while formations of perturbations are observed in Fig. 5d, e and the spheroidized IDC phase is visible in Fig. 5f.

## 4 Discussion

### *4.1 Morphological Changes of Secondary Phases*

In accordance with the findings of ex-situ experiments by Eivani et al. [16, 17], it could be noticed that the dissolution process starts simultaneously with both the eutectic and divorced eutectic morphologies (Fig. 2). However, morphological changes during the dissolution of the eutectic mixture and divorced eutectic phases appear to be different. The dissolution of the lath-shaped divorced eutectic phase, which is a Zn-rich Mg $(Zn, Cu, Al)_2$-based $\eta$ phase [8], begins with perturbation-like discontinuous thinning along the length of the phase (circle enclosed part of Fig. 2d). On the other hand, the dissolution of eutectic phase

mixture (α-Al solid solution (dark) and Mg (Zn, Cu, Al)$_2$-based $\eta$ phase (bright)) follows the classical discontinuous coarsening mechanism (the spheroidization) [18]. With the increasing temperature of soaking to 350 °C, the divorced eutectic phases tend to attain complete dissolution, whereas the eutectic part remains partially dissolved and spheroidized state. Recently, a specific dissolution mechanism called *thinning*, *discontinuation and full dissolution* (TDFD) has been forwarded by Eivani et al. [16] to account for the dissolution mechanism of grain boundary phases in Al–Zn–Mg alloy. It has been shown that a particle situated at IDC develops initial protrusions on its surface and grows into an ellipse shape. Further spheroidization continues till the IDC particle assumes a nearly spheroidal shape with a protruded surface, and finally, IDC particles tend to acquire spherical shape with the removal of surface protrusions in order to minimize the particle–matrix interfacial area and resultant surface energy.

The present results suggest that the dissolution of divorced eutectic grossly follows the mechanism suggested by Eivani et al. [16], although at a lower temperature of annealing (i.e., 300 °C) the discontinuation could not be observed even after 40 h of soaking. The difference in dissolution behavior could be attributed to the compositional variation of the alloys. The alloys used by Eivani et al. can be categorized as a compositionally lean alloy compared to the present alloy having a significantly higher amount of Zn, Mg, and Cu. According to the section of the quaternary Al–Zn–Mg–Cu phase diagram for 6 wt.% Zn at 460 °C [19], the present alloy composition falls under a two-phase field (α-Al + S). Hence, complete dissolution depends strongly on the composition [8]. With still higher Zn content and lower temperature the present alloy composition will tend to move toward α-Al + S + Z (AlZnMgCu) phase field [28]. It is, therefore, suggested that for the compositionally rich alloy such as the present one the mechanism could be visualized as the *thinning*, *discontinuation*, *and spheroidization* (TDS).

## 4.2 Quantitative Analysis of Secondary Phase Dissolution

The quantitative analysis of the area fraction of secondary phases in the alloy was investigated using BSE micrographs of as-cast sample and samples homogenized for different time intervals. The analyses of the BSE images indicate that the fraction of the secondary phase particles decreases even during in-situ soaking at 300 and 350 °C as well as ex-situ soaking at 400 °C, in addition to the morphological changes toward spheroidization.

The results (as shown in Fig. 6) show that the area fraction of secondary phases comprising of the eutectic and divorced eutectic regions gradually decreases with the increase in soaking time at 400 °C. On the other hand, there is a rapid reduction of the secondary phase fraction at the initial stage for soaking at 450 °C, followed by rather sluggish dissolution kinetics. The average rate of change in area fraction during soaking is higher at 450 °C than that at 400 °C. The total decrease in area fraction of secondary phases at 400 °C is approx 42%, while it is 72% at 450 °C for

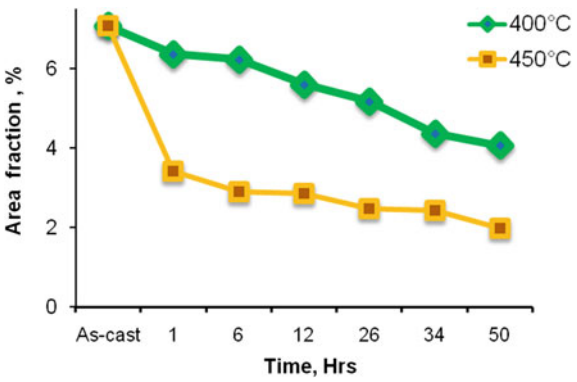


**Fig. 6** Evolution of area fraction of secondary phase during homogenization at 400 and 450 °C

the same total duration of homogenization (after 50 h). The results indicate that as expected, 450 °C temperature is more effective for homogenization as the diffusion of alloying elements is faster compared to 400 °C.

## *4.3 Pros-n-Cons of In-Situ Experiments*

The present study reports for the first time the in-situ dissolution behavior of the secondary phases of an AA7055 Al under high vacuum conditions in the temperature range of 350–350 °C. One of the key objectives of such experimentation has been to examine the morphological modifications during the soaking. The results of morphological variations have been documented in the previous sections in conjunction with the results of conventional ex-situ experiments. Although the findings are quite interesting, the unavoidable consequences need to be kept in mind for future research plans.

It could be noticed that the kinetics of secondary phase dissolution during in-situ experimentations under high vacuum conditions is significantly faster even at a much lower temperature compared to that of ex-situ experiments. In order to get a direct correlation, further in-situ experiments have been conducted at 400 °C. The results are reported in detail elsewhere [15]. Unexpectedly, it has been found that complete dissolution occurs within 30 min of soaking. In order to get insight into such an extraordinarily fast rate of dissolution kinetics, the in-situ experiments are interrupted at different times, and the chemical compositions of the phases are evaluated by EDS. It indicates that during soaking at 400 °C, the Zn content of the η-phase and the matrix vanishes rapidly such that the sample after complete dissolution of secondary phases shows negligible Zn content at the surface. This is consistent with the fact that the operating condition of the in-situ experiment inside the SEM chamber ($\sim 10^{-6}$ torr vacuum, 400 °C) coincides with the triple point of Zn. This further explains the relatively faster dissolution rate of the secondary phases at 370 °C with a higher rate of heating. It is to be noted that during the faster

rate of heating, a temperature shoot up of 10–15 °C occurs at the beginning before the specimen temperature stabilizes. Such as temperature shoot up enables reduction of Zn content of the system and therefore, dissolution of secondary alloy phases happens at a faster rate. The phenomenon also points out the possibility of the composition induced dissolution reaction (i.e., $\eta \rightarrow \alpha$ (solid solution)) implying thermodynamic instability of Zn-rich secondary alloy phases due to Zn-loss.

Although the consequences described above point towards apparent drawback of the technique, it evokes a hitherto unreported result that it is the Zn content of the secondary phases that control the dissolution processes during homogenization. Such information could potentially dictate the future high strength aluminum alloy development based on the Al–Zn–Mg–Cu system since the complete dissolution of secondary alloy phases remains one of the key considerations for the new age high solute 7xxx series alloys.

## 5 Conclusions

(1) The major secondary phases present in the as-cast microstructure of AA7055 Al alloy are $\eta$- and *T*-base quaternary phases as identified by XRD and EDS analysis, whereas traces of the Fe-bearing phase have been detected through quantitative EDS analysis only. Following ex situ homogenization at 400–450 °C, Mg (Zn, Cu, Al)$_2$-based $\eta$ phase is found to survive the homogenization with compositional modification and a transformed $Al_2CuMg$-base S phase is identified apart from insoluble Fe-rich phase.

(2) A series of in-situ heating experiments in the range of 300–350 °C has been carried inside an SEM to directly monitor the morphological modifications occurring in secondary alloy phases during intermediate temperature homogenization. Dissolution of divorced eutectic is significantly sluggish compared to the eutectic phase mixture which is first of its kind observation and grossly follows *the thinning*, *discontinuation*, *and spheroidization* (TDS) model at an intermediate temperature of soaking. This validates the model experimentally.

(3) The kinetics of secondary phase dissolution during in-situ experimentations under high vacuum conditions is significantly faster even at a much lower temperature compared to that of ex-situ experiments. Faster dissolution of secondary phases (especially near 400 °C) under ultra-high vacuum is associated with the 'loss' of Zn content of the phase.

**Acknowledgements** The authors would like to thank the Director, DMRL for his constant support and encouragement. This research work has been funded by the Defence Research and Development Organization (DRDO), Government of India.

## References


1. Deng Y, Yin Z, Cong F (2012) Intermetallic phase evolution of 7050 aluminum alloy during homogenization. Intermetallics 26:114–121. https://doi.org/10.1016/j.intermet.2012.03.006
2. Ciesler M, Bajer J, Hajek M, Ocenasek V (2012) In-situ electron microscopy observation of the microstructure changes in the 6082 Aluminium alloy during homogenization. Metal 2012 5:23–25
3. Sha G, Cerezo A (2004) Early-stage precipitation in Al–Zn–Mg–Cu alloy (7050). Acta Mater 52:4503–4516
4. Xie F, Yan X, Ding L, Zhang F, Chen S, Chu MG, Chang YA (2003) A study of microstructure and microsegregation of aluminum 7050 alloy. Mat Sci Eng A 355:144–153
5. Xu D, Li Z, Wang G, Li X, Lv X, Zhang Y, Fan Y, Xiong B (2017) Phase transformation and microstructure evolution of an ultra-high strength Al-Zn-Mg-Cu alloy during homogenization. Mater Charact 131:285–297
6. Li W-B, Pan Q-L, Xiao Y-P, He Y-B, Liu X-Y (2011) Microstructural evolution of ultra-high strength Al-Zn-Cu-Mg-Zr alloy containing Sc during homogenization. Trans Nonferrous Met Soc China 21:2127–2133
7. Polmear IJ (2006) Light alloys-from traditional alloys to nanocrystals, 4th edn. Butterworth-Heinemann
8. Mondal C, Mukhopadhyay AK (2005) On the nature of T(Al2Mg3Zn3) and S(Al2CuMg) phases present in as-cast and annealed 7055 aluminum alloy. Mat Sci Eng A 391:367–376. https://doi.org/10.1016/j.msea.2004.09.013
9. Jia P, Cao Y, Geng Y, He L, Xiao N, Cui J (2014) Studies on the microstructures and properties in phase transformation of homogenized 7050 alloy. Mat Sci Eng A 612:335–342
10. Xi-gang F, Da-ming J, Qing-chang M, Bao-you Z, Tao W (2006) Evolution of eutectic structures in Al-Zn-Mg-Cu alloys during heat treatment. Trans Nonferrous Met Soc China 16:577–581
11. Xie FY, Kraft T, Zuo Y, Moon CH, Chang YA (1999) Microstructure and microsegregation in Al-rich Al–Cu–Mg alloys. Acta Mater 47:489–500
12. Chen K, Liu H, Zhang Z, Li S, Todd RI (2003) The improvement of constituent dissolution and mechanical properties of 7055 aluminum alloy by stepped heat treatments. J Mater Process Technol 142:190–196
13. Deng Y-L, Wan L, Wu L-H, Zhang Y-Y, Zhang X-M (2011) Microstructural evolution of Al–Zn–Mg–Cu alloy during homogenization. J Mater Sci 46:875–881
14. He L-Z, Jia P-F, Zhang L, Cui J-Z (2016) Evolution of secondary phases and properties of 7B04 aluminum alloy during DC homogenization. Trans Nonferrous Met Soc China 26:319−327
15. Sarkar R, Mondal C, Deepak K, Saha S, Atul K, Ghosal P (2016) Structure-property characterisation at nanoscale using in-situ TEM and SEM. Defence Sci J 66:381–390
16. Eivani AR, Ahmed H, Zhou J, Duszczyk J (2009) Evolution of grain boundary phases during the homogenization of AA7020 aluminum alloy. Metall Mater Trans A 40:717–728
17. Eivani AR, Ahmed H, Zhou J, Duszczyk J (2010) Modeling the TDFD dissolution of Al–Fe–Mn–Si particles in an Al–4.5Zn–1Mg alloy. Phil Mag 90:2865–2897
18. Eivani AR, Ahmed H, Zhou J, Duszczyk J (2010) Modelling dissolution of low melting point phases during the homogenisation of AA7020 aluminium alloy. Mat Sci Technol 26:215
19. Strawbridge DJ, Hume-Rothery W and Little AT (1948) The constitution of aluminum-copper-magnesium-zinc alloys at 460 degree C. J Inst Met 74: 191–225
20. Guo W, Guo J, Wang J, Yang M, Li H, Wen X, Zhang J (2015) Evolution of precipitate microstructure during stress aging of an Al–Zn–Mg–Cu alloy. Mat Sci Eng A 634:167–175
21. Li Y, Li P, Zhao G, Liu X, Cui J (2005) The constituents in Al–10Zn–2.5Mg–2.5Cu aluminum alloy. Mat Sci Eng A 397:204–208

22. She H, Shu D, Chu W, Wang J, Sun B (2013) Microstructural aspects of second phases in as-cast and homogenized 7055 aluminum alloy with different impurity contents. Metall Mater Trans A 44:3504–3510
23. Liu Y, Jiang D, Xie W, Hu J, Ma B (2014) Solidification phases and their evolution during homogenization of a DC cast Al–8.35Zn–2.5Mg–2.25Cu alloy. Mater Charact 93:173–183
24. Wang H, Xu J, Kang Y, Tang M, Zhang Z (2014) Study on inhomogeneous characteristics and optimize homogenization treatment parameter for large size DC ingots of Al–Zn–Mg–Cu alloys. J Alloys Compd 585:19–24
25. Robson JD (2004) Microstructural evolution in aluminium alloy 7050 during processing. Mat Sci Eng A 382:112–121
26. Shi Y-J, Pan Q-L, Li M-J, Liu Z-M, Huang Z-Q (2015) Microstructural evolution during homogenization of DC cast 7085 aluminum alloy. Trans Nonferrous Met Soc China 25: 3560−3568
27. Torres EA, Ramírez AJ (2011) In situ scanning electron microscopy. Sci Technol Weld Joining 16:68–78
28. Cieslar M, Bajer J, Hajek M, Ocenasek V (2014) High-Temperature Processes Occurring During Homogenization of AA6082 Aluminum Alloy. In: Grandfield J. (eds) Light Metals 2014. Springer, Cham. pp 237–241. https://doi.org/10.1007/978-3-319-48144-9_41

# Microstructural Attributes to the Stability of 'Brass'-Texture During Cold Rolling of AA7010 High Strength Aluminium Alloy


**Chandan Mondal, Vipin S. Ramteke, Vajinder Singh, Rajdeep Sarkar, and R. K. Satpathy**

**Abstract** Orientation stability of a unique rotated-Brass (rBs)-{110}⟨556⟩ texture during cold rolling of an Al–Zn–Mg–Cu-based 7010 aluminium alloy has been systematically investigated by X-ray diffraction, electron back-scattered diffraction, and transmission electron microscopy. It has been found that during unidirectional cold rolling, the rBs-{110}⟨556⟩ component retains the location of intensity maxima, but the maximum intensity decreases sharply up to 60% reductions in thickness with a concomitant increase in orientation spread. At lower strains (∼30%), the deformation appears to be homogeneous and the texture can still be described by a strong rBs component. Deformation becomes more and more heterogeneous and above 50% cold-rolling reduction, grain-scale shear bands forms. The width of such bands does not increase with deformation, but sharp misorientations are developed across them. Detailed analysis of microtexture in conjunction with TEM studies establishes that the rotation around the ⟨112⟩ axis within the shear band area is facilitated by the change of the co-planar slip systems to a single slip. This can lead to a texture development near the Bs-S regions of the β-fibre in accordance with the 'Dillamore theory'.

**Keywords** 7010 Al alloy · Crystallographic texture · Cold rolling · EBSD · TEM

## 1 Introduction

Investigations on the evolution of crystallographic texture have become an essential part of widespread industrial applications owing to its growing importance in the possibility of tailoring the engineering properties of the products. It is well known that during fabrication, the processing parameters strongly influence microstructural development and induce crystallographic texture in metallic materials. However,

C. Mondal (✉) · V. S. Ramteke · V. Singh · R. Sarkar · R. K. Satpathy
Defence Metallurgical Research Laboratory (DMRL), Kanchanbagh, Hyderabad 500058, India
e-mail: c_mondal@dmrl.drdo.in



P. Ghosal et al. (eds.), *Applications of Microscopy in Materials and Life Sciences*, Springer Proceedings in Materials 11,
https://doi.org/10.1007/978-981-16-2982-2_16

the development of texture and the resultant anisotropy in mechanical properties can be either advantageous or disadvantageous depending on the applications involved [1]. Control of texture by various modifications of processing schedule, therefore, has become an indispensable component of alloy and product development programs.

The evolution of texture during hot deformation of aluminium alloys has been studied extensively over the past several decades aiming towards characterization and control of texture components [2–4]. Depending on the alloy composition, the rolling temperature, and the mode of deformation, various texture components such as Copper (Cu)-$\{112\}\langle 111\rangle$, Brass (Bs)-$\{110\}\langle 112\rangle$, S-$\{123\}\langle 634\rangle$, cube-$\{100\}\langle 001\rangle$, and Goss (G)-$\{110\}\langle 001\rangle$ are formed. During hot rolling, the texture development of aluminium alloys can adequately be described by β-fibre orientation distribution spanning the four major components, namely Cu, S, $\{168\}\langle 211\rangle$ and Bs [4]. In recent years, the development of a strong, single component rotated-Brass (rBs) texture has been reported in a 7010 Al alloy [5] and this provides a unique opportunity to study the stability of such texture in 7010 Al alloy. The present article reports the microstructural attributes for the stability of such a strong rBs texture during subsequent cold rolling.

## 2 Experimental Procedure

A 6-mm-thick hot rolled AA7010 Al alloy sheet was used in the present investigation. The analysed chemical composition is shown in Table 1. The alloy was prepared via conventional ingot metallurgical route and the as-cast ingot was homogenized at 465 °C for 30 h followed by air cooling. The homogenized and scalped slab of dimension 200 mm × 150 mm × 80 mm was hot cross-rolled to a 92% total reduction in thickness. A detailed description of the processing schedule and corresponding textural evolution has been described elsewhere [5, 6]. The test coupons of dimension 50 mm (l) × 30 mm (w) × 5 mm (t) were solutionized at 465 °C for 1.5 h and quenched in water at ambient temperature. For studying the stability of Bs texture, the heat-treated test coupons cold-rolled unidirectionally to 30, 50, and 60% reduction in thickness.

The development of crystallographic texture was measured at the half-thickness of the sheet specimens in the as-rolled condition using an Inel G3000 X-ray texture goniometer by Schultz back reflection technique. Four incomplete pole figures ($\{111\}$, $\{200\}$, $\{220\}$, and $\{311\}$) of the matrix phase were measured with 15 mm specimen translation, and the orientation distribution function (ODF) plots were

**Table 1** Chemical composition of the AA7010 Al alloy

| Elements | Zn | Mg | Cu | Zr | Fe | Si | Al |
|---|---|---|---|---|---|---|---|
| Wt. % | 6.2 | 2.3 | 1.6 | 0.13 | 0.14 | 0.12 | Balance |

calculated. From the ODFs, the recalculated pole figures were generated. Selected samples were subjected to microtexture study using a field emission gun scanning electron microscope (FEG-SEM) (Model: Zeiss Supra-55) with electron back-scattered diffraction (EBSD) facility. TEM characterization was carried out using a Technai G2 microscope operating at 200 kV.

## 3 Results and Discussion

The initial material is a solution treated hot cross-rolled alloy having a strong rotated 'Brass' (rBs) texture [5]. It has been found that the main attributes for the evolution of the strong rotated-Bs texture are (i) stability of rotated-Bs orientations under multi-step cross-rolling deformation, (ii) partially recrystallized microstructure having a high propensity of rotated-cube and -Goss orientations during inter-pass annealing, (iii) strong recrystallization resistance of near Bs oriented elongated grains, and (iv) retention of elongated grain morphology produced by Zener pinning during hot rolling [5]. The detailed mechanism of evolution of texture and microstructure of the hot cross-rolled AA7010 Al alloy and the thermal stability of the texture during extended solution heat treatments are described elsewhere [5–7].

### *3.1 Evolution of Texture and Microstructure During Cold Rolling*

The solution treated specimens are subjected to cold deformation by unidirectional rolling to study mechanical stability of the single component rBs-$\{110\}\langle 556\rangle$ texture. The cold-rolling reduction has been continued up to 60% reduction in thickness till cracks appear at the edges on further deformation. Development of texture in the specimens subjected to 30, 50, and 60% reductions in thickness has been characterized and presented in Fig. 1 in terms of $\{002\}$ pole figures and corresponding orientation intensity distribution along the α- and β-fibres. The pole figure of the 30% deformed specimen shows that the starting texture of the solution treated specimen is retained with a marginal reduction of texture intensity and concomitant increase in the spread of orientation. From the ODF analysis, the major component is found to be $\{1\ 12\ 15\}\langle 12\ \ 11\ \ 8\rangle$ with $f(g) = 17$. With further increase in deformation to 50%, the orientation distribution tends to spread between Bs and S orientations (Fig. 1b). Maximum orientation density, however, is still observed near the rotated Bs (S/Bs) orientation at $\{169\}\langle 654\rangle$ with $f(g) = 8.5$. The orientation spread reaches towards S component and a weak component $\{214\}\langle 4\ \ 12\ \ 5\rangle$ with $f(g) = 2$ can be noticed at $\varphi_2 = 65°$. For the 60% cold-rolled specimen, the maximum orientation density is found near the S/Bs

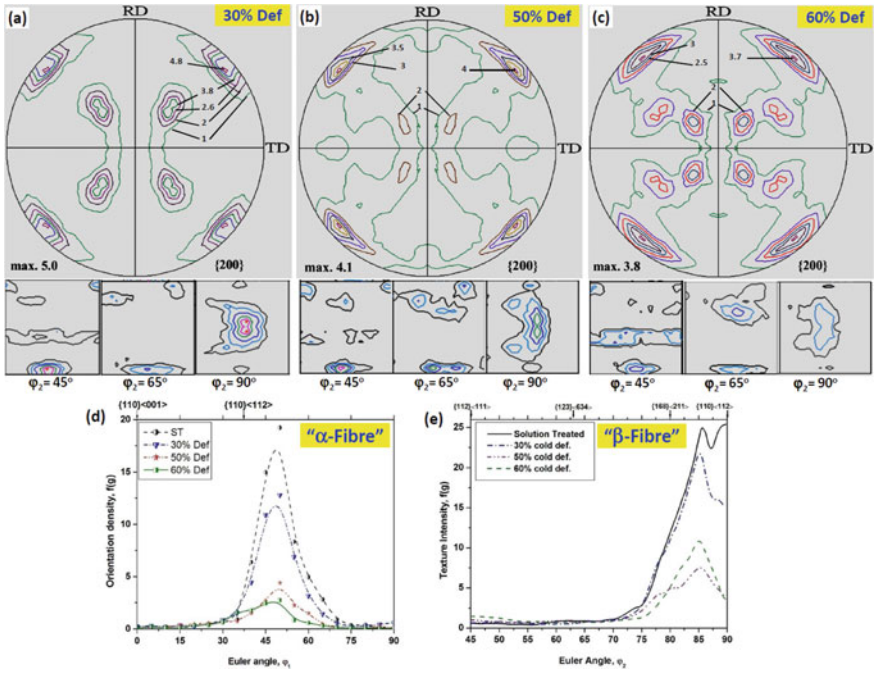


**Fig. 1** Experimentally determined {200} pole figures and $\varphi_2$ = 45, 65, and 90° ODF sections at successive stages of cold deformations: **a** 30%, **b** 50%, and **c** 60%.**d-e** corresponding orientation intensity distribution across the α- and β-fibres, respectively

component at $\{169\}\langle 12 \quad 7 \quad 6\rangle$ with $f(g) = 10$. Similar to the 50% deformed specimen, an orientation spread towards S component at $\{214\}\langle 121\rangle$ with $f(g) = 3.5$ can be noticed at $\varphi_2 = 65°$ along with an inhomogeneous $\langle 111\rangle$ fibre at $\varphi_2 = 45°$ section (Fig. 1c). Quantitative comparison of the texture with respect to the starting specimen is depicted through the α-fibre and β-fibre intensities as shown in Fig. 1d, e.

It is evident that the strong Bs component retains the location of intensity maxima during cold rolling, but the intensity maximum decreases sharply up to 60% rolling reductions. The rolling reduction also considerably increases orientation spread. The development of optical microstructure of the deformed is shown in Fig. 2. The microstructure of the 30% cold-rolled specimen (Fig. 2a) exhibits homogeneous deformation of the grains. On the other hand, the elongated grains with grain-scale shear bands (Cu-type shear bands) represent the microstructure of both the 50 and 60% deformed specimens. For the 50% deformed specimen, one set of shear bands are observed approximately at 35° to the rolling plane in few grains, whereas two sets of intersecting shear bands at $\sim \pm 38°$ in most of the grains of 60% deformed specimen. A typical intersection of shear bands producing an 'X'-junction is shown in the inset of Fig. 2c.

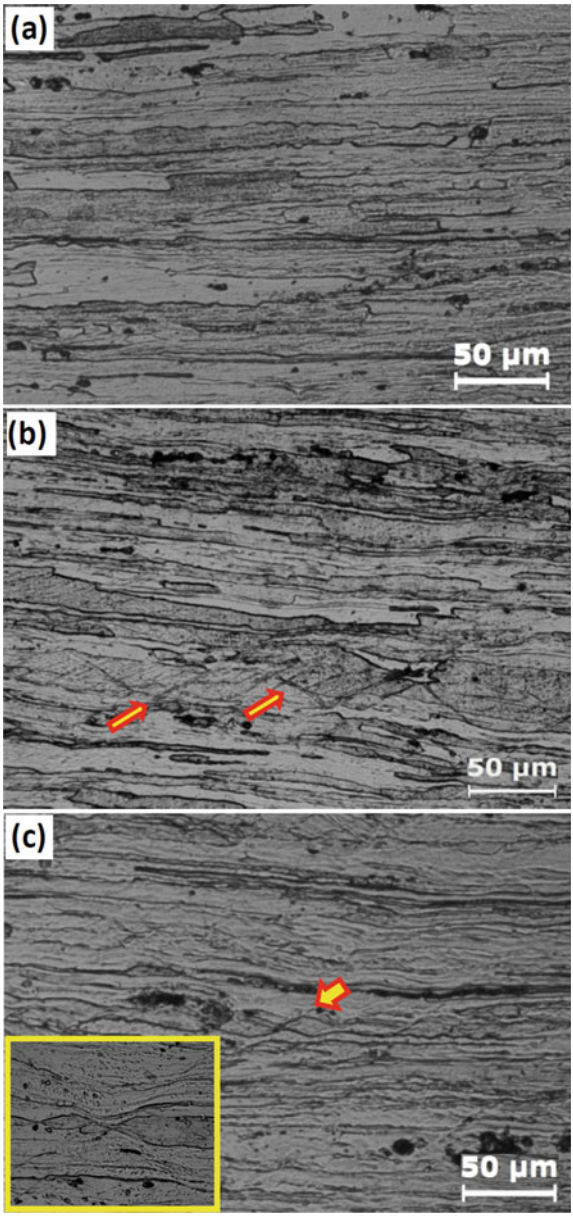


**Fig. 2** Optical microstructures observed at the long transverse sections of the specimens cold rolled to **a** 30%, **b** 50%, and **c** 60% deformation (presence of shear bands marked by arrows). **c**-Inset: magnified view of the shear band crossing

A detailed study based on EBSD analysis incorporating orientation, grain boundary character, and misorientation distribution has been carried out on the deformed specimens. The inverse pole figure (IPF) maps of the deformed specimens further corroborate the optical microstructural features in conjunction with misorientation histograms and kernel average misorientation maps (Fig. 3). Grains

of 30% deformed specimen are uniformly deformed and traces of localization of slip activities (marked by arrows) can be noticed. Deformation becomes significantly heterogeneous with the increase in rolling reduction, and at 50% cold-rolling reduction, grain-scale shear bands form (Fig. 3b). Following 60 and 60% cold deformations, grains become severely fragmented by the presence of shear bands extending a few grains and producing clear grain boundary offsets (Fig. 3c). The formation of extensive shear bands is accompanied by an increase in the grain misorientation spread in agreement with the observations of global texture analysis. The gradual increase in misorientation (Both LAGB and HAGB) with deformation is evident from the histograms (Fig. 3d–f) in conjunction with a sharpening of orientation gradients across the grains as depicted by the KAM maps (Fig. 3g–i).

Characterization of deformed microstructure has further been complemented by transmission electron microscopy. Figure 4 represents montages of bright field images of the longitudinal sections of 50, and 60% deformed specimens. Typical deformation microstructure at low strains consisting of basic '*pre-shear band-like structures*' (microbands) is believed to be developed by slip only and distinguishing features of such microstructures is the formation of thin microbands (usually 0.1–0.5 μm thick) on the slip planes. Microbands are observed in isolated grains spreading across a few subgrains parallel to {111} plane traces, and in few localized areas along the microband propagation path, they are hardly distinguishable from the matrix losing their structural features (Fig. 4a). Furthermore, bands have a

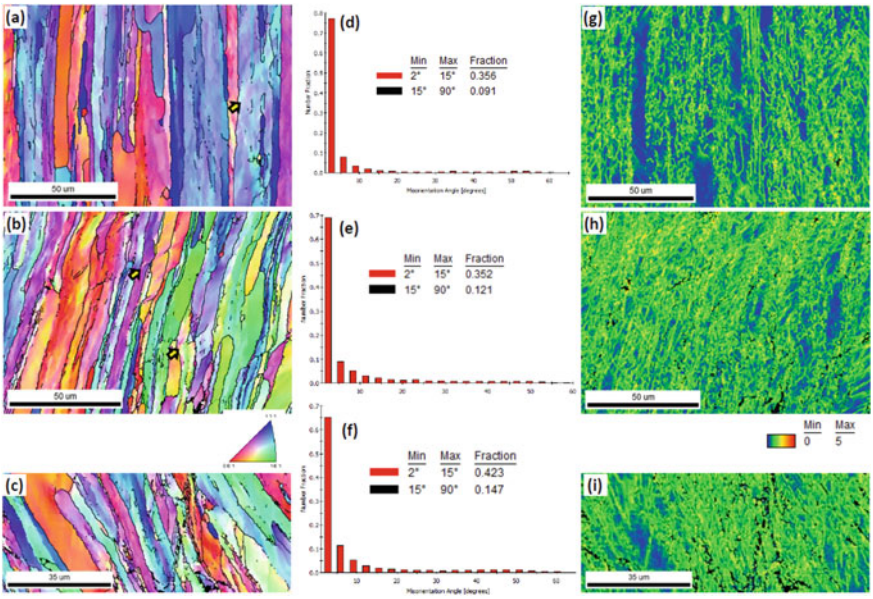


**Fig. 3** EBSD IPF maps, corresponding misorientation distribution histograms, and KAM maps of the cold-rolled specimens subjected to **a**, **d**, **g** 30% deformation, **b**, **e**, **h** 50% deformation, and **c**, **f**, **i** 60% deformation

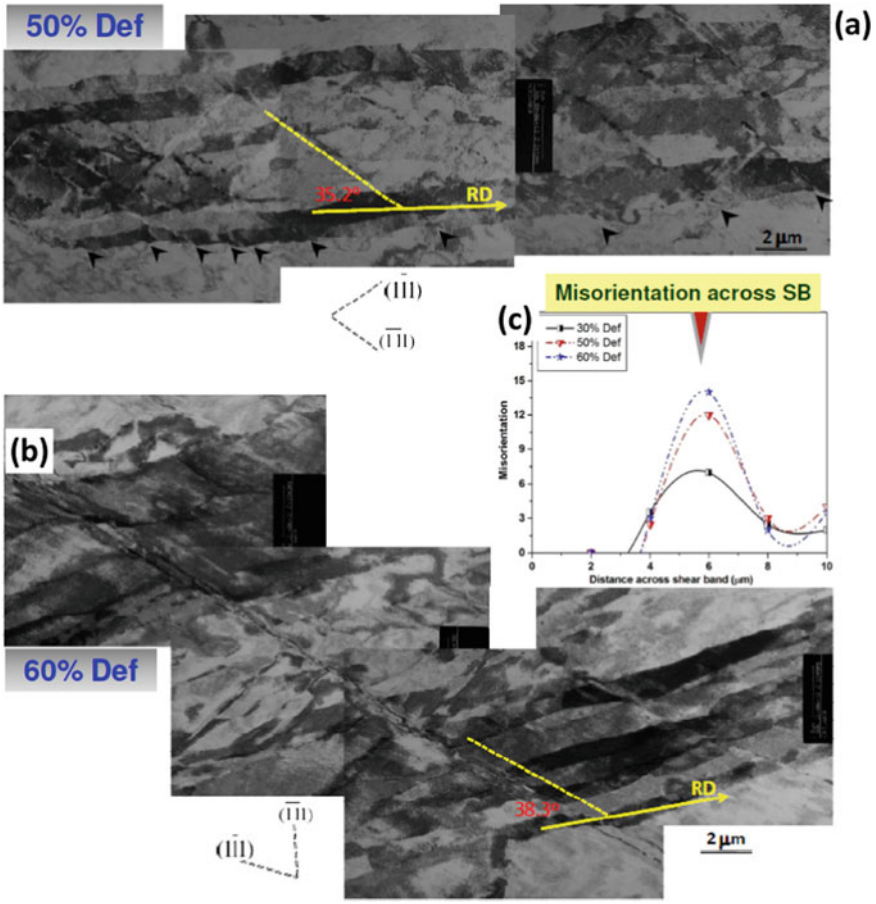


**Fig. 4** **a**, **b** Montages of TEM micrographs for 50 and 60% deformed specimens showing the spread of shear bands (SB) across the subgrains. [Electron beam is nearly parallel to $\langle 110 \rangle_{Al}$] **c** average misorientations across the SBs as a function of deformation percentage

non-uniform dislocation distribution along the length forming the so-called island structure at the front of the band. Observations are in agreement with that of Korbel and Martin [8]. With increasing, deformation level abundance of microbands turning into shear bands increases sharply producing sharp boundary offsets. The shear strain in the band, determined at the offset length, has been measured to be as high as 6 with a concomitant increase in misorientation across them (Fig. 4c). However, the width of the microband-turned shear bands do not vary significantly with increasing strain levels. The salient features of the deformation microstructures can be summarized as (i) propagation of shear bands through subboundaries resulting in distinct shear offsets at the boundaries, (ii) discrete shear bands parallel to the operating slip plane {111} with almost no increase in bandwidth, and

(iii) misorientation increases across the shear bands a function of deformation. It is clear from the foregoing discussion that the evolution of microstructural features and consequential variations in texture are associated with the formation of microbands and shear bands. The relationship between the orientation stability and shear band formation is discussed further in the following section.

### *3.2 Effect of Shear Band Formation on Texture Stability*

The evolution of crystallographic texture and microstructure in the present study has two prominent features: (i) the maximum texture intensity continues to be near the Bs orientation following unidirectional cold rolling up to 60% thickness reduction, although with the increase in deformation, the pole figures tend to show a considerable spread of orientations, and (ii) orientation spread near the Bs-S components across the β-fibre becomes predominant as the amount of deformation increases. Concomitantly, it has been observed that conversion of the microbands into the shear bands occurs with increasing cold deformation level and results in considerable misorientation across them. This is consistent with the observations and mechanisms proposed earlier [9–13].

It is well known that macroscopic shear bands have precursors in microbands that represent an avalanche of dislocation glide in a crystallographic slip system [10, 11]. Investigations aimed at revealing the mechanism by which microbands are organized into the macroscopic shear bands suggest that instability of dislocation substructure is responsible for nucleation, while its growth is facilitated by the stress concentrations [11]. The evolution of shear band structure with increasing deformation is analysed through high-resolution EBSD band contrast maps superimposed with boundaries as depicted in Fig. 5. It can be observed that the mechanism of formation of a macroscopic shear band is essentially considered to be a two-stepped process that involves nucleation of microbands by dislocation avalanche and its subsequent conversion into a macroscopic shear band when encountering grain boundary or an obstacle that prevents long-distance dislocation glide. High local misorientations generated across these bands suggest a large stress concentration at the front of the bands (Fig. 4c). Furthermore, it is often observed that in process of converting a microband into shear bands, some microbands are effectively stopped at the grain boundaries giving a strain contour, while the others are able to penetrate the boundaries with a prominent slip offset which is consistent with the observation by Korbel and Martin [8].

It has been pointed out by Dillamore et al. [12] that shear bands form due to plastic instability triggered by geometrical softening and it has been shown that the presence of preferred orientation is an important factor in determining the angle. Dillamore et al. [12] have formulated a necessary condition for the formation of a grain-scale shear band as:

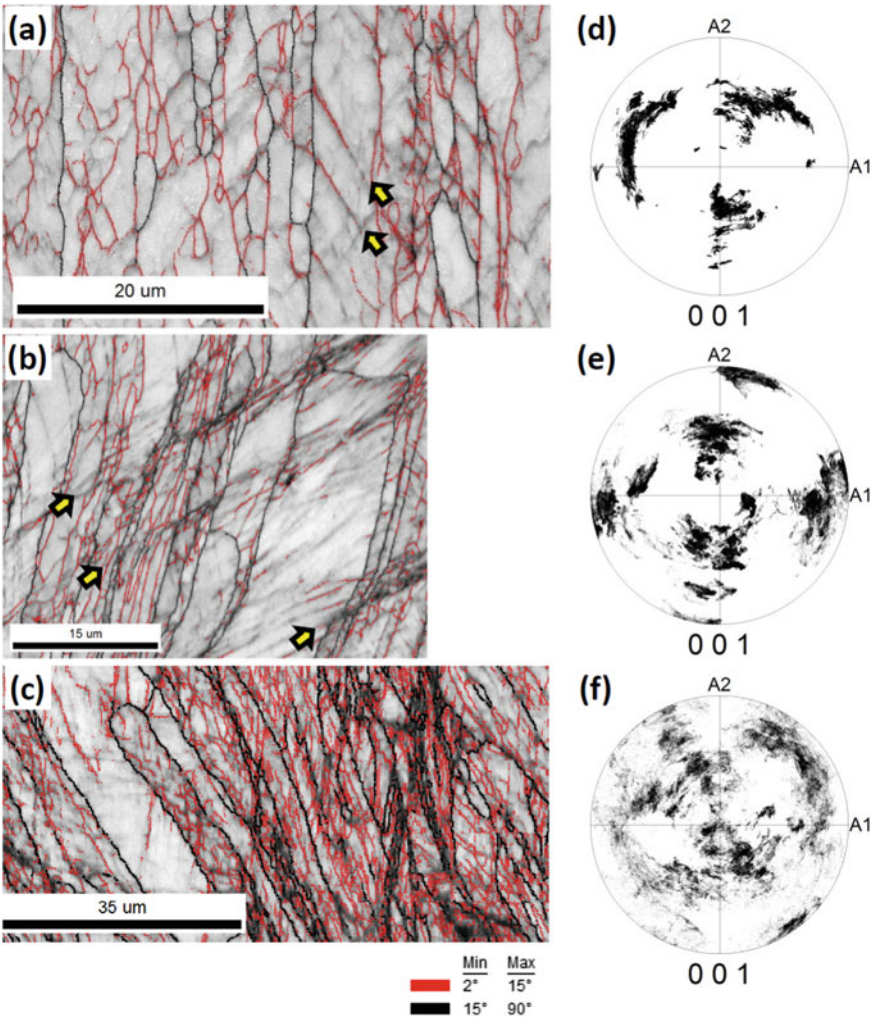


**Fig. 5** EBSD band contrast maps overlaid with low and high angle boundaries of **a** 30%, **b** 50%, and **c** 60% deformed samples (presence of shear bands marked by arrows). **d–f** Corresponding {002} pole figures showing orientation spread

$$\frac{1}{\sigma}\frac{\mathrm{d}\sigma}{\mathrm{d}\varepsilon} = \frac{n}{\varepsilon} + \frac{m}{\dot{\varepsilon}}\frac{\mathrm{d}\dot{\varepsilon}}{\mathrm{d}\varepsilon} + \left(\frac{1+n+m}{M}\right)\frac{\mathrm{d}M}{\mathrm{d}\varepsilon} - \frac{m}{N}\frac{\mathrm{d}N}{\mathrm{d}\varepsilon} \leq 0$$

where **n** and **m** represent the work hardening exponent and strain rate sensitivity, respectively; **M** is the Taylor factor, and **N** is the mobile dislocation density. With the usual behaviour of materials with positive strain, work hardening rate, and strain rate sensitivity, it is apparent that a probable factor in holding the above inequality

permissible is the term ($dM/d\varepsilon$) that corresponds to geometrical softening. Shen and Duggan [9] have considered the effect of microband formation on the orientation meta-stability during cold deformation. It has been shown that microbands can occur in the grains with orientations such that its transverse direction (TD) is nearly parallel to either ⟨110⟩ or ⟨111⟩ axes and the rolling direction along the high slip fraction direction. In such a case, grain rotation is oscillatory between the two orientations having a variation in rotation rate from negative to positive. This leads to stability of texture components that satisfy the criteria such as the {110}⟨556⟩ in the present case. With increasing the level of deformation, however, the microbands are converted into shear bands and the strain becomes increasingly localized within these bands leading to a net positive rotation around the TD as observed experimentally in the present study (Fig. 5d–f). The situation has been described by Paul et al. [13]. The salient feature of the texture evolution is the rotation around the ⟨112⟩ axis within the shear band area facilitated by a change of the initially co-planar slip systems to a single slip. This can lead to texture development near the Bs-S regions of the β-fibre. The present case can, therefore, be considered as an experimental verification for the above mechanism.

In summary, microstructural evolution shows the formation of grain-scale and discrete shear bands with increasing cold deformation. The width of such bands does not increase with deformation but sharp misorientations are developed across them. It indicates a strong tendency for a localized slip with a single slip operation. Detailed analysis of microtexture in conjunction with TEM studies establishes that the rotation around the ⟨112⟩ axis within the shear band area is facilitated by the change of the co-planar slip systems to a single slip. This can lead to texture development near the Bs-S regions of the β-fibre. This type of rotation within well-developed shear bands is believed to be responsible for the evolution of texture components near the Bs-S fibre. Finally, it is to be noted that the development of such shear band induced texture could possibly be deleterious to the mechanical properties, especially in terms of uniform elongation, as it could promote severe deformation localization and associated shear failure. Since the shear band development is intensified by the relatively coarser grain size, a possible remedy may lie in the grain refinement by the application of a suitable thermo-mechanical processing schedule.

## 4 Conclusions

(1) Unidirectional cold rolling results in retention of the rotated-Bs component with a continuous decrease in intensity of this component as well as a substantial increase in the spread of orientation. Microstructural evolution shows the formation of grain-scale and discrete shear bands. The width of such bands does not increase with deformation but sharp misorientations are developed across them.

(2) At low deformations (∼30%), homogeneous deformation of the material facilitates the retention of rBs orientation, while at higher deformation, the localized shear band formation results in orientation spread.

**Acknowledgements** The authors would like to thank the Director, DMRL for his constant support and encouragement. This research work has been funded by the Defence Research and Development Organization (DRDO), Government of India.

## References

1. Hosford WF (1966) Texture strengthening. Metals Eng Qtrly 13–19
2. Bull MJ, Lloyd DJ (1986) Proceedings of 3rd international conference on Al-Li alloys (Baker C, Gregson PJ, Harris SJ, Peel CJ (eds)). The Institute of Metals, London, pp 402–441
3. Hirsch JR (1990) International conference on recrystallization in metallic materials (recrystallization '90) (Chandra T (ed)). The Minerals, Metals and Materials Society, Warrendale, pp 759–768
4. Singh AK, Saha GG, Gokhale AA, Ray RK (1998) Evolution of texture and microstructure in a thermomechanically processed Al-Li-Cu-Mg alloy. Metall Mater Trans A 29A:665.https://doi.org/10.1007/s11661-998-0147-5
5. Mondal C, Singh AK, Mukhopadhyay AK, Chattopadhyay K (2011) Formation of a single, rotated-brass {110} ⟨556⟩ texture by hot cross-rolling of an Al–Zn–Mg–Cu–Zr alloy. Scripta Mater 64:446
6. Mondal C, Singh AK, Mukhopadhyay AK, Chattopadhyay K (2013) Effects of different modes of hot cross-rolling in 7010 aluminum alloy: part I. Evolution of microstructure and texture. Metall Mater Trans A 44:2746–2763. https://doi.org/10.1007/s11661-013-1626-x
7. Mondal C, Singh AK, Mukhopadhyay AK, Chattopadhyay K (2012) Thermal and mechanical stability of the single component rotated brass texture in a 7010 aluminum alloy. Mater Sci Forum 702–703:279–282. https://doi.org/10.4028/www.scientific.net/MSF.702-703.279
8. Korbel A, Martin P (1986) Microscopic versus macroscopic aspect of shear bands deformation. Acta Metall 34:1905
9. Shen K, Duggan BJ (2007) Microbands and crystal orientation metastability in cold rolled interstitial-free steel. Acta Mater 55:1137
10. Malin AS, Hatherly M (1979) Microstructure of cold-rolled copper. Met Sci 13:463
11. Korbel A, Embury JD, Hatherly M, Martin PL, Erbsloh HW (1986) Microstructural aspects of strain localization in Al-Mg alloys. Acta Metall 34:1999
12. Dillamore IL, Roberts JG, Bush AC (1979) Occurrence of shear bands in heavily rolled cubic metals. Met Sci **13**:73
13. Paul H, Driver JH, Maurice C, Piatkowski A (2007) The role of shear banding on deformation texture in low stacking fault energy metals as characterized on model Ag crystals. Acta Mater **55**:575

# Microscopic and Magnetic Investigations in Sputtered Sm-Fe Thin Films


**Himalay Basumatary, J. Arout Chelvane, Vajinder Singh, and Rajeev Ranjan**

**Abstract** This article reports the structure, microstructure, and magnetic properties of Sm-Fe films grown on Si <100> by DC magnetron sputtering. Films were grown with varying argon gas pressures, namely 5, 10 and 15 m.Torr, and keeping the sputtering power constant at 100 W. All the films were found to be amorphous in nature irrespective of the processing conditions. Microscopic investigation of film surface showed an island kind of surface morphology in the form of globules, whose sizes increased with increase in argon gas pressure. Thermomagnetic measurements indicated ferromagnetic behavior at room temperature for the film deposited with 10 and 15 m.Torr gas pressures. Magnetic measurements showed low anisotropy coupled with low coercivity for the films grown at higher gas pressures. A maximum magnetostriction of about 390 micro-strains has been achieved for an applied magnetic field of about 6 kOe.

**Keywords** Magnetostrictive thin films · Scanning electron microscopy · Magnetization measurements

## 1 Introduction

Magnetostrictive materials form an important class of smart materials that can be strained with the application of an external magnetic field. These materials convert energy between magnetic and elastic states, and for this reason, magnetostrictive material has been employed for a wide variety of applications such as actuators, sensors, and transducers. Magnetostriction being an inherent property of ferromagnetic materials, it does not degrade with respect to time as do some poled piezoelectric materials. C15 based rare earth transition metal intermetallics exhibit high magnetostriction owing to strong magnetic anisotropy. Among the binary

H. Basumatary · J. Arout Chelvane (✉) · V. Singh
Defence Metallurgical Research Laboratory, Hyderabad, India

H. Basumatary · R. Ranjan
Department of Materials Engineering, Indian Institute of Science, Bangalore, India



P. Ghosal et al. (eds.), *Applications of Microscopy in Materials and Life Sciences*, Springer Proceedings in Materials 11,
https://doi.org/10.1007/978-981-16-2982-2_17

alloys, $TbFe_2$ and $SmFe_2$ alloys exhibit highest positive and negative magnetostriction, respectively [1]. Although a plethora of literature is available on Tb-Fe based magnetostrictive alloys, studies on $SmFe_2$ based alloys are limited owing to the challenges such as (i) process optimization due to high vapor pressure of Sm, (ii) reactivity of Sm-Fe alloy, and (iii) complexity in device design. [2]. However, $SmFe_2$ alloy in thin-film form finds wide applications as magnetic microdevices [3–5]. Further, the overall deflection of magnetostrictive-substrate cantilever assembly can be enhanced by utilizing a combination of positive and negative magnetostrictive thin films in the form of a bimorph structure which is desirable for microactuator applications. Considering these factors, it is important to carry out a detailed study on this thin film to understand the magnetic properties thoroughly. Further, it is observed from literature that there are only few studies on the understanding of structure and magnetic properties of sputter deposited Sm-Fe films, with respect to various processing conditions [2–8]. Hence, in the current study, an investigation has been taken up to understand the effect of one of the sputtering parameter, namely argon gas pressure on the structure, microstructure, and magnetic properties of Sm-Fe films.

## 2 Experimental Details

Sm-Fe films were deposited at room temperature on Si <100> substrates by dc magnetron sputtering (Sputtering unit make: M/s. LJ-UHV Technologies, Taiwan) employing an alloy target with a nominal composition of $Sm_{33}Fe_{67}$. Prior to sputtering, a base pressure of about $1 \times 10^{-8}$ Torr has been achieved in the sputtering chamber. Films were grown with varying argon gas pressure (viz., 5, 10, 15 m.Torr) and keeping the sputtering power constant at 100 W. The deposition time (60 min) and target to substrate distance (6 inches or 150 mm) were kept constant for all the experiments. Aluminium layer of 3 nm thin was used as a capping layer to prevent oxidation of films. Thicknesses of the films were determined by using a stylus profilometer. Surface topography of the films was traced by employing an atomic force microscope (AFM). Structural investigations were carried out by using grazing incidence X-ray diffraction (GIXRD). Surface topography of the films was evaluated with the aid of a field emission gun scanning electron microscope (FEGSEM). Magnetic measurements along in-plane direction were measured by using a SQUID magnetometer. Field-cooled (FC) and zero field-cooled (ZFC) measurements were carried out at an applied magnetic field of 0.5 kOe in the temperature range 4–390 K. Position-sensitive detector-based optical technique was used to measure magnetostriction in thin films.

**Table 1** Film thickness, surface roughness, composition, Curie temperature (Tc), and magnetostriction of Sm-Fe films deposited under varying sputtering parameters

| Sputtering parameters | | Composition (±1 at. %) | Film thickness (±2 nm) | Surface roughness (±0.1 nm) | $T_c$ (±1 K) | Magnetostriction (±5 -strains) |
|---|---|---|---|---|---|---|
| Power | Ar pressure | | | | | |
| 100 | 5 | $Sm_{42}Fe_{58}$ | 205 | 2.7 | 250 | – |
| 100 | 10 | $Sm_{38}Fe_{62}$ | 250 | 2.8 | 370 | 390 |
| 100 | 15 | $Sm_{38.5}Fe_{61.5}$ | 270 | 2.9 | 370 | 380 |

## 3 Results and Discussions

The variation of film thickness for films grown with different Ar pressure is given in Table 1. It is evident from the table that with increase in Ar gas pressures, the thickness of Sm-Fe film increases. This could be correlated with the increase in the number of Ar ions with increase in gas pressure. Increase in the number of Ar ions dislodges more atoms from the sputtering target which in turn increases the overall film thickness. The AFM images of Sm-Fe films grown at different gas pressures such as 5, 10, and 15 m.Torr are shown in Fig. 1a–c, respectively. All the films are found to exhibit an island kind of morphology in the form of globules whose sizes increase with increase in gas Ar pressure. This can be attributed to the increase in film thickness with increase in Ar pressure. The rms surface roughness estimated from AFM images are displayed in Table 1. With increase in argon gas pressure, there is a slight increase in the surface roughness of the films. This can be correlated with the increase in the size of the globules with increase in processing gas pressure.

Figure 2a–c shows the FEGSEM micrographs of Sm-Fe thin films deposited under varying gas pressures, namely 5, 10, and 15 m.Torr, respectively. The film processed with lower gas pressure, viz., 5 m.Torr exhibit a random distribution of fine globular islands. However, with subsequent increase in Ar gas pressure, the sizes of islands are found to increase considerably. This again can be attributed to the increase in the thickness of the films with increase in Ar pressure as observed from Table 1. FESEM microscopy observations are found to be in good agreement with the AFM studies shown in Fig. 1. The composition of the films determined using energy-dispersive spectroscopy technique is found to vary with change in processing gas pressure (Table 1). The concentration of Fe in the film is found to increase from 58 at.% to 62 at.% when the Ar pressure is increased from 5 to 10 m. Torr. At 15 m.Torr Ar pressure, the film composition is found to be saturated. This could be attributed to the increase in sputtering yield with increase in number of Ar ions. Usually, the sputtering yield increases initially with increase in Ar ions and reaches a maximum value, and then, it decreases again [9, 10]. Fe being relatively lighter, increase in sputtering yield of Fe can be more prominent when compared to heavier Sm atoms. As a result, Fe concentration in the film increases. With further increase in Ar pressure, collision among the Ar gas atoms also increases which

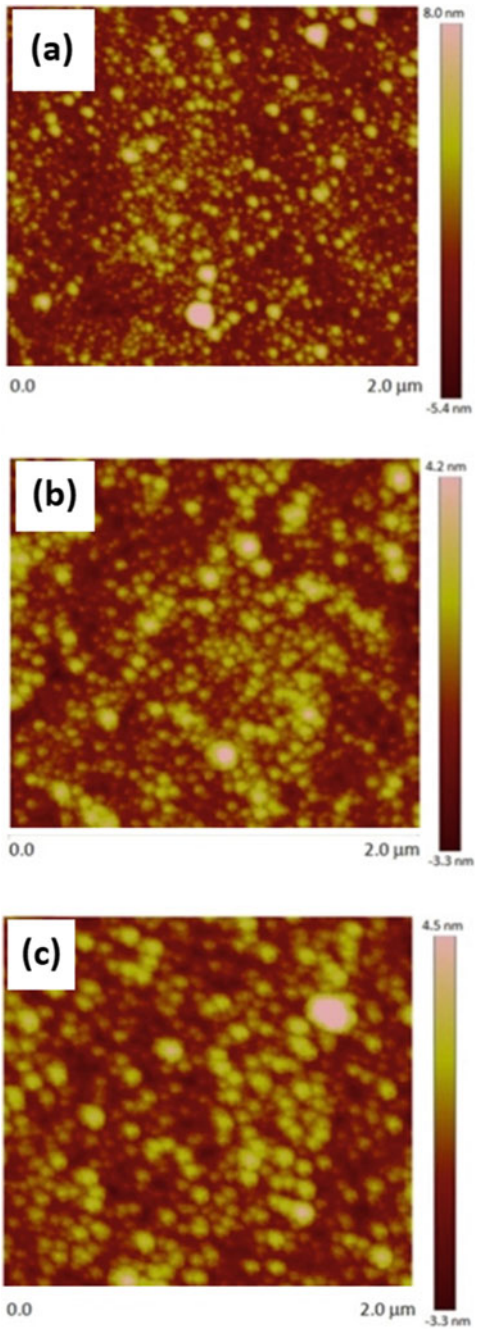


**Fig. 1** AFM images of Sm-Fe films deposited at different sputtering Ar pressure, **a** 100 W & 5 m. Torr, **b** 100 W & 10 m.Torr, **c** 100 W and 15 m.Torr

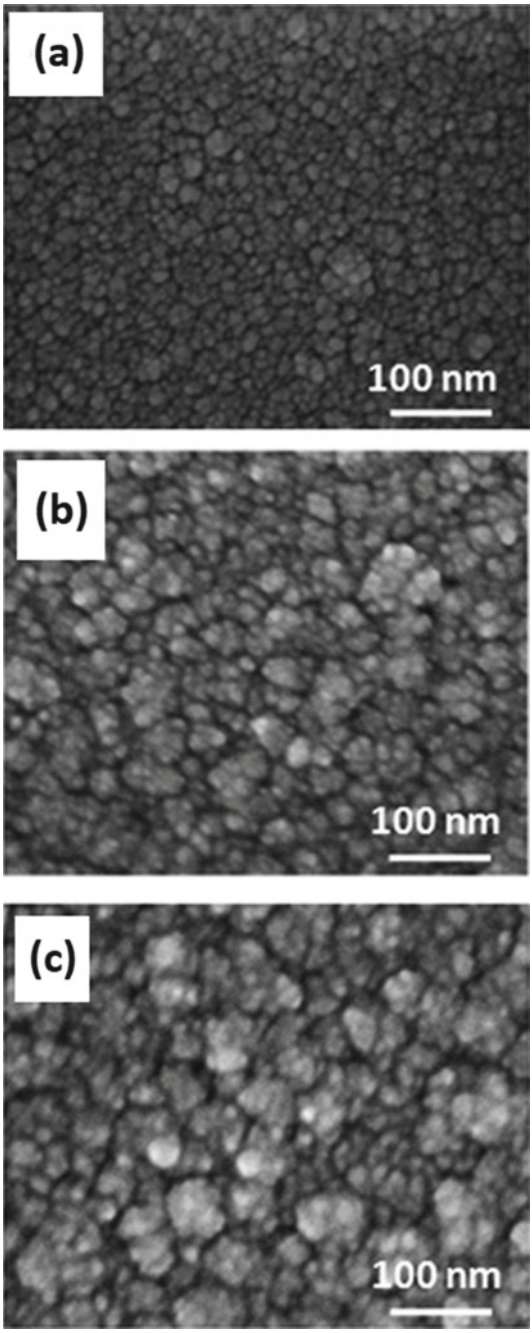


**Fig. 2** FEGSEM images of Sm-Fe films deposited at different sputtering Ar pressure. **a** 100 W & 5 m. Torr, **b** 100 W & 10 m.Torr, **c** 100 W and 15 m.Torr

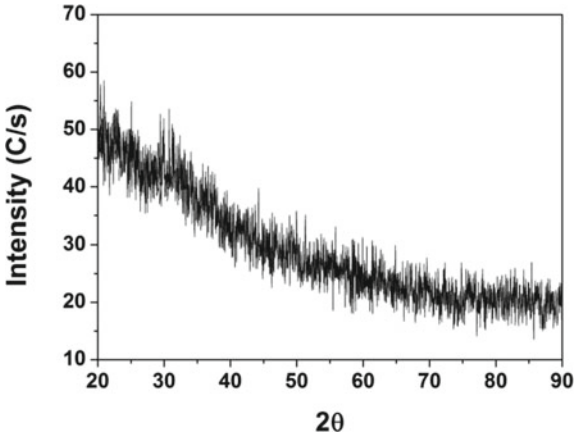


**Fig. 3** GIXRD pattern of Sm-Fe film deposited at 100 W power and 15 m.Torr Ar pressure

nullify the increase in sputtering yield. Therefore, at 15 m.Torr Ar pressure, the film composition is found to be nearly constant.

Structural properties of Sm-Fe films deposited under different gas pressures were studied using GIXRD. A representative GIXRD pattern of Sm-Fe film deposited at 100 W sputtering power and 15 m.Torr Ar gas pressure is shown in Fig. 3. All the films are found to be amorphous in nature irrespective of the sputtering processing conditions. This can be attributed to the large difference in atomic size between Sm & Fe and very fast cooling involved during sputtering process. Sputter-deposited Tb-Fe thin films have shown similar structural behavior with change in processing conditions [11].

Thermomagnetic studies on Sm-Fe films were carried out by measuring the magnetization with respect to temperature under ZFC and FC conditions in the temperature range of 4–390 K. For each film, ZFC and FC plots were traced at a constant magnetic field of about 0.5 kOe and such thermomagnetic measurements are shown in Fig. 4. The film deposited at 5 m.Torr gas pressure exhibits Curie temperature less than room temperature. However, with subsequent increase in processing gas pressure, the Curie temperature is found to increase. The magnetic ordering temperature estimated from thermomagnetic plots are shown in Table 1. The increase in Curie temperature with increase in the Ar gas pressure can be corroborated with the increase in the Fe content with increase in gas pressure. In addition to this formation of larger islands with increase in Ar gas pressure as evidenced from AFM and FEGSEM, studies can also aid in increasing the Curie temperature [12, 13]. Presence of bigger islands could also increase the Curie temperature of Sm-Fe films owing to the increase the exchange interactions. Island size-dependent magnetic properties in Tb-Fe films have been reported earlier by Basumatary et al. [11]. Further, from the thermomagnetic plots, it is also interesting to note that the film deposited at lower Ar gas pressure exhibits large irreversibility between the ZFC and FC plots. This could be probably due to the presence of large anisotropy in the film owing to the high Sm content present in the film.

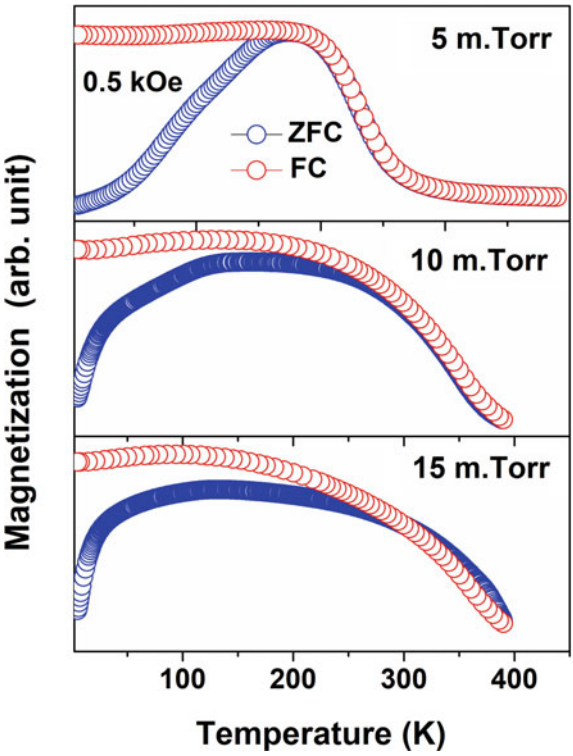


**Fig. 4** Thermomagnetic plots measured at 0.5 kOe magnetic field for Sm-Fe films deposited under varying sputtering Ar pressure. **a** 100 W, 5 m.Torr, **b** 100 W, 10 m.Torr and **c** 100 W, 15 m.Torr

The decrease in the anisotropy with increase in gas pressure is clearly seen from the magnetization measurements as indicated in Fig. 5. When the sample is cooled down to low temperature without magnetic field, the moments are freezed and application of magnetic field does not change the magnetization value. However, as the temperature is increased, the magnetization also increases due to contribution from the thermal energies and reaches an equilibrium value. Further increase in temperature leads to decrease in magnetization which is in accordance with the Curie–Wiess law [14]. During FC, the magnetization state is retained and a large difference in ZFC and FC curve is obtained at low temperature. The large irreversibility in ZFC and FC plots in this film indicates presence of strong anisotropy in this film (at low temperature). This can further be evidenced from the low temperature magnetization measurements which show a large coercivity at 5 K (Fig. 5). The bifurcation of ZFC and FC is found to be small for the films deposited at higher gas pressure (100 W, 10–15 m.Torr) (Fig. 3). With increase in magnetic field strength, the ZFC and FC plots are found to merge with each other. The magnetization measurements carried out for the films processed at higher gas pressures indicate a strong ferromagnetic behavior at room temperature with low coercivity. From the magnetization measurements, it is clearly evident that films grown at higher gas pressure namely 10 and 15 m.Torr are suitable for practical magnetostrictive applications.

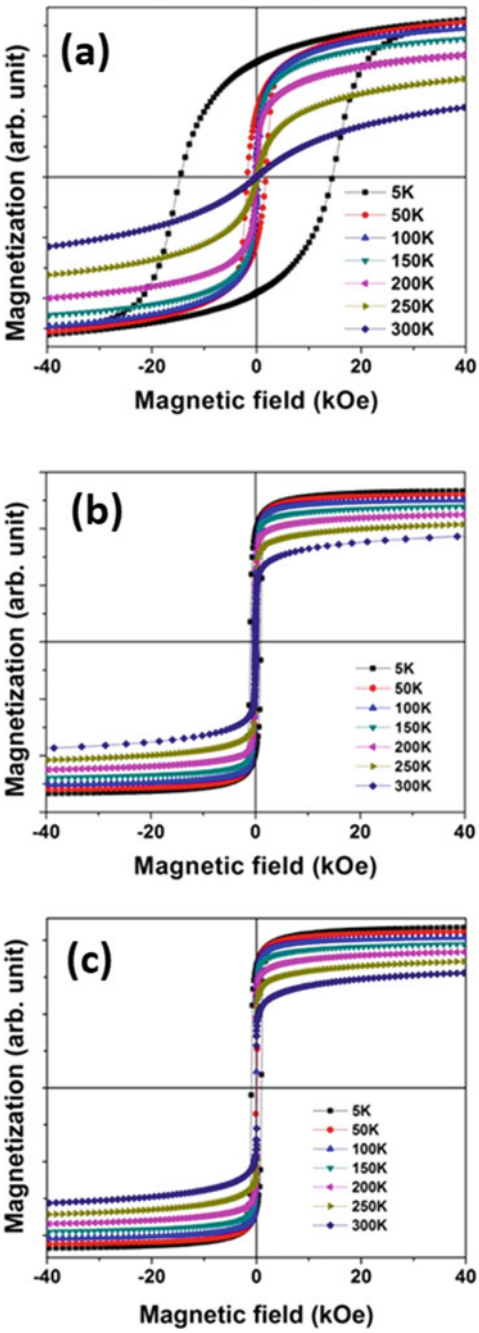


**Fig. 5** Magnetization curves measured at different temperatures for Sm-Fe films deposited under varying sputtering Ar pressure. **a** 100 W, 5 m.Torr, **b** 100 W, 10 m.Torr and **c** 100 W, 15 m.Torr

Using optical technique, magnetostriction was measured for the films deposited at 100 W sputtering power and Ar pressure of 10 m.Torr and 15 m.Torr, as these two films only exhibit Curie temperature above room temperature (Table 1). A maximum magnetostriction of $\sim -390$ micro-strains at a magnetic field of 6 kOe has been obtained in the film deposited at 10 m.Torr. Nearly same value of magnetostriction is obtained for the film deposited at 15 m.Torr Ar pressure. This can be attributed to the similarity in film composition and thicknesses of the two films. The magnetostriction value obtained from the current study is comparable with the value reported by Honda [3].

## 4 Conclusions

Structural, microstructural, and magnetic properties of Sm-Fe thin films deposited on Si (100) substrates under different sputtering Ar gas pressures were investigated. AFM and FEGSEM studies indicated an island kind of surface morphology whose sizes increased with increase in Ar gas pressure. GIXRD studies showed that all the as deposited Sm-Fe films are amorphous in nature. Thermomagnetic measurements indicated Sm-Fe films deposited at lower Ar pressure exhibited Curie temperature below the room temperature. This was attributed to the presence of very fine islands and composition rich in Sm content. Curie temperature of about 380 K was obtained for the films deposited at higher gas pressures. A maximum magnetostriction of $\sim 390$ micro-strains has been obtained at magnetic field strength of 6 kOe for the film deposited at 100 W sputtering power and 10 m.Torr Ar pressure.

**Acknowledgements** Authors thank Group Head and Members of AMG for their constant support and encouragements. Authors are grateful to Director, DMRL, for giving the permission to publish this work.

## References

1. Clark AE (1977) Introduction to highly magnetostrictive rare-Earth-materials. U S Navy J. Underwater Acoustics 27:109
2. Lim SH, Choi YS, Han SH, Kim HJ, Shima T, Fujimori H (1998) Magnetostrictiion of Sm-Fe and Sm-Fe-B thin films fabricated by RF magnetron sputtering. J Magn Magn Mater 189:1–7
3. Honda T (1993) Magnetostriction of sputtered Sm-Fe thin films. IEEE Trans Magn 29(6): 3126–3128
4. Honda T, Arai KI, Yamaguchi M (1994) Fabrication of magnetostrictive actuators using rare-earth (Tb, Sm)-Fe thin films. J Appl Phys 76:6994–6999
5. Hayashi Y, Honda T, Arai KI, Ishiyama K, Yamaguchi M (1993) Dependence of magnetostriction of sputtered Tb-Fe films on preparation conditions. IEEE Trans Magn 29(6):3129–3131
6. Sun H, Tomida T, Hirosawa S (1997) Magnetic properties and microstructure studies on Sm-Fe magnetic thin films. J Appl Phys 81:328

7. Hwang SW, Kim J, Lim SU, Kim CK, Yoon CS (2007) Magnetostrictive properties and microstructure of thermally annealed Sm–Fe thin films. Mater Sci Eng A 449–451:378–381
8. Lou C, Kou Y, Lyu X, Zhang W (2015) Electrodeposition of Sm-Fe thin film in aqueous solution under a high magnetic field. Int J Electrochem Sci 10:9687–9694
9. Chopra KL (1969) Thin film phenomena. McGraw-Hill
10. Harsha KSS (2006) Principle of physical vapor deposition. Elsevier
11. Basumatary H, Arout Chelvane J, Sridhara Rao DV, Kamat SV, Ranjan R (2016) Effect of sputtering parameters on the structure, microstructure and magnetic properties of Tb-Fe films. Thin Solid Films 583:1
12. du Tremolet E, de Lacheisserie K, Mackay JB, Peuzin JC (1998) From bulk to film magnetostrictive actuators. J Alloy Compd 275–277:685–691
13. Betz J, Mackay K, Givord D (1999) Magnetic and magnetostrictive properties of amorphous $Tb_{(1-x)}Co_x$ thin films. J Magn Magn Mater 207:180–187
14. Cullity BD, Graham CD (2008) Introduction to magnetic materials, 2nd edn. Wiley-IEEE Press

# Expanding the Application Space of Ion Microscopy


**Fabián Pérez-Willard, Alexandre Laquerre, Tobias Volkenandt, Michael W. Phaneuf, Raymond Hill, and John A. Notte**

**Abstract** In this paper, we review selected recent innovations to focused ion beam (FIB) instrumentation. Three examples show how new inventions and refinement of existing workflows continue to expand the large application space already covered today by FIB, FIB-SEM, and FIB-FIB solutions enabling improved or even completely new workflows for sample preparation and microstructure characterization. At one end of the FIB application space, the recent addition of a high-efficiency magnetic sector field spectrometer to gas-field ion source (GFIS) systems now adds sub-15 nm analytical spectrometry to most precise ion imaging and patterning capabilities. At the opposite end, the combination with ultra-short pulsed laser ablation allows to link FIB analyses to macroscopic scales up to the mm range. Even well-established workflows like FIB-SEM tomography continue being optimized striving for a more and more accurate 3D representation of matter.

**Keywords** HIM · SIMS · Nanopatterning · FIB-SEM · FIB-SEM Tomography · LaserFIB

## 1 Introduction—Different Ion Species for Different Applications

Focused ion beams have been demonstrated from many of the elements in the periodic table [1–3]. Different source types are used for their generation: The liquid metal ion source (LMIS), the plasma ion source, and the gas-field ion source (GFIS) are widely commercially available and used on multi-purpose FIB systems [4, 5].

F. Pérez-Willard (✉) · T. Volkenandt
Carl Zeiss Microscopy GmbH, Carl-Zeiss-Str. 22, 73447 Oberkochen, Germany
e-mail: fabian.perez-willard@zeiss.com

A. Laquerre · M. W. Phaneuf
Fibics Inc., 1431 Merivale Rd 100, Ottawa, ON K2E 0B9, Canada

R. Hill · J. A. Notte
Carl Zeiss SMT, Inc., Peabody, MA 01960, USA



P. Ghosal et al. (eds.), *Applications of Microscopy in Materials and Life Sciences*, Springer Proceedings in Materials 11,
https://doi.org/10.1007/978-981-16-2982-2_18

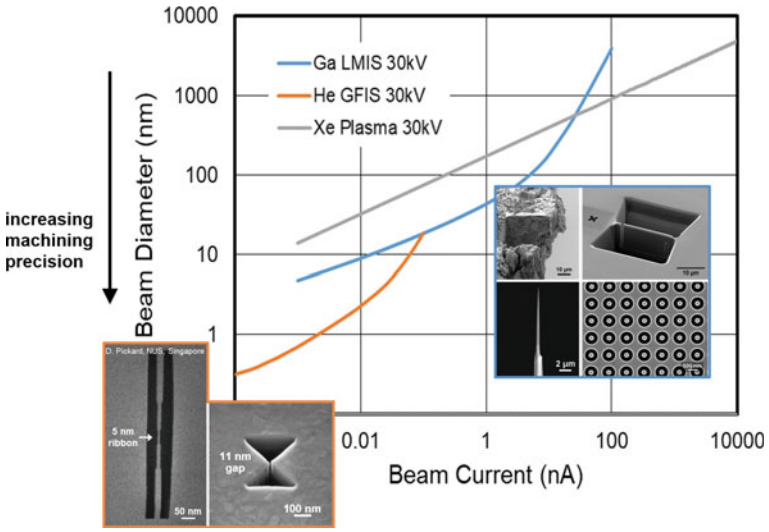


**Fig. 1** Beam size versus current for the Ga LMIS, the Xe plasma source and the He GFIS operated at 30 kV. Decreasing beam diameter directly translates to increasing machining precision. The Xe plasma data was reproduced from [7]. The images are examples of structures prepared with Ga (blue frame) and He beams (orange frame, left image courtesy of D. Pickard, NUS, Singapore)

Research is ongoing on alternative sources like the low temperature ion source (LoTIS) [2] and the nano-aperture ion source (NAIS) [6].

The choice of the appropriate ion species and source type depends on the application. Figure 1 shows the beam diameter d50—containing 50% of the total beam current—as a function of beam current for 30 kV $He^+$, $Ga^+$, and $Xe^+$ ion beams in a double logarithmic plot. The $He^+$ and $Ga^+$ data result from ion optical simulations of ZEISS Orion GFIS and ZEISS Capella GaFIB columns of recent generation. The Xe plasma data points were extracted from [7]. Along the plot vertical axis with decreasing beam diameter, imaging and thus machining resolution improve.

In the central area of the plot, between some tens of pA and up to around 50 nA, the Ga FIB (blue line in Fig. 1) offers the best performance with beam sizes of approximately 10 nm to 1 µm. In this area, the combination of precision and material removal rates is optimal to address important applications like standard cross-sectioning work, TEM and atom probe sample preparation, and nano-patterning. This is the reason why Ga LMIS FIBs are so popular, making up more than 95% of FIBs in use today on multi-purpose ion microscopes. The Ga LMIS has a high brightness of $\sim 10^6$ $Am^{-2}sr^{-1}$ $V^{-1}$, an energy spread of $\sim 5$ eV [4] and covers a current range of 1 pA to 100 nA in today's state-of-the-art Ga FIB columns. In the last five years, Ga FIBs have been developed further mainly targeting source stability (for long-term experiments), maximum current (milling throughput), and low kV performance (surface quality) improvements. The latter are important in the context of, e.g., TEM sample preparation to reduce the extent of amorphization in the FIB thinned area.

Other applications like the preparation of very large cross sections [8] or the tomography of large volumes [9] can benefit from the larger currents offered by plasma sources (see gray curve in Fig. 1). Commercial Xe plasma FIB systems are specified with 2–2.5 μA maximum current. Theoretically this source can even deliver up to 10 μA current [4]. As compared to the Ga LMIS, the energy spread of the plasma source is similar, $\sim 5$ eV, and the brightness two order of magnitudes lower, $\sim 10^4$ $Am^{-2}sr^{-1}$ $V^{-1}$ [4].

At the other end of the graph, the GFIS column offers the smallest ion beam probe for the highest resolution ion imaging or most precise nano-patterning tasks [10–12]. See Reference [13] for a comprehensive review about the He/Ne GFIS microscope and its applications. Of the three sources discussed, the GFIS has by far the smallest virtual size—a single atom—, the highest brightness, and a lower energy spread of $\sim 1$ eV. Operating currents are in the range of few 100's of fA to 100 pA.

The He GFIS was first commercialized in 2006. In its early years, its quantitative analytical capabilities were limited to doing spectroscopy of the backscattered He ions using an adapted silicon drift detector [14, 15]. Since 2012, this same GFIS source can be operated with Ne gas. The Ne ion offers a much higher sputter yield per ion than He, and still a sub-2 nm probe. The advent of Ne opened the possibility of doing secondary ion mass spectrometry (SIMS) in the He/Ne GFIS instrument. SIMS spectrometers have now become available capable of efficiently collecting and analyzing the small number of secondary ions generated by the few-picoamps Ne beam.

## 2 SIMS on the He/Ne GFIS Microscope

Such a SIMS detector, specifically designed for use in the He/Ne GFIS microscope, was developed at the Luxembourg Institute for Science and Technology (LIST) jointly with the company ZEISS [16, 17]. In this setup, a magnetic sector type detector is used. The magnetic field separates the different secondary ions according to their mass/charge ratio physically in space. Four individual detectors (one fixed and three movable) can collect signals from four different ion masses of choice in parallel [17].

Figure 2a shows a first example: the SIMS $Al^+$ map of a GaAs/$Al_{(0.7)}Ga_{(0.3)}$As multilayer cross section sample, BAM-L200 [18], obtained using the magnetic sector detector. The BAM-L200 sample is a standard often used to quantify the spatial resolution of SIMS instrumentation. The plot below the map corresponds to the $Al^+$ average signal intensity as a function of position, where the position axis is perpendicular to the multilayer stack. A 3.5 nm single thin layer of AlGaAs can be resolved. The same is true for all neighboring AlGaAs/GaAs/AlGaAs sandwich structures to the right of the 3.5 nm line. From left to right, the periods or line pair pitches of the sandwich structures are 17.5, 23, 31, 42, 57, and 76.5 nm (all three layers of each sandwich structure have the same thickness). Resolution can be defined as the half of the resolved pitch. With this criterion, the SIMS map would

show a spatial resolution of 9 nm. An alternative—more conservative—resolution criterion, in which the $Al^+$ signal in the central GaAs is required to drop below 50% of the maximum intensity in the AlGaAs layers, would yield a resolution of 15 nm (corresponding to the 31 nm line pair pitch). In any case, a resolution of around 10–15 nm is to the best of our knowledge, unmatched by any other SIMS technique and only limited by the interaction of the Ne beam with the sample [17].

Figure 2b shows a second example. In this case, the sample is a fully processed thin-film copper indium gallium diselenide (CIGS) solar cell on a glass substrate. Using a Ga FIB, a cross section was cut at an angle of 15° relative to the sample surface. The Ne GFIS SIMS analysis was done on the freshly cut surface of the sample. A second experiment was done on a reference CIGS on alumina sample (not shown). For the measurements, a Ne beam current of 8–9 pA was used. Mapping resolution was 1024 × 1024 Pixels with a dwell time of 1.5 ms/pixel, totaling an acquisition time of about 25 min per measurement. These are typical acquisition parameters. The FOV was 15 µm (left image of Fig. 2b).

Ne GFIS SIMS reveals the distribution of the alkali elements Na (in green color) and K (red) in the CIGS layer in detail. The alkalis originate from the glass substrate, which contains these two elements. During solar cell fabrication, Na and K diffuse from the glass into the active layer material. The experiment shows that Na and K are found preferentially at the grain boundaries of the active material. The grain boundaries are "decorated" with the alkalis forming roughly 100-nm wide bands. The Ga background signal (blue) comes from the CIGS material. As compared to atom probe tomography [19], Ne GFIS SIMS allows to study a large number of grain boundaries (within a FOV of 15 µm for this example), so that the gained information can be put more easily into the context of the full solar cell.

As expected, in the CIGS layer of the reference sample (alumina substrate), which was processed in the same way, no Na and K was detected. This is because the alumina substrate does not contain these elements.

## 3 Toward 1 nm-Voxel FIB-SEM Tomography

A second innovation relates to advanced FIB-SEM (or FIB-FIB) tomography. It introduces the concepts of "True Z" and "Thin & Fast." These target most accurate 3D reconstructions even of challenging beam sensitive samples.

In FIB-SEM tomography, the sample is sliced by FIB (usually Ga or Xe) and the cross section (XY plane) imaged by SEM (or FIB) [20]. For an accurate 3D data acquisition, it is important to correct for sample drift due to charging or thermal effects during the run. This is especially true when aiming for high 3D resolutions with small—typically 2–10 nm—isometric voxels. Advanced FIB-SEM tomography solutions correct sample drift by cross-correlation imaging of distinct fiducials on the sample. FIB or SEM image-based drift correction is performed regularly during the run on these fiducials. The SEM based approach described in [21] has the advantage that drift correction is done using a "fresh" fiducial after every single

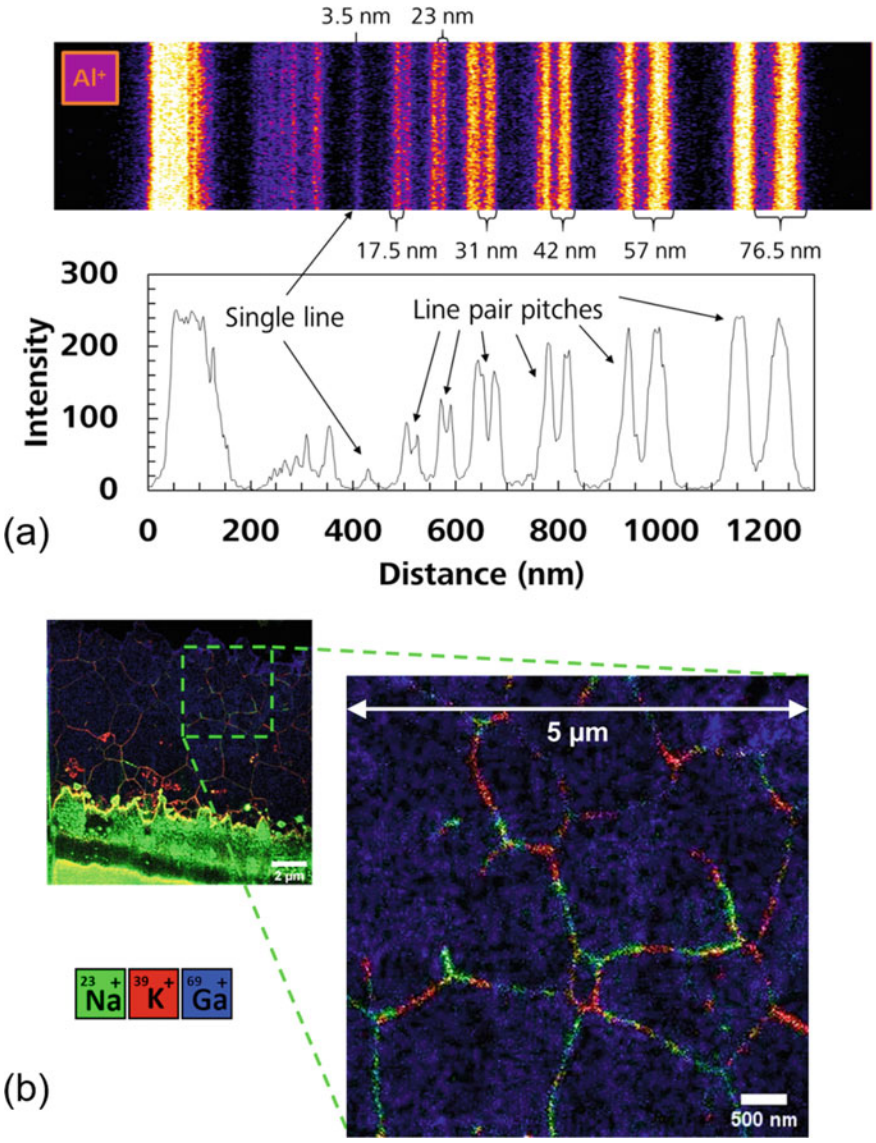


**Fig. 2** SIMS data collected by Ne SIMS. **a** Al SIMS signal on a BAM-L200 resolution standard [18]. The sample consists of an AlGaAs/GaAs heterostructure. A 3.5 nm wide AlGaAs single line and an AlGaAs/GaAs line pair with a total width of 17.5 nm can be resolved. **b** Na, K, and Ga SIMS maps of a thin-film CIGS solar cell showing the distribution of the alkali elements at grain boundaries (sample courtesy of T. Magorian-Friedlmeier, ZSW, Stuttgart, Germany)

slicing step. Further, SEM imaging, as opposed to FIB imaging, does not affect the shape of the fiducial. The slice thickness information can be fed back to the acquisition system to adapt FIB milling progression into the sample. Therefore, slice thickness homogeneity across the image stack is improved. Furthermore, any stabilization required, e.g., at the beginning of the 3D acquisition or after any unexpected change in the environmental conditions around the microscope, is shorten [21].

However, despite this feedback loop during FIB, milling deviations from the targeted slice thickness can still occur. As an example, Fig. 3a shows a very unstable section of a run. The slice thickness deviates substantially from the targeted thickness of 6 nm by −4 to +6 nm. Not surprisingly, a reconstruction assuming the nominal slice thickness of 6 nm leads to artifacts: As shown in Fig. 3b, a reference straight line shows wiggles in the reconstructed virtual XZ plane. A much more truthful reconstruction, see Fig. 3c, is achieved by taking the actual measured Z position of each slice, i.e., the "true" Z value, into account. This is done by resampling the 3D dataset in Z to produce a new stack of images with the actual targeted slice thickness. In summary, "True Z" combines precise measurement of slice position in Z and adaptive milling control, both accomplished during acquisition, and the post-acquisition resampling of the 3D dataset prior to 3D analysis (segmentation, reconstruction, metrology).

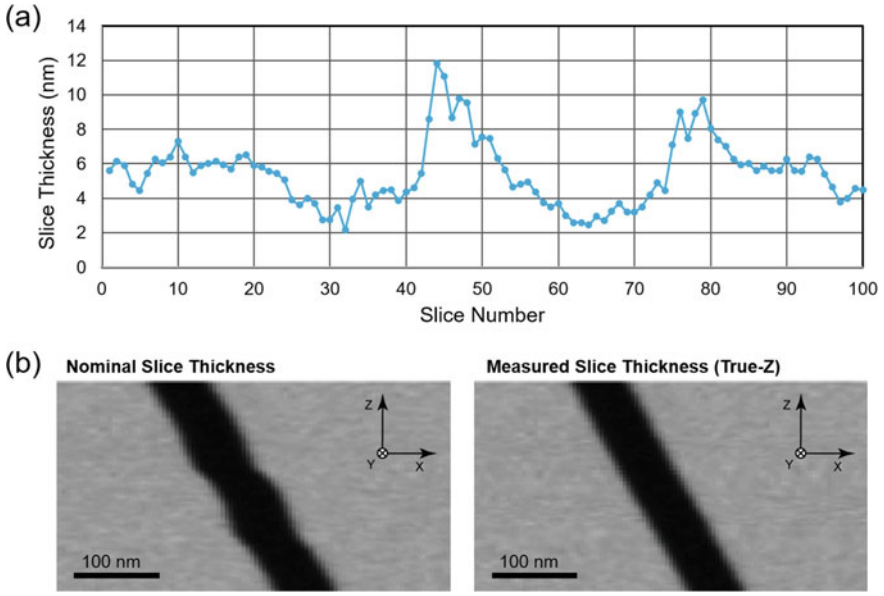


**Fig. 3** **a** Measured slice thickness versus slice number for 100 slices of a FIB-SEM tomography run in which strong sample drift is observed. **b** Virtual XZ views of a straight line using the nominal (left) and the measured slice thicknesses (right) for reconstruction

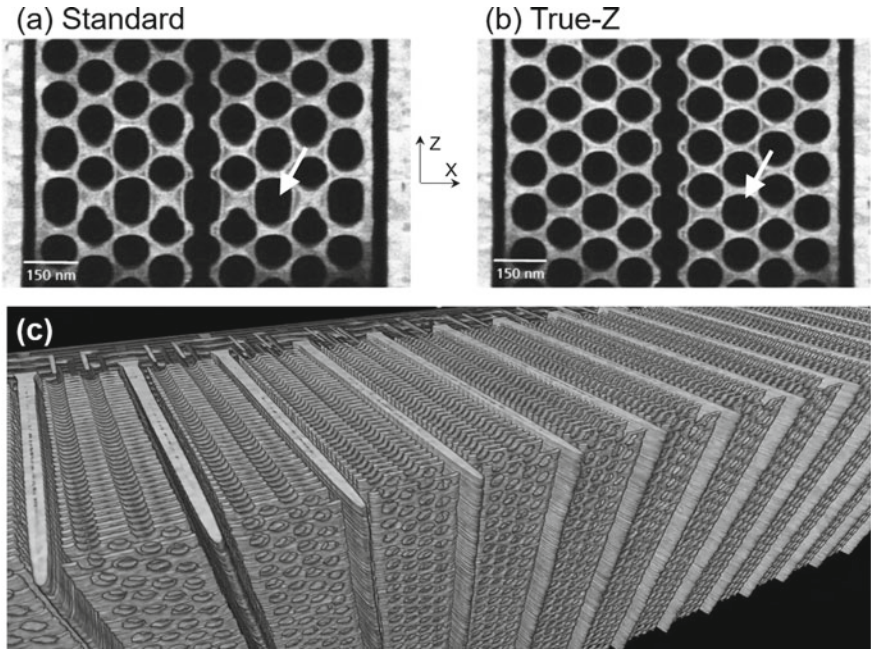


**Fig. 4** FIB-SEM tomography data of a flash memory device. **a** Virtual XZ planes after standard reconstruction. **b** XZ plane after "True Z" reconstruction. The arrows point onto the same feature on both images. **c** Volume of interest after "True Z" reconstruction to allow improved metrology

In Fig. 4, the impact of "True Z" on metrology of a NAND flash memory device is illustrated. Figure 4a, b, shows the virtual XZ planes after standard and "True Z" reconstruction. The device shows a periodic structure that is clearly disrupted at the bottom half of the image, where slices thinner than expected were collected. This transforms circular features into oblong ones. See, e.g., the feature highlighted by the arrows. Therefore, any attempt to extract metrology data would lead to errors (+35% in Z dimension for the highlighted feature) and most probably to wrong conclusions. Figure 4c shows the "True Z" reconstruction of this dataset, which now allows improved metrology.

Another challenge of advanced FIB-SEM tomography is faced when dealing with beam-sensitive samples. Prominent examples are epoxy-embedded biological samples. These suffer from "shrinkage" when dosed with the SEM beam during the tomography acquisition (see Fig. 5a). A similar behavior is observed when sections of epoxy-embedded samples are imaged under TEM [22]. The higher the electron imaging dose, the more pronounced is the shrinkage. Often, the top of the volume is not affected, but the artifacts gradually start appearing with increasing depth. This is the case in Fig. 5a. In severe cases, when dealing with very soft epoxy resins, the artifacts can be even visible on the full depth of the cross section face. Effectively, the shrinkage leads to a tilt of the cross section face plane, i.e., the imaging plane,

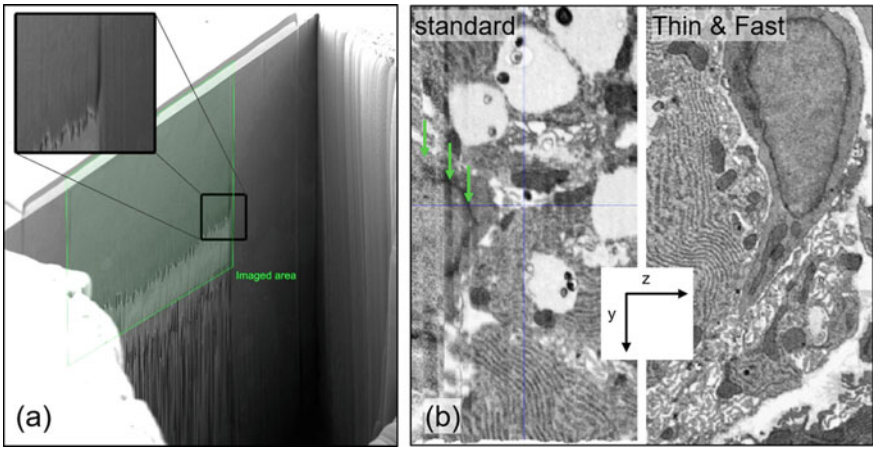


**Fig. 5** FIB-SEM tomography results on a mammalian salivary gland sample (sample courtesy of K. Narayan, Center for Molecular Microscopy, Frederick National Laboratory for Cancer Research, NIH, USA). **a** SEM overview of the area of interest after acquisition. The inset shows the shrinkage artifact. This is a particularly pronounced manifestation of the shrinkage of the e-beam dosed polymer. **b** Reconstructed YZ planes using the standard (left) and the new "Thin & Fast" approach (right). The arrows highlight artifacts (e.g., striping) of the standard acquisition

that keeps changing erratically during the tomography acquisition. This introduces unwanted artifacts in the reconstruction, which become most obvious when analyzing the virtual planes XZ and YZ, see Fig. 5b.

Cutting very thin slices, e.g., 1 nm thick or less, and imaging the block face with fast scans, is an effective way to reduce this problem on this type of samples. The fast scans keep the electron dose low, below the activation threshold of shrinkage, at the expense of lower signal-to-noise ratios (SNR). However, multiple of these low SNR images are then accumulated to restore the intended signal-to-noise level and targeted slice thickness (Z). Thus, the name "Thin & Fast" for this acquisition strategy. We have found this approach to work very well on differently embedded biological samples. Figure 5b shows Thin & Fast versus standard acquisition results on a mammalian salivary gland sample. Details can be found in [23].

## 4 The LaserFIB—A New Instrument Class

Finally, a third innovation is the LaserFIB, i.e., a femtosecond (fs) laser integrated to a FIB-SEM. The laser allows to gain rapid access to structures buried deeply in a sample for their subsequent FIB-SEM analysis [24]. In this context, samples can be packaged electronics or display devices, or engineering materials that have been previously characterized by a non-destructive 3D imaging technique (e.g., synchrotron, CT, XRM).

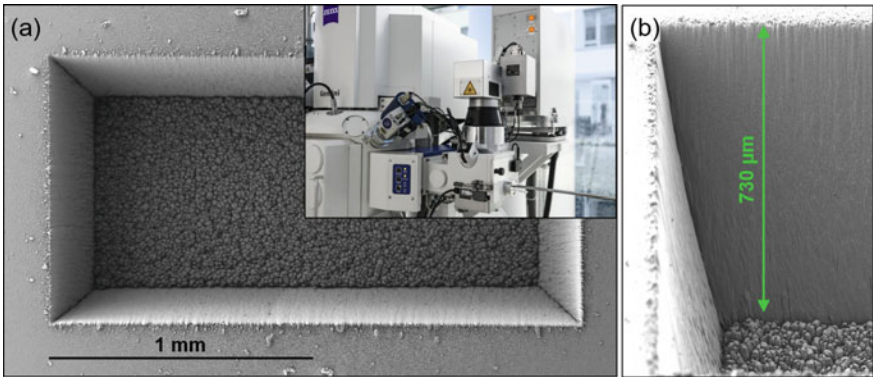


**Fig. 6** LaserFIB machining of <100> silicon. **a** SEM overview image of a 2 mm × 1 mm trench. The inset shows a photograph of a LaserFIB system with the laser machining unit attached to a dedicated side chamber (in the foreground). **b** SEM tilted image of the side wall of the trench showing a depth of 730 µm that was reached after a laser processing time of 300 s

Figure 6 shows a simple experiment in silicon that illustrates nicely the enormous gain in material removal speed as compared to any focused ion beam. A 2 mm × 1 mm × 730 µm trench was cut in 5 min. This corresponds to a removed material volume of $1.5 \times 10^9$ µm$^3$ and a removal rate of 5 million µm$^3$/s. For comparison, let us consider the maximum achievable sputter rate by FIB: Assuming an ideal scenario in which we consider a 2.5 µA Xe plasma FIB and a sputter yield of 5.2 atoms/Xe ion in silicon [25], the maximum ablation rate that can be reached by FIB is still below 1600 µm$^3$/s. (In practice, this limit is lower due to a loss in FIB current density at very high currents.) Thus, the laser removes material more than three orders of magnitude faster than any FIB. For the example shown in Fig. 6, our ideal-scenario FIB would require at least 25 days of milling time. In other words, this preparation task simply cannot be accomplished by FIB on a realistic time scale. On the other hand, some applications, e.g., failure analysis in state-of-the-art packaged display or electronic devices, do require site-specific material removal at this scale. As of today, only the LaserFIB can tackle such preparation challenges opening a new application space that was previously not accessible for FIB instrumentation.

The inset of Fig. 6 shows a LaserFIB by ZEISS. An alternative approach was chosen in [26] and has been recently commercialized, too [27]. In the depicted system, the laser machining work is done in a separate dedicated chamber to avoid contamination of the main FIB-SEM chamber. The sample is shuttled between both chambers using a correlative approach to lock the coordinate system of sample holder, FIB-SEM, and laser to each other, thus allowing targeted site-specific laser work with an accuracy of down to 2 µm [28].

In the field of materials science, there are other interesting applications for LaserFIBs, see Fig. 7, for example, the (site-specific) preparation of very large cross sections (Fig. 7a) or of cantilevers or pillars (see Fig. 7c) for micromechanical

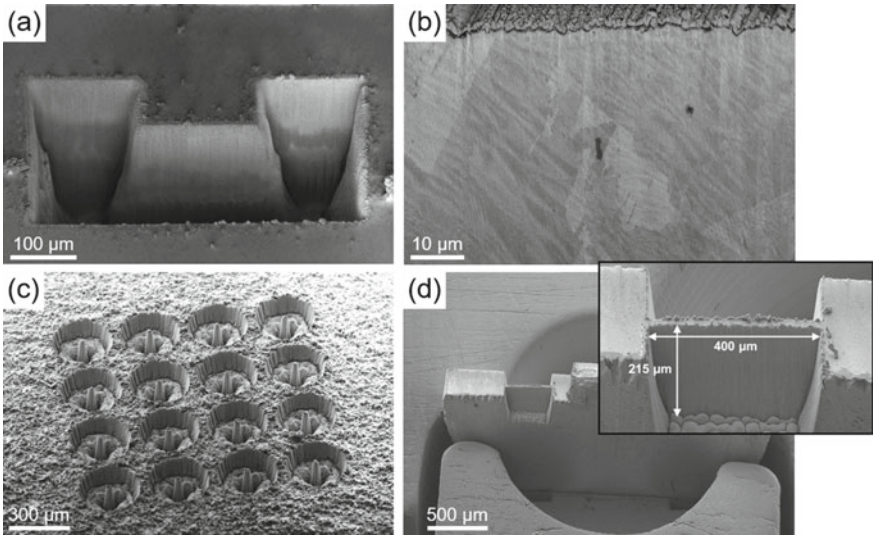


**Fig. 7** Examples of LaserFIB work. **a** Preparation of a large 200 µm × 200 µm free standing cross section. **b** Detail of a laser-polished steel surface. **c** Array of laser-machined pillars. Such pillars are suitable for synchrotron or laboratory-based X-ray microscopy, or as micromechanical testing objects. **d** H-bar preparation in copper. The inset shows one H-bar window, 400 µm × 215 µm, machined in 34 s

testing with dimensions of up to millimeters [29]. Remarkably, fs laser-induced sample damage or heat effects are minimal as shown by EBSD analysis of laser-machined surfaces [26, 28, 29]. Figure 7b shows the microstructure of a laser cross section in steel directly after the laser polishing step (no FIB polish). Figure 7d illustrates another possible use case for this technology in the context of TEM sample preparation of deeply buried features. The LaserFIB technology is still in its infancy but is rapidly gaining adopters in science and industry.

## 5 Summary

Innovation in FIB microscopy continues to take place at a high pace aiming to provide increased precision, maximum information from the sample, and faster times-to-result. In this paper, we discussed three good examples.

A newly developed SIMS detector for the He/Ne GFIS microscope adds analytical capabilities to this unique imaging and nano-structuring tool. In combination with the Ne GFIS beam, SIMS studies can be done with unprecedented spatial resolution below 15 nm.

In the area of high-resolution FIB-SEM tomography, techniques like True Z and Thin & Fast satisfy the demand for a more accurate 3D reconstruction of volumes

of interest. Such reconstructions allow to extract more precise measurements in 3D for process and quality control in semiconductor, materials, and life sciences.

Finally, the addition of a fs laser beam to ion beam instrumentation in LaserFIB systems allows to expand site-specific sample preparation beyond the traditional application space of focused ion beams into the macroscopic regime.

## References


1. Bischoff L, Mazarov P, Bruchhaus L, Gierak J (2016) Appl Phys Rev 3:021101
2. McClelland JJ, Steele AV, Knuffman B, Twedt KA, Schwarzkopf A, Wilson TM (2016) Appl Phys Rev 3:011302
3. Bruchhaus L, Mazarov P, Bischoff L, Gierak J, Wieck AD, Hövel H (2017) Appl Phys Rev 4:011302
4. Smith NS, Notte JA, Steele AV (2014) MRS Bull 39:329
5. Bassim N, Notte, J (2019) ASM Handbook Vol. 10: materials characterization, 635
6. van Kouwen L, Kruit P (2018) J Vac Sci Technol B36, 06J901
7. Bassim N, Scott K, Giannuzzi LA (2014) MRS Bull 39:317
8. Hrnčíř T, Dluhoš J, Hladík L, Moyal E, Teshima J, Kopeček J (2014) Proc ISTFA, 136
9. Burnett TL, Kelley R, Winiarski B, Contreras L, Daly M, Gholinia A, Burke MG, Withers PJ (2016) Ultramicroscopy 161, 119
10. Kollmann H, Piao X, Esmann M, Becker SF, Hou D, Huynh C, Kautschor L-O, Bösker G, Vieker H, Beyer A, Gölzhäuser A, Park N, Vogelgesang R, Silies M, Lienau C (2014) Nano Lett 14:4778
11. Klein J, Lorke M, Florian M, Sigger F, Sigl L, Rey S, Wierzbowski J, Cerne J, Müller K, Mitterreiter E, Zimmermann P, Taniguchi T, Watanabe K, Wurstbauer U, Kaniber M, Knap M, Schmidt R, Finley JJ, Holleitner AW (2019) Nat Commun 10:2755
12. Mitterreiter E, Schuler B, Cochrane KA, Wurstbauer U, Weber-Bargioni A, Kastl C, Holleitner AW (2020) Nano Lett 20:4437
13. Hlawacek G, Gölzhäuser A (2016) Helium Ion Microscopy. Springer International Publishing, Switzerland
14. Sijbrandij S, Notte J, Scipioni L, Huynh C, Sanford C (2010) J Vac Sci Technol B 28:73
15. Behan G, Zhou D, Boese M, Wang RM, Zhang HZ (2012) J Nanosci Nanotechnol 12:1094
16. Wirtz T, Dowsett D, Philipp P (2016) Chap. 13, in helium ion microscopy, Springer International Publishing, Switzerland, 297
17. Sijbrandij S, Lombardi A, Sireuil A, Khanom F, Lewis B, Guillermier C, Runt D, Notte J (2019) Micros Today 27:22
18. Available from BAM, Richard-Willstätter-Str. 11, 12489 Berlin, Germany
19. Choi P-P, Cojocaru-Mirédin O, Abou-Ras D, Caballero R, Raabe D, Smentkowski VS, Park CG, Gu GH, Mazumder B, Wong MH, Hu Y-L, Melo TP, Speck JS (2012) Micros Today 20:18
20. Holzer L, Cantoni M (2012) Chap. 11, Nanofabrication using focused ion and electron beams: principles and applications. Oxford University Press, New York, 410
21. Narayan K, Danielson CM, Lagarec K, Lowekamp BC, Coffman P, Laquerre A, Phaneuf MW, Hope TJ, Subramaniam S (2014) J Struct Biol 185:278
22. Lamvik MK (1991) J Microsc 161:171
23. Narayan K et al (in preparation)
24. Kaestner M, Mueller S, Gregorich T, Hartfield C, Nolan C, Schulmeyer I (2019) Proc CSTIC —Semicon China, 1
25. Orloff J, Utlaut M, Swanson L (2003) High resolution focused ion beams: FIB and its applications. Kluwer Academic/Plenum Publishers, New York

26. Echlin MP, Straw M, Randolph S, Filevich J, Pollock TM (2015) Mater Charact 100:1
27. Randolph SJ, Geurts R, Wang J, Winiarski B, Rue C (2019) Microsc Microanal 25(Suppl 2): 352
28. Tordoff B, Hartfield C, Holwell AJ, Hiller S, Kaestner M, Kelly S, Lee J, Müller S, Perez-Willard F, Volkenandt T, White R, Rodgers T (2020) Appl Microscopy 50:24
29. Pfeifenberger MJ, Mangang M, Wurster S, Reiser J, Hohenwarter A, Pfleging W, Kiener D, Pippan R (2017) Mater Des 121:109

# Life Science

# A Novel Method for Electron Microscopy Processing Using a Decade Old Archived Paraffin-Embedded Tissues


**R. Yanti, H. L. Hing, K. G. Hanan, A. M. H. Muhd, Z. Zaida, J. S. Nurul, and S. S. Galvin**

**Abstract** This study investigates the effectiveness of new SEM and TEM processing protocols on tissues obtained from archived paraffin blocks and compared to the tissues processed for electron microscopy using the standard processing methods. The samples used for this study were fresh mouse brain tissues in newly prepared paraffin blocks and archived brain tissues in paraffin blocks. Both groups were stained with H&E stain and observed via light microscopy before both samples underwent conventional and our alternative electron microscopy protocols. In the proposed protocol, distilled water replaces xylene for dewaxing step, and the post-fixation process is omitted. The microscopic images were observed, the landmark organelles were measured, and the effects of processing temporal variations were assessed. Comparable morphological organelle dimensions were observed from both the conventional as well as the alternative protocol for fresh and the archived sample. To summarize, the alternative method for reusing archived FFPE blocks has successfully retained the ultrastructure of the tissues, thus proving to be a promising potential as a new protocol for reusing archived FFPE blocks.

**Keywords** FFPE tissue · SEM processing protocol

R. Yanti (✉) · A. M. H. Muhd · Z. Zaida · J. S. Nurul · S. S. Galvin
Faculty of Health Science, Biomedical Science Programme, Center for Toxicology & Health Risk Studies (CORE), Universiti Kebangsaan Malaysia, Bandar Baru Bangi, Malaysia
e-mail: yanti_rosli@ukm.edu.my

H. L. Hing
Faculty of Health Science, Environmental Health & Industrial Safety Programme, Center for Toxicology & Health Risk Studies (CORE), Universiti Kebangsaan Malaysia, Bandar Baru Bangi, Malaysia

K. G. Hanan
Institute of Medical Science Technology (MESTECH), Universiti Kuala Lumpur, Kuala Lumpur, Malaysia



P. Ghosal et al. (eds.), *Applications of Microscopy in Materials and Life Sciences*, Springer Proceedings in Materials 11,
https://doi.org/10.1007/978-981-16-2982-2_19

# 1 Introduction

Patient diagnosis has been essential in diagnosing the condition of patients since the dawn of health care. In our day and age, hospitals carry out this process by obtaining specimens such as body fluids and tissue biopsy for diagnosis. Tissue biopsy is preserved in formalin and will be sent to the laboratory to be turned into formalin-fixed paraffin-embedded tissue (FFPE) blocks. Through testing of said blocks, FFPE blocks are important in diagnosing a lexicon of diseases based on the pathology of the tissue [4]. These blocks can be stored and archived for many years on end as stated by Kokkat et al. [2]. Formalin acts as a preservative that maintains the morphology and cellular components for histological observation and immunohistochemistry testing [1].

Formalin-fixed paraffin-embedded tissue (FFPE) is a technique heavily applied in clinical and research laboratories. Tissue samples from patients are preserved or fixed in formalin and are processed in laboratories. The tissue is then embedded into paraffin wax to produce FFPE. The block is sliced very thinly with a microtome to obtain thin samples. These blocks can be archived for years on end [7]. Furthermore, techniques for antigen retrieval for extraction of DNA, RNA, and proteins from the FFPE blocks make this technique viable in terms of effective preservation for both the morphology and the molecules in said blocks [2]. In addition, miRNAs that are being reliant on for diagnosis, prognosis as well as disease prediction can be preserved. miRNAs has become increasingly significant in disease diagnosis therefore, the isolation of these materials from FFPE blocks has increased clinical value. However, due to the rough protocol of tissue processing into FFPE blocks, important clinical material can be fragmented immensely while formalin chemically cross links them.

Xylene and osmium tetroxide are carcinogenic agents that are used in tissue processing. Xylene is greatly used in the clinical field as a solvent; however, it has adverse effects toward organs such as the lungs and liver over prolonged exposure and symptoms such as breathing difficulties, anemia, and abnormalities in ECG readings may manifest. Studies have been conducted to replace xylene from slide preparation for histological observation [8].

# 2 Materials and Methods

## *2.1 Sampling*

This study was carried out on the brain tissues of six adult female *Mus musculus* sp., weighing between 120 and 140 g, and a decade old FFPE blocks. The mice were obtained from the Animal Unit of Universiti Kebangsaan Malaysia, and we

adhered to all ethic procedures (Universiti Kebangsaan Malaysia Animal Ethics Committee FSK/2016//YANTI/28-JAN./727-FEB.-2016-JAN.-2017) and (FSKB/BIOMED/2008/YANTI/12-AUGUST/231-SEPT-2008-JUNE-2011). The brains were removed and fixated with 10% formalin before embedding into paraffin wax. The blocks were sectioned using a microtome (Leica Biosystems) and processed into slides which are then observed under a light microscope for histological observations. This process was repeated with the archived FFPE blocks using the conventional deparaffinization protocol. Both samples were stained with H&E stain. Both fresh and archived FFPE blocks were put through the conventional and alternative protocols.

### *2.2 Proposed Modifications*

The tissue processing followed the protocol by Lighezan et al. [3] using osmium tetroxide ($OsO_4$) as the control group, whereas the test group omitted the $OsO_4$ totally. The deparaffinization process for both control and test groups was subcategorized into group with xylene substituted with hot distilled water (45 °C) and those that follow the regular deparaffinization process. The slides were then observed under an SEM and TEM, and ultrastructural observations were carried out.

### *2.3 Conventional and Modified TEM Steps*

See Fig. 1.

## 3 Results

### *3.1 Histological Observation-Light Microscopy*

See Photograph 1.

### *3.2 Histological Observation-TEM*

#### 3.2.1 Histological Observation (Conventional Protocol)

See Photograph 2.

| Conventional TEM Steps | Time | Temp (°C) |
|---|---|---|
| Xylene I and II | 30 min | 60 |
| Xylene | 12 hour | |
| Xylene: ethanol (1:1) | 5 min | |
| Ethanol 100% | 2 min | |
| Ethanol 95% I and II | 3 min | |
| Ethanol 80% I and II | 3 min | |
| Ethanol 70% I and II | 3 min | |
| Wash with 0.1M PBS | 10 min | |
| *Post-fixing with $OsO_4$ | 60 min | 4 |
| Distilled water I and II | 10 min | |
| Ethanol 70% I and II | 15 min | |
| Ethanol 80% I and II | 15 min | |
| Ethanol 96% I and II | 15 min | |
| Ethanol 100% I and II | 15 min | |
| Acetone I and II | 15 min | |
| Resin Infiltration | 3 hour | |
| Resin polymerisation | 24hour | 60 |

| Modified TEM Steps | Time | Temp (°C) |
|---|---|---|
| Hot distilled water I | 30 min | 45 |
| Hot distilled water II | 30 min | |
| Xylene :ethanol (1:1) | 5 min | |
| Ethanol 100% | 2 min | |
| Ethanol 95% I and II | 3 min | |
| Ethanol 80% I and II | 3 min | |
| Ethanol 70% I and II | 3 min | |
| Wash with 0.1M PBS | 10 min | |
| Skip $OsO_4$ | - | |
| Distilled water I and II | 10 min | |
| Ethanol 70% I and II | 15 min | |
| Ethanol 80% I and II | 15 min | |
| Ethanol 96% I and II | 15 min | |
| Ethanol 100% I and II | 15 min | |
| Acetone I and II | 15 min | |
| Resin Infiltration | 3 hour | |
| Resin polymerisation | 24 hour | 60 |

**Fig. 1** Conventional and the modified TEM steps where the modified steps showed (1) Hot water replacing xylene, (2) $OsO_4$ staining was omitted

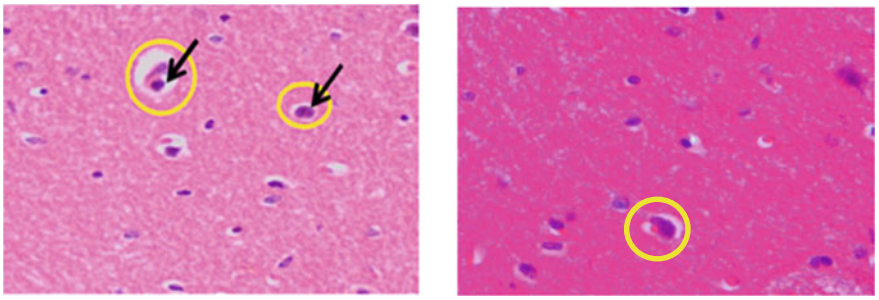

**Photograph 1** Photograph on the left shows the light microscopy observation for a cerebellum tissue slide prepared from freshly prepared FFPE and compared to photograph on the right shows the archived cerebellum tissue slide. Both were stained with hematoxylin and eosin and are under 40× magnification. Black arrow indicates myelin sheaths while yellow circle indicates neuronal structures

### 3.2.2 Histological Observation (Modified Protocol)

See Photograph 3.

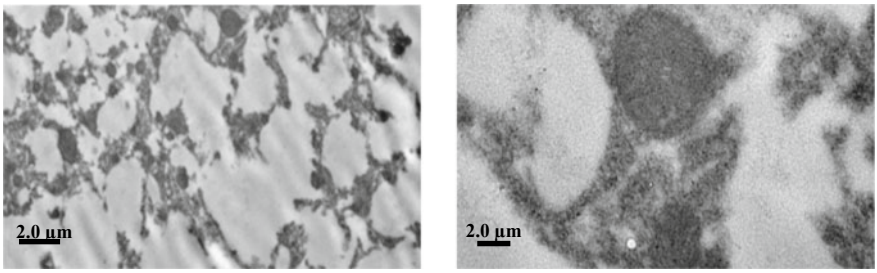


**Photograph 2** Photograph on the left (15,000× magnification) shows the conventional protocol that is successful in retaining the tissue ultrastructure although the technique can be sharpened during processing. Photograph on the right (30.0 k × magnification) shows the neuronal cell that has maintained its size and has not shown shrinkage (size for neurons is 5–10 µm)

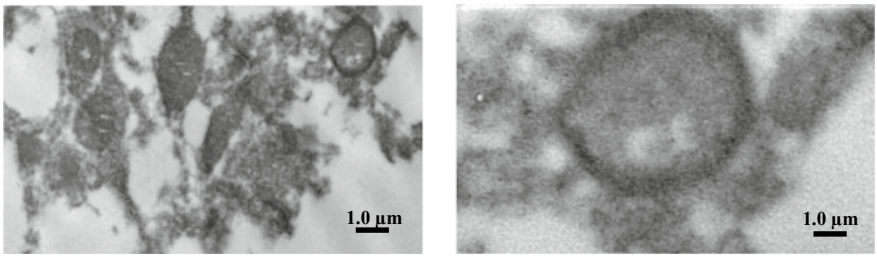


**Photograph 3** Photograph on the left (15,000× magnification) shows the quality of the image acquired that is good and is comparable to the image from the conventional protocol. Photograph on the right (60.0 k × magnification) shows an axon still surrounded by its myelin sheath (diameter of the axon = 414 nm)

## *3.3 Histological Observation-SEM*

### 3.3.1 Histological Observation (Conventional Protocol)

See Photograph 4.

### 3.3.2 Histological Observation (Modified Protocol)

See Photograph 5.

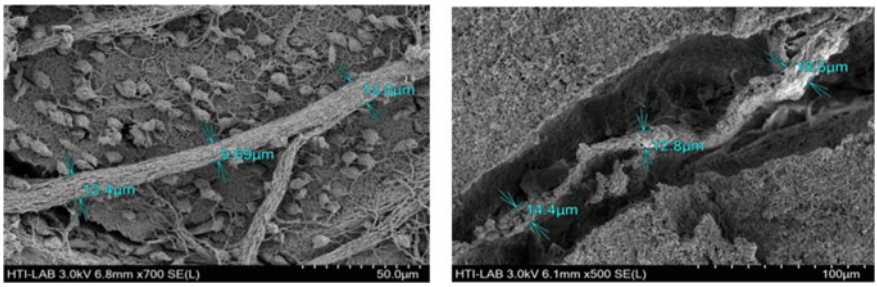


**Photograph 4** Photograph on the left shows fresh blocks compared to the archived FFPE block on the right. It is noted that even after dewaxing in hot water, the ultrastructure of the neurons in the archived FFPE tissues is preserved and comparable to the freshly prepared paraffin blocks

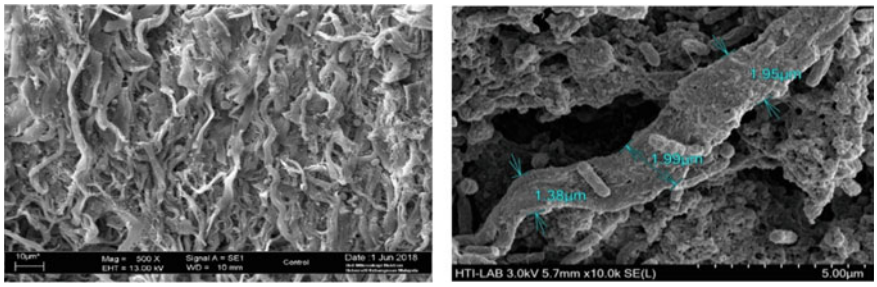


**Photograph 5** Photograph shows the comparison between freshly prepared paraffin blocks on the left and archived FFPE blocks undergoing the modified protocol on the right

## 4 Discussion

The results from the light microscopy observations on freshly prepared tissues in paraffin blocks and the ones from the archived FFPE blocks has shown the neuron were about similar in size, which is about 5.4 mm average in length. This finding suggests to us that the tissues from our archived blocks are at the very least morphologically sound to be used to test out our alternative electron microscopy protocols.

Based on the observation in the micrographs, the usage of hot water in our proposed protocol was sufficient for deparaffinization purposes, freeing up tissues without damaging tissues. The quality of the images from the protocols using xylene and hot water did not show elements of damages, for example, the myelin sheaths were intact around the 404 nm (Photograph 3) in diameter of the axon from our sample using the alternative protocol.

$OsO_4$ acts as a negative stain and stains lipids in membranes and vesicles. Although paramount in its use in the EM protocols, $OsO_4$ has toxic effects if there is prolonged exposure [5]. A study conducted by Moran and Coats [6] states that the

use of $OsO_4$ is unnecessary in the EM protocols as the image quality obtained without $OsO_4$ is similar to the image obtained with using $OsO_4$. Our proposed protocol in this study yields similar results as well since the image obtained by the EM show intact cellular structure and clarity although the contrast of the image is different compared to the conventional protocol using $OsO_4$.

The preservation of the cellular structures such as the axons and neurons can be observed and identified in both fresh and archived tissue in the modified method. The modified method has its advantages as it drastically reduces the tissue processing time and is cost effective. Thirteen hour from the dewaxing phase can be saved by replacing distilled water with xylene, whereas skipping $OsO_4$ saves an additional hour not to mention being cost effective as xylene and especially $OsO_4$ is costly. Replacing and removing these steps still yield viable images as shown by this study as the morphological ultrastructure of the cells is preserved and can still be used in diagnosis.

## 5 Conclusion

The results of the study show that the modified technique for specimen preparation from archived FFPE tissue to samples for electron microscopy is possible and has been shown to preserve the comparable morphological ultrastructure and integrity of the freshly prepared tissues as observed in our micrographs. This novel technique is quicker in the tissue preparation phase by up to 85% compared to the conventional technique. Thus, this novel technique shows immense potential to be considered as the new protocol for reusing archived FFPE tissues as it is proven to be more effective and viable. It will be exciting to be able to retrieve protein antigens from the archived FFPE and study them further with the latest instruments which were not available before.

**Acknowledgements** The authors wish to thank Hi-Tech Instruments (Malaysia) Berhad, Mr KY Tay and Dr Abby Soo for their technical supports in making this study possible.

## References

1. Groelz D, Sobin L, Branton P, Compton C, Wyrich R, Rainen L (2013) Non-formalin fixative versus formalin-fixed tissue: a comparison of histology and RNA quality. Exp Mol Pathol 94(1):188–194
2. Kokkat TJ, Patel MS, Mcgarvey D, Livolsi VA, Baloch ZW (2013) Archived formalin-fixed parafin-embedded (Ffpe) blocks: a valuable underexploited resource for extraction of DNA, RNA, and protein. Biopreservation Biobanking 11(2):101–106
3. Lighezan R, Baderca F, Alexa A, Iacovliev M, Bonţe D, Murărescu ED, Nebunu (2009) The value of the reprocessing method of parafin-embedded biopsies for transmission electron microscopy. Rom J Morphol Embryol 50(4):613–617

4. Mansour A, Chatila R, Bejjani N, Dagher C, Faour WH (2014) A novel xylene-free deparaffinization method for the extraction of proteins from 54 human derived formalin-fixed paraffin embedded (Ffpe) archival tissue blocks. MethodsX 1:90–95
5. Mclaughlin AIG, Milton R, Perry KMA (1946) Toxic manifestations of osmium tetroxide. Br J Ind Med 3(3):183–186
6. Moran P, Coats B (2012) Biological sample preparation for SEM imaging of porcine retina. Microsc Today 20. https://doi.org/10.1017/S1551929511001374
7. Sadeghipour A, Babaheidarian P (2019) Making formalin-fixed, paraffin embedded blocks. In: Yong W (eds) Biobanking. Methods in molecular biology, vol 1897. Humana Press, New York, NY
8. Stockert J, López-Arias B, Del Castillo P, Rmeoro A, Blázquez-Castro A (2012) Replacing xylene with N-heptane for parafin embedding. Biotech Histochem 87(7):464–467

# Intracellular Localization of Micronutrients in Algae Cells Using Scanning Transmission Electron Microscopy–Energy-Dispersive X-ray Spectroscopy (STEM-EDX)


**Purbasha Sarkar, Manish R. Shukla, Priyanka Kumbhar, Suvarna Manjre, Santanu Dasgupta, and Vishnupriya Bhakthavatsalam**

**Abstract** Various elements including iron play a vital role as micronutrients in growth and development of algae cells. Understanding the process of element uptake, assimilation and utilization of these elements by algae cells are essential for optimizing growth conditions in algae ponds, for cost-effective biomass production. In addition to bulk elemental analysis methods, electron microscopy-based semi-quantitative elemental analysis methods can provide high-resolution spatial information about element distribution in algal cultures for a comprehensive and accurate understanding of the element utilization processes. Toward this goal, we standardized a protocol for localizing various elements within unicellular algae cells using scanning transmission electron microscopy–energy-dispersive X-ray spectroscopy (S/TEM–EDX). We applied this method to study iron uptake and intracellular distribution process by algae cells over a week of cultivation.

**Keywords** Algae · Iron uptake · Micronutrients · STEM-EDX

## 1 Introduction

Microalgae are rich source of lipid, protein, carbohydrates, vitamins, micronutrients, and pigments, which can be utilized in production of biofuel, nutraceuticals, dietary supplements, cosmetics, animal fodder, and many other green products [5].

P. Sarkar (✉) · P. Kumbhar · S. Manjre · V. Bhakthavatsalam
Advanced Analytical Sciences, Reliance Industries Limited, Reliance Corporate Park, Navi Mumbai 400701, India
e-mail: purbasha.sarkar@ril.com

M. R. Shukla · S. Dasgupta
Algae to Oil, Research and Development, Reliance Industries Limited, Reliance Corporate Park, Navi Mumbai 400701, India



P. Ghosal et al. (eds.), *Applications of Microscopy in Materials and Life Sciences*, Springer Proceedings in Materials 11,
https://doi.org/10.1007/978-981-16-2982-2_20

They are photosynthetic organisms that utilize atmospheric $CO_2$ to grow and require minimal other external resources. They can grow in wide range of water bodies including freshwater, seawater, and even wastewater. They can tolerate wide range of temperatures, salinities, pH, and light conditions. They have short life cycle allowing faster harvesting of desirable products compared to plants. Their productivity can be further improved by growth condition manipulation and genetic engineering. All these characteristics have made microalgae a valuable feedstock for various industries. They also are gaining interest due to their application in wastewater treatment and atmospheric $CO_2$ mitigation [5].

Algae cells utilize various elements available in different forms in the environment for their growth and development. These micronutrients are utilized directly or indirectly for several crucial processes occurring in the cells, such as photosynthesis and respiration. The cells can either utilize these elements immediately after uptake or store it for future use. Growth and biomass production by algae cells are directly dependent upon uptake, assimilation, and utilization of essential elements by these cells [4]. Presence of excess elements in the growth media can cause cell toxicity and is a waste of expensive nutrients. Understanding the process of uptake, assimilation, and utilization of essential elements by algae cells can aid in formulation of optimum dosage for these micronutrients during algae cultivation. Such knowledge will be of additional value for development of micronutrient-rich dietary supplements and animal feed products from algae.

Algae-based food and feed products are rich source of iron for the consumers. The micronutrient iron (Fe) has a major effect on the intracellular and extracellular environment of the algal species [9]. Iron is essential for cellular processes such as respiration, photosynthesis, nitrogen assimilation and fixation, and DNA synthesis, where it acts as electron donor in its ferrous state, and as electron acceptor in its ferric state [1, 3]. Iron, however, is also a limiting factor for growth of marine algae as it is highly insoluble in seawater and the dissolved iron has low bioavailability [12]. Understanding the iron uptake and utilization in a spatio-temporal manner thus becomes critical for optimizing iron requirement of the algal cells. This knowledge can aid in formulation of optimum inoculum protocol for iron in algae cultures that will be support maximum cell growth and development while controlling elemental toxicity.

Bulk elemental analysis of algal biomass is done by biochemical and spectroscopic analysis methods [6, 8, 10]. SEM–EDX is used for elemental mapping of outer surface of algae cells [6]. However, intracellular localization of iron and other elements is not possible by these techniques. Optical microscopy using iron-specific stains are used to study iron assimilation patterns within relatively large multicellular algal cells [7]. However, the limitation is that it cannot resolve finer details within unicellular algae such as *Nanochloropsis, Chlorella, and Chlamydomonas*. Transmission electron microscopy (TEM) is a method widely used by biologists to image ultrastructure of individual cells. Scanning TEM (STEM) that has better spatial resolution than conventional TEM is primarily used for analysis of materials. STEM paired with energy-dispersive X-ray spectroscopy (EDX) is used for elemental identification and mapping. EDX detector can identify individual elements

present in a sample based on their characteristic X-ray peaks produced due to their unique atomic structure and difference in energy of inner and outer electronic shells. Elements with low atomic number cannot be detected by EDX, although advances in technology in last decade has made it possible to detect boron, carbon, and nitrogen [2]. STEM-EDX is predominantly used for materials research; however, its application for biological studies is gaining interest in recent years [11, 14].

In this report, we standardized a protocol for localizing various elements within unicellular algae cells using STEM-EDX. Using this method, we mapped the various microelements in and around individual algae cells. We further focused on the elemental iron distribution pattern in algae cultures exposed to varying ionic iron content in growth media. Our study shows that STEM-EDX has great potential for simultaneous ultrastructural imaging with elemental mapping of biological samples such as cells and tissues, for studying elemental uptake physiology.

## 2 Experimental

***Cell culture***: Algae cells (*Nanochloropsis* sp.) were grown in sea water-based media with urea and phosphoric acid, in Kuhner shaker at 30 °C with 400 μE light illumination for 12 h. Culture flasks were shaken at 100 rpm, and $CO_2$ environment was maintained inside the incubation chamber during the photosynthetic light period. Iron concentration in the culture was varied by addition of ferric chloride stock solution at (a) 2X, for a normal iron condition, and (b) 4X, for a high iron condition. Following incubation, cultures were harvested at 0, 1, 4, and 7 days, washed in normal sea water media to remove the excess iron not attached to algae cells, and processed for electron microscopy.

***STEM-EDX***: All fresh algae cells were harvested at various time points, centrifuged, and the cell pellets were immediately fixed in 2.5% glutaraldehyde and 4% paraformaldehyde in seawater media. Fixed samples were incubated at 4 °C overnight, washed thrice in seawater media, followed by a final wash in distilled water. Samples were then dehydrated in an ethanol series (25, 50, 75, 90, 100%), then infiltrated in an epon-araldite resin series (25, 50, 75, 100%). All samples were finally embedded and polymerized in 100% resin mixed with accelerator. Ultra-thin sections (70–100 nm) were cut using Leica Ultracut-7 ultra-microtome, collected on formvar-carbon-coated copper mesh TEM grids (Electron Microscopy Sciences, USA) for STEM-EDX analysis. STEM imaging was done with Titan G2 60–300 TEM (FEI Company, USA) equipped with X-FEG electron gun operating at 300 kV which was used to find well-preserved cells in multiple sections from each sample type. Nanometer-resolution *in situ* elemental maps for several individual cells and their surroundings in each sample type were then obtained using Chemi-STEM EDX detectors. The beam intensity was optimized to get a minimum 1 kcps in the energy spectrum for at least 15 min to obtain false color elemental mapping of each sample.

## 3 Results

***Detection and mapping of elements by STEM-EDX***: Presence of several elements including nitrogen (N), oxygen (O), sodium (Na), magnesium (Mg), aluminum (Al), silicon (Si), phosphorus (P), sulphur (S), chlorine (Cl), potassium (K), calcium (Ca), and iron (Fe) could be detected in variable intensity in algae cells from all the above-mentioned cultures. Location of these elements could be mapped in and around individual algae cells to the spatial resolution of few nanometers (Fig. 1).

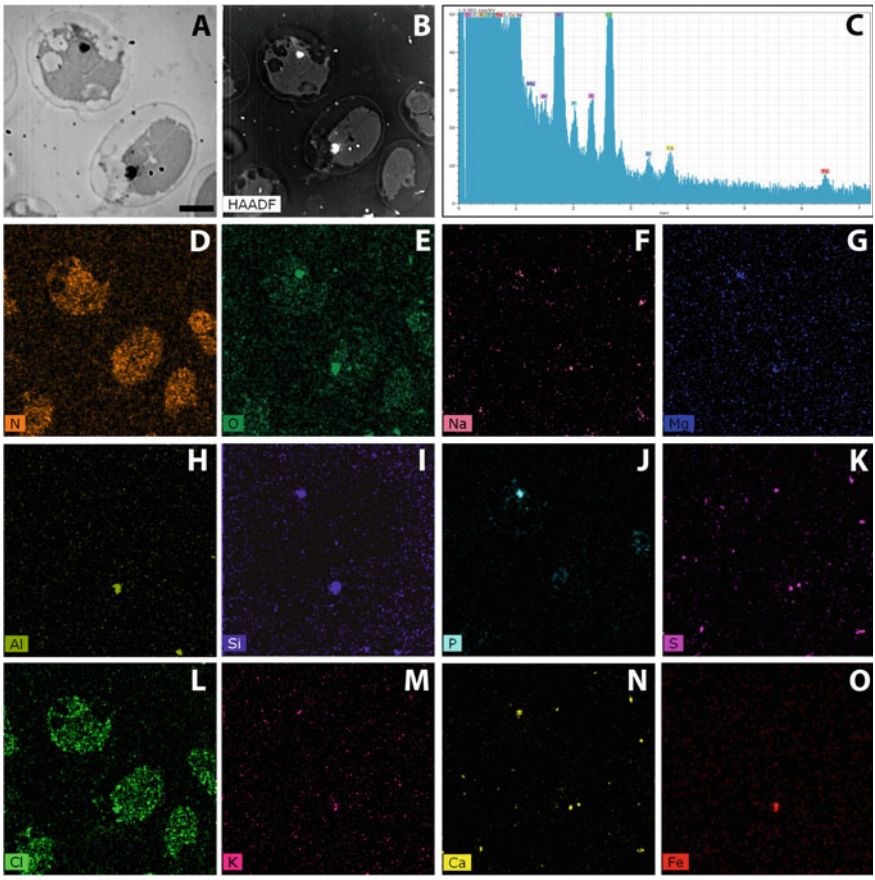


**Fig. 1** Detection and intercellular localization of elements in algae cell cultures by STEM-EDX mapping. (**a**–**o**) Cells grown in normal Fe (2X) for 7 days. **a** STEM bright field image of cells mapped. **b** High angle annular dark field (HAADF) image of cells mapped. **c** EDX Spectrum showing elements detected in area scan of B. **d**–**o** STEM-EDX maps of elements detected in spectrum. Scale bar = 2 μm

Some of these elements such as carbon, nitrogen, oxygen, and chlorine were observed to be present throughout all cells, whereas other elements were localized as tiny electron-dense particles in different parts of cells.

***Spatial localization of iron (Fe)***: Variation in elemental Fe concentration in the growth media resulted in different localization patterns in and around the algae cells at various time series points (Fig. 2a–j). A very low intensity of Fe signal was detected throughout the cells in all cultures, which can be considered as basal Fe content of each cell. In cultures grown with normal iron concentration (2X), cells with only such basal Fe content was observed at Day-0 (Fig. 2a), Day-1 (Fig. 2b) and Day-4 (Fig. 2c). Such cells were also predominant in cultures grown upto 7 days. However, in few cells ($\sim$1–2% of population), tiny electron-dense deposits of Fe could be observed inside the cells (Fig. 2d). Small clumps of Fe were also visible outside the cells in 2X cultures grown for 1, 4, and 7 days (Fig. 2b–d).

In cultures grown with high iron concentration (4X), cells with only basal Fe content were predominant for all time series data points as in 2X samples. However, unlike 2X samples, electron-dense Fe deposits could be seen within individual cells as early as Day-1 (Fig. 2f) and was also present in Day-4 (Fig. 2h) and Day-7 (Fig. 2j) samples. Fe deposits were detected on the plasma membrane in Day-1 cultures (Fig. 2f). By Day-4, Fe deposits could be detected in the cytoplasm as well as in the chloroplasts apart from being attached to plasma membrane (Fig. 2h). By Day-7, slightly larger deposits of Fe, compared to those seen at earlier time series points, were localized only within the chloroplasts (Fig. 2j). Large chunks of Fe precipitates were found lying outside, but in close proximity to the algae cells at all time series points with 4X iron in media (Fig. 2e, g, i). These external Fe deposits were often attached to broken pieces of membranes and other cell debris.

## 4 Discussion

These results suggest that addition of higher concentration of Fe in algae growth media can cause accumulation of Fe as dense aggregated particles within the cells, although the frequency of such cells remain extremely low ($\sim$1–2% of a population) when cultures are grown for 1–7 days. Most of the extra Fe seems to get precipitated as large aggregates outside in close proximity to the cells. Above indicates possible presence of a regulated Fe uptake mechanism in these algae cells, as previously suggested by physiological studies of marine microalgae [13]. Further STEM-EDX studies combined with molecular biology experiments would be required for a clear understanding of the mutiple steps and players involved in the Fe uptake, accumulation and utilization pathways of these algae cells. Similar studies can be conducted for other elements and other algal species, which will help in optimizing pond culture conditions for various algae strains based on their respective elemental requirements. The results of the current study also shows that addition of excess Fe did not bring any noticeable increase in algae cell size. Addition of excess Fe will hence be waste and could even help cohabitating

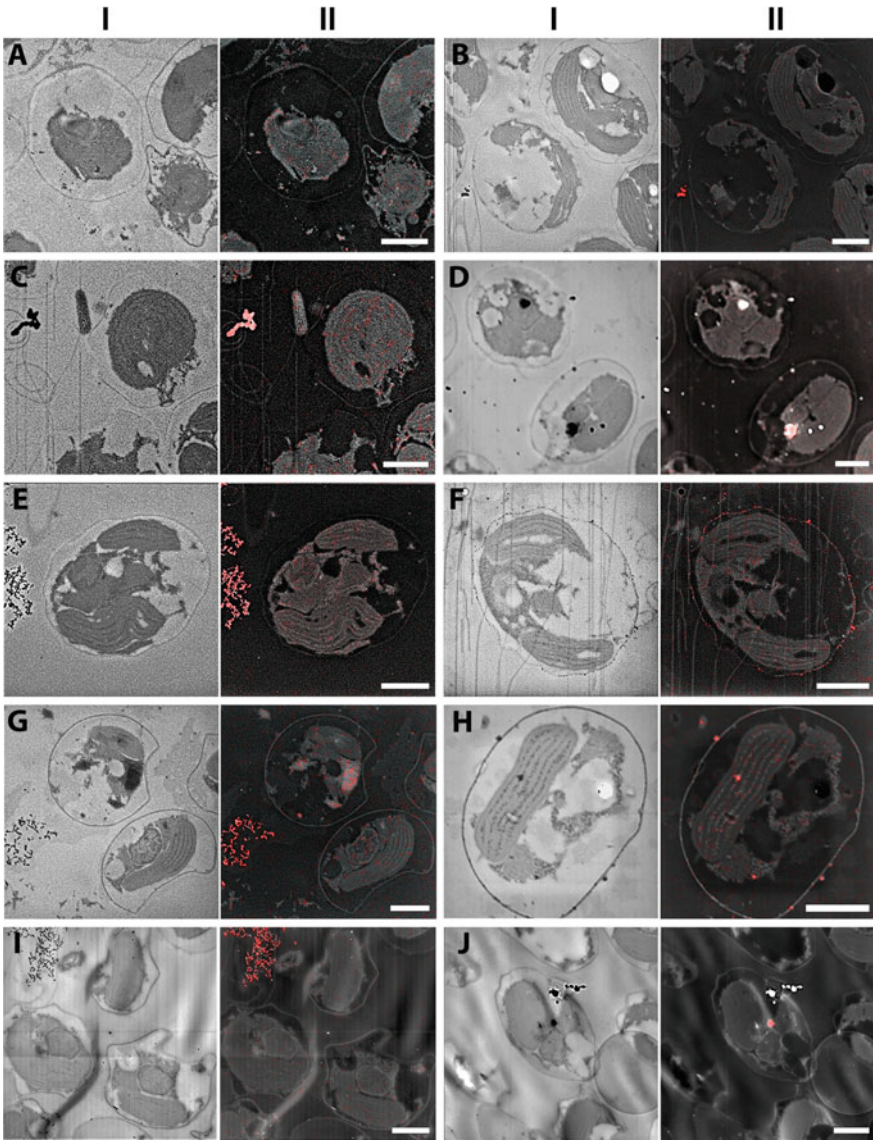


**Fig. 2** Localization of iron (Fe) in algae cell cultures by STEM-EDX mapping. **a**–**d** Cells grown in normal Fe (2X) for **a** 0 day, **b** 1 day, **c** 4 days, **d** 7 days, **e**–**j** Cells grown in high Fe (4X) for (**e**, **f**) 1 day (**g**, **h**) 4 days (**i**, **j**) 7 days. **Panel I**: STEM bright field images of cells mapped. **Panel II**: Fe maps overlaid on respective high angle annular dark field (HAADF) images. Scale bars = 2 μm

contaminant organisms in open pond cultures. Hence, knowledge of optimum dose of Fe and other elements will also help in reducing contamination load in the ponds using inoculum-based elements input.

## 5 Conclusion

This study demonstrates that STEM-EDX can be used for cellular localization of elements of unicellular algae cells. Such studies can add valuable spatial information to elemental uptake studies that are mostly limited to bulk analysis techniques.

**Acknowledgements** The authors are thankful to Dr Vinod Nagle of A2O-Germplasm team for providing the algae strains, and the management of Reliance Industries Ltd. for supporting this work.

## References

1. Adetola TG (2011) Effect of nitrogen, iron and temperature on yield and composition of microalgae. Thesis. Master of Science in Plant and Soil Sciences. Oklahoma State University Stillwater, Oklahoma
2. Berlin J (2011) Analysis of boron with energy dispersive X-ray spectrometry: advances in light element analysis with SDD technology. Imaging Microsc 13:19–21
3. Briat JF, Curie C, Gaymard F (2007) Iron utilization and metabolism in plants. Curr Opin Plant Biol 10:276–282
4. Healey FP (1973) Inorganic nutrient uptake and deficiency in algae. CRC Crit Rev Microbiol 3(1):69–113
5. Khan MI, Shin JH, Kim JD (2018) The promising future of microalgae: current status, challenges, and optimization of a sustainable and renewable industry for biofuels, feed, and other products. Microb Cell Fact 17:36
6. Michalak I, Mironiuk M, Marycz K (2018) A comprehensive analysis of biosorption of metal ions by macroalgae using ICP-OES, SEM-EDX and FTIR techniques. PloS One 13(10): e0205590
7. Miller EP, Böttger LH, Weerasinghe AJ, Crumbliss AL, Matzanke BF, Meyer-Klaucke W, Küpper FC, Carrano CJ (2013) Surface-bound iron: a metal ion buffer in the marine brown alga *Ectocarpus siliculosus*? J Exp Bot 65:585–594
8. Mori JF, Neu TR, Lu S, Händel M, Totsche KU, Küsel K (2015) Iron encrustations on filamentous algae colonized by *Gallionella*-related bacteria in a metal-polluted freshwater stream. Biogeosciences 12:5277–5289
9. Morrissey J, Bowler C (2012) Iron utilization in marine cyanobacteria and eukaryotic algae. Front Microbiol 3:1–13
10. Nayak M, Karemore A, Sen R (2016) Sustainable valorization of flue gas $CO_2$ and wastewater for the production of microalgal biomass as a biofuel feedstock in closed and open reactor systems. RSC Adv 6:91111–91120
11. Ponce A, Mejía-Rosales S, José-Yacamán M (2012) Scanning transmission electron microscopy methods for the analysis of nanoparticles. In: Soloviev M (ed) Nanoparticles in biology and medicine: methods and protocols, methods in molecular biology, vol 906, pp 453–470
12. Su H, Yang R, Pižeta I, Omanović D, Wang S, Li Y (2016) Distribution and speciation of dissolved iron in Jiaozhou Bay (Yellow Sea, China). Front Mar Sci 3:99

13. Sutak R, Botebol H, Blaiseau PL, Léger T, Bouget FY, Camadro JM, Lesuisse E (2012) A comparative study of iron uptake mechanisms in marine microalgae: iron binding at the cell surface is a critical step. Plant Physiol 160(4):2271-84
14. Wu JS, Kim AM, Bleher R, Myers BD, Marvin RG, Inada H, Nakamura K, Zhang XF, Roth E, Li SY, Woodruff TK, O'Halloran TV, Dravid VP (2013) Imaging and elemental mapping of biological specimens with a dual-EDS dedicated scanning transmission electron microscope. Ultramicroscopy 128:24–31

# Cryo-EM Structure of Rotavirus VP3 Reveals Novel Insights into Its Role in RNA Capping and Endogenous Transcription


**Dilip Kumar, Xinzhe Yu, Sue E. Crawford, Liya Hu, Mary K. Estes, Zhao Wang, and B. V. Venkataram Prasad**

**Keywords** Rotavirus · VP3 · Structure · Cryo-EM · RNA capping enzyme · Helicase · RTPase · Endogenous transcription

## 1 Introduction

Rotavirus (RV) is a major causative agent of severe diarrhea among infants and children (<5 years of age). RV infections are responsible for more than 200,000 deaths annually [2]. RV belongs to the family Reoviridae and contains a segmented double-stranded RNA (dsRNA) genome [8]. The infectious virion, also known as a triple-layered particle (TLP), consists of three layers formed by six viral proteins (VPs). The outer, middle, and inner capsid layers of the TLP are formed by VP7 and the spike protein VP4, VP6, and VP2, respectively. The innermost core of the virion composed of the VP2 layer contains the RNA-dependent RNA polymerase (RdRp), VP1, a capping enzyme, VP3, and the eleven segments of dsRNA genome (Fig. 1a). During the process of virus entry into the host cell, RV sheds the outer

D. Kumar · X. Yu · L. Hu · Z. Wang · B. V. Venkataram Prasad (✉)
Verna and Marrs McLean Department of Biochemistry and Molecular Biology, Baylor College of Medicine, Houston, TX 77030, USA
e-mail: vprasad@bcm.edu

S. E. Crawford · M. K. Estes · B. V. Venkataram Prasad
Department of Molecular Virology and Microbiology, Baylor College of Medicine, Houston, TX 77030, USA

M. K. Estes
Department of Medicine, Baylor College of Medicine, Houston, TX 77030, USA

Z. Wang
CryoEM Core, Baylor College of Medicine, Houston, TX 77030, USA

Z. Wang
Department of Molecular and Cellular Biology, Baylor College of Medicine, Houston, TX 77030, USA



P. Ghosal et al. (eds.), *Applications of Microscopy in Materials and Life Sciences*, Springer Proceedings in Materials 11,
https://doi.org/10.1007/978-981-16-2982-2_21

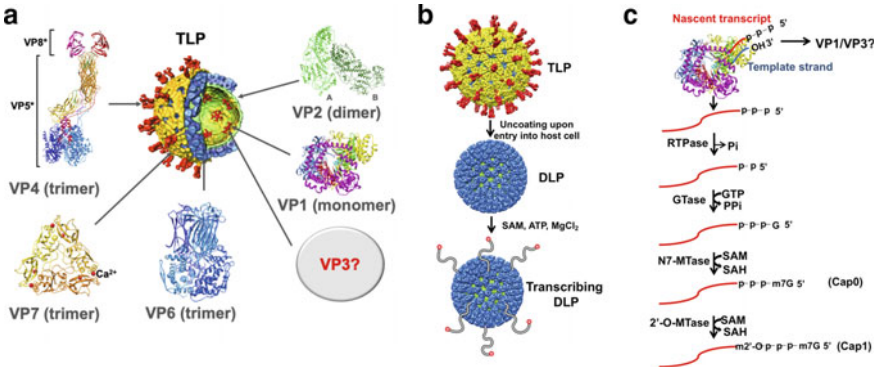


**Fig. 1** Structural organization of rotavirus particle and RNA capping during endogenous transcription. **a** Rotavirus TLP structure consisting of six viral proteins. Structural proteins are represented in the ribbon model, and their spatial arrangement in TLP is denoted by arrows. Structures are prepared from PBD IDs: 2R7R (VP1), 3KZ4 (VP2), 3IYU (VP4), 3KZ4 (VP6), 3FMG(VP7), 3IYU (TLP), and 3N09 (DLP). The location of VP3 inside the particle remains unclear. **b** During the rotavirus replication cycle, the outer VP7/VP4 layer is released, and the resulting form of DLP actively transcribes genomic dsRNA transcripts. DLPs can also transcribe the genome segments in vitro in the presence of SAM, ATP, and $MgCl_2$. **c** The transient duplex formed between the template and nascent strand needs to be separated (possibly by VP1 or VP3 or both) followed by 5′-capping which involves multiple enzymatic activities

layer of VP7 and VP4, and the resulting double-layered particle (DLP) released in the cytoplasm adopts a transcriptionally active form to transcribe the genomic dsRNA segments [20, 29]. The capped mRNA is extruded from inside the core of the DLP through channels at the icosahedral fivefold axes (Fig. 1b) [18]. The endogenous transcription in the DLPs can also be activated in vitro in the presence of S-adenosyl methionine (SAM), ATP, and divalent metal ion ($MgCl_2$) [18, 19] (Fig. 1b). The DLPs are molecular machines that can transcribe the genomic segments continuously without compromising their structural integrity as long as the metabolites required for transcription are made available. It is suggested that all the 11 segments are transcribed simultaneously in equimolar ratios during endogenous transcription [18, 24]. How the viral polymerase VP1 and the capping enzyme VP3 inside the core of the structurally intact DLP coordinate this process of simultaneous transcription of 11 dsRNA segments is a mystery.

The nascent positive-strands emerging from VP1 during transcription are capped by VP3 before their exit through the channels at the fivefold axes of the DLPs [19]. 5′-RNA capping, a conserved cellular process, is adopted by several viruses. In addition to facilitating efficient translation, the 5′-RNA cap also protects viral mRNA from cellular nucleases and aids in evading the host immune response [25]. The 5′-mRNA capping involves a concerted series of enzymatic steps. In the initiation step, the terminal γ-phosphate of the nascent RNA, following its separation from the template RNA strand, has to be removed using RNA triphosphatase (RTPase) activity. The second step involves the transfer of GMP onto the 5′-end of

the nascent transcript by the guanylyltransferase (GTase) that links the GMP to the first nucleotide through a 5′-5′ triphosphate linkage. Two additional steps by the methyltransferase (MTase) add a methyl group at the N7-position of the GMP (m7G; cap0) and then at the 2′-O-ribose sugar of the first nucleotide (Cap1) [25] (Fig. 1c). While GTase and MTase activities for VP3 have been established [5, 21], it is unclear whether VP3 harbors RTPase activity, how the nascent RNA is separated from the template (helicase activity), and whether VP3 is involved in this process.

The overall structure of the TLP along with the individual capsid proteins at near-atomic resolution has been determined except for the structure of VP3 until recently [17, 29]. Although it has been possible to visualize the structure of VP1 from cryo-EM images of the TLP or DLP using focused refinement techniques, the structure or the location of VP3 inside the particle has been elusive [10, 14]. Except for the X-ray crystallographic structure of the C-terminal domain of VP3, which exhibits phosphodiesterase (PDE) activity that is suggested to be responsible for antagonizing the OAS/RNAase L antiviral pathway [22, 30], the structural details of the full-length VP3 have been lacking. Recently, using high-resolution cryo-EM techniques, we have determined a 2.7 Å structure of full-length VP3 [17]. Together with X-ray crystallography and complementary biophysical and biochemical analysis, we have provided a comprehensive description of the VP3 structure in relation to its various enzymatic activities along with a plausible model for how VP3, along with VP1, coordinates endogenous transcription inside the RV particle.

## 2 Cryo-EM Structure of VP3 Exhibits Stable Tetrameric Assembly with a Modular Domain Organization

We used the baculovirus Sf9 insect cell expression system to express full-length RV VP3 and purified the protein using the Ni–NTA affinity-based purification system. The purified VP3 was used for crystallization at room temperature using the hanging drop vapor diffusion method. The crystals obtained were harvested in liquid nitrogen, and X-ray diffraction data were collected at the Advanced Light Source, Lawrence Berkeley National Laboratory beamline 5.0.2. Our attempts to solve the phase problem using molecular replacement methods were unsuccessful in the absence of any homologous structures. Structure solution using selenomethionine-substituted VP3 was also not successful as these crystals did not diffract to high-enough resolution, and also the anomalous signal was weak. This prompted us to undertake structure determination using single-particle cryo-EM techniques. The recent developments in cryo-EM sample grid preparation methods, improvements in direct electron detectors, and significant developments in data processing software have revolutionized the resolution that can be achieved for macromolecular structures by cryo-EM [16]. Considering that VP3 forms a stable tetrameric molecular assembly, as observed by gel-filtration and analytical

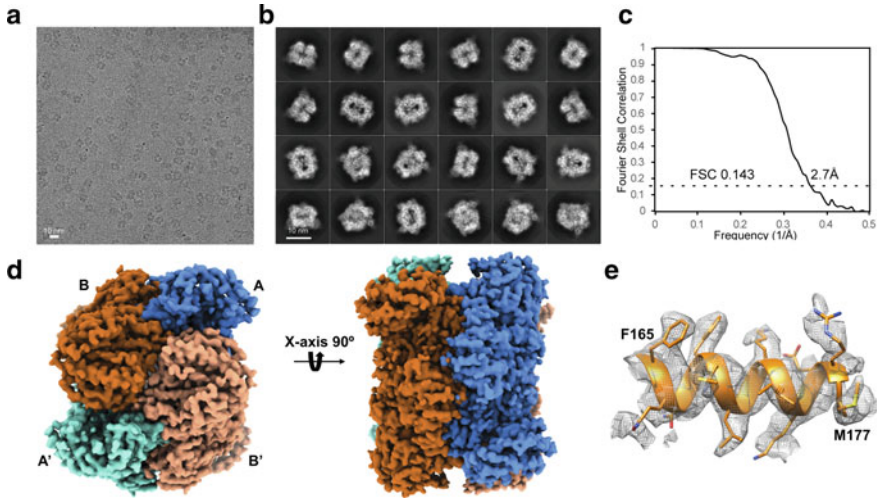


**Fig. 2** Cryo-EM structure of RV VP3 using single-particle reconstruction methods [17]. **a** Raw micrograph of VP3 showing homogenously distributed VP3 particles on the grid. **b** 2D class averages showing multiple orientations of VP3 particles. **c** FSC curve showing 2.7 Å resolution at 0.143. **d** The final structure of the VP3 tetramer (EMDB ID: EMD-0632) is shown along the twofold axes of the D2 symmetry. Individual subunits chain A (deep sky blue) and chain B (chocolate brown) and their two-old related symmetry pairs chain A′ (cyan) and chain B′ (salmon) are shown in shades of blue and brown. **e** A representative sample of cryo-EM density showing side-chain densities

ultracentrifugation analysis, with a total molecular weight of ~392 kDa, VP3, is a suitable target for high-resolution cryo-EM structure determination. Cryo-EM grid optimization was performed by using Vitrobot (Mark IV, FEI) with a well-established vitrification protocol [12]. The flash-frozen hydrated VP3 sample was imaged on a 300 kV JEM-3200FSC electron microscope (JEOL) equipped with a K2 Summit direct electron detector (Gatan). From 1,690 movie stacks, 133,712 particles were boxed by EMAN 2.2 and used for generating initial reference-free 2D class averages using RELION 2.1 (Fig. 2a, b) [4, 26]. The initial 3D model was generated in e2initialmodel.py [28] using good 2D classes and further refined in RELION [26]. A total of 70,892 particle images were used for a final reconstruction yielding a resolution of 2.7 Å at a 0.143 threshold of the Fourier shell correlation (FSC) after post-processing (Fig. 2c). For model building, we used a secondary structure prediction of the VP3 amino acid sequence followed by manual model building in COOT [13] and model refinement using techniques as implemented in the PHENIX software and in Rosetta software for density refinement with secondary structure and Ramachandran restraints [1, 9]. The final model was validated using MolProbity and EMRinger software [3, 6]. The availability of the subunit structure from the cryo-EM allowed us to revisit the X-ray diffraction data and determine the crystallographic structure of VP3 using molecular

replacement method to ~3.5 Å resolution (PDB ID: 6O3V), which showed the formation of an identical tetrameric assembly as observed in solution (see Kumar et al. [17] for detailed methods).

The tetrameric assembly of VP3 consists of two sets of antiparallel dimers intertwined around each other with D2 symmetry (Fig. 2d). The large total buried surface area (~17,080 Å$^2$) is consistent with a highly stable tetrameric assembly. Such a stable tetrameric assembly, as observed with VP3, is rather a unique feature for a capping enzyme and was not observed in the structure of the orthologous bluetongue virus (BTV) capping enzyme VP4 [27]. The final model shows electron density for the side chains of amino acid residues across the structure (Fig. 2e). Each VP3 subunit exhibits a modular domain organization with each of the domains involved in oligomeric contacts facilitating the stabilization of the tetrameric assembly (Fig. 3a, b). The structural comparison with the closest structural homolog VP4 from BTV [27] reveals the enzymatic domains required for critical steps of mRNA capping which are conserved with subtle differences in the N- and C-terminal domain. Despite conserved enzymatic folds (GTase and MTase), the relative domain organization shows significant variability with a high r. m. s. d. value of 5.6 Å upon the superposition of RV VP3 with BTV VP4. The N-terminal kinase-like (KL) or MAVS domain [11] exhibits the least structural and sequence

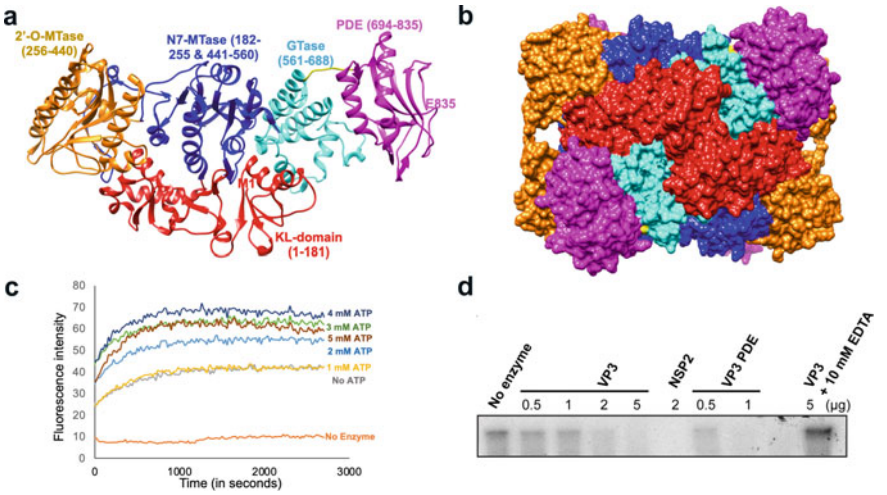


**Fig. 3** Structural and enzymatic features of RV VP3 [17]. **a** The full-length structure of a monomeric subunit of RV VP3 with each domain is colored separately. N- and C-terminal are labeled in respective domain colors. **b** The surface representation of the tetrameric assembly with domains in each subunit colored as in A. Individual domains participate extensively in stabilizing the tetrameric assembly of RV VP3. **c** VP3 shows ATP modulated helicase activity. Fluorescence intensity is measured for 6-FAM labeled RNA when it gets separated from a complementary strand labeled with BHQ-1 quencher. **d** VP3 and PDE domain alone exhibit RTPase activity. The 32-P-ϒ-Labeled RNA was incubated with enzymes, and loss of radioactivity was observed on radiography film. RV NSP2 was used as a positive control

conservation with BTV VP4 suggesting its possible role in interacting with viral or host proteins. The KL domain in RV VP3 (~181 aa) is also significantly larger than in the BTV VP4 (~108 aa) and contains an additional uncharacterized fold [17]. So far, no catalytic activity has been proposed or determined for the KL- or MAVS domain. We also observed a cognate ligand GMP interacting with the catalytically conserved residues [23] in the GTase domain of VP3 both in the X-ray and cryo-EM structures. Additionally, we observed a sulfate group in our X-ray structure bound to the conserved His41 in the N-terminal domain, possibly analogous to phosphate released after GTase activity [7]. Both the MTase domains (N7-MTase and 2′-O-MTase) contain a conserved MTase fold with subtle variations in substrate binding regions. An additional difference between the RV VP3 and BTV VP4 is the presence of a C-terminal domain with PDE activity in the RV VP3, which is implicated in countering the antiviral OAS-RNase L pathway [30]. Consistent with the role of VP3 in the RNA capping, our bio-layer interferometry analysis demonstrated that VP3 binds to ssRNA with nanomolar binding affinity. Similar high-affinity binding was also observed with VP3-PDE domain alone suggesting that the C-terminal PDE domain is principally involved in binding to RNA, which was further confirmed by a preliminary cryo-EM structure of VP3 in complex with 8-mer ssRNA (5′-rG.rG.rC.rU.rU.rU.rU.rA-3′).

## 3 VP3 Exhibits Helicase and RTPase Activity

To explore if VP3 can play a role in separating the transient template-nascent transcript strand duplex, we performed a fluorescence-based helicase assay. This assay revealed that VP3 exhibits RNA helicase activity, which can be modulated by ATP and $MgCl_2$ (Fig. 3c). This clarified a novel role for VP3; separating the nascent transcript from the template strand as it exits from the viral polymerase VP1 during endogenous transcription [14]. Following strand separation and binding to the nascent transcript, the next step in the capping is the removal of the terminal phosphate from the nascent transcript. Does VP3 exhibit the required RTPase activity? Consistent with the involvement of the C-terminal PDE domain in binding to ssRNA, our biochemical analysis demonstrated that this domain exhibits RTPase activity (Fig. 3d). Thus, in addition to the previously demonstrated GTase and MTase activities required for the capping process and the phosphodiesterase activity, our studies revealed that VP3 exhibits RTPase and RNA helicase activities. Such a combination of as many as five distinct enzymatic activities in a single protein is indeed unique.

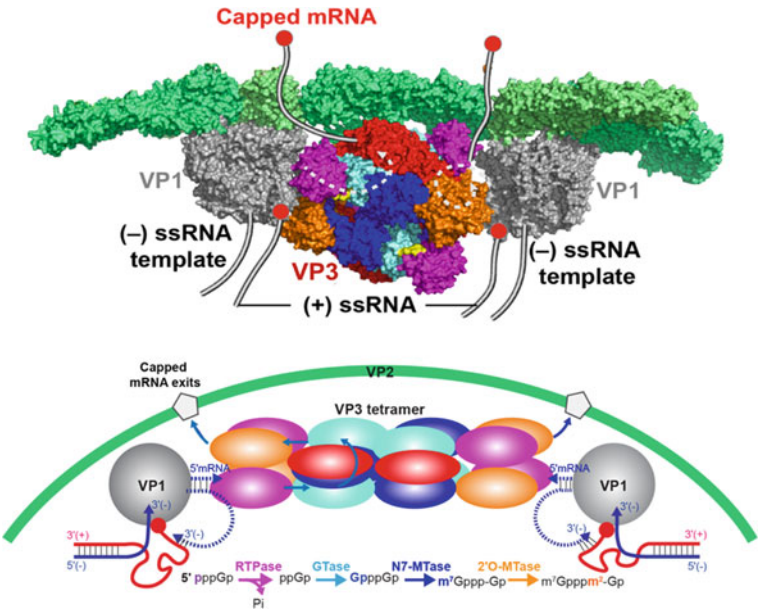


**Fig. 4** Proposed mechanism of VP3 associated capping during endogenous transcription [17]. VP3 (each domain colored individually as in Fig. 3a) placed in between two adjacent VP1 molecules (gray) attached to the innermost VP2 layer (green) close to fivefold axes caps the nascent transcript. Lower panel represents the schematic cartoon representation of simultaneous capping activities performed by VP3 tetramer inside the particle during endogenous transcription. The surface representation in upper panel is rendered from PDB IDs: 6O6B (VP3) and 4F5X (VP1 and VP2)

## 4 A Plausible Model for RNA Capping in RV

Considering our observations that VP3 forms a highly stable tetramer, that it can effectively bridge the distance between a neighboring pair of VP1 molecules inside the particle core, and that the C-terminal domain with RNA binding and RTPase activities is distally located, we have proposed a plausible model as to how VP3 inside the RV core is involved in capping the nascent transcript to support simultaneous transcription of the dsRNA segments [17]. In this model, one VP3 tetramer is localized between every non-redundant pair of VP1 molecules inside the core with each end of VP3 tetramer facing a VP1 molecule (Fig. 4). In such an arrangement each VP3 tetramer can simultaneously cap two transcripts exiting from the VP1 molecules.

## 5 The Future Perspectives

Our studies, while answering several fundamental questions about RV VP3, has raised several new questions that need to be addressed in future studies. First, can VP3 be visualized inside the core of the particles during endogenous transcription? Although it has been possible to visualize VP1 inside the particle in both quiescent and actively transcribing states using the cryo-EM technique [10, 14], curiously it has not been possible to visualize VP3. There could be several reasons including a possible dynamic association of VP3 with VP1 during transcription or suboptimal protocols for activating the endogenous transcription such that the transcripts are efficiently capped favoring a sustained association with VP1. It will be exciting to validate our proposed model particularly if the tetrameric form of VP3 is the functional state during endogenous transcription in RV, or to determine whether during the assembly of the nascent RV core, VP3 is destabilized and incorporated into the particle as a monomer or a dimer. Secondly, further studies are required to address other fascinating questions such as a) how does the transcript traverse through the various domains in VP3 during the process of acquiring the cap, b) are there significant conformational changes associated with this process, and c) how does the capped transcript exit the transcribing particle. It is evident that further elaborate cryo-EM studies with appropriate image processing and refinement techniques, together with clever biochemical manipulations are necessary to address these questions. What is the oligomeric state of VP3 during replication, does it exist as a tetramer during its role as an antagonist of the antiviral OAS/RNase pathway, and what is the role of the KL domain are other outstanding questions that merit further investigation perhaps leveraging the recent advances in the successful implementation of the rotavirus reverse genetics system [15].

**Acknowledgements** We acknowledge support from NIH grant AI36040 (to BVVP), R01 AI080656 (to MKE), the Robert Welch Foundation (Q1279) to BVVP and (Q1967) to ZW. Crystal data was collected at the Berkeley Center for Structural Biology supported in part by the NIH, National Institute of General Medical Sciences, and the Howard Hughes Medical Institute. The Advanced Light Source is supported by the Director, Office of Science, Office of Basic Energy Sciences, of the U.S. Department of Energy under Contract No. DE-AC02-05CH11231. The Cryo-EM is supported by Advanced Technology Cores (ATC) Cryo-EM/ET core at BCM.

## References

1. Afonine PV et al (2018) Real-space refinement in PHENIX for cryo-EM and crystallography. Acta Crystallographica Section D: Struct Biol. https://doi.org/10.1107/S2059798318006551
2. Bányai K et al (2018) Viral gastroenteritis. The Lancet. https://doi.org/10.1016/S0140-6736(18)31128-0
3. Barad BA et al (2015) EMRinger: side chain-directed model and map validation for 3D cryo-electron microscopy. Nat Methods. https://doi.org/10.1038/nmeth.3541
4. Bell JM et al (2016) High resolution single particle refinement in EMAN2.1. Methods. https://doi.org/10.1016/j.ymeth.2016.02.018

5. Chen D et al (1999) Rotavirus open cores catalyze 5′-capping and methylation of exogenous RNA: evidence that VP3 is a methyltransferase. Virology. https://doi.org/10.1006/viro.1999.0029
6. Chen VB et al (2010) MolProbity: all-atom structure validation for macromolecular crystallography. Acta Crystallogr Sect D: Biol Crystallogr. https://doi.org/10.1107/S0907444909042073
7. Chu C et al (2011) Structure of the guanylyltransferase domain of human mRNA capping enzyme. Proc Natl Acad Sci. https://doi.org/10.1073/pnas.1106610108
8. Desselberger U (2014) Rotaviruses review. Virus Res. https://doi.org/10.1016/j.virusres.2014.06.016
9. Dimaio F et al (2015) Atomic-accuracy models from 4.5-Å cryo-electron microscopy data with density-guided iterative local refinement. Nat Methods. https://doi.org/10.1038/nmeth.3286
10. Ding K et al (2019) In situ structures of rotavirus polymerase in action and mechanism of mRNA transcription and release. Nat Commun. https://doi.org/10.1038/s41467-019-10236-7
11. Ding S et al (2018) Rotavirus VP3 targets MAVS for degradation to inhibit type III interferon expression in intestinal epithelial cells. eLife. https://doi.org/10.7554/eLife.39494
12. Dubochet J et al (1987) Cryoelectron microscopy of vitrified specimens. In: Cryotechniques in biological electron microscopy. https://doi.org/10.1007/978-3-642-72815-0_5
13. Emsley P et al (2010) Features and development of Coot. Acta Crystallogr D Biol Crystallogr. https://doi.org/10.1107/s0907444910007493
14. Jenni S et al (2019) In situ structure of rotavirus VP1 RNA-dependent RNA polymerase. J Mol Biol. https://doi.org/10.1016/j.jmb.2019.06.016
15. Kanai Y et al (2017) Entirely plasmid-based reverse genetics system for rotaviruses. Proc Natl Acad Sci USA. https://doi.org/10.1073/pnas.1618424114
16. Kühlbrandt W (2014) The resolution revolution. Science. https://doi.org/10.1126/science.1251652
17. Kumar D et al (2020) 2.7 Å cryo-EM structure of rotavirus core protein VP3, a unique capping machine with a helicase activity. Sci Adv. https://doi.org/10.1126/sciadv.aay6410
18. Lawton JA, Estes MK, Prasad BVV (1997) Three-dimensional visualization of mRNA release from actively transcribing rotavirus particles. Nat Struct Biol. https://doi.org/10.1038/nsb0297-118
19. Lawton JA, Estes MK, Prasad BVV (2002) Identification and characterization of a transcription pause site in rotavirus. J Virol. https://doi.org/10.1128/jvi.75.4.1632-1642.2001
20. Lawton JA, Estes MK, Venkataram Prasad BV (2000) Mechanism of genome transcription in segmented dsRNA viruses. Adv Virus Res. https://doi.org/10.1016/s0065-3527(00)55004-0
21. Liu M, Mattion NM, Estes MK (1992) Rotavirus VP3 expressed in insect cells possesses guanylyltransferase activity. Virology. https://doi.org/10.1016/0042-6822(92)90736-9
22. Ogden K et al (2015) Structural Basis for 2′-5′-oligoadenylate binding and enzyme activity of a viral RNase L antagonist. J Virol. https://doi.org/10.1128/jvi.00701-15
23. Ogden KM et al (2014) Predicted structure and domain organization of rotavirus capping enzyme and innate immune antagonist VP3. J Virol. https://doi.org/10.1128/jvi.00923-14
24. Periz J et al (2013) Rotavirus mRNAS are released by transcript-specific channels in the double-layered viral capsid. Proc Natl Acad Sci USA. https://doi.org/10.1073/pnas.1220345110
25. Ramanathan A, Robb GB, Chan SH (2016) mRNA capping: biological functions and applications. Nucleic Acids Res. https://doi.org/10.1093/nar/gkw551
26. Scheres SHW (2012) RELION: implementation of a Bayesian approach to cryo-EM structure determination. J Struct Biol. https://doi.org/10.1016/j.jsb.2012.09.006
27. Sutton G et al (2007) Bluetongue virus VP4 is an RNA-capping assembly line. Nat Struct Mol Biol. https://doi.org/10.1038/nsmb1225
28. Tang G et al (2007) EMAN2: an extensible image processing suite for electron microscopy. J Struct Biol. https://doi.org/10.1016/j.jsb.2006.05.009

29. Trask SD, McDonald SM, Patton JT (2012) Structural insights into the coupling of virion assembly and rotavirus replication. Nat Rev Microbiol. https://doi.org/10.1038/nrmicro2673
30. Zhang R et al (2013) Homologous 2′,5′-phosphodiesterases from disparate RNA viruses antagonize antiviral innate immunity. Proc Natl Acad Sci. https://doi.org/10.1073/pnas.1306917110

# A Microscopic Analysis of Liposome Based Hydrophobic Drug Delivery


**Tejaswini Appidi, Syed Baseeruddin Alvi, P. V. P. Deepak Bharadwaj, and Aravind Kumar Rengan**

**Abstract** Microscopy plays a crucial role in understanding the materials at nanoscale and evaluating inter & intra cellular processes at the nano/micro scale and beyond. Many hydrophobic drugs and agents encapsulated within nanosystems are reported for their enhanced therapeutic efficiency. In this paper, we discuss the differences in the drug dynamics and cellular uptake of two hydrophobic fluorescent compounds: Chlorophyll rich fraction of *Anthocephalous cadamba* (CfAc) & curcumin encapsulated within a liposomal nanosystem. The dynamics of hydrophobic drug release and its cellular interaction in vitro were studied by transmission electron microscopy (TEM) and confocal laser scanning microscopy (CLSM), respectively. Though CfAc and curcumin are both hydrophobic, they differ in their drug release dynamics. In the case of CfAc, the drug is released in its nano form directly into the cells. Whereas in the case of curcumin, the drug initially releases in the form of nano crystals which coalesce to form micron-sized crystalline depots. These depots then tend to release the drug in the localized cellular environment. The drug release patterns of both CfAc & curcumin were evidenced by using both TEM & CLSM.

Tejaswini Appidi and Syed Baseeruddin Alvi authors contributed equally.

T. Appidi · S. B. Alvi · A. K. Rengan (✉)
Department of Biomedical Engineering, Indian Institute of Technology Hyderabad, Kandi, Telangana 502285, India
e-mail: aravind@bme.iith.ac.in

P. V. P. Deepak Bharadwaj
Department of Pharmacology and Toxicology, National Institute of Pharmaceutical Education and Research, Guwahati, Assam 781101, India



P. Ghosal et al. (eds.), *Applications of Microscopy in Materials and Life Sciences*, Springer Proceedings in Materials 11,
https://doi.org/10.1007/978-981-16-2982-2_22

**Graphical Abstract** The differences in drug dynamics and cellular uptake of two fluorescent hydrophobic anti-cancer agents: CfAc & curcumin [7–9, 16]

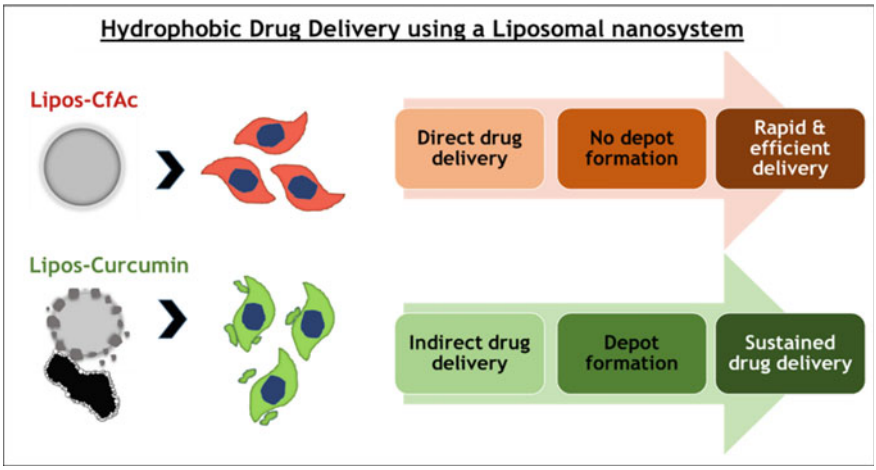


**Keywords** Liposomes · Curcumin · Hydrophobic drug delivery · Photothermal therapy

## 1 Introduction

Microscopy has been a very useful and an important tool in understanding the potential of the nanomaterials for various biological applications. The electron and optical microscopies have helped the researchers visualize the nanomaterials and their subsequent effects on the intra-cellular processes leading to the development of advanced functional materials for diagnostic & therapeutic applications. The morphology of nanosystems, their disintegration facilitating drug release, subsequent intra-cellular changes and therapeutic efficiency can be studied using microscopy. The efforts to understand and validate the mechanism of therapy are substantiated by the observations and findings recorded using microscopes: both optical and electron.

Optical microscopes, both light and fluorescent helped understand the biological processes in cells with well-suited resolutions and availability of diverse range of fluorescent probes to mark proteins, organelles, and other structures for imaging [1]. Electron microscopes like scanning electron microscope & transmission electron microscopes have been used to understand the morphology of nanosystems for drug delivery and the changes in their structure with the drug release profile [2].

Transmission electron microscopy is considered a valuable technique not just for the physico-chemical characterization of nanomaterials, but also to understand their effects on biological systems [3].

The systemic delivery of hydrophobic pharmacophore is not accessible due to its higher partition coefficient. In other words, the hydrophobic drugs tend to precipitate/degrade when exposed to aqueous environment, thus requiring nanoparticles for its delivery in vivo [4]. The liposomal nanosystem has long been investigated for the delivery of hydrophobic drugs. Currently, there are several clinically approved liposomal formulations available in the market as pharmaceutical (drugs) and nutraceuticals (Phytochemicals). The in-situ cellular interactions and release kinetics of the liposomal delivery impacts the pharmacokinetics and pharmacodynamics of these nanoformulations. Thus, it is essential to investigate the dynamics of drug release by adopting appropriate in-vitro models that helps in designing new therapeutic strategies. In the current study, the drug dynamics and cellular uptake of two hydrophobic compounds, CfAc (Chlorophyll rich fraction of *Anthocephalous Cadamba*) & curcumin encapsulated in a liposomal nanosystem were studied using microscopy. The photothermal mediated release of CfAc and its effect on cancer cells was also evaluated. Transmission electron microscope (TEM) was employed to understand the morphological changes with drug release; fluorescence and confocal microscope were used to understand the cellular uptake of these hydrophobic compounds (i.e., CfAc and curcumin) in cancer cells. TEM analysis of Lipos-Cur NPs showed the formation of micro and nanocrystals of curcumin resulting in the sustained delivery. The cellular uptake studies of CfAc and curcumin showed two types of drug delivery mechanisms, owing to the physical composition of the drugs independent of the delivery vehicle.

## 2 Materials and Methods

### *2.1 Materials*

The lipid hydrogenated soy phosphatidyl choline (HSPC) & 1,2-Distearoyl-sn-glycero-3-phosphocholine (DSPC) were a generous gift from Lipoid, Germany. IR-780 iodide, 4′,6-diamidine-2′-phenylindole dihydrochloride (DAPI), were purchased from Sigma Ltd. (U.S.A). Curcumin, Soya PC, methanol, chloroform, were procured from SRL chemicals, India. Phosphate buffer pH 7.0, Trypsin–EDTA, DMEM, RPMI, Calf Serum (US origin), were purchased from Hi-media Chemicals, (Mumbai, India). All the chemicals were used as received without any further purification.

## 2.2 Cell Lines and Maintenance

Cancer cell lines (B16, MCF-7) were obtained from the National Center for Cell Sciences (NCCS), Pune, India. The cell lines were cultured in DMEM/RPMI medium supplemented with 10% (v/v) Fetal bovine serum (FBS), 1% L-Glutamine, and 100 U/ml penicillin/streptomycin and were maintained at 37 °C in a humidified atmosphere containing 5% $CO_2$ under sterile conditions.

## 2.3 Synthesis of Liposomes Encapsulating Hydrophobic Anti-Cancer Agents

Liposomes encapsulating hydrophobic anti-cancer agents CfAc and Curcumin were prepared by thin film hydration method [5, 6]. CfAc was obtained as reported earlier [7]. The Lipos-CfAc (liposomes encapsulating CfAc) & Lipos-Cur (liposomes encapsulating curcumin) NPs were prepared as follows. Briefly, 10:1 ratio of lipid (Soya PC/HSPC/DSPC) & anti-cancer agent were dissolved in an organic solvent (chloroform/methanol). The prepared solution was then subjected to vacuum evaporation using rotary evaporator. The dried film was hydrated using distilled water @ 60 °C for 1 h. Following the hydration, the solution was subjected to probe sonication for a total of three cycles (each cycle was for 10 min with 2 s on/off). The unentrapped drug was separated by centrifugation [8, 9]. Liposomes encapsulating CfAc and IR780 (an NIR dye) (LCIR NPs) were also synthesized using the same protocol as mentioned above.

## 2.4 Drug Release with Photothermal Trigger

LCIR NPs & control (Milli Q Water) were exposed to NIR laser irradiation (808 nm, 0.6 W) (Shanghai Inter-Diff Optoelectronics Technology Ltd., Shanghai, China) and the increment in temperature was recorded, using a thermal imaging camera (Chauvin Arnoux, CA, 1950 IR camera). The release of CfAc was quantified by the measuring the flourescence intenisty at 680 nm (for an excitation of 410 nm) with laser irradiation time [10–13].

## 2.5 Cell Viability Assay

The cytotoxic effects of the LCIR NPs in cancer cells was evaluated using a photothermal trigger [14]. Briefly, the cells were seeded into 96 well plates in triplicates at a density of $1 \times 10^4$ cells/well overnight. The cells were treated with

LCIR NPs and subjected to laser irradiation for a duration of 4 min per well and incubated at 37 °C for 24 h. Cells without laser irradiation were considered as controls. The cell viability was measured by MTT assay [15].

### *2.6 Microscopic Analysis of Lipos NPs and Their Cellular Uptake*

(a) Transmission Electron Microscopy imaging: The prepared Lipos NPs, both Lipos-CfAc & Lipos-Cur NPs were drop casted on a copper grid. The imaging was performed and in-situ formed nano/micro crystals were observed using transmission electron microscopy (JEOL, JEM 2100, USA). The grids were stained with uranyl acetate prior to imaging [8]. (b) In-vitro drug release and cellular uptake: Cancer cells were treated with Lipos NPs. The cells after an incubation period of 5 h were stained with DAPI to stain the nucleus and imaged using confocal laser scanning microscopy (CLSM, Leica, Germany). Lipos-Cur NPs were subjected to centrifugation (2000 rpm for 10 min) in order to isolate microcrystals formed from Lipos-Cur NPs. The pelleted crystals were treated with cells and CLSM imaging was performed [8].

## 3 Results and Discussions

Liposomes encapsulating curcumin, (Lipos-Cur NPs) and liposomes encapsulating CfAc, (Lipos-CfAc NPs) showed green and red fluorescence, respectively, owing to their inherent fluorescence properties [7, 8, 16]. The differences in the drug dynamics and cellular uptake of these two fluorescent anti-cancer agents were evidenced by transmission electron microscopy and confocal scanning laser microscopy. The drug release from liposomal nanosystem using an external photothermal trigger and its effect on cancer cells is discussed first. Liposomes encapsulating CfAc & NIR dye IR780 (LCIR NPs) were used to understand the photothermal mediated drug release and its therapeutic efficacy. Photothermal therapy uses NIR active nanomaterials which convert light energy to heat energy. The heat generated facilitates the drug release at the desired site. The photothermal agent, i.e., IR780, makes the nanoparticles responsive to the NIR laser irradiation. The absorbance of LCIR NPs (Fig. 1a) at 680 and 796 nm, indicates the encapsulation of CfAc & IR780 dyes, respectively. These LCIR NPs when subjected to NIR laser irradiation absorb the light energy and convert it to heat, resulting in an increase in temperature (Fig. 1b). The rise in temperature was recorded, and the corresponding thermal images were captured by an infrared thermal camera (Fig. 1c). The heat generated facilitates the release of CfAc as evidenced by an increase in its fluorescence (Em: 680 nm) with irradiation time (Fig. 1d). The inset shows the release of CfAc with red fluorescence under UV light. The therapeutic efficacy of LCIR NPs against two different types of

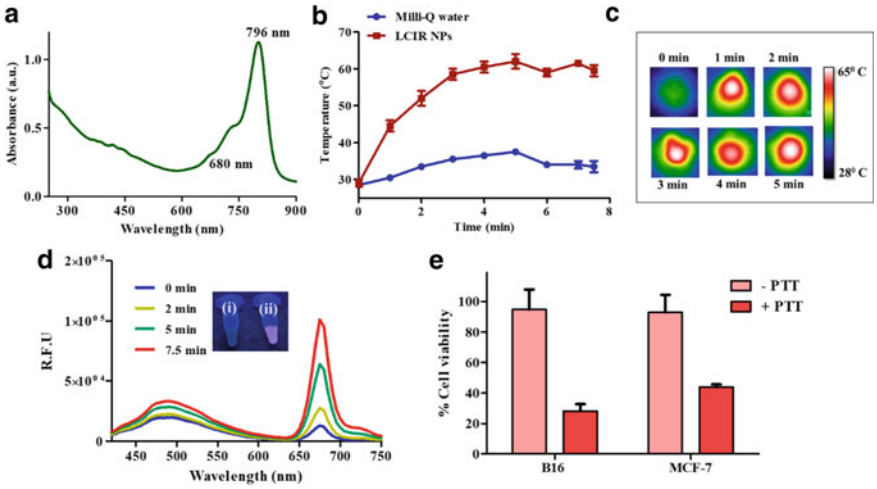


**Fig. 1** Drug release & therapeutic efficacy with photothermal trigger: **a** Absorbance spectra of LCIR NPs, **b** Increase in temperature &, **c** Infrared thermal images of LCIR NPs subjected to photothermal trigger, **d** Increase in fluorescence with photothermal trigger indicating the drug release *(inset shows the fluorescence of LCIR NPs (i) before & (ii) after laser irradiation)*, **e** % of viable cells treated with LCIR NPs and activated with photothermal trigger (PTT)

cancer cells, i.e., B16 (skin cancer cell line) & MCF-7 (breast cancer cell line) are shown in Fig. 1e. LCIR NPs when activated using photothermal trigger resulted in significant cell death (~70% & 60% cell death was recorded for B16 & MCF-7 cells, respectively), while cells treated with LCIR NPs only remained unaffected. Hence we demonstrated an external photothermal trigger mediated drug delivery resulting in a combinational therapeutic effect (of both photo thermal heat and released drug). The synergistic effect of combinational therapies over individual therapies was discussed in detail in our earlier reports [7, 16]. Most of the nanosystems are evaluated for their drug delivery & therapeutic efficacy, similar to LCIR NPs as discussed above. The in-vitro drug release patterns help determine the dosage for the treatment against cancer cells and their therapeutic efficacy will be evaluated by a viability assay. But in this paper, we further tried to explore and understand the basic differences in drug release dynamics and cellular uptake of hydrophobic drugs delivered by a liposomal carrier system.

In addition to various internal & external stimuli for drug release, liposomes are known for their drug release by fusion of lipid bilayers with cell membrane phospholipids in-vitro [17]. Drugs also leach out from the liposomal membranes resulting in their slow release. As most of the currently available active pharmaceutical ingredients are hydrophobic in nature, the drug release from formulations and its interaction with cells must be evaluated. To understand the dynamics of hydrophobic drug release, CfAc & curcumin were chosen. Lipos-CfAc & Lipos-Cur NPs were subjected to transmission electron microscopy & confocal laser scanning microscopy.

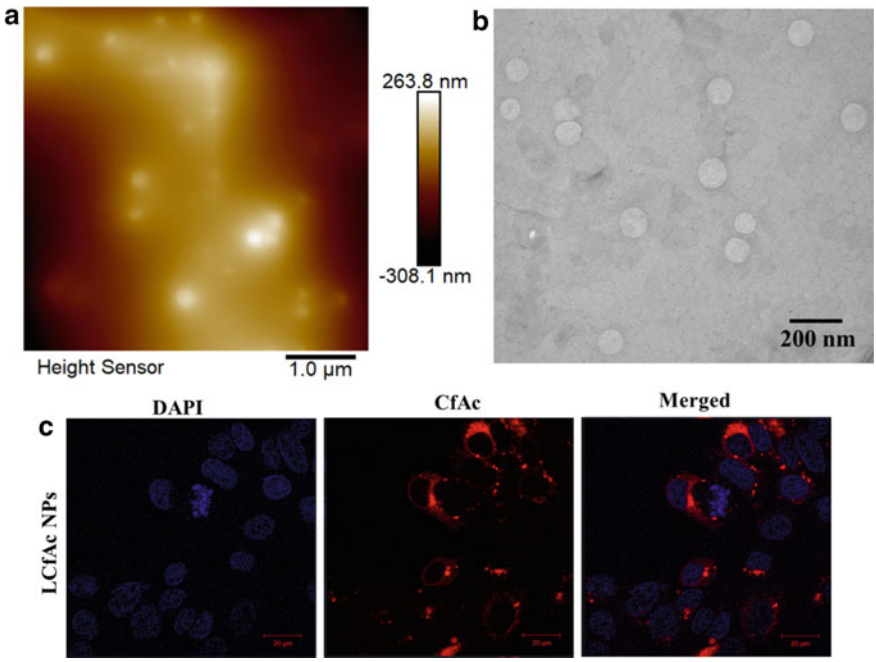


**Fig. 2** Microscopic analysis of drug dynamics & cellular uptake **a** AFM imaging of Lipos-CfAc NPs, **b** Negatively stained TEM image of CfAc loaded liposomes showing no crystalline drug deposition, **c** CLSM imaging of cellular uptake of CfAc loaded liposomes in cancer cells.

The atomic force microscope imaging of Lipos-CfAc NPs, is presented in Fig. 2a. Figure 2b shows the TEM image of uniformly dispersed liposomes loaded with CfAc. The liposomes were spherical with sizes ranging from 100 to 150 nm, uniformly dispersed without any aggregations or depositions. Cellular uptake of Lipos-CfAc NPs in cancer cells can be observed from the CLSM images shown in Fig. 2c. DAPI stains the nucleus of the cells and presence of CfAc was identified by its inherent red fluorescence. As can be seen from the merged image, the red fluorescence indicating the presence of CfAc was observed in the cytoplasm of the cell. The CfAc was delivered directly to the cells, without any depot or crystal formation resulting in a rapid and efficient drug delivery.

The dynamics of curcumin released from the liposome (Lipos-Cur NPs) were studied by TEM imaging of freshly prepared liposomes entrapping curcumin (Lipos-Cur NPs). Curcumin was selected as a model drug due to its hydrophobic nature and fluorescence properties. With the advent and availability of versatile microscopic techniques like TEM imaging we can understand the dynamic of drug released from a nanoparticle. As shown in Fig. 3a the Lipos-Cur NPs were observed as spherical lamellar structures entrapping curcumin ($\sim$200 nm). It was also observed that the smaller nanocrystals of curcumin were either associated with liposomes (Red arrows) or released from the nanosystem (inset-black arrows).

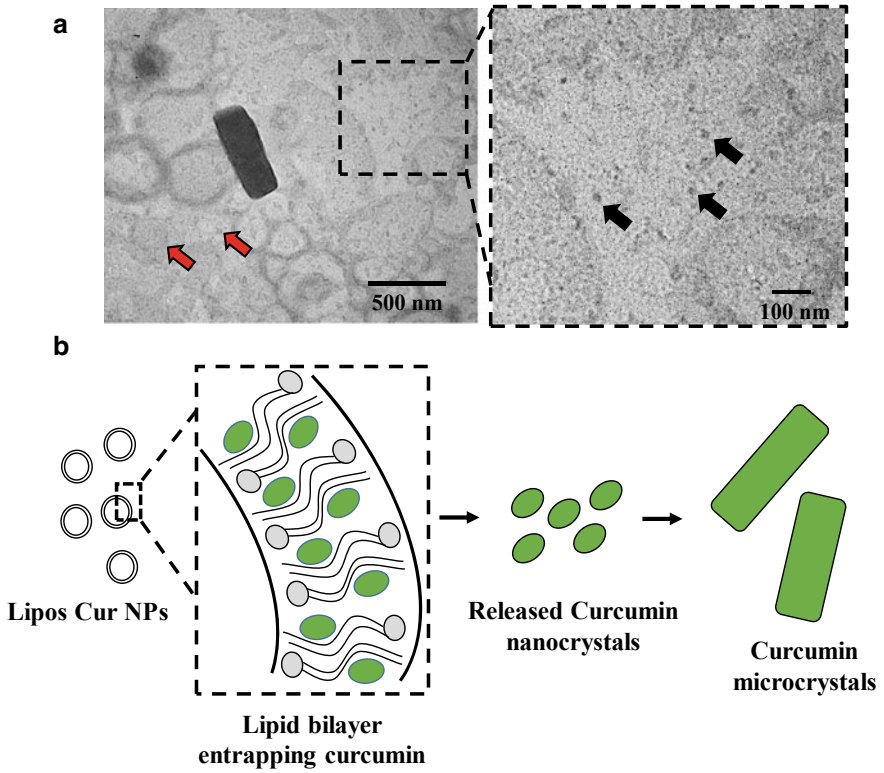


**Fig. 3** The drug release dynamics of hydrophobic curcumin from Lipos-Cur NPs. A. Negatively stained TEM image of curcumin nanocrystals released from Lipos-Cur NPs and curcumin microcrystals, red arrows shows nanocrystals associated with lipid membranes and black arrows shows released curcumin nanocrystals. B. Schematic representation of release, aggregation and formation of curcumin microcrystals

These curcumin nanocrystal further aggregates to form micro crystals, slowly due to hydrophobic interactions [18]. It is also reported that the curcumin due to its hydrophobic nature tends to interact by sharing hydrogen bonding with neighboring curcumin molecule [19]. As a result of these interactions, nuclei are formed which further grows to form a nano crystal and finally a microcrystal (Fig. 3b) [20]. These results demonstrate the transition of a hydrophobic drug from a nano dispersion to a microcrystal by in-situ aggregation. The microcrystals formed were stable and exhibited sustained drug release leading to formation of a depot.

We have then evaluated the cellular interaction of so formed curcumin microcrystals with cancer cells. The cancer cells treated with isolated curcumin microcrystals were imaged using CLSM. Figure 4 shows the interaction of a curcumin microcrystal with cancer cells. It can be observed that the green fluorescence was evenly distributed with in the cytoplasmic site depicting the uniform uptake of curcumin. More interestingly the intense green signal arising from the attached

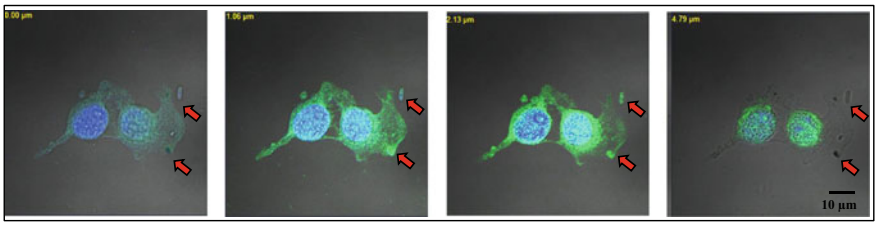


**Fig. 4** Intra-cellular uptake and localization of curcumin microcrystal depots in B16 cells (red arrows shows the location of microcrystal attachment to the cancer cells)

microcrystals suggests that the curcumin was released from these micro depots into the cell cytoplasm. The site of microcrystal attachment to the cell was observed by a z-scan, and it was observed that the crystals were firmly attached on the cell surface in spite of several wash cycles. These findings suggest that the curcumin exhibits nano to micro transition when subjected to aqueous environment and the microcrystals formed acts as a drug depot. The sustained availability of curcumin in situ can lead to suppression of cancer cell for prolonged duration [21].

## 4 Conclusions

In this paper, we evaluated the drug release dynamics and cellular uptake of two hydrophobic anti-cancer agents (CfAc [7] & Curcumin [9]) delivered by a liposomal nanosystem. We also demonstrated photothermal mediated drug release of CfAc and its effects in-vitro. Lipos-CfAc NPs showed an in-situ, rapid delivery and cellular uptake of CfAc, while Lipos-Cur NPs showed a sustained release of curcumin through depot formation. A direct drug delivery without any depot formation was observed for Lipos-CfAc NPs, while crystalline depots were observed in the case of Lipos-Cur NPs leading to indirect and sustained delivery. The same has been observed in-vitro, in cancer cells. Two hydrophobic drugs, despite being released from a similar type of nanosystem, showed differences in their drug release patterns & cellular uptake, indicating that uptake of hydrophobic drugs depends entirely upon the physico-chemical properties of the drug. The two different types of drug release patterns observed here are equally important as therapeutic applications may warrant either a rapid or slow & sustained drug delivery depending on the disease conditions.

**Acknowledgements** The authors acknowledge MHRD IMPRINT (4291), DST-Inspire (DST/INSPIRE/04/2015/000377), DST-AMT (DST/TDT/AMT/2017/227(G)), DST/SERB-CRG (CRG/2020/005069), Govt. of India for the research funding. Authors acknowledge the generous financial support by Vasudha foundations, Hyderabad, India. The authors also acknowlege Indian Institute of Technology Hyderabad for the characterization facilities. Tejaswini Appidi acknowledges Dept. of Science & Technology, Govt. of India for DST-Inspire fellowship (IF160291).

## References


1. Thorn K (2016) A quick guide to light microscopy in cell biology. Mol Biol Cell 27:219–222
2. Manna S, Wu Y, Wang Y, Koo B, Chen L, Petrochenko P et al (2019) Probing the mechanism of bupivacaine drug release from multivesicular liposomes. J Controlled Release 294:279–287
3. Malatesta M (2016) Transmission electron microscopy for nanomedicine: novel applications for long-established techniques. Eur J Histochem: EJH. 60
4. Anand P, Kunnumakkara AB, Newman RA, Aggarwal BB (2007) Bioavailability of curcumin: problems and promises. Mol Pharm 4:807–818
5. Rengan AK, Bukhari AB, Pradhan A, Malhotra R, Banerjee R, Srivastava R et al (2015) In vivo analysis of biodegradable liposome gold nanoparticles as efficient agents for photothermal therapy of cancer. Nano Lett 15:842–848
6. Rengan AK, Jagtap M, De A, Banerjee R, Srivastava R (2014) Multifunctional gold-coated thermo-sensitive liposomes for multimodal imaging and photo-thermal therapy of breast cancer cells. Nanoscale 6:916–923
7. Pemmaraju D, Appidi T, Minhas G, Singh SP, Khan N, Pal M, et al (2018) Chlorophyll rich biomolecular fraction of A. cadamba loaded into polymeric nanosystem coupled with photothermal therapy: a synergistic approach for cancer theranostics. Int J Biol Macromol 110:383–391
8. Alvi SB, Appidi T, Deepak BP, Rajalakshmi P, Minhas G, Singh SP et al (2019) The "nano to micro" transition of hydrophobic curcumin crystals leading to in-situ adjuvant depots for Au-liposome nanoparticle mediated enhanced photothermal therapy. Biomater Sci 7:3866–3875
9. Singh SP, Alvi SB, Bharadwaj D, Singh AD, Manda SV, Srivastava R et al (2018) NIR triggered liposome gold nanoparticles entrapping curcumin as in-situ adjuvant for photothermal treatment of skin cancer. Int J Biol Macromol 110:375–382
10. Wang K, Zhang Y, Wang J, Yuan A, Sun M, Wu J et al (2016) Self-assembled IR780-loaded transferrin nanoparticles as an imaging, targeting and PDT/PTT agent for cancer therapy. Sci Rep 6:27421
11. Rengan AK, Banerjee R, Srivastava R. Thermosensitive gold-liposome hybrid nanostructures for photothermal therapy of cancer. In: 2012 12th IEEE conference on nanotechnology (IEEE-NANO), IEEE; 2012, pp 1–4
12. Chen Y, Li Z, Wang H, Wang Y, Han H, Jin Q et al (2016) IR-780 loaded phospholipid mimicking homopolymeric micelles for near-IR imaging and photothermal therapy of pancreatic cancer. ACS Appl Mater Interfaces 8:6852–6858
13. Rengan AK, Kundu G, Banerjee R, Srivastava R (2014) Gold nanocages as effective photothermal transducers in killing highly tumorigenic cancer cells. Part Part Syst Charact 31:398–405
14. Shi J, Wang L, Zhang J, Ma R, Gao J, Liu Y et al (2014) A tumor-targeting near-infrared laser-triggered drug delivery system based on GO@ Ag nanoparticles for chemo-photothermal therapy and X-ray imaging. Biomaterials 35:5847–5861
15. Pemmaraju DB, Appidi T, Rengan AK (2019) Photothermal therapy assisted bioactive nanoprobes for effective cancer theranostics
16. Appidi T, Pemmaraju DB, Khan RA, Alvi SB, Srivastava R, Pal M et al (2020) Light-triggered selective ROS-dependent autophagy by bioactive nanoliposomes for efficient cancer theranostics. Nanoscale 12:2028–2039
17. Yadav D, Sandeep K, Pandey D, Dutta RK (2017) Liposomes for drug delivery. J Biotechnol Biomater. 7:276
18. Zheng B, Zhang X, Peng S, McClements DJ (2019) Impact of curcumin delivery system format on bioaccessibility: nanocrystals, nanoemulsion droplets, and natural oil bodies. Food Funct 10:4339–4349
19. Sanphui P, Rajesh Goud N, Rao Khandavilli UB, Bhanoth S, Nangia A (2011) New polymorphs of curcumin. Chem Commun 16:5013–5015

20. Thorat AA, Dalvi SV (2014) Particle formation pathways and polymorphism of curcumin induced by ultrasound and additives during liquid antisolvent precipitation. CrystEngComm 16:11102–11114
21. Alvi SB, Paradkar S, Pradhan A, Srivastava R, Rengan AK (2019) Timing the therapeutic trigger of Au Lipos-Cur NPs for effective photothermal therapy. In: Proceedings of the 13th IEEE international conference on nano/molecular medicine and engineering, Nov 21–24

# Cryo-EM and ED with a Cold-Field Emission Beam and Energy Filtration


**Koji Yonekura, Saori Maki-Yonekura, Tasuku Hamaguchi, Hisashi Naitow, Kiyofumi Takaba, and Keisuke Kawakami**

**Abstract** A cryo-electron microscopy (cryo-EM) system equipped with a cold-field emission gun and an energy filter is well-suited for higher-resolution single particle analysis and high-precision 3D electron crystallography. We designed such system and installed a JEOL CRYO ARM 300 electron microscope-the first machine of this model. The microscope has provided high quality data in both imaging and diffraction since July 2018. For single particle analysis, we are routinely able to reconstruct higher-resolution structures with better estimated B-factors for map sharpening from smaller numbers of images than can be obtained with conventional Schottky emission. For 3D electron crystallography, we are also routinely able to obtain highest-quality diffraction data thanks to higher-energy electrons and energy filtration. Automated data collection allows high-throughput structure determination in both applications. This review introduces our recent results, progress, and perspective for running such cryo-EM system.

**Keywords** CFEG · Energy filter · Single particle analysis · Electron 3D crystallography (3D ED/MicroED) · eEFD · CRYO ARM

K. Yonekura (✉) · S. Maki-Yonekura · T. Hamaguchi · H. Naitow · K. Takaba · K. Kawakami
Biostructural Mechanism Laboratory, RIKEN, SPring-8 Center, 1-1-1 Kouto, Sayo 679-5148, Hyogo, Japan
e-mail: yone@spring8.or.jp

K. Yonekura
Advanced Electron Microscope Development Unit, RIKEN-JEOL Collaboration Center, RIKEN Baton Zone Program, 1-1-1 Kouto, Sayo 679-5148, Hyogo, Japan

K. Yonekura
Institute of Multidisciplinary Research for Advanced Materials, Tohoku University, 2-1-1 Katahira, Aoba-ku, Sendai 980-8577, Japan



P. Ghosal et al. (eds.), *Applications of Microscopy in Materials and Life Sciences*, Springer Proceedings in Materials 11,
https://doi.org/10.1007/978-981-16-2982-2_23

## 1 Introduction

Cryo-electron microscopy (cryo-EM) can yield high-resolution structures of biological and other complex molecules in imaging and diffraction modes. Imaging mode is used mainly for single particle analysis of protein molecules and complexes embedded in thin ice. This technique can produce 3D reconstruction from projection images, and thus is targeted for larger-sized molecules that yield good image contrast in vitreous ice. 3D electron crystallography utilizes diffraction mode to obtain diffraction patterns of small and thin crystals, and is applicable to tiny crystals of smaller molecules, which are hard to solve by single particle analysis and do not grow to a suitable size for X-ray diffraction even with a high-intensity synchrotron radiation beam.

It is a challenge to further improve cryo-EM applications. We designed a new cryo-EM system for higher-resolution single particle analysis and high-precision 3D electron crystallography, and installed a JEOL CRYO ARM 300 electron microscope as the first machine of this model in RIKEN SPring-8 Center (Fig. 1a). The model is operated at an accelerating voltage of 300 kV and equipped with a cold-field emission gun (CFEG). The CFEG produces an electron beam with high temporal-coherence and superior high-resolution signals beyond 2 Å over that from the Schottky gun ([2]; Fig. 1b). It also has a new in-column energy filter cooled with water flow. Filtration of inelastically scattered electrons remarkably reduces background noise and improves the signal-to-noise ratio of diffraction spots [12, 14, 17].

Operation of the system started in July 2018. Despite initial flaws and bugs as can be expected with any new machine, the system is now much improved and has successfully yielded high quality data in both applications. This review introduces some recent results, progress and future plan for running such cryo-EM machines.

## 2 Single Particle Analysis with CFEG

We have carried out single particle analysis of various samples from ~50 kD to super macromolecular complexes, which include membrane proteins. We have already achieved a 1.5 Å resolution structure of mouse apoferritin (Fig. 2a; EM Data Resource ID: EMD-9865;EMPIAR ID: 10248) from ~120,000 particle images out of 840 movie frames imaged with a CFEG and collected on a GATAN K2 Summit camera. It was the highest resolution single particle reconstruction at that time. A recent report claimed that a new program suite M in Warp improved the resolution to 1.3 Å resolution from the same dataset [10]. Using a K3 camera, we also obtained a 1.6 Å resolution apoferritin structure (Fig. 2b).

Biologically important targets examined with this system so far include apple latent spherical virus (ALSV; [7] and photo system I of *Acaryochloris* [3]. We have determined the structure of ALSV at 2.9 Å resolution, which is the first structure solved in the genus *Cheravirus* of picorna-like plant viruses (Fig. 3). The 3D map

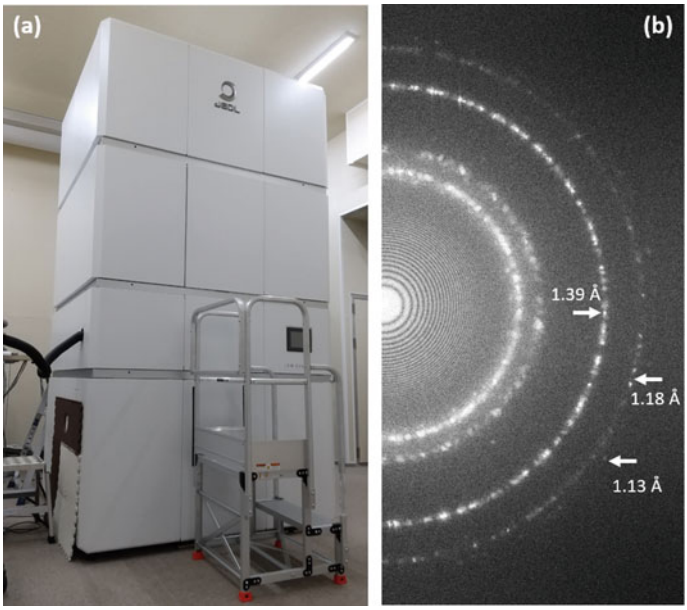


**Fig. 1** A cryo-EM system in RIKEN SPring-8 Center and signals obtained with the CFEG. **a** A CRYO ARM 300 electron microscope. Installed as the first machine of this model. **b** Power spectrum of a Pt-Ir image taken with the CFEG. CTF ring patterns are clear up to a ring of ∼1.13 Å. See also Hamaguchi et al. [2]

was reconstructed from a relatively smaller number of particle images (∼8000) with an improved B-factor (−29.7 $Å^2$) for map sharpening. As the particle size of ALSV is large (∼300 Å), we took images at a relatively lower nominal magnification of 40,000×, and the resolution could be improved if a higher magnification is used. Most of the side chains as well as the main chain are clear in the map, which allowed de novo modeling of atomic coordinates for the whole virus capsid. Thus, the structure reveals that three capsid proteins have a unique folds that contribute to capsid stabilization. Image analysis also resolves RNA leaking from protrusions of the virus particles (Fig. 3). The results suggest how capsid stabilization is achieved and how virus genome is released.

*Acaryochloris marina* is a cyanobacterium that can, uniquely, use far-red light for oxygenic photosynthesis. We have determined the structure of *A. Marina* photosystem I by single particle analysis with a cold-field emission beam at 2.5 Å resolution reconstructed using ∼86,000 particle images from ∼4000 movie frames [3]. The structure reveals a unique arrangement of electron carriers and light-harvesting pigments (Fig. 4). Indeed, the pigment molecules are well-resolved in the cryo-EM map (Fig. 4b). Thus, the analysis has shed light on how the low energy yield from far-red light is efficiently utilized for driving oxygenic photosynthesis.

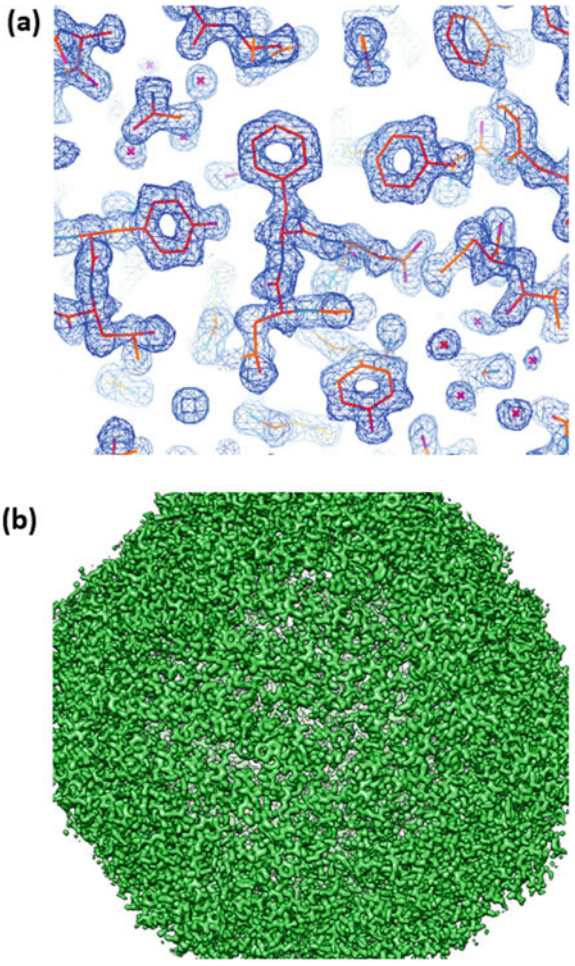


**Fig. 2** Single particle analysis of mouse apoferritin. **a** Zoom-up view of a 1.5 Å resolution reconstruction (EMDataResource ID: EMD-9865; EMPIAR ID: 10248). Reconstructed from 120,295 particle images out of 840 movie frames collected on a GATAN K2 Summit camera. **b** A 1.6 Å resolution reconstruction [5]. Collected on a K3 camera

We are now routinely able to reconstruct higher-resolution structures with better estimated B-factors for map sharpening from smaller numbers of images than can be obtained with conventional Schottky emission (e.g., [2, 3, 7]).

## 3 3D Electron Crystallography by eEFD

In the standard scheme of 3D electron crystallography, sequential frames of rotational diffraction patterns are recorded on the detector of an electron microscope, while the sample crystal is continuously rotated (e.g., [8, 11, 14]) as in macromolecular X-ray crystallography.

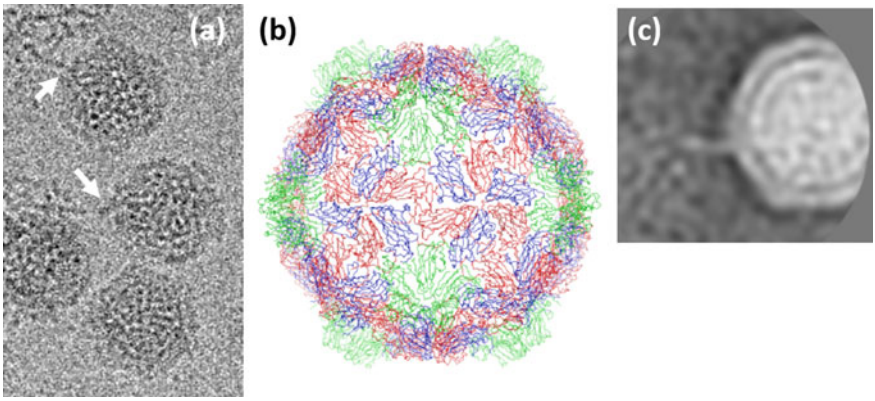


**Fig. 3** Single particle analysis of ALSV. **a** Typical cryo-EM images of ALSV. Arrows indicate points where RNA chains exit the capsid. **b** Atomic model of the overall structure, built on a 2.9 Å resolution structure. Reconstructed from 8018 particle images out of 110 movie frames collected on a GATAN K2 Summit camera. **c** A class average of selected cryo-EM images. Leakage of RNA genome is resolved to come from the vertex of the virion. See Naitow et al. [7] for details

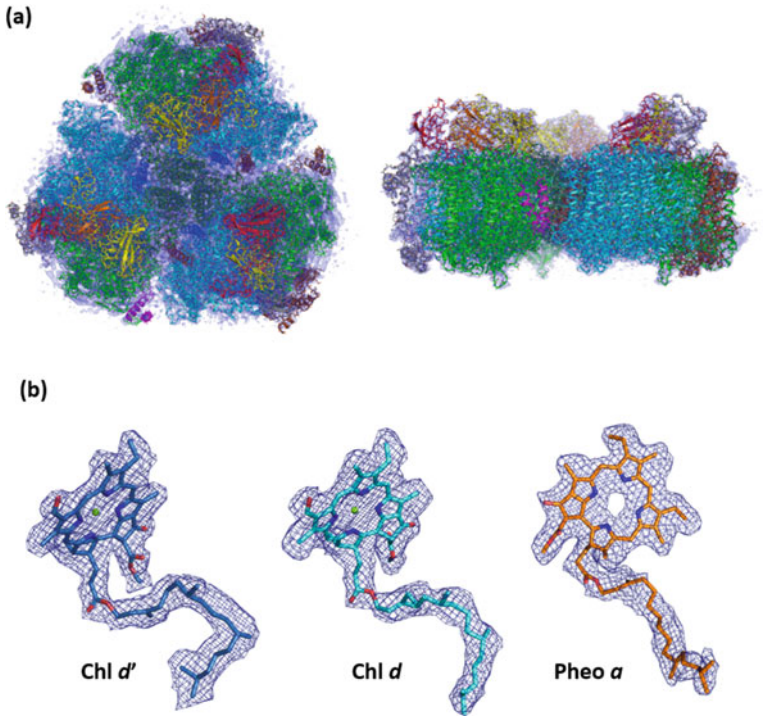


**Fig. 4** Single particle analysis of *A. marina* photosystem I. **a** Top (left) and side (right) views of the cryo-EM map determined to 2.5 Å resolution. Reconstructed from 86,419 particle images out of 4237 movie frames collected on a GATAN K2 Summit camera. Overlaid with the atomic model built on the map. **b** Typical light-harvesting pigments. Density maps are well-fitted with the atomic models. See Hamaguchi et al. [3] for details

Filtration of inelastically scattered electrons from a sample can improve image contrast by boosting amplitude contrast [13]. Yet, this effect is more prominent in electron diffraction from small crystals, especially protein crystals embedded in thin amorphous ice [12, 14, 17]. The sample and particularly the surrounding ice yield many inelastically scattered electrons, which result in higher backgrounds in diffraction ([12] and [17]). This effect is worse for thick crystals and/or highly tilted crystals due to the strong interaction of electrons with the sample and the shorter mean free path of inelastically scattered electrons compared to elastically scattered ones [1]. Energy filtration can remove these energy-losing electrons, while at the same time reducing multiple scattered electrons as they are likely to be inelastically scattered at least once. Moreover, only elastically scattered electrons represent correct Coulomb potentials, which provide charge information on molecules ([14–16]). In addition to energy filtration, a higher energy electron is also beneficial, as it has higher penetrating power through the sample and reduces multiple scattering and radiation damage [17].

The CRYO ARM 300 microscope has the traditional in-column Ω-type energy filter in JEOL microscopes with a new water-cooling system. This new energy filter is stable for a session of 1—a few days without re-tuning by the operator. However, the goniometer of the sample stage had only supported stepwise tilt with a constant speed in the original design of the CRYO ARM microscope. So, we implemented a custom-designed rotational goniometer with variable rotation speeds, which were measured to be accurate and consistent [5].

Thus, the 300 kV microscope with an energy filter and a stable rotational goniometer is very advantageous for 3D electron crystallography. Indeed, we have already shown that the cryo-EM system has also yielded data quality and structure-refinement statistics superior to those obtained with other microscope systems ([17]; Fig. 5). We named this approach as eEFD (electron energy-filtered diffraction of 3D crystals; [17]).

We have also developed a scheme for automated data collection of rotational electron diffraction patterns by combined use of SerialEM [6] for positioning of sample crystals and ParallEM [17] for rotational data collection [9]. This remarkably accelerates data collection from many crystals, which allowed us to obtain very high-resolution structures including hydrogen atoms from thin crystals of several organic molecules including a nanographene fiber ([4]; Fig. 6).

## 4 Perspective

Following our success, more than five CRYO ARM 300 microscopes with the same as or a similar specification to our first machine will be installed throughout Japan and more be all over the world including India. One of them will be in RIKEN SPring-8 Center for shared use of single particle analysis.

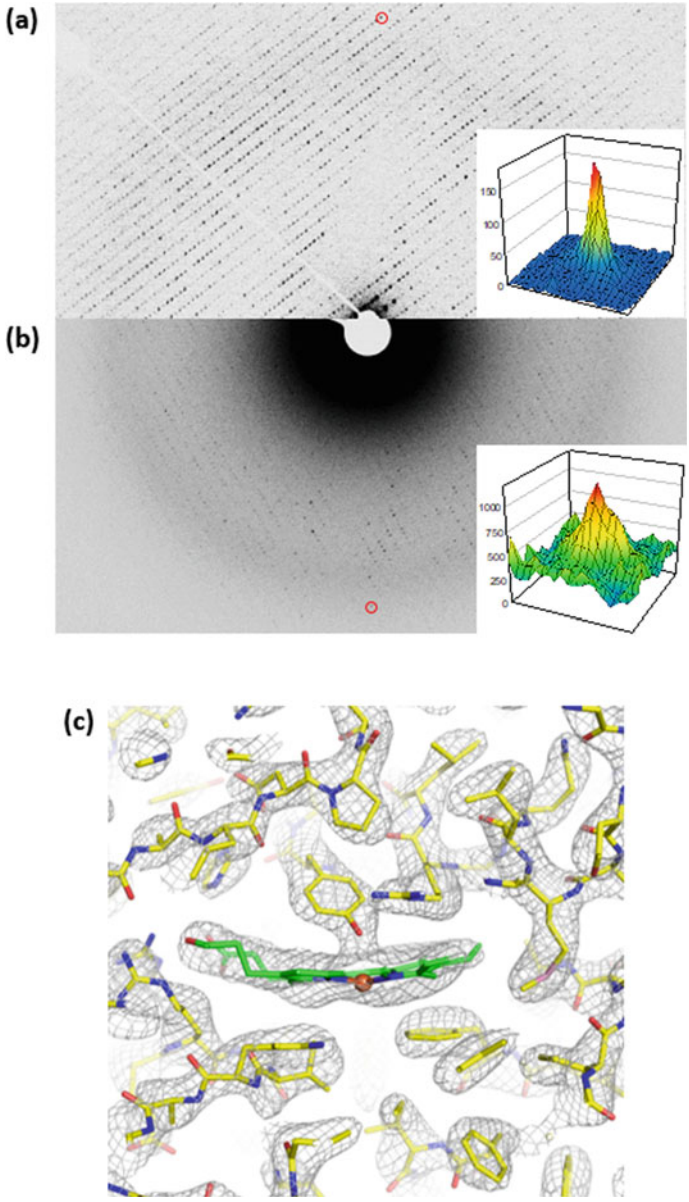


**Fig. 5** Electron 3D crystallography of thin 3D catalase crystals. **a** A diffraction frame taken with the CRYO ARM 300 microscope at an accelerating voltage of 300 kV and with energy filtration. **b** A frame taken with a JEOL JEM-2100 microscope at 200 kV and without energy filtration. Intensity profiles of diffraction spots at ~3 Å (indicated by red circles) are overlaid on the diffraction patterns. **c** A Coulomb potential map of catalase around the heme-binding site overlaid with the atomic model built on the map. Calculated from one rotational dataset as in (**a**). See also Yonekura et al. [17]

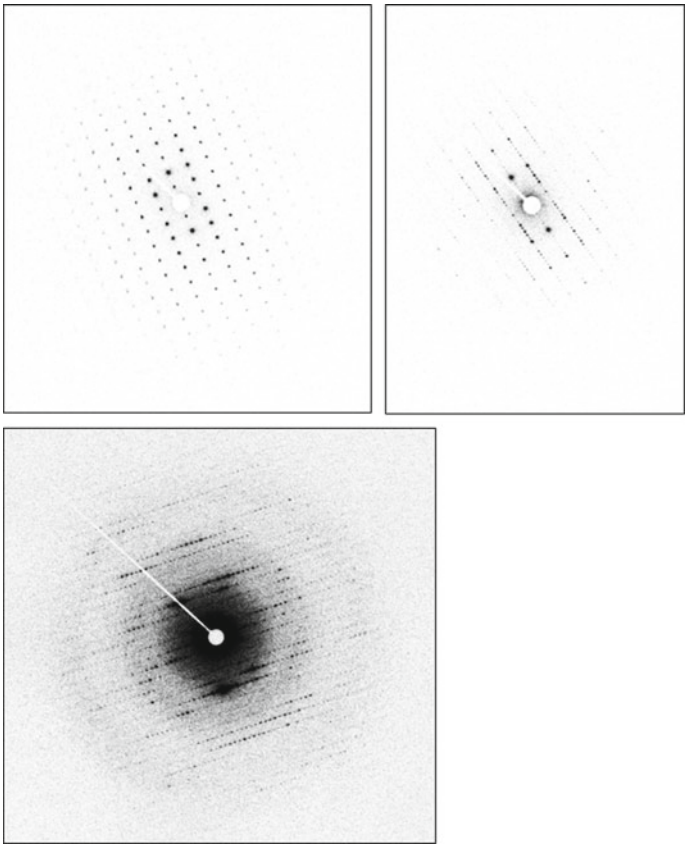

**Fig. 6** eEFD patterns from thin crystals of three different organic molecules. Diffraction spots are visible up to 0.8–0.5 Å resolution depending on the sample. Recorded on a TVIPS XF416 detector

**Acknowledgements** We thank the JEOL cryo-EM group for technical assistance in setting up the CRYO ARM 300 electron microscope, Yasuhiro Kashino for collaborative work on *A. marina* photosystem I, NobuyukiYoshikawa for providing the ALSV sample, Haruaki Yanagisawa for providing a plasmid of mouse apoferritin, Satoru Inoue, Tatsuo Hasegawa, Yasutomo Segawa for providing crystal samples of organic molecules. The works presented in this review were partly supported by Japan Society for the Promotion of Science Grant-in-Aid for Scientific Research Grant 16H04757 (to K.Y.), Japan Society for the Promotion of Science Grant-in-Aid for Challenging Exploratory Research Grant 24657111 (to K.Y.), the RIKEN Pioneering Project, Dynamic Structural Biology (to K.Y., S.M.-Y., T.H., H.N. and K.T.), the Cyclic Innovation for Clinical Empowerment (CiCLE) from the Japan Agency for Medical Research and Development, AMED(to K.Y.), JST CREST Grant Number JPMJCR18J2, Japan (to K.Y.), and JST-Mirai Program Grant Number JPMJMI20G5 (to K.Y.).

## References


1. Angert I, Burmester C, Dinges C, Rose H, Schröder RR (1996) Elastic and inelastic scattering cross sections of amorphous layers of carbon and vitrified ice. Ultramicroscopy 63:181–192
2. Hamaguchi T, Maki-Yonekura S, Naitow H, Matsuura Y, Ishikawa T, Yonekura K (2019) A new cryo-EM system for single particle analysis. J Struct Biol 207(1):40–48
3. Hamaguchi T, Kawakami K, Shinzawa-Itoh K, Inoue-Kashino N, Itoh S, Ifuku K, Yamashita E, Maeda K, Yonekura K, Kashino Y (2021) Structure of the far-red light utilizing photosystem I of *Acaryochloris*. Nat Commun 12:2333
4. Kato K, Takaba K, Maki-Yonekura S, Mitoma N, Nakanishi Y, Nishihara T, Hatakeyama T, Kawada T, Hijikata Y, Pirillo J, Scott LT, Yonekura K, Segawa Y, Itami K (2021) Double-helix supramolecular nanofibers assembled from negatively curved nanographenes. J Am Chem Soc 143(14):5465–5469
5. Maki-Yonekura S, Hamaguchi T, Naitow H, Takaba K, Yonekura K (2021) Advances in Cryo-EM and ED with a cold-field emission beam and energy filtration. Refinements of the CRYO ARM 300 System in RIKEN SPring-8 Center. Microscopy 70(2):232–240
6. Mastronarde DN (2005) Automated electron microscope tomography using robust prediction of specimen movements. J Struct Biol 152(1):36–51
7. Naitow H, Hamaguchi T, Maki-Yonekura S, Isogai M, Yoshikawa N, Yonekura K (2020) Apple latent spherical virus structure with stable capsid frame supports quasi-stable protrusions expediting genome release. Commun Biol 3:488
8. Nannenga BL, Shi D, Leslie AGW, Gonen T (2014) High-resolution structure determination by continuous-rotation data collection in MicroED. Nat Methods 11(9):927–930
9. Takaba K, Maki-Yonekura S, Yonekura K (2020) Collecting large datasets of rotational electron diffraction with ParallEM and SerialEM. J Struct Biol 211(2):107549
10. Tegunov D, Xue L, Dienemann C, Cramer P, Mahamid J (2021) Multi-particle cryo-EM refinement with M visualizesribosome-antibiotic complex at 3.7 Å inside cells. Nat Methods 18(2):186–193
11. van Genderen E, Clabbers MTB, Das PP, Stewart A, Nederlof I, Barentsen KC, Portillo Q, Pannu NS, Nicolopoulos S, Gruene T, Abrahams JP (2016) *Ab initio* structure determination of nanocrystals of organic pharmaceutical compounds by electron diffraction at room temperature using a Timepix quantum area direct electron detector. Acta Crystallogr A 72(2): 236–242
12. Yonekura K, Maki-Yonekura S, Namba K (2002) Quantitative comparison of zero-loss and conventional electron diffraction from 2D and thin 3D protein crystals. Biophys J 82(5): 2784–2797
13. Yonekura K, Braunfeld MB, Maki-Yonekura S, Agard DA (2006) Electron energy filtering significantly improves amplitude contrast of frozen-hydrated protein at 300 kV. J Struct Biol 156(3):524–536
14. Yonekura K, Kato K, Ogasawara M, Tomita M, Toyoshima C (2015) Electron crystallography of ultra-thin 3D protein crystals: atomic model with charges. Proc Natl Acad Sci USA 112(11):3368–3373
15. Yonekura K, Maki-Yonekura S (2016) Refinement of cryo-EM structures using scattering factors of charged atoms. J Appl Cryst 49:1517–1523
16. Yonekura K, Matsuoka R, Yamashita Y, Yamane T, Ikeguchi M, Kidera A, Maki-Yonekura S (2018) Ionic scattering factors of atoms that compose biological molecules. IUCrJ 5:348–353
17. Yonekura K, Ishikawa T, Maki-Yonekura S (2019) A new cryo-EM system for electron 3D crystallography by eEFD. J Struct Biol 206(2):243–253

# A Correlative Fluorescent and Electron Microscopic Technique for Ultralocalization of Trichocyte Keratins


**Sailakshmi Velamoor, Sharon Lequeux, Richard Easingwood, Allan Mitchell, Jeffery Plowman, Mihnea Bostina, and Duane Harland**

**Abstract** Trichocyte keratin heterodimers in the cortex of hair occur as intermediate filaments (IF) within geometrically organized bundles (macrofibrils). To understand how heterodimerization of various keratin species contributes to IF and macrofibril formation, it is important to track the sub-cellular relationship between different keratin types in hair follicles. Distribution and localization of keratins, at an ultrastructural level, can be determined through immuno-ultrastructural studies. However, the conventional fixative-tissue interaction, dehydration and plastic embedding process, along with heavy metal staining potentially obscures the antigenic epitopes accessibility. Here, we demonstrate a sample preparation method for confocal fluorescent and electron microscopy of high-pressure frozen and freeze-substituted wool follicles that provides clear ultrastructural preservation and keratin labelling while minimizing common artefacts associated with conventional fixation. The contrast obtained using dark-field scanning transmission electron microscopy (DF-STEM) is sufficient to obtain high-resolution images without any further post-staining or silver enhancement.

**Keywords** Electron microscopy · Hair follicle · Trichokeratin · Antibody probe · Immunohistochemistry · Wool · High-pressure freezing · Freeze substitution

S. Velamoor (✉) · J. Plowman · D. Harland
Proteins and Metabolites, AgResearch Limited, Lincoln, New Zealand

S. Velamoor · M. Bostina
Department of Microbiology and Immunology, University of Otago, Dunedin, New Zealand

S. Lequeux · R. Easingwood · A. Mitchell · M. Bostina
Otago Micro and Nano Imaging, University of Otago, Dunedin, New Zealand



P. Ghosal et al. (eds.), *Applications of Microscopy in Materials and Life Sciences*,
Springer Proceedings in Materials 11,
https://doi.org/10.1007/978-981-16-2982-2_24

## 1 Introduction

The hair follicle is a complex miniature cylindrical organ consisting of different cell lineages arranged in laterally concentric layers, and within which a hair develops though a series of steps in an axial direction. Firstly, cells at the base of the follicle undergo continuous division and then differentiate to produce six (or seven in medullated fibres) cell types that develop into tightly coordinated cylindrical layers. Each cell line has a distinct pattern of maturation during hair growth including gene expression, morphological shaping and cell–cell junction development [1]. Trichocyte keratins are of two types, Type I and Type II, which form promiscuous heterodimers. These heterodimers are localized to the cytoplasm of cortical cells and, in combination with keratin-associated proteins (KAPs) self-organize to produce macrofibrils that fill the cortex of the hair shaft (it is primary structural component). Localization of keratins is prerequisite for identifying interactions of keratins with other keratins, KAPs and other cellular components such as cell junctions that contribute to structure assembly. Numerous studies using antibody markers have aided in characterizing and localizing keratins in hair follicles [2–8]. Most immunolabelling studies have been restricted to fresh tissues because accessing antigenic epitopes in fixed samples was challenging. In recent years, immunogold labelling techniques have been carried out on Lowicryl embedded sections to determine the sub-cellular locations of keratins in the human hair follicle [4, 7]. However, these and earlier studies used chemical fixation and dehydration. Recently, we reported [9] a method for ultrastructural preservation of intact wool follicles using high-pressure freezing, freeze substitution (HPF-FS) in epoxy resin. In this study, we extend that method to immunohistochemistry. Correlative fluorescent and electron microscopy were used to localize keratin K85 in follicles subjected to high-pressure freezing and freeze substitution (HPF-FS). Since high-temperature polymerization and strong cross-linking properties in epoxy might reduce the antigenicity of the biological sample, the samples were embedded in Lowicryl resin [10, 11]. While fluorescence microscopy enabled patterns of keratins to be observed across a large space, electron microscopy then enabled ultrastructural (sub-cellular) location of keratins in a small part of the same section.

## 2 Methods

**High-pressure freezing and freeze substitution**. Skin biopsies ($\sim$4 mm diameter) were collected and individual follicles were dissected and high-pressure frozen as described in Velamoor et al. [9]. For freeze substitution (FS), the frozen carriers were transferred into precooled moulds in a Leica AFS2 device (Leica Microsystems, Germany) containing the FS media (0.5% uranyl acetate (UA) dissolved in methanol and 5% water) for 56 h at −90 °C. The temperature was then gradually raised (at a rate of 5 °C per hour over 9 h) to −45 °C. The FS media was

removed and the follicles were washed and rinsed in 4× methanol for about 2 h. The samples were then infiltrated for about 2 h each with 10, 25, 50, 70, 90 and 100% Lowicryl resin, prepared as per manufacturer's instructions (Electron Microscopy Sciences, Cat# 14,340). The temperature was slowly raised from −45 to −25 °C for 8 h during these infiltration steps. The samples were then replaced with fresh 100% Lowicryl resin at regular intervals over 36 h at −25 °C. The samples were then UV polymerized with fresh resin for about 48 h at −25 °C. Then, the temperature was slowly raised to 20 °C (at 1.8 °C per hour over 24 h) and maintained for another 48 h. After removing the carriers, the samples were sectioned (100 nm) using an ultramicrotome (Leica UC6 and UCT ultramicrotomes, Leica Microsystems), collected on formvar-coated nickel grids and processed for immunolabelling experiments.

**Immunolabelling**. The sections were incubated with 0.1 M glycine and blocking solution (1% bovine serum albumin and 0.2% cold fish skin gelatin in 1× phosphate buffer saline (PBS)) for 30 min each to remove any residual aldehydes and to block non-specific binding of antibodies, respectively. After thorough washing with 1× PBS, the sections were incubated with primary keratin polyclonal antibodies (raised in rabbit against K85 tail domain: 466–485; IASGPVATGGSITVLAP) at 1:200 dilution, overnight at 4 °C. Then, the samples were incubated in Alexa Fluor® 488 goat α rabbit conjugated to 5 nm gold (1:15 dilution; Life technologies, cat # A31565) for 2 h at room temperature.

**Imaging**. Fluorescence imaging was carried out using an Olympus BX61 Montaging light microscope. Philips CM100 (operated at 100 kV) and JEOL 2200FS 200 kV TEM fitted with a TVIPS F416 CMOS camera (TVIPS, Gauting, Germany) were used for electron microscopy. Dark-field imaging was carried out using scanning image device (ASID) with upper dark-field detector and SightX software.

## 3 Results

**Ultrastructure of the follicle**. The preservation of ultrastructural details along the axis of the follicle through zones associated with stages of hair growth [12, 13] with HPF-FS followed by Lowicryl embedding was assessed at two points (Fig. 1a): lower bulb (below Auber's level), top of the bulb (above Auber's level and Orwin's threshold). At the base of the follicle, cells from the germinative matrix, adjacent to the dermal papilla (DP), differentiating into the Henle's, Huxley's and inner root sheath cuticle (IRSc) layers were clearly visible (Fig. 1b, c). Trichohyalin granules were evident only in the Henle's layer. The cuticle cells appeared cuboidal in shape and had clearly defined cell membranes and intact nuclei. In contrast, cortical cell

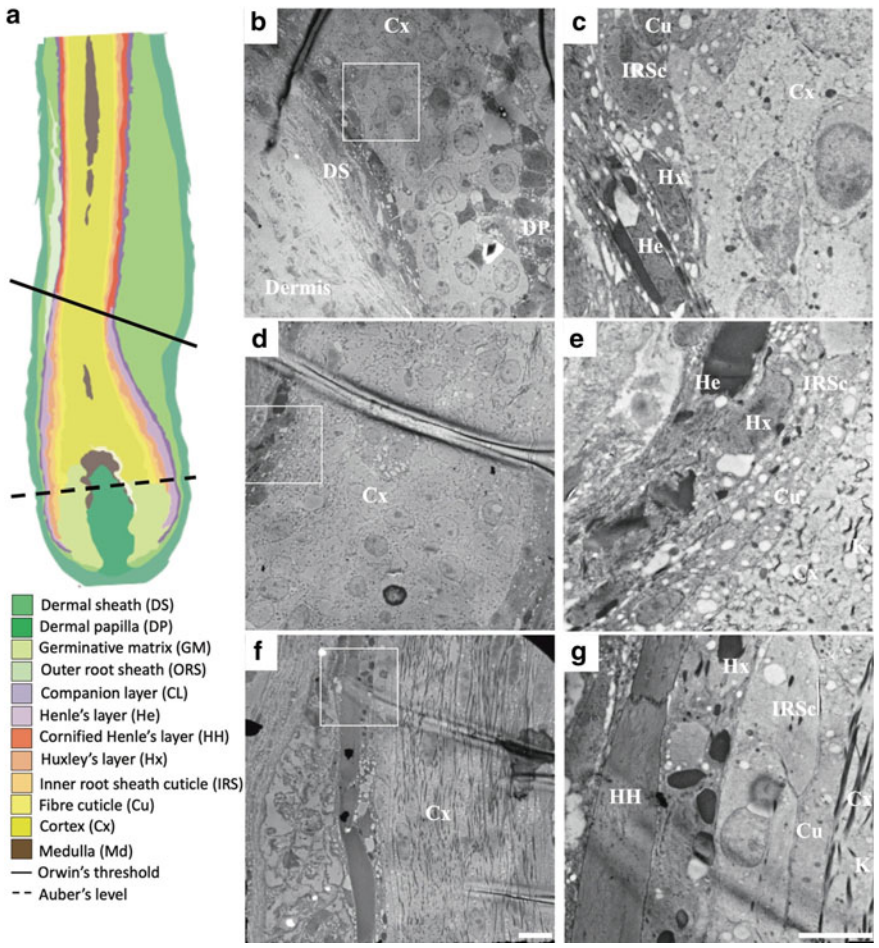


**Fig. 1** Uranyl acetate mediated Lowicryl embedded wool follicle. **a** Schematic representation of wool follicle. **b** Low magnification micrographs below Auber's level. **c** Inset from (**b**) showing the different compartments in the IRS, and the hair shaft's Cu and Cx. Trichohyalin granules (TG) were identified only in the He at this level in the follicle. **d** Micrograph of follicle above Auber's level. **e** Inset from (**d**) showing keratin (K) fibres inside the cortex. **e** Micrograph of the follicle post-Orwin's threshold. **g** High magnification image from inset (**f**) post-He layer's cornification, showing accumulation of keratin fibres. Scale bar presents 10 μm (**b**, **d** and **f**) and 5 μm (**c**, **e** and **g**)

membranes were not well defined (Fig. 1b). However, the nucleus and fine keratin fibres were well defined (Fig. 1b, c). The difference in staining contrast clearly distinguished the dermal papilla from the cortex (Fig. 1b).

At the distal end of the follicle bulb Henle's layer hardens (Orwin's threshold). Distal of this point trichohyalin granules were observed only in the Huxley's layer (Fig. 1d). The intensity of keratin increased tremendously. At high magnification,

the fine fibres were aggregated into bundles, forming developing macrofibrils (Fig. 1e). Further up from the Orwin's threshold (keratogenous zone), the IRS contained cornified Henle's, Huxley's and IRS cells, and the hair shaft cuticle and cortical cells were clearly distinguishable (Fig. 1f, g). Keratin filament structures were clearly defined and had increased contrast compared with more proximal parts of the cortex. The natural degradation of cytoplasmic features in cortical cells that forms part of the hair maturation process was well preserved (e.g. condensation of nuclear material).

**Keratin localization during fibre growth**. Wool follicles were immunolabelled with an antibody against keratin, K85, tagged with a fluorophore conjugated to 5 nm gold. The fluorescent labelling shows the localization of K85 (Fig. 2a) matches up to the densely stained fibrous keratin bundles, amongst the ultrastructural features of the follicle (Fig. 2b). The lack of fluorescent labelling in the germinative matrix and IRS shows that the K85 is localized primarily in the cortex and possibly diffusely in the fibre cuticle cells at this mid-bulb location (elongation zone) along the follicle axis (Fig. 2c).

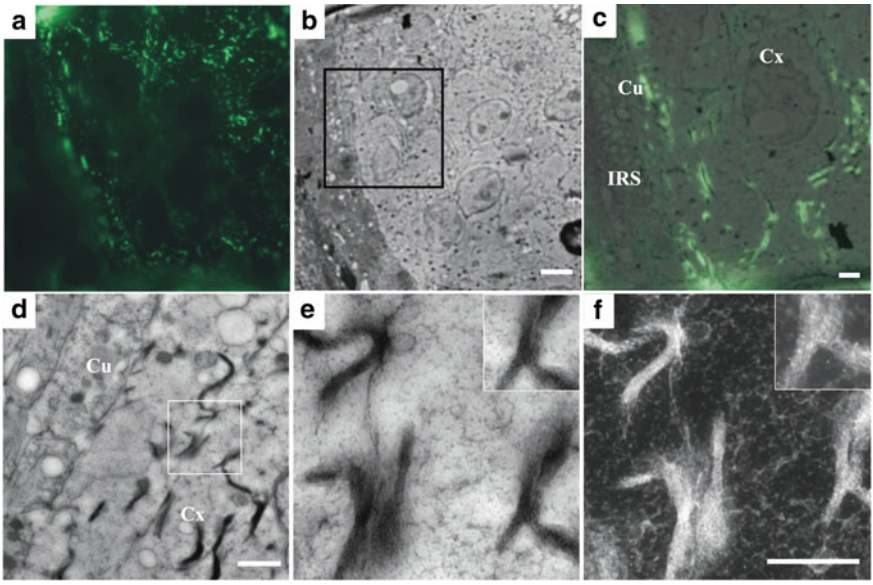


**Fig. 2** Correlative K85 antibody-labelled fluorescent and electron microscopy of a wool follicle. **a** Fluorescent labelled mid-bulb (elongation) region. **b** Electron micrograph corresponding to (**a**). **c** Correlated fluorescent and electron micrographs from inset (**b**). Scale bar: 5 μm in (**a**–**c**). **d** Electron micrograph of follicle in the elongation zone. **e** Inset from (**d**), showing keratin K85 immuno-labelled with 5 nm gold. **f** Keratin K85 immunogold labelling obtained using DF-STEM in comparison with (**e**). Scale bar: 1 μm in (**d**) and 500 nm in (**e**, **f**)

To localize K85 that had been detected by antibodies conjugated to 5 nm gold at an ultrastructural level (Fig. 2d–f), both regular and DF-STEM methods were effective. Although the 5 nm gold labels were detectable as electron dense dots using regular TEM (Fig. 2e), the gold labels were better visualized from the background using dark-field (DF) STEM (Fig. 2f). A few nanogold particles were clearly located in the cytosol (Fig. 2d), but most were localized within the fibrous bundles.

**Keratin localization distal of Henle's hardening**. The localization of K85 was observed at Orwin's threshold (where Henle's layer hardens) and more distally in the keratogenous zone (Fig. 3a–c). The correlative fluorescent and electron microscopy show K85 labelling localized to long filamentous structures inside the cortex and to a less extent in the cuticle cells. No evident labelling was observed in the IRS. Lack of gold markers in the IRS and localization of the gold with keratin fibres from high-resolution images from DF-STEM emphasizes the specificity of the K85 antibody (Fig. 3d, e).

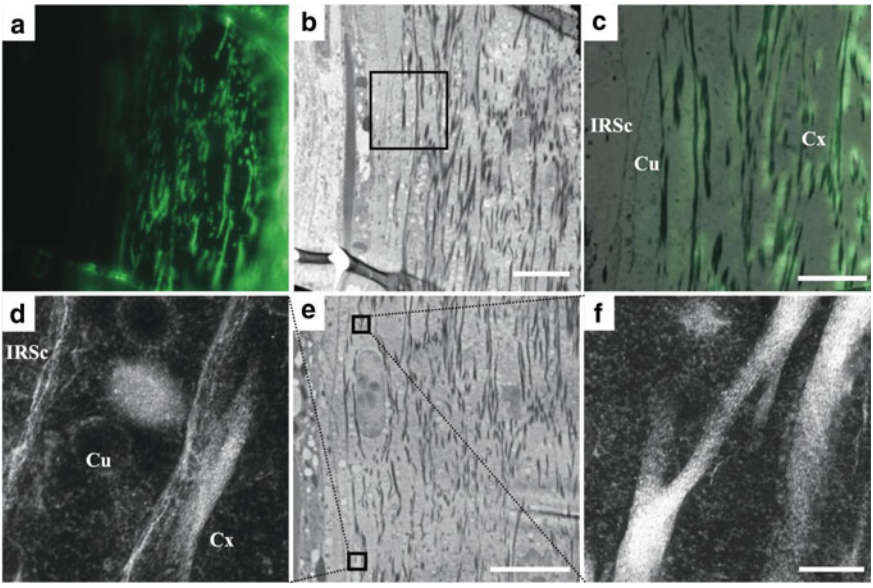


**Fig. 3** Immunolabelling of wool follicle with K85 distal of Orwin's threshold. **a** Fluorescent labelling of wool follicle in the distal keratogenous zone. **b** Electron micrograph corresponding to (**a**). **c** Correlated fluorescent and electron micrographs at high magnification from inset (**b**). Scale bar: 10 μm in (**a**, **b**) and 5 μm in (**c**, **d**). **d** Inset from (**e**) showing K85 immuno-labelled with 5 nm gold in the cortex and cuticle using ADF-STEM. **e** Micrograph of the follicle in keratogenous zone at lower magnification. **f** Inset from (**e**) showing keratin K85 localization in upper keratogenous zone. Scale bar: 10 μm in (**e**); 200 nm in (**d**, **f**)

## 4 Discussion

**Ultrastructure with Lowicryl embedding**. This is the first study to embed HPF-FS follicles in Lowicryl resin for ultrastructural immunolabelling. The structure of different cell types and cytosolic components such as the nucleus, mitochondria, keratin and trichohyalin granules were easily distinguished within the follicle. Fine details of interactions between keratin intermediate filaments (IFs) and cell junctions were also clear at higher magnification (image not shown). However, the preservation of fine sub-cellular details such as the desmosomes and interaction between IFs and trichohyalin granules were less clear compared to samples previously published from epoxy embedded sections [9].

**Primary antibody labelling**. The labelling of keratin, K85, in the ultrastructure was exclusively in the cortex and cuticle cells. These findings are in agreement with previously published studies [4, 6, 7]. Lack of staining in the dermal papilla, germinative matrix and IRS cells shows the specificity of the antibody. An increase in labelling intensity in the keratogenous zone was also observed in the present study. K81 and K86 sequentially switch upon differentiation, especially above Auber's level and keratogenous zone. Thus, the increase in labelling intensity is suggested to be an effect of epitope masking resulting in identifying a closely related K86 keratin, along with K85 [4, 6, 14, 15]. Follicles in this study were subjected to HPF-FS. The preservation of structural integrity following HPF-FS has been published recently [9]. While HPF preserves the follicle structural integrity close to native state, freeze substitution replaces vitrified ice with organic solvents at −90 °C. At such low temperatures, these fixatives remain unreactive and homogeneously diffuse through these immobilized structures. Therefore, masking of epitopes due to fixative interaction is minimal. Increased accumulation and aggregation of keratin IFs following cellular degradation could be a potential reason for the increase in K85 intensity.

**TEM processing**. Apart from fixative effects, post-staining of sections with uranyl acetate followed by lead citrate staining is a common source of artefacts. While insufficient staining results in loss of structural context, over staining could obscure the signal originating from the secondary antibody conjugated to gold nanoparticles. In addition, the size of the gold nanoparticles is often increased using a silver enhancement procedure. Although silver is a noble metal, it is not completely inert to chemical reactions. For instance, aldehydes frequently used as fixatives are known to reduce silver [16]. In recent years, DF-STEM has become a powerful tool to characterize nanogold particles labelling specific proteins. In this study, we have shown that the nanogold particles conjugated to the secondary antibody could be visualized clearly without any further staining or silver enhancement technique. In conclusion, DF-STEM reduces the need for post-preparation processing such as double staining and silver enhancement for localizing the immunolabelling. In combination with HPF-FS, it better resolves the ultrastructural details of keratin localization in wool follicles.

## References


1. Plowman JE, Deb-Choudhury S, Clerens S, Thomas A, Cornellison CD, Dyer JM (2012) Unravelling the proteome of wool: towards markers of wool quality traits. J Proteomics 75:4315–4324
2. Jones L, Rogers G, Rufaut N, Sinclair R (2010) Location of keratin-associated proteins in developing fiber cuticle cells using immunoelectron microscopy. Int J Trichol 2:89–95
3. French PW, Hewish DR (1986) Localization of low-sulfur keratin proteins in the wool follicle using monoclonal antibodies. J Cell Biol 102:1412–1418
4. Alibardi L (2017) Ultrastructural localization of hair keratins, high sulfur keratin-associated proteins and sulfhydryl oxidase in the human hair. Anat Sci Int 92:248–261
5. Westgate GE, Tidman N, Berker DD, Blount MA, Philpott MP, Leigh IM (1997) Characterization of LHTric-1, a new monospecific monoclonal antibody to the trichocyte keratin Ha1. Br J Dermatol 137:24–30
6. Langbein L, Rogers MA, Winter H, Praetzel S, Schweizer J (2001) The catalog of human hair keratins. II. Expression of the six type II members in the hair follicle and the combined catalog of human type I and II keratins. J Biol Chem 276:35123–35132
7. Langbein L, Yoshida H, Praetzel-Wunder S, Parry DA, Schweizer J (2010) The keratins of the human beard hair medulla: the riddle in the middle. J Investig Dermatol 130:55–73
8. Morgan HJ, Benketah A, Olivero C, Rees E, Ziaj S, Mukhtar A, Lanfredini S, Patel GK (2020) Hair follicle differentiation-specific keratin expression in human basal cell carcinoma. Clin Exp Dermatol 45:417–425
9. Velamoor S, Richena M, Mitchell A, Lequeux S, Bostina M, Harland D (2020) High-pressure freezing followed by freeze substitution of a complex and variable density miniorgan: the wool follicle. J Microsc 278:18–28
10. Newman GR, Hobot JA (1999) Resins for combined light and electron microscopy: a half century of development. Histochem J 31:495–505
11. Stirling JW (1990) Immuno- and affinity probes for electron microscopy: a review of labeling and preparation techniques. J Histochem Cytochem 38:145–157
12. Harland DP (2018) Introduction to hair development. In: Plowman JE, Harland DP, Deb-Choudhury S (ed) The hair fibre: proteins, structure and development. Springer Singapore, Singapore, pp 89–96. https://doi.org/10.1007/978-981-10-8195-8_8
13. Orwin DFG (1979) The cytology and cytochemistry of the wool follicle. In: Bourne GH, Danlelli JF, Jeon KW (ed) International review of cytology, vol 60. Academic Press, pp 331–374
14. Langbein L, Schweizer J (2005) Keratins of the human hair follicle. Int Rev Cytol 243:1–78
15. Moll R, Divo M, Langbein L (2008) The human keratins: biology and pathology. Histochem Cell Biol 129:705
16. Chen S, Goode AE, Skepper JN, Thorley AJ, Seiffert JM, Chung KF, Tetley TD, Shaffer MSP, Ryan MP, Porter AE (2016) Avoiding artefacts during electron microscopy of silver nanomaterials exposed to biological environments. J Microsc 261:157–166

# Volume Microscopy of Nudivirus Infected Cells


**Bruno M. Humbel, Sailakshmi Velamoor, Allan Mitchell, and Mihnea Bostina**

**Abstract** Volume microscopy is an ideal method to investigate microbial infections. In this study, we used *Oryctes rhinoceros* nudivirus (OrNV) as a model to illustrate the power of this technology in deciphering morphological changes associated with viral replication. Nudiviruses are large dsDNA rod-shaped enveloped viruses infecting a wide range of hosts. The best characterized member of the family, OrNV, infects rhinoceros beetle, a devastating pest damaging coconut and oil palm trees in Southeast Asia and the Pacific islands. Although previous electron microscopy studies have described the cellular changes associated with OrNV infection, little is known regarding the mechanism of viral assembly and egress. Here we used focussed ion beam and scanning electron microscopy to characterize the cellular remodelling associated with OrNV infection.

**Keywords** Volume microscopy · FIB-SEM · Virus assembly · Virus egress · Nudiviruses

## 1 Introduction

Volume electron microscopy enables three-dimensional visualization of biological specimens with unprecedented details [1, 2]. Ultrathin sections are only accidentally capable to capture special events such as membrane fusion sites [3]; therefore, we merely can speculate if, e.g. a vesicle has any connection to an outside organelle. Using volume microscopy we can image hundreds of sections, at a very high

B. M. Humbel
IMG, Okinawa Institute of Science and Technology, Okinawa, Japan

S. Velamoor · M. Bostina (✉)
Department of Microbiology and Immunology, University of Otago, Dunedin, New Zealand
e-mail: mihnea.bostina@otago.ac.nz

A. Mitchell · M. Bostina
Electron Microscopy, Otago Micro and Nano Imaging, University of Otago, Dunedin, New Zealand



P. Ghosal et al. (eds.), *Applications of Microscopy in Materials and Life Sciences*, Springer Proceedings in Materials 11,
https://doi.org/10.1007/978-981-16-2982-2_25

Z-resolution of few nanometers that allows to follow and reconstruct completely an organelle structure. By providing us reliable information in the third dimension no such events could escape our observation. Volume microscopy can be performed using serial sectioning TEM or using an SEM with its different applications of array tomography [4–6], serial block-face tomography [7] or focussed ion beam (FIB) tomography [8]. Although each technique has its own pros and cons [9], FIB-SEM tomography currently offers the highest voxel resolution of serial imaging modalities at $\sim 5\ nm^3$ [10]. This study demonstrates the power of FIB-SEM in obtaining detailed structural information of the mechanism of viral replication using OrNV as a model.

The *Nudivirdae* family comprises a series of diverse members of large dsDNA rod-shaped enveloped viruses reported to infect a wide range of invertebrate hosts belonging to the Coleoptera, Lepidoptera, Orthoptera, Diptera, Siphonaptera, Hymenoptera, Thysanura, Trichoptera, Neuroptera, Homoptera, Acarina, Araneina, and Crustacea. They were previously described as "nonoccluded baculoviruses". Similar to baculoviruses, nudiviruses have a circular dsDNA genome and replicate in the nuclei of host cells [11].

The best characterized member of the *Nudiviridae* family is *Oryctes* Nudivirus (OrNV), first observed in the nuclei of fat body cells of infected *Oryctes rhinoceros* beetle [12, 13]. Rhinoceros beetle is a devastating pest damaging coconut and oil palm trees in Southeast Asia and the Pacific islands. Being pathogenic to invertebrates, when orally transmitted, OrNV first infects the midgut epithelial cells and further spreads to other tissues. Since OrNV is capable of killing both adults and larvae, it is widely used as a biocontrol agent against this beetle [12]. Currently, DSIR-HA-1179 cell line, isolated from *Heteronychus arator* (HA), is the only cell line susceptible and permissive to OrNV infection [14–17]. Electron microscopy studies have established the basic steps of virus entry and exit [18]. While electron tomography is crucial for understanding the nuclear and cytoplasmic changes associated with viral replication and assembly, the limited tilt angle reduces the quality of 3D information. Here, we used FIB volume electron microscopy to characterize the membranous and cellular changes incurred during virus assembly, nucleocytoplasmic transport and viral egress following OrNV infection.

## 2 Methods

***Cell line and virus***. DSIR-HA-1179 cells were maintained at 27 °C as attached cultures in 25 $cm^2$ tissue culture flasks in TC-100 insect cell medium (Sigma) supplemented with 10% foetal bovine serum (FBS) (Life technologies, NZ). For long-term storage, $1 \times 10^7$ DSIR-HA-1179 cells were resuspended in freezing medium (TC-100, 10% FBS, 10% DMSO), allowed to freeze gradually using a "Mr. Frosty" freezing container (Nalgene) and later transferred to liquid nitrogen. Confluent monolayers of attached DSIR-HA-1179 cells at day ten of culture were treated with TrypLE™ Express as previously described [16] to dissociate the cell

monolayer into a single cell suspension. The number of cells in suspension was counted on a haemocytometer. Approximately $2 \times 10^5$ viable cells were transferred per well in a six-well plate (Day 0) in a culture volume of 2 mL and incubated for five days. At day five, the cells in one well were dissociated with TrypLE™ Express and counted. Medium was replaced, and cells were inoculated with OrNV virus (strain X2B) at a multiplicity of infection (MOI) of 2000 virus particles per cell and incubated at 27 °C. After 72 h, the insect cells were detached, briefly centrifuged, resuspended in approximately 20 µl growth medium and further prepared for microscopy. Uninfected control cells were processed in the same manner.

Oryctes nudivirus strain X2B was propagated in DSIR-HA-1179 cells. Briefly, DSIR-HA-1179 cells grown to confluency in a T75 flask were inoculated with OrNV virus stock and monitored for cytopathic effect. When the majority of cells presented cytopathic effect, the flask with cells and medium was frozen (−80 °C) and thawed at room temperature (RT) to release the virus from cells. The lysate was centrifuged for 5 min at 2500× g. Clarified lysate was quantified for OrNV infectious particles using the end-point dilution method, aliquoted, and stored at −20 °C.

***High-pressure freezing***. Approximately 0.5 µl of concentrated cells were loaded into a 200 µm deep copper membrane carriers (Engineering Office M Wohlwend GmbH, Switzerland), precoated with hexadecane (Sigma-Aldrich). The membrane carriers with the sample were then transferred into the Leica EMPACT 2 Bayonet pod. Filler solution (10% Ficoll in 0.1 M cacodylate buffer, pH 7.4) was added, and the transfer pod was torqued down and sealed. The samples were frozen using the EMPACT2 high-pressure freezing machine (Leica Microsystems, Vienna, Austria). The membrane carriers with frozen samples were removed from the transfer pod under liquid nitrogen and processed for freeze substitution.

***Freeze substitution***. For volume electron microscopy, samples were treated with various contrast enhancing agents as follows: after the acetone washes and removing the samples from the AFS machine, they were treated with 1% thiocarbohydrazine in acetone at 40 °C (Acros Organics 207,530,050) for 30 min, followed by acetone washes at room temperature and 2% $OsO_4$ in acetone at 40 °C for 30 and 60 min, respectively. Following further acetone washes at room temperature, the samples were then incubated with 2% uranyl acetate (in acetone) at 4 °C overnight. The sample was than washed twice with acetone and twice with methanol at room temperature followed by 2% lead acetate in methanol (Sigma-Aldrich 215,902) for an hour at 40 °C. This last contrasting step was followed by methanol washes, methanol/acetone and then acetone washes at room temperature. The samples were then gradually infiltrated with increasing concentrations of epoxy resin in acetone and finally embedded in Epoxy embed 812 resin (EMS EmBed 812), following manufacturer's instructions. The protocol following regular freeze substitution was based on previously described methods [19].

***Imaging and analysis***. Volume microscopy was done with a focussed ion beam scanning electron microscope (Helios 650, FEI Company, Eindhoven, The Netherlands). Milling was done with a gallium ion beam at 30 kV and 2.4 nA.

The imaging was done at 1.5 keV, 800 pA, 6144 × 4096 frame size, with 71.4 Å pixel size and 100 Å section thickness. Sequential images were aligned with IMOD using cross-correlation [20]. Manually traced segmentation of the features was carried out using "drawing" and "interpolation" in IMOD and was further refined with UCSF Chimera [21].

## 3 Results

High-pressure freezing and freeze substitution (HPF-FS) followed by volume microscopy enabled us to study the fine ultrastructural changes happening during several stages of OrNV life cycle (Fig. 1). Segmentation of the membranous and cellular structures allowed us to track changes that occurred during virus assembly, the transition via the nuclear lumen, and virion shedding to extracellular space.

***Changes in nucleoplasm***. Similar to baculoviruses, nudiviruses replicate and assemble inside the nucleus [18]. Our volume microscopy data show a significant remodelling of the nucleus during OrNV infection (Fig. 2a–c). Chromatin condenses while a large part of the nucleus is dedicated to viral replication and assembly, and it displays a less dense appearance. The nucleus becomes populated with numerous membrane structures associated either with the process of virion assembly or with the traffic across the nuclear envelope.

Numerous long tubules (Fig. 1) with dimension and structure compatible with that of the mature virions are clearly visible (Fig. 2d), and their dense interior suggests the insertion of dsDNA similar to that of full virions. Enveloped virions are present inside the nucleus either free or enclosed inside vesicles connected to the inner nuclear membrane (INM). Their origin is suggested by prominent INM invaginations that penetrate inside the nucleus and engulf virions. From this position, they can be further transported to the nuclear envelope lumen (NE).

***Nucleocytoplasmic transport***. Virions inside the NE were mostly observed inside convoluted vesicles (Fig. 2e, f). Notably, no non-enveloped capsids were observed inside the NE which indicates that during this nucleocytoplasmic traffic the virions are always presented with their original membrane derived from the nuclear tubules. Despite the numerous structural changes observed, the integrity of the nuclear envelope is maintained overall.

***Cytoplasmic changes***. Cytoplasm of the OrNV infected cells undergoes dramatic changes. We can observe large multi-membrane vesicles (MMVs) that contain enveloped virions (Fig. 2g–i) in single or convoluted membranes (Fig. 2h). Additionally, single virions are observed in the cytoplasm. The morphology of Golgi bodies looks distorted (Figs. 2i and 3e), while herniation of mitochondria (Fig. 3a, b) and releasing of small vesicles from ER (Fig. 3b, d) are also clearly visible at this resolution.

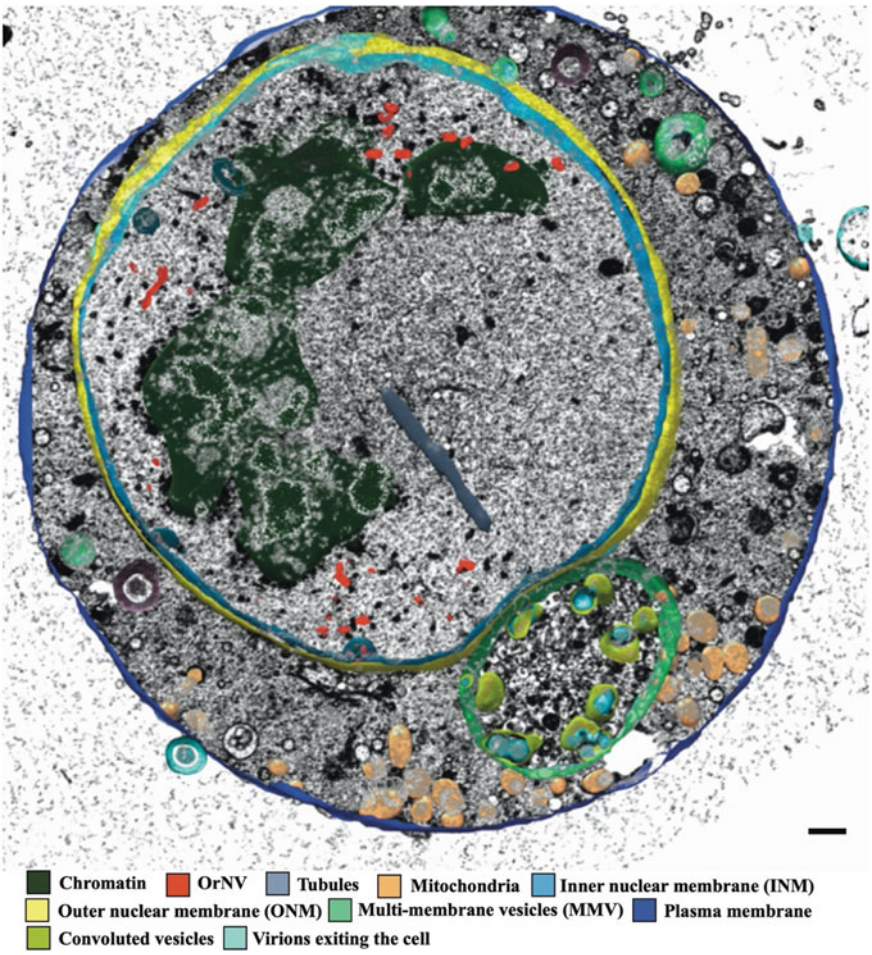


**Fig. 1** Volume microscopy of an OrNV infected cell. The thickness of the segmented section is ~420 nm. Virions assemble from long tubules clustered around macrovesicles are packaged into the nuclear lumen, and further egress into the cytoplasm. Cytoplasmic space contains numerous organelles such the mitochondria, Golgi and ER, along with numerous MMVs containing virions. Few virions, enclosed in vesicles, are seen shedding from the plasma membrane. Scale bar, 1 μm

***Viral egress***. The virions egress into the extracellular space seems to occur in an exosome-like fashion (Fig. 3a–c). Most of the observed viruses are encapsulated either in single membrane vesicles or in multi-membrane vesicles. Their fusion with the plasma membrane will allow the shedding of virions either as single mature particles or as enclosed in a cellular derived membrane (Fig. 3c, f).

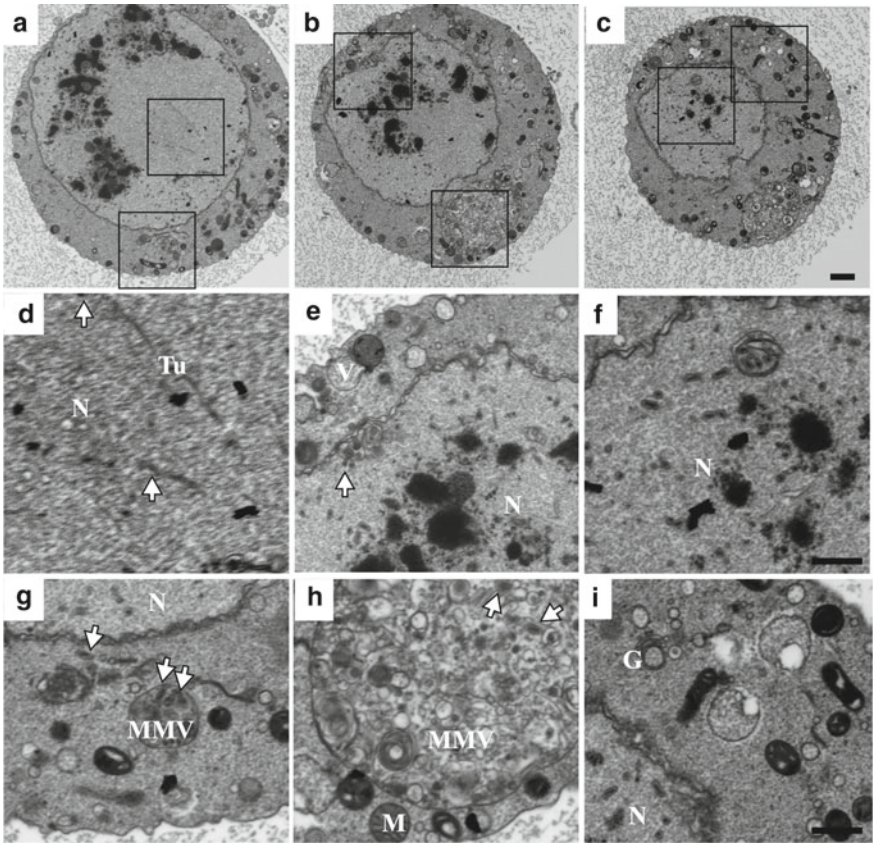


**Fig. 2** Changes in the nucleus and cytoplasm during OrNV infection. **a–c** Sequential sections through the reconstructed volume at the centre of the nucleus (N) and below, ~1 μm apart. Scale bar presents 2 μm. **d** Region displaying virions (white arrows) shedding from long tubules (Tu) inside the nucleus. **e** Virions, packaged into vesicles, fuse with the INM. **f** Vesicles enclosing virions are present inside nucleus. **g** Free-floating virions and virions enclosed in MMVs (white arrows) are observed in the cytoplasm. **h** Virions encapsulated in MMVs. **i** Despite considerable remodelling, the nuclear membrane remains intact and cytoplasmic components such as mitochondria (M) and Golgi (G) are clearly distinguishable. Enlarged views from inset (**d–i**) are 50 nm thick. Scale bar (**d–i**), 2 μm

## 4 Discussion

This study establishes volume microscopy as an ideal method to follow the process of microbial infections using OrNV infected cells as a model. Despite the structural, genetic and biological similarities shared with baculoviruses, the mechanisms of nudivirus assembly and egress poses some specific problems. The absence of occlusion bodies implies the need of supplemental membrane material to envelope individual viral capsids. By using volume microscopy, we have characterized a

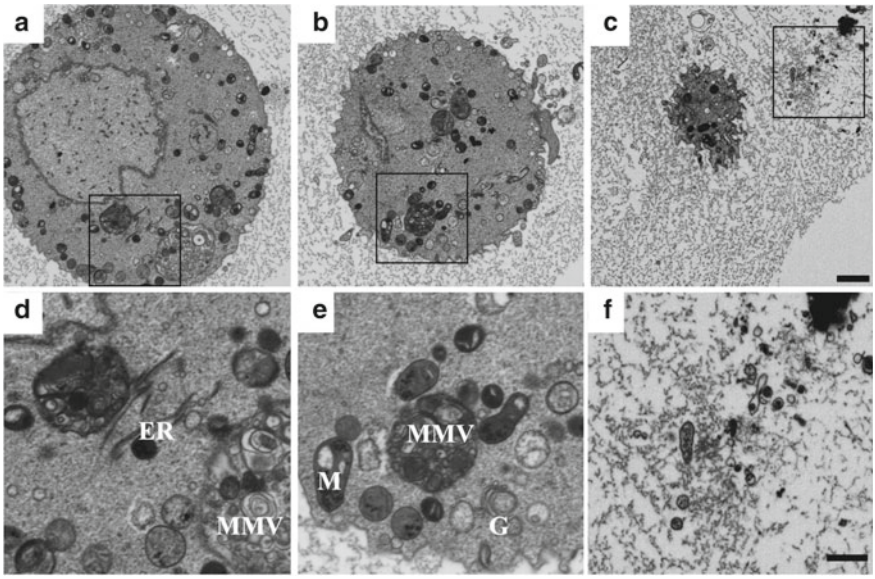


**Fig. 3** Changes in the cytoplasmic organelles following viral entry and viral exit from cytoplasm (**a**–**c**). Scale bar 2 μm. **d** Enlarged view from inset (**a**) shows macrovesicles released from ER. **e** Herniation of mitochondria and association of Golgi with vesicles are evident. **f** Single viruses enclosed inside vesicles are observed in the extracellular matrix. Enlarged images from inset (**d**–**i**) are 50 nm thick. Scale bar (**d**–**f**), 1 μm

dramatic remodelling of the nuclear landscape which brings large quantities of membrane material inside the nucleus close to viral replication sites. It also allowed to follow the trajectory of virions from the assembly site to the extracellular space. Differently from other cases of viruses replicating inside the nucleus, OrNV appears to assemble into a mature particle inside the nuclear compartment and to cross the nuclear envelope using a series of membrane vesicles, to transit through the cytoplasm inside some vesicular bodies, before being released into the extracellular space either as single virions or a as virions contained inside vesicles. The presence of long tubular membranous structures or the existence of thin connections between double membrane vesicles and the inner nuclear membrane raises challenges which volume microscopy is uniquely qualified to solve. Our sample preparation protocol and imaging parameters resulted in high-quality spatial information which permitted to describe unambiguously the nature of these structures in a way which neither EM of serial sections nor electron tomography would be capable. In conclusion, volume microscopy delivers simultaneously the high resolution needed to precisely describe subtle changes occurring inside cellular organelles and the large volumetric information necessary to obtain an adequate morphological context.

## References


1. Helmstaedter M, Briggman KL, Denk W (2008) 3D structural imaging of the brain with photons and electrons. Curr Opin Neurobiol 18:633–641
2. Kasthuri N, Hayworth Kenneth J, Berger Daniel R, Schalek Richard L, Conchello José A, Knowles-Barley S, Lee D, Vázquez-Reina A, Kaynig V, Jones Thouis R, Roberts M, Morgan Josh L, Tapia Juan C, Seung HS, Roncal William G, Vogelstein Joshua T, Burns R, Sussman Daniel L, Priebe Carey E, Pfister H, Lichtman JW (2015) Saturated reconstruction of a volume of neocortex. Cell 162:648–661
3. Heuser JE, Reese TS, Dennis MJ, Jan Y, Jan L, Evans L (1979) Synaptic vesicle exocytosis captured by quick freezing and correlated with quantal transmitter release. J Cell Biol 81: 275–300
4. Hayworth KJ, Kasthuri N, Schalek R, Lichtman JW (2006) Automating the collection of ultrathin serial sections for large volume TEM reconstructions. Microsc Microanal 12:86–87
5. Hayworth KJ, Morgan JL, Schalek R, Berger DR, Hildebrand DGC, Lichtman JW (2014) Imaging ATUM ultrathin section libraries with WaferMapper: a multi-scale approach to EM reconstruction of neural circuits. Front Neural Circuits 8:68–68
6. Leighton SB (1981) SEM images of block faces, cut by a miniature microtome within the SEM—a technical note. Scan Electron Microsc, 73–76
7. Denk W, Horstmann H (2004) Serial block-face scanning electron microscopy to reconstruct three-dimensional tissue nanostructure. PLoS Biol 2:e329
8. Kizilyaprak C, Bittermann AG, Daraspe J, Humbel BM (2014) FIB-SEM tomography in biology. Methods Mol Biol 1117:541–558
9. Titze B, Genoud C (2016) Volume scanning electron microscopy for imaging biological ultrastructure. Biol Cell 108:307–323
10. Wanner AA, Kirschmann MA, Genoud C (2015) Challenges of microtome-based serial block-face scanning electron microscopy in neuroscience. J Microsc 259:137–142
11. Wang Y, Kleespies RG, Ramle MB, Jehle JA (2008) Sequencing of the large dsDNA genome of Oryctes rhinoceros nudivirus using multiple displacement amplification of nanogram amounts of virus DNA. J Virol Methods 152:106–108
12. Payne CC (1974) The isolation and characterization of a virus from Oryctes rhinoceros. J Gen Virol 25:105–116
13. Wang Y, Bininda-Emonds OR, van Oers MM, Vlak JM, Jehle JA (2011) The genome of Oryctes rhinoceros nudivirus provides novel insight into the evolution of nuclear arthropod-specific large circular double-stranded DNA viruses. Virus Genes 42:444–456
14. Moslim R, Kamarudin N, Abd. Ghani I, Wahid MB, Jackson TA, Tey CC, Ahdly AM (2011) Molecular approaches in the assessment of oryctes rhinoceros virus for the control of rhinoceros beetle in oil palm plantations. J Oil Palm Res 23:1096–1109
15. Peddie CJ, Collinson LM (2014) Exploring the third dimension: volume electron microscopy comes of age. Micron 61:9–19
16. Pushparajan C, Claus JD, Marshall SDG, Visnovsky G (2013) Characterization of growth and Oryctes rhinoceros nudivirus production in attached cultures of the DSIR-HA-1179 coleopteran insect cell line. Cytotechnology 65:1003–1016
17. Pushparajan C, Claus JD, Marshall SDG, Visnovsky G (2017) Nutritional demands and metabolic characteristics of the DSIR-HA-1179 insect cell line during growth and infection with the Oryctes nudivirus. Vitro Cell Dev Biol Anim 53:908–921
18. Crawford AM, Sheehan C (1985) Replication of oryctes baculovirus in cell-culture—viral morphogenesis, infectivity and protein-synthesis. J Gen Virol 66:529–539
19. Webb RI, Schieber NL (2018) Volume scanning electron microscopy: serial block-face scanning electron microscopy focussed ion beam scanning electron microscopy. In: Hanssen E (ed) Cellular Imaging: electron tomography and related techniques, pp 117–148. Springer International Publishing, Cham. https://doi.org/10.1007/978-3-319-68997-5_5

20. Kremer JR, Mastronarde DN, McIntosh JR (1996) Computer visualization of three-dimensional image data using IMOD. J Struct Biol 116:71–76
21. Pettersen EF, Goddard TD, Huang CC, Couch GS, Greenblatt DM, Meng EC, Ferrin TE (2004) UCSF Chimera–a visualization system for exploratory research and analysis. J Comput Chem 25:1605–1612

# Structural Biology Research in India: A Thriving Cryo-EM Community Heralds a New Era


**Jayati Sengupta**

**Abstract** The 'resolution-revolution' in the electron cryo-microscopy (cryo-EM) field has made cryo-EM a preferred tool for determining molecular structures of intrinsically dynamic biological macromolecules, since it allows visualization of the molecular intricacies without crystallization. The significance of cryo-EM has been recognized by the scientific community, and the Chemistry Nobel Prize in 2017 was awarded to three eminent early developers of this astounding technique, Professors Jacques Dubochet, Richard Henderson and Joachim Frank. The recent APMC meeting held at Hyderabad has showcased the increasing community of cryo-EM in India. Scientists with expertise in this field have joined together in various Indian Institutes, making the cryo-EM society of India a fertile ground for new accomplishments for many years to come. I highlight here, the current status of cryo-EM in India and its prospect in contributing novel research findings to the structural biology field.

**Keywords** Indian science · Structural biology · Cryo-EM

## 1 Introduction

The Electron Microscope Society of India (EMSI) hosted the 12th Asia Pacific Microscopy Conference (APMC-2020) during 03–07 February, 2020 at Hyderabad, India. APMC-2020 has attracted researchers, academicians and industry experts from diverse backgrounds and provided a global forum for the representatives to present their research.

J. Sengupta (✉)
Structural Biology and Bio-Informatics Division, CSIR-Indian Institute of Chemical Biology, 4, Raja S.C. Mullick Road, Kolkata 700032, India
e-mail: jayati@iicb.res.in

J. Sengupta
Academy of Scientific and Innovative Research (AcSIR), Ghaziabad 201002, India



P. Ghosal et al. (eds.), *Applications of Microscopy in Materials and Life Sciences*, Springer Proceedings in Materials 11,
https://doi.org/10.1007/978-981-16-2982-2_26

Electron microscopy for life sciences was one of the theme events among diverse area of spectroscopy and microscopy applications covered in the meeting. Plenary lectures of international experts enlightened us on cutting-edge research in the cryo-EM field. The meeting gathered together researchers of the cryo-EM community of India and allowed them to report their results to the international group of experts. The conference also brought a golden opportunity to the young and enthusiastic investigators, who have joined the Indian cryo-EM group in recent years, to exchange their ideas.

Indian structural biology field bears a long tradition of X-ray crystallography. The first facility, established at the Indian Association for the Cultivation of Science (IACS), Kolkata, laid the foundation for biological crystallography. Later, Professor M. Vijayan and his colleagues were at the front line to establish X-ray crystallography as a tool for determining structures of proteins and other biomacromolecules in other Indian scientific institutions.

To my knowledge, I was the first person to come back from abroad to start a new-generation cryo-EM research. My association with cryo-EM field was started somewhat suddenly, after I got a chance to join Professor Joachim Frank's ribosome research group as a postdoctoral researcher with a vague idea about cryo-EM and its application for structure determination of biological macromolecules. A trip down memory lane brings me back to that gloomy day of February 2000 when I arrived at Frank's laboratory in Albany, New York. Eventually however, the vibrant atmosphere of the lab, brilliant co-workers, and a fabulous mentor made my days brighter and brighter. I was fortunate to take part in several groundbreaking discoveries of Dr. Frank's group that unveiled different aspects of the protein translation process. With the knowledge of single particle cryo-EM and fondness for the astonishing molecular machine ribosome, I left Frank's laboratory in 2008 and started my independent one at the Structural Biology and Bioinformatics Division of CSIR-Indian Institute of Chemical Biology (CSIR-IICB), Kolkata.

Within a year or so of my joining the institute, a talented virologist trained in structural virology lab of Prof. Jack Johnson (The Scripps Research Institute, USA), Dr. Manidipa Banerjee, joined IIT, Delhi. Following that, Dr. Vinothkumar Kutti, who was associated with the Nobel Laureate Prof. Richard Henderson, joined the National Centre for Biological Sciences (NCBS), Bangalore, and more recently two other experts, trained in renowned cryo-EM labs, Dr. Somnath Dutta and Dr. Tanweer Hussain, have joined the Indian Institute of Science (IISc), Bangalore. In due course, several other young and enthusiastic scientists from cryo-EM field joined in various Indian research laboratories. This young brigade has quickly brought the cryo-EM field in India from infancy to a fast-growing stage.

## 2 Setting up of Cryo-EM Facilities in India

Professor A. N. Ghosh, a veteran electron microscopist (an able student of Professor N. N. Dasgupta who made Asia's first electron microscope in India) first started cryo-electron microscopy, with amazing customized tools and a 120 kV

electron microscope at the National Institute of Cholera and Enteric Diseases (NICED), Kolkata. Dr. Manidipa Banerjee first established a new-generation cryo-EM facility at IIT Delhi, equipped with a 200 kV Tecnai F20 microscope. Eventually, the-then Director Professor Siddhartha Roy's fervor made it possible to establish a cryo-EM facility at CSIR-IICB too, with a 300 kV dedicated cryo-microscope Tecnai Polara in 2014.

Meanwhile, invention of direct detector revolutionized the cryo-EM field almost overnight in terms of resolution [1]. Couple of years ago, a DBT-sponsored National cryo-EM facility, equipped with direct electron detectors, had been created at NCBS (Titan KRIOS), under the leadership of Dr. Vinothkumar Kutti. More recently, another National Facility has been established at IISc, Bangalore (furnished with Talos Arctica and direct detector), under the supervision of Dr. Somnath Dutta and Dr. Tanweer Hussain (Fig. 1).


**Fig. 1** Some of the cryo-EM facilities established in India. Tecnai T20 is the first new-generation microscope installed at IIT, Delhi. At CSIR-IICB, Tecnai G2 Polara has been installed. National cryo-EM facility at NCBS, Bangalore, equipped with TITAN Krios and direct detectors, has been created. IISc, Bangalore houses the new TALOS series microscope Arctica with direct detector

## 3 Initiatives of Indian Cryo-EM Community

The first cryo-EM structure from India, even though at low resolution, was published by Professor A. N. Ghosh's group [2]. Subsequently, a cryo-EM study representing the first structure of Mycobacterium ribosomes [3] was published by my laboratory, which identified additional ribosomal RNA and protein features displaying structural diversity in bacterial ribosomes (Fig. 2a). Following resolution-revolution, several high resolution structures have come up from different groups in recent years, which reinforced our observations of additional features in mycobacterium ribosome.

Dr. Manidipa's group has produced interesting results on virus structures (Fig. 2b). One of their early works was on Flock House Virus (FHV), a model non-enveloped virus, that aimed to understand the mechanistic details of non-enveloped virus interaction with host cell membranes [4]. Quite recently,

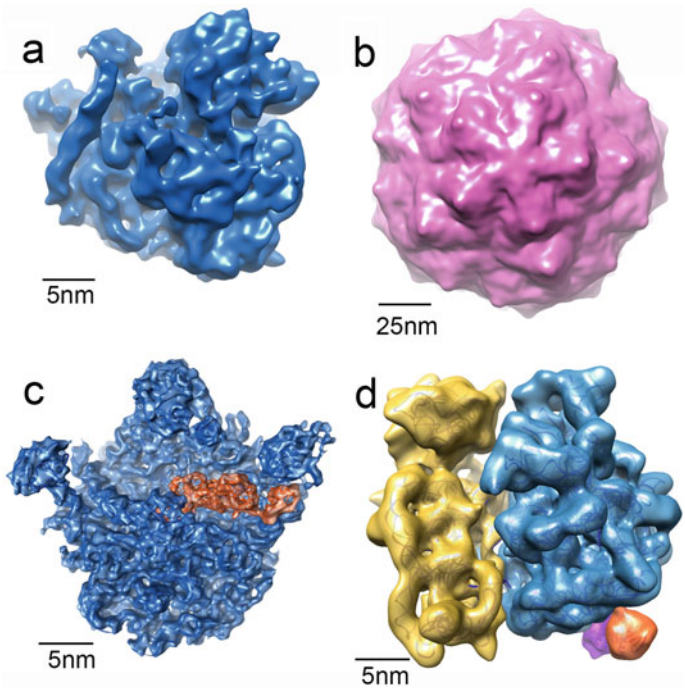


**Fig. 2** Examples of cryo-EM structures generated in India. **a** The first structure of Mycobacterium ribosome identifying additional rRNA expansions was published by our laboratory (EMD-5307). **b** A large virus structure was published by Dr. Manidipa's lab (EMD-6639). **c** The *E. coli* 50S ribosomal subunit in complex with a heat-shock related protein HflX, representing the first sub-nanometer resolution structure (~8 Å) published from India (EMD-6979). **d** The first structure of full-length protein biogenesis enzymes peptide deformylase (PDF) and methionine aminopeptidase (MetAP) in complex with *E. coli* ribosome (EMD-9753)

Dr. Janesh Kumar's group at the National Centre For Cell Science (NCCS), Pune, has published subnanometer structures of the ionotropic glutamate receptor GluD1 [5].

## 4 Cryo-EM Studies Contributed by Our Laboratory

The aim of our lab-research is to structurally characterize biological macromolecules which are important drug targets. We primarily focus on bacterial ribosome, the nanomachine for protein synthesis inside living cells. Albeit low resolutions (8–10 Å), in accordance with the current benchmark, our studies have revealed important aspects related to bacterial ribosome functions [6–8], which I have presented in my lecture at APMC-2020. We have shown ATP-dependent RNA helicase activity of a bacterial stress-related protein HflX, known as a GTPase [7]. This study has greatly enhanced our understanding of the regulatory role of non-canonical protein factors during protein synthesis under environmental stress conditions (Fig. 2c). Another study from our group (Fig. 2d) demonstrated the first structures of bacterial ribosome in complex with nascent chain processing factors [6].

Moreover, a collaborative work on the activation of transcriptional co-activator p300 mediated by the tumor suppressor protein p53, a key molecular player in cancer progression, furnished evidences for pivotal conformational changes of the macromolecules responsible for their functions [9].

## 5 High-Resolution Cryo-EM Structures Started Emerging

As stated by Dr. Vinothkumar, the scientist in charge of the national facility at NCBS (InStem), and colleagues [10], 'the resolution revolution has reached India', as several high resolution cryo-EM maps describing macromolecules involved in crucial cellular functions have been published within last one year. Dr. Vinothkumar has published very recently high resolution structures of diverse range of biomolecules [11, 12]. Dr. Saikrishnan, in collaboration with Dr. Vinothkumar, has published a 3.6 Å structure of the AAA+ domain of McrB GTPase in complex with the endonuclease McrC [13]. These emerging findings (Fig. 3) unveil mechanisms of important cellular processes and enrich the field of structural biology in India, as well as worldwide.

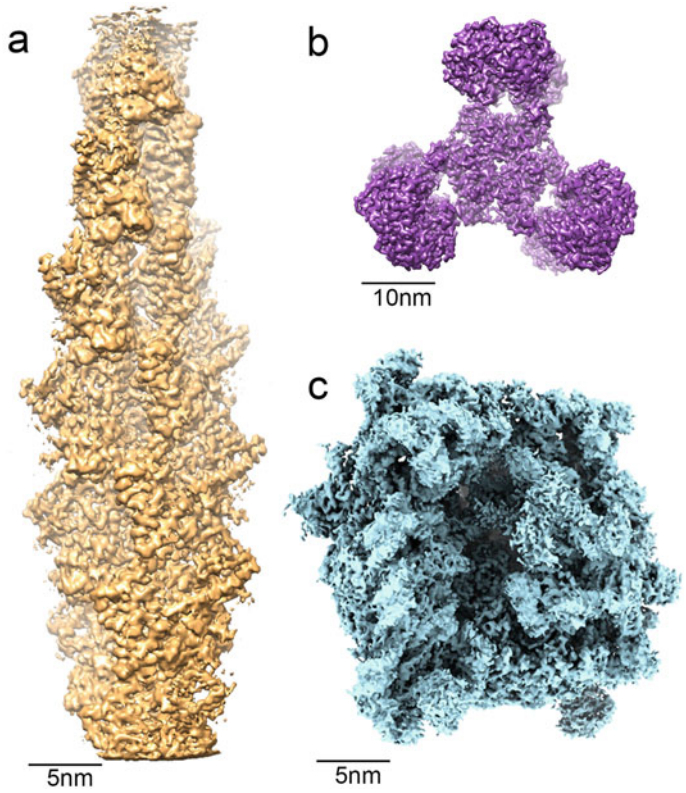


**Fig. 3** High resolution cryo-EM structures determined in India. In recent years several near-atomic resolution structures have been determined in India. For example, **a** shows 3.6 Å structure of F-actin in complex with commonly used cellular actin marker utrophin (EMD-30085), **b** is a 2.9 Å structure of PaaZ, a crucial multidomain enzyme in bacterial phenylacetic acid degradation pathway (EMDB-9873), and **c** represents a high-resolution structure (~3.4 Å) of nascent chain processing protein biogenesis factors in complex with the *E. coli* 70S ribosome generated in our lab (unpublished)

## 6 Concluding Remarks

Establishment of National facilities in India for high resolution cryo-EM holds a huge promise for conducting exciting new scientific projects. A handful of researchers, trained in the cryo-EM field, established the very first cryo-EM laboratories in India about a decade ago. Nonetheless, in recent days several young researchers have brought their expertise to numerous other research laboratories throughout India. Various Indian Institutes are now ready to set up their own state-of-the-art cryo-EM facilities. Department of Science and Technology (DST), India, has recognized cryo-EM as a cutting-edge structural biology technique and announced funding opportunity recently for establishing the new facilities, which

will certainly drive progress in the field. All-in-all, Indian structural biology community is now geared up for contributing in the field of high-resolution cryo-EM of biological macromolecules in a grand manner. We look forward to that picturesque image of cryo-EM research in India.

## 7 Conflict of Interest Statement

The author declares no conflict of interest.

**Acknowledgements** Our lab research has been supported by SERB, DST (India) sponsored projects (SB/SO/BB-0025/2014 and CRG/2019/001788), CSIR network project (UNSEEN), and CSIR-Indian Institute of Chemical Biology, Kolkata, India. I would like to thank my student Mr. Sayan Bhakta for assistance with the preparation of illustrations.

## References

1. Akbar S, Mozumder S, Sengupta J (2020) Retrospect and prospect of single particle cryo-electron microscopy: the class of integral membrane proteins as an example. J Chem Inf Model 60(5):2448–2457
2. Dutta S, Mazumdar B, Banerjee KK, Ghosh AN (2010) Three-dimensional structure of different functional forms of the vibrio cholerae hemolysin oligomer: a cryo-electron microscopic study. J Bacteriol 192(1):169–178
3. Shasmal M, Sengupta J (2012) Structural diversity in bacterial ribosomes: mycobacterial 70S ribosome structure reveals novel features. PLoS ONE 7(2):e31742
4. Bajaj S, Dey D, Bhukar R, Kumar M, Banerjee M (2016) Non-enveloped virus entry: structural determinants and mechanism of functioning of a viral lytic peptide. J Mol Biol 428(17):3540–3556
5. Burada AP, Vinnakota R, Kumar J (2020) Cryo-EM structures of the ionotropic glutamate receptor GluD1 reveal a non-swapped architecture. Nat Struct Mol Biol 27(1):84–91
6. Bhakta S, Akbar S, Sengupta J (2019) Cryo-EM structures reveal relocalization of MetAP in the presence of other protein biogenesis factors at the ribosomal tunnel exit. J Mol Biol 431(7):1426–1439
7. Dey S, Biswas C, Sengupta J (2018) The universally conserved GTPase HflX is an RNA helicase that restores heat-damaged *Escherichia coli* ribosomes. J Cell Biol 217(7):2519–2529
8. Shasmal M, Dey S, Shaikh TR, Bhakta S, Sengupta J (2016) *E. coli* metabolic protein aldehyde-alcohol dehydrogenase-E binds to the ribosome: a unique moonlighting action revealed. Scientific reports, vol 6, p 19936
9. Ghosh R et al (2019) Tumor suppressor p53-mediated structural reorganization of the transcriptional coactivator p300. Biochemistry 58(32):3434–3443
10. Subramanian R, Mayor S, Vinothkumar KR (2019) The resolution revolution reaches India. Biophys Rev 513–514
11. Kumari A, Kesarwani S, Javoor MG, Vinothkumar KR, Sirajuddin M (2020) Structural insights into actin filament recognition by commonly used cellular actin markers. EMBO J 39(14):e104006

12. Sathyanarayanan N et al (2019) Molecular basis for metabolite channeling in a ring opening enzyme of the phenylacetate degradation pathway. Nat Commun 10(1):4127
13. Nirwan N et al (2019) Structure-based mechanism for activation of the AAA+ GTPase McrB by the endonuclease McrC. Nat Commun 10(1):3058